Metallurgical mechanisms and their interactions during the annealing of cold-rolled ferrite-pearlite steels : characterization and modeling

Marc Moreno

THÈSE

Pour l'obtention du titre de :

DOCTEUR de L'UNIVERSITÉ DE LORRAINE

Spécialité : Sciences des Matériaux

Présentée par :

MARC MORENO

Mécanismes métallurgiques et leurs interactions au recuit d'aciers ferrito-perlitiques laminés: Caractérisation et modélisation

Soutenue publiquement le 18/06/2019 à Nancy devant le jury composé de :

Mme Anna FRACZKIEWICZ	Professeure à l'Ecole des Mines de Saint-Etienne, France	Rapporteur
M. Hatem ZUROB	Professeur à l'Université de Mc Master, Hamilton, Canada	Rapporteur
Mme Sabine DENIS	Professeure à l'Université de Lorraine, France	Présidente
Mme Caroline TOFFOLON	Ingénieure de Recherche au CEA, France	Examinateur
M. Frédéric BONNET	Ingénieur ArcelorMittal Maizières Research SA	Invité
M. Julien TEIXEIRA	Chargé de Recherche au CNRS, Institut Jean Lamour, France	Co-directeur de thèse
M. Sébastien ALLAIN	Professeur à l'Université de Lorraine, France	Directeur de thèse

IJL Institut Jean Lamour UMR CNRS 7198 Campus ARTEM, 54000 Nancy

Université de Lorraine – Pôle M4 : matière, matériaux, métallurgie, mécanique

ACKNOWLEDGEMENTS

First of all, I would like to thank my supervisor's team and Sabine DENIS who introduced me in the domain of the material sciences. Sébastien ALLAIN, Julien TEIXEIRA and Frédéric BONNET for the generous efforts they made in order to guaranty a constant progress of the investigations. Their impressive skills have permitted to me to always find alternative solutions to circumvent all type of issues. They also introduced me in the field of the academic publications and international meetings, being in my opinion one the most remarkable experiences of this PhD.

Secondly, I would like to thank all people who helped me to prepare experiences whose results were determining for the success of this PhD:

- Jaafar GHANBAJA and Sylvie MIGOT who helped me to prepare reliable thin foils and perform the EDXS / EELS measurements in a very enjoyable ambience.

- Carla OBERBILLIG for her huge participation. Carla carried out many interrupted heat treatments, successive metallographic preparations and SEM characterizations to enable to the investigations to respect the deadlines. This consequent work also widely contributed to the achievement of the related publications.

- Mathieu SALIB who performed useful additional verifications with EBSD to support our experimental approach.

- Benoit DENAND who gave a lot of its time to help me to deal with the numerous thermal treatments.

- Florimonde LEBEL and Erwan ETIENNE who taught me many techniques to prepare samples intended to metallographic observations.

- Guillaume GEANDIER, whose skill in the X-Ray Diffraction was a prerequisite to obtain valuable results from the HE-XRD experiments.

Lastly, I would like to thank Astrid PERLADE, Jean-Christophe HELL, Artem ARLAZAROV, Thierry IUNG, Michel SOLER and Patrick BARGES for the fruitful discussions on different topics in context of internal of international meetings.

I have special thoughts for my lovely workmates, who have been like sunbeams passing through a cloudy sky: Mathias LAMARI, Meriem BEN HAJ SLAMA, Arnaud VOIGNIER, Gaël PIERSON, Hélène ANSELMI, Solenne COLLOMB, Cécile RAMPELBERG, Jérémy CHAULET, Joseph ANTOINNE, Hélène QUEHEN, Morgan GOETZ, Nazim ABDEDOU, Dorra IBRAHIM, Léa DECULTOT and Raphaël MARIN.

I would like to thank again Julien TEIXEIRA and Sébastien ALLAIN for their support in the redaction of the manuscript.

RESUME FRANÇAIS

Préambule

Ces travaux de thèse ont été financés par ArcelorMittal Maizières Research SA et le CNRS dans le cadre d'une convention de recherche. Les expériences de ce travail ont été réalisées à l'Institut Jean Lamour (MET), à ArcelorMittal (MEB) et sur la ligne de lumière synchrotron DESY à Hambourg dans le cadre d'un projet DOOR.

Introduction

Les aciers Dual Phase (DP) sont très utilisés sous la forme de tôles minces dans l'industrie automobile en raison de leur excellent compromis résistance/ductilité et donc pour leur potentiel d'allègement.

Les aciers DP présentent stricto sensu une microstructure biphasée, constituée d'une matrice ferritique de morphologie polygonale (polycristalline) et d'un réseau d'ilots martensitiques riches en carbone. La fraction de cette dernière phase peut être très variable d'un acier DP à un autre (de 5 à 15% typiquement) en fonction de la résistance visée. En première approximation, les aciers DP peuvent être vus comme des microstructures composites avec une matrice ferritique molle et des renforts martensitiques durs. En pratique, il est important de noter que les aciers DP industriels peuvent aussi contenir une fraction significative de bainite.

Il est bien établi que les propriétés mécaniques de traction des aciers DP dépendent principalement de leur fraction de martensite et de leur teneur en carbone. Allain *et al*. [ALL'15] ont montré par exemple, que la sensibilité de la résistance mécanique à cette fraction pouvait attendre 15 $MPa.\%^{-1}$ pour un acier bas carbone. Cette forte sensibilité explique la flexibilité de ce concept microstructural pour atteindre une large gamme de propriétés mécaniques.

La nature composite des aciers DP explique aussi leur faible et souvent imprévisible résistance à l'endommagement (rupture, ténacité). Cette dernière propriété dépend de la nature et de la fraction des phases mais aussi de leurs tailles, de leurs morphologies et leurs distributions spatiales. Pour un fabricant d'aciers, Il est donc important que non seulement la fraction de martensite soit parfaitement respectée lors de l'élaboration d'un acier DP, mais aussi que l'on puisse mettre sous contrôle d'autres paramètres comme la morphologie ou la topologie des microstructures.

Les bobines d'aciers Dual-Phase industriels de faible épaisseur sont élaborées par coulée continue, laminage à chaud et froid suivis d'un recuit continu. Cette dernière étape de recuit est l'étape clef pour la formation des microstructures DP. Durant ce traitement thermique, la bande est chauffée puis maintenue dans le domaine intercritique pour former une microstructure ferrito-austénitique avant un refroidissement au cours duquel l'austénite se transforme principalement en martensite. La morphogénèse de la structure ferrito-austénitique conditionne donc en grande partie les propriétés finales du produit.

Les bandes aciers soumises à ce recuit sont issues d'un processus de laminage à chaud et à froid. Elles présentent donc une microstructure ferrito-perlitique déformée (NB : la perlite est une famille lamellaire de ferrite et de cémentite). Différents mécanismes seront donc à l'œuvre lors du recuit intercritique d'une telle microstructure, comme la maturation de la cémentite, la restauration et la recristallisation de la ferrite et la transformation austénitique. Comme tous ces mécanismes métallurgiques sont susceptibles d'interactions, ils sont extrêmement sensibles à la vitesse de chauffe utilisée [HUA'04].

Dans les mécanismes précités, l'élément d'alliage manganèse joue un rôle clef. Gouné *et al*. [GOU'12] ont montré par exemple que si la cémentite est fortement enrichie avant la transformation austénitique, les cinétiques de dissolution concomitantes de cette dernière s'en trouvent fortement réduites. En conséquence, les mécanismes actifs lors du recuit dépendront de l'état de la microstructure élaborée en tôle à chaud, ce que l'on appelle un effet d'héritage.

Dans ce travail de thèse, nous avons donc cherché à caractériser *in situ* ou à différentes échelles ces mécanismes métallurgiques, à comprendre leurs interactions grâce à des modèles thermocinétiques et à proposer des modèles opérationnels afin de piloter une possible production industrielle.

Ce manuscrit est divisé en 5 chapitres. Nous ne présenterons pas de chapitre dédié à l'étude de la bibliographie compte tenu du grand nombre de mécanismes en jeu. Nous avons fait au contraire le choix de proposer des états de l'art et des discussions sur chacun d'eux dans les chapitres qui leur sont consacrés.

Après un premier chapitre dédié aux techniques expérimentales et de modélisation utilisées, le second chapitre de ce travail s'intéresse principalement à la caractérisation expérimentale en microscopie électronique à balayage (MEB) de la morphogénèse des microstructures ferrito-austénitiques. Le troisième chapitre est une étude détaillée en Microscopie Electronique à Transmission (MET) et par modélisation thermocinétique (ThermoCalc, DICTRA) de la composition des carbures tout au long du processus, du laminage à chaud au recuit. Restauration et recristallisation sont étudiées au chapitre 4 principalement par Diffraction des Rayons X à Haute Energie (DRXHE) *in situ* sur ligne de lumière synchrotron et modélisées par une approche originale à champs moyens. Enfin, le chapitre 5 propose une étude thermocinétique sous DICTRA pour comprendre les cinétiques de transformation austénitique en fonction des vitesses de chauffe. Cette approche est novatrice à plusieurs titres : elle repose sur la prise en compte des carbures intergranulaires de la ferrite, elle a été conduite en conditions réellement anisothermes et elle propose une analyse fine des conditions d'interface (transition LE/LENP) associées au manganèse, élément clef de la composition de ces alliages.

Chapitre I : Techniques expérimentales et de modélisation utilisées

Le chapitre présente les techniques expérimentales et de modélisation commerciales utilisées dans ce travail de thèse.

L'acier étudié a été fourni par le partenaire industriel de cette étude sous la forme d'une tôle à chaud industrielle. Ce semi-produit est destiné à la production d'un acier DP600 et présente la composition suivante : Fe-0.1C-1.9Mn-0.2Cr-0.2Si (en % massique). Pour les besoins de l'étude, l'acier a été laminé à froid en laboratoire à deux différents taux de réduction (30 et 60%). Les simulations de recuit ont été conduites sur des dilatomètres, pour permettre des observations métallographiques ou pour réaliser des essais *in situ*.

Les échantillons issus de ces traitements thermiques ont été observés soit en MEB (JEOL JSM-IT300 / XL-30 FEG-SEM) conventionnel après attaque (chapitre 2) ou par EBSD (chapitre 4), soit en MET (chapitre 3). La MET (JEOL ARM 200F FEG) a principalement servi à mesurer les gradients de composition en éléments d'alliage dans les carbures en EDX, donc à l'échelle nanométrique. Une autre partie importante de ce travail de thèse a été conduit par DRXHE sur ligne de lumière synchrotron (DESY Petra-III ligne P-07 à Hambourg) pour suivre in situ les processus de restauration, recristallisation et transformation de phase au cours de recuits de notre acier [MOR'18]. La DRXHE a été réalisé en transmission selon une configuration de diffraction de poudres en lumière monochromatique (100 keV) avec un détecteur 2D pour capter des anneaux de Debye-Scherrer complets. Le flux incident et la qualité

du détecteur utilisé permettent une fréquence d'acquisition de 10 Hz et donc de suivre en temps réel les évolutions métallurgiques de nos échantillons lors du recuit. Les techniques de dépouillement des spectres de diffraction pour caractériser les phases en présence sont aussi détaillées dans ce chapitre (intégration circulaire, affinement Rietveld principalement).

La seconde partie de ce chapitre est consacrée aux techniques de modélisations thermocinétiques commerciales utilisées. Dans ce travail, nous avons principalement fait appel à ThermoCalc et DICTRA dans leurs versions 2017a et aux bases de données TCFE9 pour les équilibres et MOBFE2 pour les mobilités. Ces deux logiciels ont été principalement utilisés dans le chapitre 3 pour étudier les mécanismes en enrichissement en manganèse des carbures entre le laminage à chaud et le recuit et dans le chapitre 5 pour étudier la transformation austénitique et la dissolution des carbures.

Chapitre II : Morphogénèse des microstructures lors d'un recuit intercritique

Le second chapitre de cette thèse aborde la morphogenèse de la microstructure ferrito-austénitique pendant le recuit intercritique de la microstructure initiale ferrito-perlitique laminée à froid, c'est-à-dire des différents mécanismes métallurgiques et de leurs interactions expliquant la morphologie et la topologie des phases après transformation.

Il s'agit d'un sujet clé pour les sidérurgistes parce que les configurations des installations industrielles sont telles que les interactions peuvent être faibles ou fortes selon la technologie de chauffage utilisée. La microstructure de ferrite/austénite présente une configuration « en collier » après chauffage lent, alors que la microstructure est « en bande » après un chauffage rapide.

Les microstructures ferrito-perlitique de cette étude sont produites lors de l'étape de laminage à chaud par décomposition de l'austénite à haute température. La perlite lamellaire se forme sous la forme d'ilots après la transformation ferritique pro-eutectoïde et juste avant l'étape de bobinage de chaud. Ces deux transformations s'accompagnent aussi de la précipitation de carbures isolés entre les grains de ferrite dont les mécanismes sont peu étudiés. Dans l'acier de notre étude, environ 1/3 du carbone de l'alliage est présent dans ces carbures qui jouent, selon nous, un grand rôle dans le processus. Notre acier après laminage à chaud présente des tailles de grains ferritiques de l'ordre de 5 µm, une fraction de perlite lamellaire de 16 % avec un espacement interlamellaire de 82 nm. Les ilots perlitiques se trouvent généralement dans des zones ségrégées positivement en manganèse (typiquement 2.2 %Mn au lieu de 1.9% en nominal) issue de la solidification. Les carbures isolés intergranulaires se présentent principalement sous la forme de filaments avec une taille équivalente de 90 nm environ.

Le laminage à froid induit une déformation plastique sévère des phases en présence (120% de la ferrite et 67% de la perlite, soit 106% en moyenne) et s'accompagne d'une fragmentation des carbures lamellaires. Ces carbures se retrouvent alors distribués autour des grains de ferrite déformés et donc principalement alignés dans la direction de laminage.

Notre état de l'art montre qu'il n'y aucun consensus à l'heure actuelle sur comment interagissent les mécanismes à l'œuvre pendant le chauffage (maturation des carbures, germination et croissance de l'austénite, germination et croissance des grains de ferrite recristallisés) et comment ils conduisent aux différentes morphologies observées. Mêmes les modèles à champs locaux ne permettent pas d'expliquer toutes les observations expérimentales. Dans les années 80, les travaux pionniers de Garcia *et al*. [GAR'81] ont montré que la germination de l'austénite dans les aciers Fe-C-Mn déformés se produisait tout d'abord sur les joints de grains de la ferrite, avant la transformation des ilots perlitiques. Huang *et al*. [HUA'04] considèrent par exemple que la nucléation ne peut se produire que sur les joints de grains recristallisés et donc sur des interfaces immobiles. Thomas *et al*. [TOM'18] et Chbihi *et al*. [CHB'14] au contraire suggèrent une nucléation sur des sous-grains et sur des particules de cémentite et Li *et al*. [LI'13] sur les carbures aux joints de grains ferritiques, en particulier aux joints triple. Selon les différents auteurs, la croissance de ces grains austénitiques peut être favorisée par une diffusion du carbone élevée soit dans les grains déformés de ferrite, soit aux joints de grains. Tous les auteurs s'accordent par contre sur le fait que la réversion de la perlite est très rapide et que l'austénite ainsi formée conserve la morphologie en bande des ilots perlitiques quelles que soient les conditions de chauffage.

Nous avons donc conduit notre propre étude microstructurale systématique en MEB, pour comprendre comment les microstructures évoluent de façon qualitative en fonction de la température selon deux vitesses de chauffe. Ce chapitre introduit tous les concepts nécessaires pour comprendre les études détaillées dans les chapitres suivants ; l'évolution de la composition des carbures au chapitre 3, la recristallisation au chapitre 4 et la transformation austénitique au chapitre 5.

Au cours du chauffage, les microstructures ferrito-perlitiques subissent de fortes évolutions avant toute transformation austénitique. Pour les deux vitesses de chauffage considérées (3 et 30°C.s^{-1}), les lamelles de cémentite dans la perlite se fragmentent et se sphéroïdisent rapidement. La coalescence des carbures commence tout juste à 700°C pour les faibles vitesses de chauffe. A faible vitesse de chauffe, la ferrite est quasiment recristallisée à 700°C. La population des carbures dans la matrice ferritique semble avoir été redistribuée mais les plus gros carbures se situent toujours en position intergranulaire. A forte vitesse, la matrice commence tout juste à recristalliser à 700°C. Les carbures isolés de la matrice ont sphéroïdisé mais peu évolué en termes de distribution et se situent toujours principalement aux anciens joints de grains de la ferrite déformée.

Quand la microstructure ferrito-perlitique est chauffée lentement (3°C.s^{-1}) dans le domaine intercritique, la germination de l'austénite commence aux joins de grains ferritiques de la matrice recristallisée vers 710° C, apparemment sur les carbures intergranulaires, même si nous n'apportons pas de preuve définitive. La croissance des grains est favorisée par la diffusion aux joints de grains qui produisent dans certains cas des morphologies en films. La nucléation de nouveaux grains et leurs directions de croissance privilégiée conduisent à la formation rapide d'une couche continue d'austénite sur ces joints, caractéristique de la microstructure « en collier ». Les carbures intra-granulaires peuvent être des sites de germination mais sans possibilité de croissance (par manque de carbone disponible très probablement).

La transformation des ilots perlitiques est rapide et se produit vers 740°C. Cette transformation produit des structures austénitiques allongées qui croissent ensuite pendant le chauffage et le maintien, alors que la croissance de l'austénite en collier semble réduite au-delà de 750°C.

Quand la microstructure ferrito-perlitique est chauffée rapidement (30°C.s^{-1}) dans le domaine intercritique, la recristallisation commence concomitamment à la transformation de phase vers 720°C. Comme à basse vitesse, la germination de l'austénite commence d'abord sur les carbures intergranulaires. La seule différence est que ces carbures sont alignés sur les joints de grains déformés. En conséquence, la croissance des grains d'austénite produit une structure alignée caractéristique de la microstructure en bande. Ce processus est renforcé par le fait que les ilots perlitiques qui se transforment vers 740°C environ produisent aussi des structures austénitiques très allongées.

Les observations que nous avons pu conduire dans ce chapitre sont en accord avec le processus proposé par Li *et al*. [LI'13], à la différence près que nous n'avons pas mesuré de différences significatives dans les évolutions de fraction transformée en fonction de la température pour les deux vitesses de chauffage. Il apparait de plus que les différences de topologie induite par les deux vitesses s'amenuisent au fur et à mesure que la transformation avance, en particulier lors d'un maintien à haute température (800°C-600s). Les aspects cinétiques de la transformation seront traités en détail dans le chapitre 5.

La figure 1 montre des micrographies MEB après attaque caractéristiques des différents états discutés, i.e. avant transformation (700°C), à la fin du chauffage (environ 770°C) et à la fin du maintien (800°C-600s). L'attaque chimique permet de révéler les grains et sous-grains de la ferrite et la présence d'austénite.

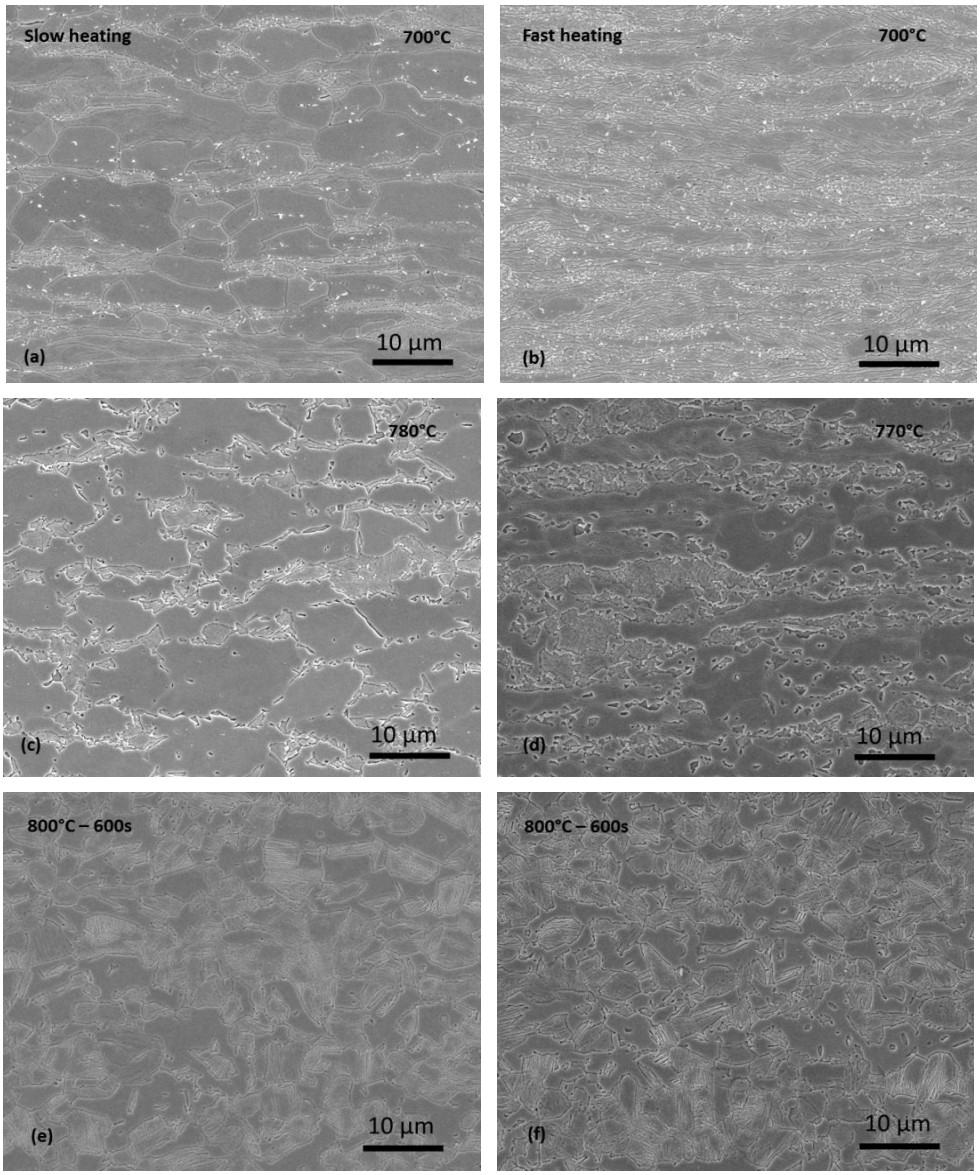

Figure 1: Micrographie MEB d'échantillons de l'acier étudié après attaque. Les échantillons ont été traités thermiquement pour reproduire des cycles de recuit interrompu avec deux vitesses de chauffage. La martensite, révélée par l'attaque chimique, indique la position de l'austénite à haute température. Les carbures apparaissent en contraste clair et les joints/sous-grains de la ferrite sont aussi attaqués. La colonne de gauche correspond à une vitesse de chauffe lente ($3°C.s^{-1}$) et celle de droite à une chauffe rapide ($30°C.s^{-1}$). (a)-(b) chauffe à 700°C (d)-(d) chauffe à 770°C/780°C (e)-(f) chauffe à 800°C puis maintien à 800°C durant 600s.

Notre étude a mis en lumière le rôle crucial des carbures isolés sur le processus d'austénitisation. C'est pour cela que nous présenterons une stratégie de modélisation des cinétiques au chapitre 5 dans laquelle carbures isolés et ilots perlitiques sont étudiés distinctement.

Chapitre 3 : Evolution de la composition de la cémentite

La microstructure de carbures (perlite et carbures isolés) héritée du laminage à chaud a un grand effet sur la distribution spatiale de l'austénite lors du recuit, car ce sont des sites privilégiés de nucléation. Beaucoup d'études comme celle de Gouné *et al.* en 2012 [GOU'12] ont aussi souligné que la composition en

manganèse de la cémentite avait un grand rôle dans la cinétique de dissolution des carbures et donc sur la cinétique de transformation. C'est pour cette raison qu'il nous a semblé important d'étudier comment la composition des carbures évolue lors du recuit. Ce travail nous a montré que pour comprendre les niveaux d'enrichissement et gradients locaux observés expérimentalement lors du recuit, il est aussi nécessaire d'étudier les conditions de formation des carbures au laminage à chaud. Dans ce chapitre, on discutera principalement du manganèse, mais des informations intéressantes sur le comportement du Si ou du Cr ont été aussi obtenues d'un point de vue expérimental.

Des observations en microscopie électronique à transmission ont été conduites pour mesurer la composition chimique locale des carbures dans différents échantillons : à l'état brut de tôle à chaud industriel (après laminage, bobinage et refroidissement lent) et après chauffage à 700°C à deux différentes vitesses de chauffage (3 et 30°C.s^{-1}). Pour compléter cette étude, nous avons aussi simulé un état microstructural représentatif des conditions de formation de perlite (vers 570°C lors du laminage à chaud) sans bobinage et sans refroidissement lent.

Cette étude expérimentale confirme que la transformation perlitique lors du laminage à chaud se déroule bien avec partition, comme suggéré par Chance et Ridley [CHA'81]. Les lamelles de cémentite montrent en effet des enrichissements uniformes de l'ordre de 6.5% Mn. Nous avons pu retrouver ce niveau de partition grâce à des calculs thermodynamique réalisés sous ThermoCalc considérant des équilibres locaux aux interfaces entre ferrite/cémentite/austénite, selon l'approche de Hutchinson *et al.* [HUT'04], modifiée par Pandit et Bhadeshia [PAN'11]. Il est aussi fortement probable que les carbures isolés qui germent à des températures proches présentent des enrichissements similaires dès leur formation.

La composition issue de la partition est loin de correspondre à celle de l'équilibre thermodynamique entre ferrite et cémentite. Lors de l'étape ultérieure de bobinage et de refroidissement, entre 570°C et la température ambiante, les carbures vont progressivement s'enrichir en manganèse. Toutefois, ce processus est limité par la faible diffusion du manganèse dans la cémentite à ces températures. Dans l'état tôle à chaud, les carbures présentent de forts gradients de composition en manganèse, comme le montre la Figure 2. La composition des interfaces est gouvernée par un équilibre local et atteint des valeurs proches de 12%. Les gradients de composition s'étendent sur 15 nm environ et montrent que la composition à cœur des carbures a peu évolué depuis leur formation.

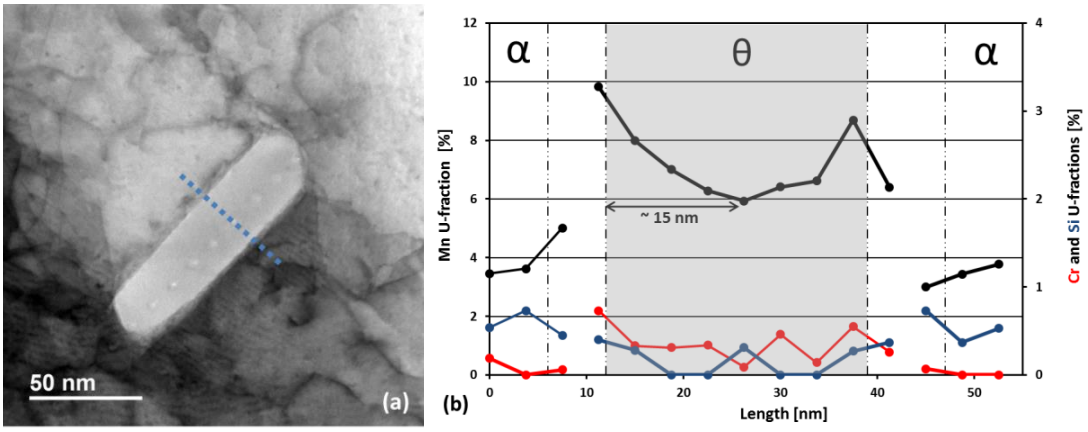

Figure 2: (a) Micrographie MET en champ d'un clair d'un carbure lamellaire dans l'état tôle à chaud (après laminage à chaud et bobinage industriel) (b) Profil de composition en manganèse, chrome et silicium le long de la ligne pointillée bleu de la figure (a).

Lors d'un chauffage ultérieur à 700°C à faible vitesse, les carbures vont continuer à s'enrichir et on observe des profils de composition uniforme dans les carbures autour de 11%. Il semblerait donc que les carbures atteignent leur composition d'ortho-équilibre en manganèse lors d'un chauffage lent. Lors d'un chauffage rapide, l'équilibre ne peut être atteint et les carbures conservent leurs gradients de composition hérités de la tôle à chaud. Ces informations sont précieuses car elles vont permettre de fixer les compositions chimiques des carbures qui seront utilisées pour les calculs de dissolution et de transformation austénitique au chapitre 5, en fonction des conditions de chauffe.

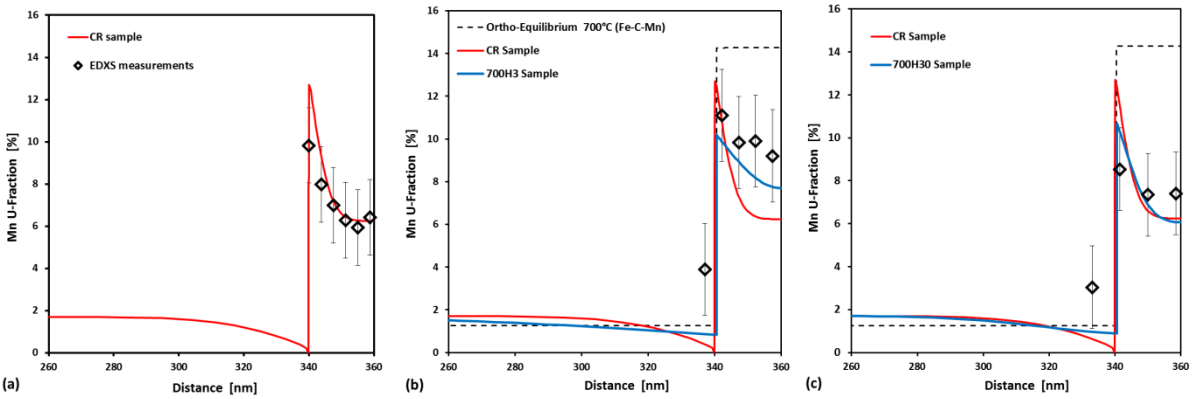

Figure 3: Profil de composition en manganèse mesurés (losange) et calculés (en rouge ou en bleu) avec DICTRA dans des particules de cémentite (a) à l'état tôle à chaud, (b) à 700°C après une chauffe lente, et (c) à 700°C après une chauffe rapide.

Des simulations DICTRA ont été conduites pour reproduire et comprendre la formation de ces gradients. Afin de reproduire les observations expérimentales, en particulier les gradients de diffusion observés à l'état tôle à chaud (cf. Figure 2), il a été nécessaire de réévaluer le coefficient de diffusion du manganèse de la cémentite (données MOBFE2 – terme pré-exponentiel multiplié par 2000) comme l'ont fait par exemple Wu *et al.* [WU'18]. Les résultats des simulations de profils sont représentés sur la Figure 3 et montrent une bonne adéquation avec les observations expérimentales. Cette comparaison montre toutefois qu'une réévaluation plus poussée de l'énergie d'activation de la diffusion du manganèse est probablement nécessaire pour pourvoir simuler convenablement tout le domaine d'étude. Ces travaux à la fois expérimentaux et de modélisation ont été publiés récemment dans Materialia [MOR'19].

Un modèle de diffusion en 1D par différence finie a été enfin développé pour reproduire les résultats DICTRA une forte efficacité calculatoire. Malgré sa simplicité, il permet de reproduire très fidèlement les résultats de DICTRA avec des temps de calcul réduits quel que soit le trajet thermique suivi.

Chapitre 4 : Restauration et Recristallisation

Dans le chapitre 2, nous avons montré que la recristallisation de la structure ferritique jouait un grand rôle dans la formation de la microstructure austénitique et en particulier d'un point de vue topologique. Dans ce travail, nous avons donc cherché à mesurer et prévoir ce processus. C'est un mécanisme de formation de nouveaux grains exempts de défaut par germination/croissance et qui trouve se force motrice dans les nombreux défauts (dislocations, sous-joints) créés lors du laminage à froid de la microstructure ferrito-perlitique. De ce fait, il entre en compétition avec la restauration qui consiste en une réduction de la densité de défauts par des processus diffusifs comme la montée de dislocations.

D'un point de vue expérimental, nous avons développé une approche cohérente en DRXHE qui nous permet de suivre simultanément restauration, recristallisation et transformation de phase en une seule expérience [MOR'18]. Les résultats relevant des transformations de phases seront présentés et discutés au chapitre 5.

L'état de restauration de nos échantillons a été suivi en observant la largeur des pics de diffraction de la ferrite. En effet, selon les travaux pionniers de Williamson et Hall [WH'53], on peut relier la largeur à mi-hauteur des pics à un état de déformation moyen de la phase considérée. Couplée à l'équation de Smallman [SMA'57], la densité de dislocations dans la ferrite peut être estimée tout au long d'un recuit. Des techniques plus précises auraient pu être mises en œuvre comme la Convolutional Multiple Whole Profile fitting (CMWP) [RIB'14] mais notre approche de premier ordre donne des résultats cohérents avec notre modèle micromécanique [BOU'02] et est suffisante observer un possible impact sur la recristallisation.

L'étude de la recristallisation nécessite le plus souvent des études microstructurales ou mécaniques post mortem sur des échantillons et peu de techniques in situ sont disponibles. Nous avons donc développé notre propre technique en s'inspirant des travaux de Jensen et al. [POU'11] pour suivre la recristallisation de nos échantillons. Cette technique consiste à dénombrer les taches de diffraction individuelles intenses qui apparaissent sur les anneaux de diffraction à cause de l'apparition des nouveaux grains recristallisés. La figure 4 montre ces taches sur un anneau de Debye-Scherrer 200 de la ferrite d'un échantillon à 700°C après un chauffage lent. La cinétique d'apparition de ces taches a été déterminée sur un signal intégré, comme celui présenté sur la figure 4(b).

Notre nouvelle approche a été testée sur des traitements thermiques en conditions anisothermes mais aussi sur une série de traitements thermiques isothermes modèles. Ce travail de validation a fait apparaitre que notre méthode permet de déterminer uniquement le comportement de la ferrite, car la perlite ne recristallise pas quelle que soit la vitesse de chauffe. De plus, par construction, elle est sensible principalement au flux de germination des grains recristallisés. Elle ne permet donc de déterminer une cinétique de recristallisation que si le processus de croissance des grains est limité, ce qui semble être le cas dans nos travaux. Cette nouvelle méthodologie mériterait sans nul doute des travaux de validation expérimentaux et théoriques plus poussés.

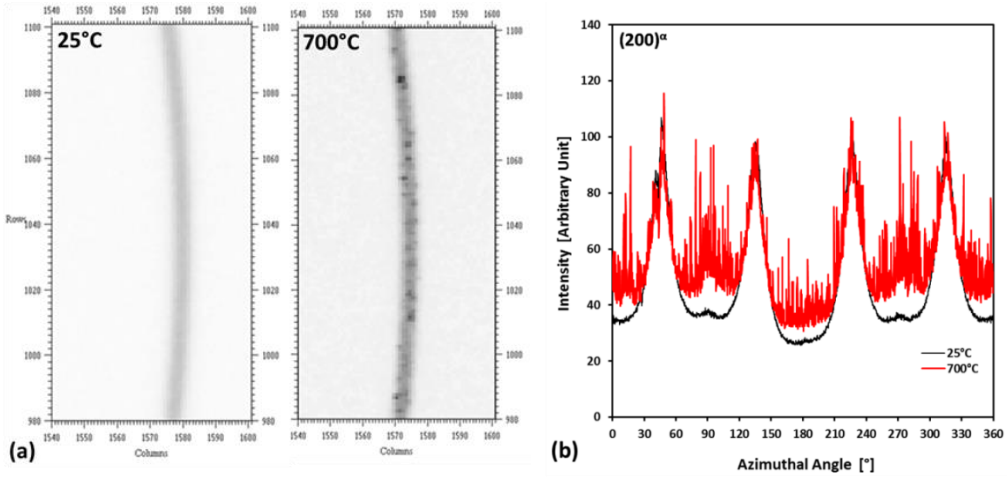

Figure 4 : (a) Anneaux de Debye-Scherrer 200 de la ferrite d'un échantillon à 25°C et à 700°C montrant des taches isolées dues aux nouveaux grains recristallisés (b) Intensités intégrées le long des anneaux de la figure précédente. Les quatre fluctuations principales à 25°C correspondent à des surintensités dues à la texture cristallographique. Les petites fluctuations observées sur le spectre rouge correspondent aux tâches isolées de la figure précédente.

Cette nouvelle méthode nous a permis d'établir que l'acier de l'étude après un taux de réduction commence à recristalliser dès 675°C à faible vitesse de chauffe. La recristallisation se termine vers 700°C comme le montre nos observations microstructurales. A haute vitesse, ce processus est décalé de 725°C à 775°C environ.

Un modèle à base physique à champ moyen a été développé pour prédire les cinétiques de restauration et de recristallisation, mais aussi les tailles de microstructures résultantes. Ce type de modèle permet d'éviter le recours à des modèles empiriques numériquement très efficaces mais qui nécessitent une calibration au cas par cas.

L'évolution de la densité de dislocations au cours du recuit a été modélisée en premier lieu car elle conditionne la force motrice pour la recristallisation. L'approche originale de Friedel [FRI'64] a été retenue car elle permet une description des tendances satisfaisante avec peu de paramètres d'ajustement. La Figure 5 montre les évolutions des densités de dislocations mesurées et calculées en fonction de la température lors de la chauffe pour deux vitesses de chauffe. Cette figure confirme qu'une forte vitesse de chauffe retarde bien la restauration. Le flux de germination des nouveaux grains recristallisés est ensuite calculé en considérant qu'un sous-grain de ferrite peut constituer un germe que s'il atteint une taille critique d'après la théorie SIBM (Strain Induced Boundary Migration). Le modèle utilisé est directement inspiré des travaux de Zurob *et al.* [ZUR'06, REH'13]. La cinétique de recristallisation globale est déterminée par la théorie des volumes étendus, en tenant compte d'une taille de grains moyenne, qui

dépend de la cinétique de croissance des grains déjà germés mais aussi du flux de germination. La loi de mobilité pour la croissance est tirée des travaux de Sinclair *et al.* [SIN'07] et a été calibrée sur les données expérimentales de l'étude. La Figure 5(a) montre les cinétiques de recristallisation expérimentales et prédites par le modèle pour deux vitesses de chauffage sur l'acier étudié. L'accord obtenu est particulièrement notable. Les tailles de grains recristallisés prédites par le modèle sont aussi en bon accord avec les données expérimentales.

Les capacités de prédiction du modèle ont été finalement éprouvées avec succès en étudiant l'effet du taux de réduction au laminage à froid sur la cinétique de recristallisation. Un décalage de 30°C dans la cinétique a été obtenu si le taux de laminage est réduit de 60 à 30% par exemple.

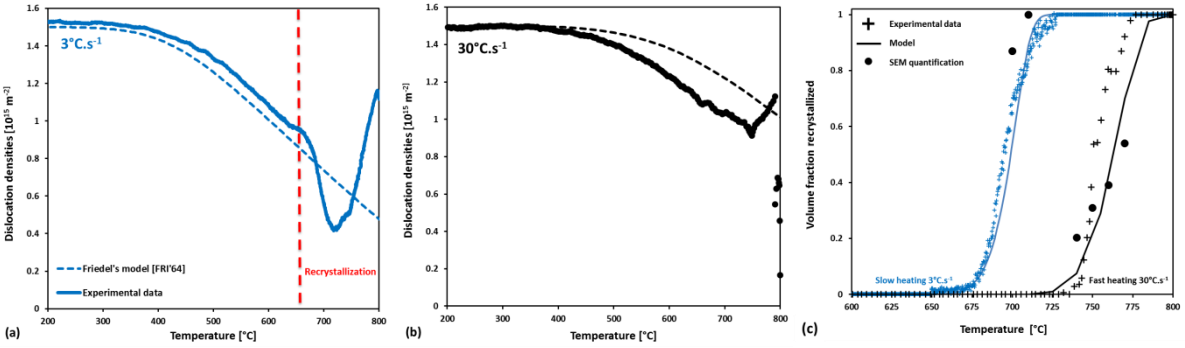

Figure 5 : Evolution mesurée (trait plein) et calculée (trait pointillé) de la densité de dislocations en fonction de la température lors de la chauffe (a) à 3°C.s^{-1} en bleu et (b) à 30°C.s^{-1} en noir respectivement. (c) Evolution de la fraction recristallisée en fonction de la température pour les deux vitesses de chauffage avec le même code couleur que précédemment. Les croix correspondent aux mesures in situ par HEXRD, les points à des mesures en MEB et les traits continus au modèle développé dans ces travaux.

Chapitre 5 : Cinétiques de transformation austénitique

Les cinétiques d'austénitisation ont été mesurées in situ en DRXHE pour diverses vitesses de chauffage lors d'un recuit à 800°C. Cette étude a permis de montrer que :

- les fractions transformées en fonction de la température en cours de chauffe à 3 et 30°C.s^{-1} sont similaires. Le décalage d'environ 10°C provient d'une transformation plus précoce à basse vitesse. En conséquence, la cinétique en fonction du temps est donc plus rapide à forte vitesse, en cohérence avec les observations du chapitre 2.
- En fin de chauffe à 800°C, environ 50% de la microstructure est austénitique, loin de l'ortho-équilibre (80%).
- lors du maintien à 800°C, la cinétique de transformation est d'autant plus rapide que la vitesse de chauffage a été forte. Des vitesses de chauffage élevées conduisent à des volumes d'austénite supérieurs à ceux attendus par l'équilibre thermodynamique en fin de maintien.

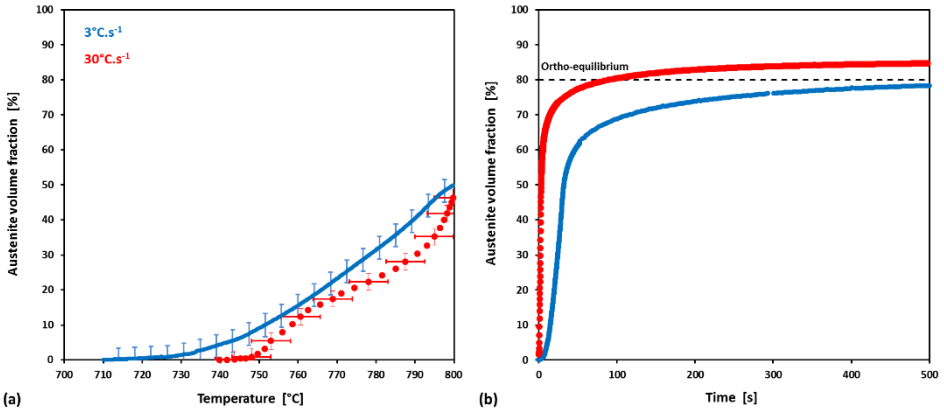

Figure 6 : Mesures *in situ* réalisés par DRXHE du volume d'austénite transformé (a) en fonction de la température et (b) du temps pour deux vitesses de chauffage (chauffage à 800°C à vitesse constante puis maintien à 800°C pendant 600s).

Comme dans le cas de la recristallisation au chapitre 4, nous avons entrepris une démarche de modélisation à base physique pour comprendre la nature de ces cinétiques de transformation en intégrant les observations microstructurales du chapitre 2 (nucléation et croissance de l'austénite) et les mesures de composition des carbures du chapitre 3 (enrichissement en manganèse). Nos observations du chapitre 2 laissent par contre penser que le rôle de l'état de recristallisation se limite à un impact topologique lors de la formation des microstructures et n'influence directement que peu les cinétiques.

Afin d'être le plus fidèle possible à nos observations microstructurales, dans les calculs DICTRA, la microstructure ferrito-perlitique modélisée a été subdivisée en deux sous-systèmes indépendants qui permettent d'étudier séparément le comportement des ilots de perlite et des carbures isolés. La mise en données a pris en compte les configurations géométriques, les tailles et compositions en manganèse observées expérimentalement et détaillées dans les chapitres précédents, mais les calculs ont été conduits sur un système ternaire Fe-Mn-C. Le seul paramètre d'ajustement est au final la fraction respective de ces sous-systèmes. Dans ce travail, nous avons proposé un ajustement cohérent avec certaines observations expérimentales, en particulier aux faibles taux de transformation (pendant la chauffe).

Dans les deux cas, la germination de l'austénite sur les carbures, la dissolution de la cémentite et la croissance de l'austénite aux dépends de la ferrite ont été modélisés avec une attention particulière portée aux conditions d'interfaces. Des travaux de la littérature ont déjà été conduits dans des configurations similaires mais uniquement lors de maintiens isothermes [GOU'12, KAM'15, LAI'16]. L'originalité de notre approche réside donc dans le traitement anisotherme de ce problème.

Pour les configurations étudiées, les résultats de simulation montrent que la dissolution des ilots de perlite ne dépend ni de la vitesse de chauffage, ni du degré d'enrichissement en manganèse de la cémentite. La dissolution de la cémentite est rapide et se termine dès que la température Ac_3 (correspondant à la chimie locale du sous-système perlite) est atteinte (750°C environ, conformément à nos observations expérimentales). Les ilots d'austénite sursaturée en carbone continuent à croitre ensuite, sans partition du Mn, donc rapidement, peu importe la vitesse de chauffage.

A faible vitesse, le taux d'austénite résultant de la croissance des bandes obtenu au cours de la chauffe respecte strictement celui prédit par l'équilibre local. A forte vitesse, la transformation n'arrive pas à former complètement le volume d'austénite attendu par l'équilibre. Au final, à cause de notre choix de segmentation, le sous-système associé à la perlite atteint une transformation austénitique complète dès le début du maintien indépendamment de la vitesse de chauffage

Concernant les carbures isolés, la dissolution de la cémentite dépend fortement de l'enrichissement préalable en manganèse. Il existe en effet une température critique de transition entre un régime de dissolution rapide et lent. Au-dessous de cette température, la lente dissolution est contrôlée par la diffusion du Mn dans l'austénite. Au-dessus de cette même température, la transformation est contrôlée par la diffusion du carbone et devient donc extrêmement rapide. Cette transition connue de la littérature en isotherme a été vérifiée et expliquée en condition de chauffage continu lors de ce travail. Ce résultat suggère que les carbures enrichis en manganèse lors du chauffage lent doivent entamer leur dissolution en régime rapide à partir d'une température plus élevée que lors d'un chauffage rapide (un décalage de 20°C maximum est attendu entre deux niveaux d'enrichissement extrêmes). Toutefois, cela ne signifie pas que le processus commence à plus haute température, car le régime lent permet de former près de 10% d'austénite depuis le début de la transformation à 720°C avant de passer en régime de dissolution rapide. Cependant, ce résultat doit être nuancé car les carbures isolés présentent sans nul doute des compositions assez variables.

Lors de la croissance de l'austénite issue de ces carbures isolés, les cinétiques dépendent fortement des vitesses de chauffe car les conditions prévalant à l'interface ferrite/austénite sont différentes.

Lors d'une chauffe lente, la transformation qui succède au processus de dissolution continue avec redistribution du Mn (condition d'équilibre local avec partition – PLE). L'interface ralentit donc fortement entre l'étape de dissolution et la pure croissance de l'austénite. Malgré la durée du traitement avant le maintien, l'enrichissement résiduel en manganèse dû à la présence du carbure est par contre conservé. Lorsque le palier isotherme est atteint, il reste peu d'austénite à transformer pour atteindre l'équilibre et le reste de la transformation se produit très rapidement toujours en condition PLE.

Lors d'une chauffe rapide, la transformation continue par contre sans redistribution du Mn (condition d'équilibre local sans partition –NPLE). Dans ces conditions, la cinétique est rapide même si le taux d'austénite obtenu à la fin du chauffage reste sensiblement inférieur à celui obtenu après chauffe lente. Pendant le maintien, la condition d'interface change à nouveau instantanément pour retrouver une croissance avec partition (PLE). La transformation austénitique se produit alors au-delà de l'équilibre

thermodynamique dans le sous-système car la ferrite présente une trop forte teneur en manganèse (un héritage de la croissance en mode NPLE). Le retour à l'équilibre thermodynamique est un processus lent car il nécessite la diffusion du manganèse sur de grandes distances. Il faut par exemple environ 100s à 800°C pour commencer à observer une décroissance de la fraction d'austénite et observer un début de retour à l'équilibre.

La mise en évidence de cette transition NPLE/PLE en condition anisotherme, en cours de transformation, est un des résultats nouveau et clef de notre étude. Les résultats de simulation montrent ainsi que les cinétiques de transformation de nos aciers dépendent plus de la vitesse de chauffage que de la composition des carbures. On retrouve ainsi que les cinétiques de transformation sont bien plus rapides à fortes vitesses, mais les fractions transformées en fonction de la température sont finalement assez proches lors de la chauffe. Cette transition permet aussi d'expliquer dans une certaine mesure pourquoi on observe aussi des taux de transformation plus élevés que l'équilibre aux fortes vitesses de chauffage.

Le deuxième résultat notable de cette étude numérique est que cette transformation austénitique conduit à de fortes hétérogénéités de composition dans l'austénite à la fois en carbone (selon l'origine de l'austénite – perlite ou carbure isolé) mais aussi en manganèse (vestige de l'enrichissement en Mn des carbures). Cette dispersion est bien connue dans les des aciers DP et notre approche à sous-système permet possiblement de la prévoir.

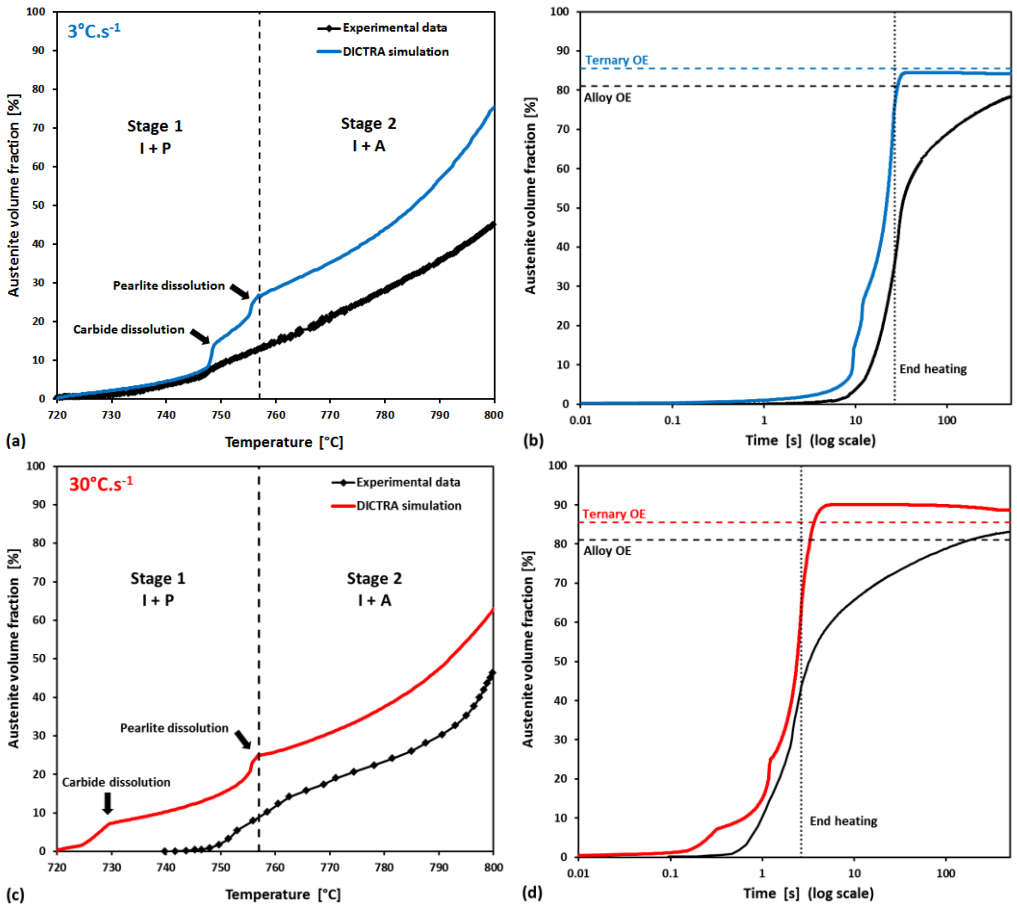

Figure 7 : Cinétiques de transformation austénitique simulées pour le système ternaire et expérimentales en fonction de la température et du temps pour des vitesses de chauffe de (a)-(b) 3°C.s^{-1} et de (c)-(d) 30°C.s^{-1}.

La figure 7 montre les cinétiques de transformations prédites en fonction de la température et du temps pour les deux vitesses de chauffage. Comme les calculs ont été conduits pour le système ternaire, les conditions d'ortho-équilibre (Ternary OE) diffèrent sensiblement de celle pour le système complet Fe-Mn-Si-Cr-C (Alloy OE). Lors de la chauffe, les résultats de simulation montrent un accord satisfaisant avec les données expérimentales, avec un décalage d'environ 20°C (possible effet de la composition ?). Les vitesses d'avancement de la transformation (pentes de courbes) sont correctement reproduites. Par

contre, à haute température et particulièrement, lors du maintien, les cinétiques prédites par notre approche à deux sous-systèmes sont trop rapides pour les deux vitesses. Les possibles origines de cet écart sont nombreuses. Les plus probables sont que nos hypothèses sur la géométrie du système (croissance sphérique) et sur l'indépendance des sous-systèmes sont bien trop fortes dès que l'austénite commence à percoler (typiquement au-delà de 40% en fraction de phase).

Conclusion et Perspectives

Cette thèse a permis de nouvelles avancées dans un domaine qui a déjà été largement étudié car nous avons utilisé non seulement des techniques expérimentales de pointe pour étudier les microstructures à différentes échelles ou leur formations in situ lors de recuit, mais aussi des approches innovantes de modélisation (codes commerciaux ou développés à dessein). Nos résultats majeurs sont les suivants :

- Le processus de recristallisation au recuit influe significativement sur la distribution des phases lors d'un recuit d'une structure ferrito-perlitique déformée. Le mécanisme d'interactions sous-jacent suggère un rôle clef joué par les carbures intergranulaires dans la ferrite, qui vont servir de sites de germination privilégiés. Un chauffage lent favorise la recristallisation de la ferrite et conduit à une microstructure « en collier ». En cas de chauffage lent, au contraire, la recristallisation intervient concomitamment avec la transformation de phase et la microstructure présente une topologie « en bandes ». Les travaux menés tendent à confirmer la représentation de Li *et al*. de ces interactions.
- Les mécanismes d'enrichissement en manganèse des carbures lors du laminage à chaud, à froid et le recuit (avant leur dissolution) ont été investigués, expliqués et modélisés à l'échelle du nanomètre. La cémentite présente dès sa formation au laminage à chaud un fort enrichissement qui se renforce lors des traitements thermiques ultérieurs. Les enrichissements rencontrés ne sont toutefois pas suffisants pour avoir un fort impact sur les cinétiques de transformation.
- Une méthodologie unique a été développée permettant de suivre in situ et en une seule expérience la restauration, la recristallisation et l'austénitisation lors de chauffage y compris rapide ($100°C.s^{-1}$) des aciers de l'étude. Cette méthode est basée sur la DRXHE sur ligne de lumière synchrotron. Les mesures effectuées ont été validés par des techniques plus conventionnelles de microscopie. Un modèle à champ moyen de recristallisation a été développé sur la base des travaux de Zurob *et al*. et validé sur les données expérimentales. Il permet en particulier de prévoir l'effet du taux de laminage sur les cinétiques.
- Une approche de simulation innovante sous DICTRA a été proposée pour modéliser la cinétique de transformation austénitique au cours d'un recuit. Elle est basée sur une segmentation du problème en deux sous-systèmes indépendants qui permettent de simuler la dissolution de la cémentite et la croissance de l'austénite au niveau des ilots perlitiques et des carbures isolés. Les différences de cinétiques observés selon les vitesses de chauffage s'expliquent par des modes de croissance différents de l'austénite, avec ou sans partition du manganèse. Les cinétiques prédites ne permettent toutefois pas de bien reproduire encore les cinétiques lentes observées lors des maintiens à haute température.

Ce travail de thèse ouvre de nombreuses perspectives, dans des domaines très variés.

- Tous les données de la campagne de mesure HDRX ne sont pas encore exploitées (effet du LAC, effet de traitements thermiques à très haute vitesse, travail sur des cycles modèles isothermes et sur des systèmes modèles ferrites ou perlitiques) !
- Pour continuer ce projet, il semble très important de mieux comprendre la formation des carbures intergranulaires lors du LAC mais aussi lors de la recristallisation (un possible mécanisme de dissolution/précipitation ?)
- La nouvelle approche pour suivre la recristallisation par DRXHE nécessiterait d'être validée sur des systèmes bien connus.
- Il serait probablement pertinent de poursuivre le travail de modélisation DICTRA sur les sous-systèmes en introduisant un système unifié et moyenné pour décrire la croissance après la percolation de l'austénite ; l'objectif étant de mieux comprendre pourquoi les cinétiques sont mal décrites lors du maintien.
- Enfin, une approche à champ local simplifié pour la croissance de l'austénite devra être développée pour permettre des calculs en conditions industrielles rapides (par exemple le modèle de Wycliffe *et al.*) [WYC'81]

Références

[ALL'15] Allain, S.Y.P., Bouaziz, O., Pushkareva, I., Scott, C.P., 2015. Towards the microstructure design of DP steels: A generic size-sensitive mean-field mechanical model. Materials Science and Engineering: A 637, 222–234. https://doi.org/10.1016/j.msea.2015.04.017

[BAR'15] Barbier, D., Germain, L., Hazotte, A., Gouné, M., Chbihi, A., 2015. Microstructures resulting from the interaction between ferrite recrystallization and austenite formation in dual-phase steels. Journal of Materials Science 50, 374–381. https://doi.org/10.1007/s10853-014-8596-2

[BOU'02] Galtier, A., Bouaziz, O., Lambert, A., 2002. Influence de la microstructure des aciers sur leur propriétés mécaniques. Mécanique & Industries 3, 457–462.

[CHB'14] Chbihi, A., Barbier, D., Germain, L., Hazotte, A., Gouné, M., 2014. Interactions between ferrite recrystallization and austenite formation in high-strength steels. Journal of Materials Science 49, 3608–3621. https://doi.org/10.1007/s10853-014-8029-2

[FRI'64] Friedel, J. (1964). "Dislocations". Pergamon. New York, 274.

[GAR'81] Garcia, C.I., Deardo, A.J., 1981. Formation of austenite in 1.5 pct Mn steels. Metallurgical Transactions A 12, 521–530. https://doi.org/10.1007/BF02648551

[GOU'12] Gouné, M., Danoix, F., Ågren, J., Bréchet, Y., Hutchinson, C.R., Militzer, M., Purdy, G., van der Zwaag, S., Zurob, H., 2015. Overview of the current issues in austenite to ferrite transformation and the role of migrating interfaces therein for low alloyed steels. Materials Science and Engineering: R: Reports 92, 1–38. https://doi.org/10.1016/j.mser.2015.03.001

[HUA'04] Huang, J., Poole, W.J., Militzer, M., 2004. Austenite formation during intercritical annealing. Metallurgical and Materials Transactions A 35, 3363–3375. https://doi.org/10.1007/s11661-004-0173-x

[HUT'04] Hutchinson, C.R., Hackenberg, R.E., Shiflet, G.J., 2004. The growth of partitioned pearlite in Fe–C–Mn steels. Acta Materialia 52, 3565–3585. https://doi.org/10.1016/j.actamat.2004.04.010

[KAM'15] Kamoutsi, H., Gioti, E., Haidemenopoulos, G.N., Cai, Z., Ding, H., 2015. Kinetics of Solute Partitioning During Intercritical Annealing of a Medium-Mn Steel. Metallurgical and Materials Transactions A 46, 4841–4846. https://doi.org/10.1007/s11661-015-3118-7

[LAI'16] Lai, Q., Gouné, M., Perlade, A., Pardoen, T., Jacques, P., Bouaziz, O., Bréchet, Y., 2016. Mechanism of Austenite Formation from Spheroidized Microstructure in an Intermediate Fe-0.1C-3.5Mn Steel. Metallurgical and Materials Transactions A 47, 3375–3386. https://doi.org/10.1007/s11661-016-3547-y

[LI'13] Li, P., Li, J., Meng, Q., Hu, W., Xu, D., 2013. Effect of heating rate on ferrite recrystallization and austenite formation of cold-roll dual phase steel. Journal of Alloys and Compounds 578, 320–327. https://doi.org/10.1016/j.jallcom.2013.05.226

[MOR'18] Moreno, M., Teixeira, J., Geandier, G., Hell, J.-C., Bonnet, F., Salib, M., Allain, S., 2018. Real-Time Investigation of Recovery, Recrystallization and Austenite Transformation during Annealing of a Cold-Rolled Steel Using High Energy X-ray Diffraction (HEXRD). Metals 9, 8. https://doi.org/10.3390/met9010008

[MOR'19] Moreno, M., Teixeira, J., Ghanbaja, J., Bonnet, F., Allain, S., 2019. Evolution of cementite composition along the processing of cold-rolled and annealed Dual-Phase steels. Materialia 6, 100179. https://doi.org/10.1016/j.mtla.2018.100179

[PAN'11] Pandit, A.S., Bhadeshia, H.K.D.H., 2011. Diffusion-controlled growth of pearlite in ternary steels. Proceedings of the Royal Society A: Mathematical, Physical and Engineering Sciences 467, 2948–2961. https://doi.org/10.1098/rspa.2011.0165

[POU'11] Poulsen, S.O., Lauridsen, E.M., Lyckegaard, A., Oddershede, J., Gundlach, C., Curfs, C., Juul Jensen, D., 2011. In situ measurements of growth rates and grain-averaged activation energies of individual grains

[REH'13] Rehman, M.K., Zurob, H.S., 2013. A Novel Approach to Model Static Recrystallization of Austenite During Hot Rolling of Nb Microalloyed Steel. Part I: Precipitate-Free Case. Metallurgical and Materials Transactions A 44, 1862–1871. https://doi.org/10.1007/s11661-012-1526-5

[RIB'04] Ribárik, G., Gubicza, J., Ungár, T., 2004. Correlation between strength and microstructure of ball-milled Al–Mg alloys determined by X-ray diffraction. Materials Science and Engineering: A 387–389, 343–347. https://doi.org/10.1016/j.msea.2004.01.089

[SIN'07] Sinclair, C.W., Hutchinson, C.R., Bréchet, Y., 2007. The Effect of Nb on the Recrystallization and Grain Growth of Ultra-High-Purity α-Fe: A Combinatorial Approach. Metallurgical and Materials Transactions A 38, 821–830. https://doi.org/10.1007/s11661-007-9106-9

[SMA'57] Smallman, R.E., Westmacott, K.H., 1957. Stacking faults in face-centred cubic metals and alloys. Philosophical Magazine 2, 669–683. https://doi.org/10.1080/14786435708242709

[TOM'18] Thomas, L.S., Matlock, D.K., 2018. Formation of Banded Microstructures with Rapid Intercritical Annealing of Cold-Rolled Sheet Steel. Metallurgical and Materials Transactions A 49, 4456–4473. https://doi.org/10.1007/s11661-018-4742-9

[WH'53] Williamson, G.., Hall, W.., 1953. X-ray line broadening from filed aluminium and wolfram. Acta Metallurgica 1, 22–31. https://doi.org/10.1016/0001-6160(53)90006-6

[WYC'81] Wycliffe, P.A., Purdy, G.R., Embury, J.D., 1981. Growth of Austenite in the Intercritical Annealing of Fe-C-Mn Dual Phase Steels. Canadian Metallurgical Quarterly 20, 339–350. https://doi.org/10.1179/cmq.1981.20.3.339

[WU'18] Wu, Y.X., Sun, W.W., Styles, M.J., Arlazarov, A., Hutchinson, C.R., 2018. Cementite coarsening during the tempering of Fe-C-Mn martensite. Acta Materialia 159, 209–224. https://doi.org/10.1016/j.actamat.2018.08.023

[ZUR'06] Zurob, H., Brechet, Y., Dunlop, J., 2006. Quantitative criterion for recrystallization nucleation in single-phase alloys: Prediction of critical strains and incubation times. Acta Materialia 54, 3983–3990. https://doi.org/10.1016/j.actamat.2006.04.028

Content

Introduction

This PhD thesis has been funded by ArcelorMittal Maizières Research SA in collaboration with the CNRS (Direction Régional Centre-Est), which are both fully acknowledged.

I. Introduction to DP steels

Dual-Phase steel sheets are extensively employed in the automotive industry for their interesting strength/ductility balance. They are well adapted for stamping / drawing / bending operations permitting the manufacturing of complex shaped automotive parts at relative low cost. At the same time, they can show high level of Ultimate Tensile Strength (UTS between 600 and 1000 MPa) that enables the production of lighter automotive components by thickness reduction. Dual-Phase (DP) steels have been industrialized since the years 1990-1995 for lightening car and trucks structures and thus reducing their energy consumption and CO_2 emissions [EEA'17]. They are nowadays essential accounting the recent and drastic evolutions of environmental regulations.

Dual-Phase steels (DP) belong to the first generation of Advanced High Strength Steel (AHSS) family, as TRIP (Transformation Induced Plasticity), CP (Complex Phase) or Martensitic steels. Even steelmakers have tried developed a second generation (austenitic TWIP - Twinning Induced Plasticity steels) and are developing a third generation of AHSS, DP steels are still widely used in the automotive field (about 2000 kt/year). The strength/ductility performances of these different industrial steels for cold stamping applications are represented in Figure 1(a). Figure 1(b) shows some possible applications of DP steels in automotive building.

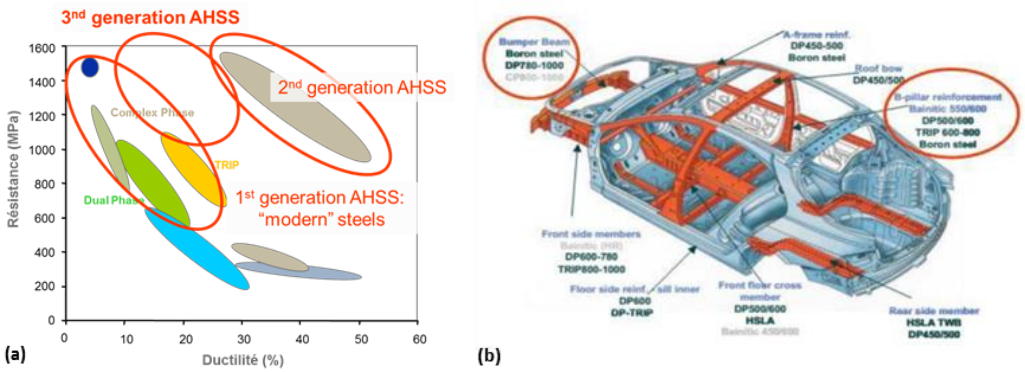

Figure 1: (a) Tensile strength/elongation properties of the AHSS grades for cold-stamping operations [MAT'06]. (b) Possible applications of various DP steels for car body-in-white manufacturing [PIN'12].

DP steel microstructures are mainly constituted of two phases, usually ferrite with a polygonal morphology (polycrystalline) and interconnected islands of carbon-enriched martensite. The fraction of the latter phase is variable (from 5% to almost 100% with various percolation states) depending on the targeted strengths. In a simple approximation, DP steel can be considered as a composite, the ferrite being the soft phase and the martensite the reinforcement of the matrix. Figure 2 shows a typical DP steel microstructure observed by SEM (Scanning Electron Microscopy) after etching. Martensite (often called α') is etched contrary to the ferritic matrix (often called α') which appears thus darker.

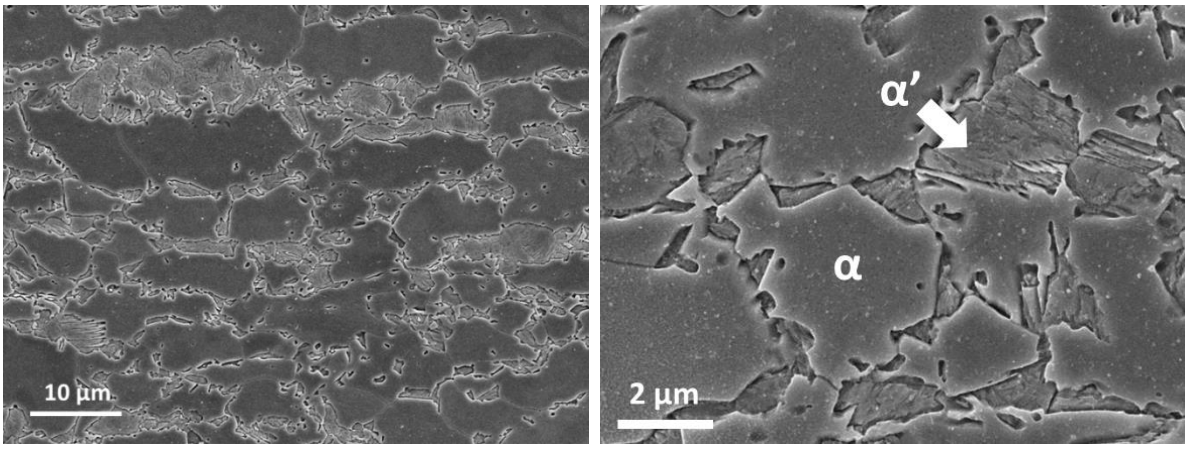

Figure 2: SEM micrographs of a ferrite-martensite DP microstructure after etching at two magnifications. Martensite (often called α') is etched contrary to the ferritic matrix (often called α') which appears thus darker.

The tensile properties of DP steels are directly related to their fraction of martensite. Allain *et al.* [ALL'15] for instance shed in light this strong dependence of the amount of martensite on the mechanical properties of DP steels. Figure 3(a) shows the predicted evolution of the Ultimate Tensile Strength (UTS), the conventional Yield Strength (YS), and the Uniform Elongation (UEI) of a DP steels as a function of the volume fraction of martensite for a given nominal composition. Each percent of martensite lead to increase in strength of about 15 Mpa in the E domain (controlled by the Elastic properties of martensite). Thus, the volume of martensite produced during the manufacturing of DP steels needs to be a carefully controlled by steels makers. It also explains the versatility of this microstructure concept that permits to access a wide range of properties.

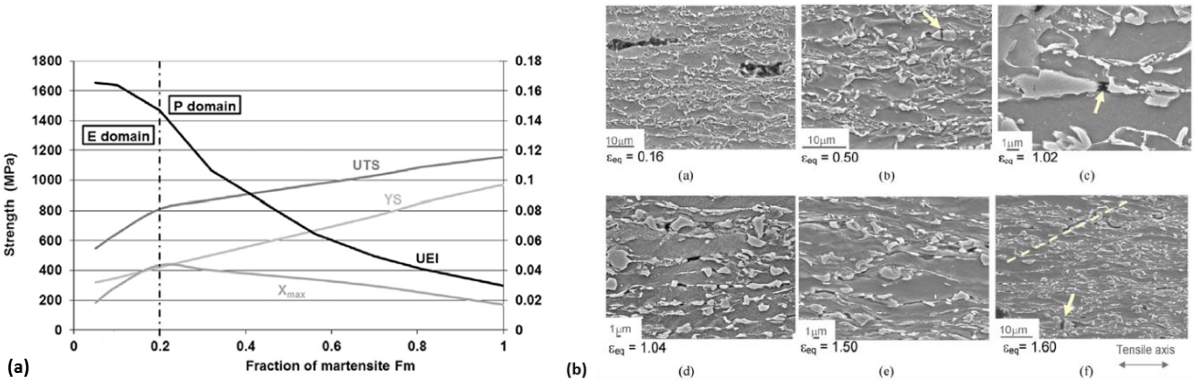

Figure 3: (a) Evolution of the engineering tensile properties of a given steel as a function of the martensite fraction, where UTS, YS and UEl stand for Ultimate Tensile Strength, conventional Yield Strength, and Uniform Elongation, respectively [ALL'15]. (b) Different possible damage processes observed in DP steels after deformation after [AVR'09].

The composite nature of DP steels explains also their poor and often unpredictable damage resistance. Damage process encompasses all mechanical mechanisms leading to the appearance of voids in the microstructures in a ductile or brittle way and leading the macroscopic fracture of the material (integrity loss of parts during manufacturing or in in-use conditions). The two main damage initiation mechanisms observed at room temperature in DP steels are interfacial decohesion between ferrite and martensite and (brittle or ductile) fracture of martensitic islands [AVR09, TAS14] as shown in Figure 3(b).

The fracture related performances of DP steels depend on several features [TAS14]; on the local behavior of the individual phases (ferrite, martensite, even bainite in the case of industrial DP steels) and

their local thermo-mechanical histories inherited from material processing (internal stresses, tempering states) but also on the 3D microstructure complexity (size, morphology, topology, percolation of hard phases). It thus not only important for steelmakers to be able to predict and monitor during manufacturing the fraction of phases in their DP steels but also their spatial distribution and their size.

II. DP manufacturing by continuous annealing

Dual-phase steel sheets can be produced either by Hot-Rolling (HR) or Cold-Rolling (CR) depending on the targeted thickness. In the frame of this thesis, we will focus only on cold-rolled and annealed steels. Figure 4 shows a simplified sketch of the manufacturing chain for such DP steels and Figure 5 the corresponding thermal schedule and the associated microstructures.

Slabs obtained by continuous casting are first heated to 1250°C (step 1). Such high temperatures permit to achieve a fully austenitic microstructure. The slabs are then hot-rolled to produce a hot band (about 3mm thick). After coiling and slow cooling, the microstructure is made of ferrite and pearlite at room temperature (end of step 1). The band is then pickled (step 2) and cold-rolled (step 3) to get its final thickness. The final DP microstructure is obtained by continuous annealing (step4) before final preparation (step 5). This thermal treatment consists in heating up the band to the intercritical temperature range, in holding it at high temperature (the so-called soaking stage) and in cooling it down to room temperature. During the heating and soaking stages, the deformed ferrite-pearlite microstructure will undergo a partial austenitic transformation. The fraction of austenite expected at equilibrium is directly given the phase diagram as shown in Figure 5(b). At the end of the soaking, the band is cooled down (generally using gas jet but also by water quenching) down to room temperature. During this operation, ferrite can grow again at the expense of austenite (epitaxial ferrite in most cases) and a bainitic transformation can take place in austenite, especially is the band is galvanized by immersion into a liquid zinc pot at 460°C. At lower temperature, residual austenite transforms into martensite. The final microstructure of industrial DP steels is thus made of recrystallized ferrite (inherited from the hot bands and appeared during final cooling), bainite and martensite.

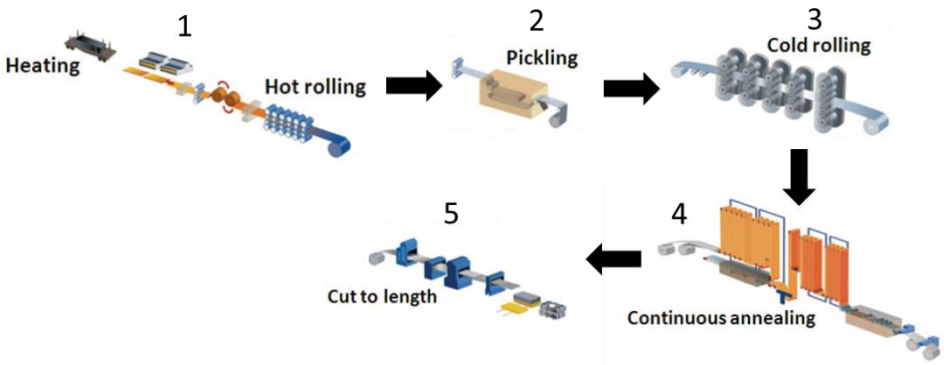

Figure 4: Simplified representation of a DP steel manufacturing chain [GRA'11].

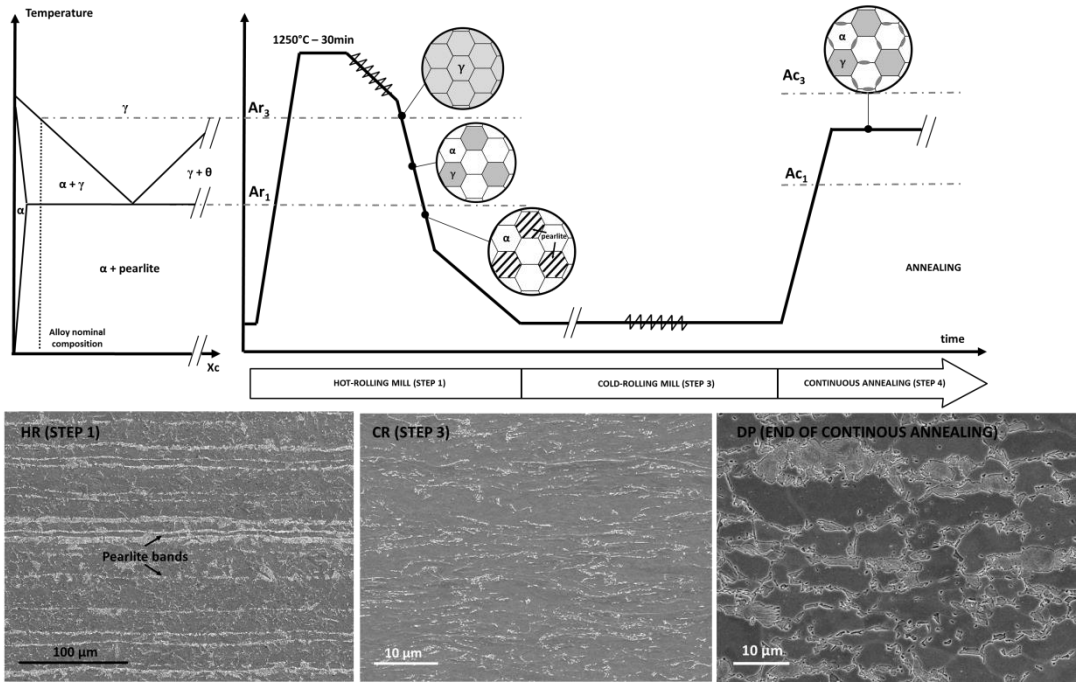

Figure 5: State of the microstructure according the consecutive processes of the DP manufacturing route. The schematic Fe-C diagram highlights temperature ranges where the initial ferrite-pearlite microstructure is transformed and when conversely the microstructure is re-austenitized during annealing.

In this thesis, we will only focus on the austenitic transformation from the deformed ferrite-pearlite. This process is already far from being simple and never reaches the equilibrium state in practice. The austenite transformation kinetics as well as the sizes, morphologies and topologies of the phases resulting from annealing depend not only on the soaking temperature but also on the heating conditions (fast or slow cooling) and the metallurgical history of the hot band (often called the "inheritance effect", related to the chemical composition of cementite in pearlite in particular).

Figure 6(a) taken from Huang *et al.* [HUA'04] illustrates well the effect of heating rate on the transformation kinetics during an isothermal holding at 750°C (soaking) for the same steel taken in two different states (as hot-rolled or as cold-rolled Fe-C-Mn-Mo steel). Figure 6(b) shows the corresponding microstructures at the end of the studied soaking. The higher the heating rate, the faster the transformation kinetics and the higher the transformed fraction. This effect is enhanced if the initial microstructure is deformed. High heating rate leads also to the formation of a typical banded structure if initial microstructure is deformed whereas a more homogeneous distribution is observed at low heating rate. In the literature, this latter effect is attributed to the interaction between deformed ferrite recrystallization and austenite phase transformation. In fact, if the recrystallization precedes the transformation a necklace microstructure (a continuous layer of austenite around recrystallized ferrite grains) can be observed after annealing. On the contrary, if austenite starts first, the final microstructure presents elongated bands of martensite and ferrite in the rolling direction. These respective "weak" and "strong" interactions depend on the deformed state of ferrite and on the heating rate.

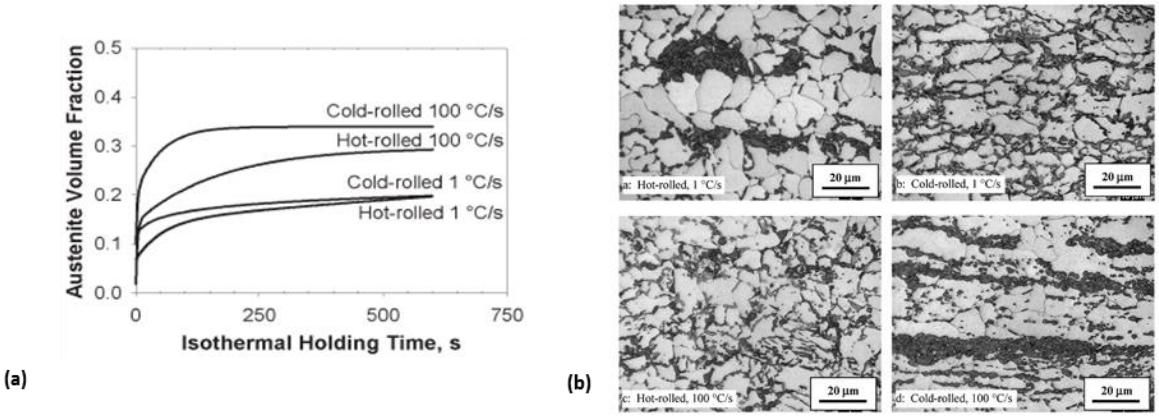

Figure 6: (a) Effect of the heating rate on the austenite fraction as function of the holding time at 750°C for two initial states (Fe-C-Mn-Mo steel) (b) Corresponding microstructures at the end of soaking observed by optical microscopy. Austenite is revealed by the presence of martensite at room temperature which appears in dark contrast. Ferritic matrix appears in clear contrast. Taken from Huang *et al.* [HUA'04]

In this thesis, we have observed the same trends on the studied steel (cf. chapter 2 for more details). Figure 7 shows SEM micrographs after etching of the samples annealed at 700°C (i.e. prior austenite transformation) and at 770°C (i.e. after partial austenitic transformation) at two different heating rates.

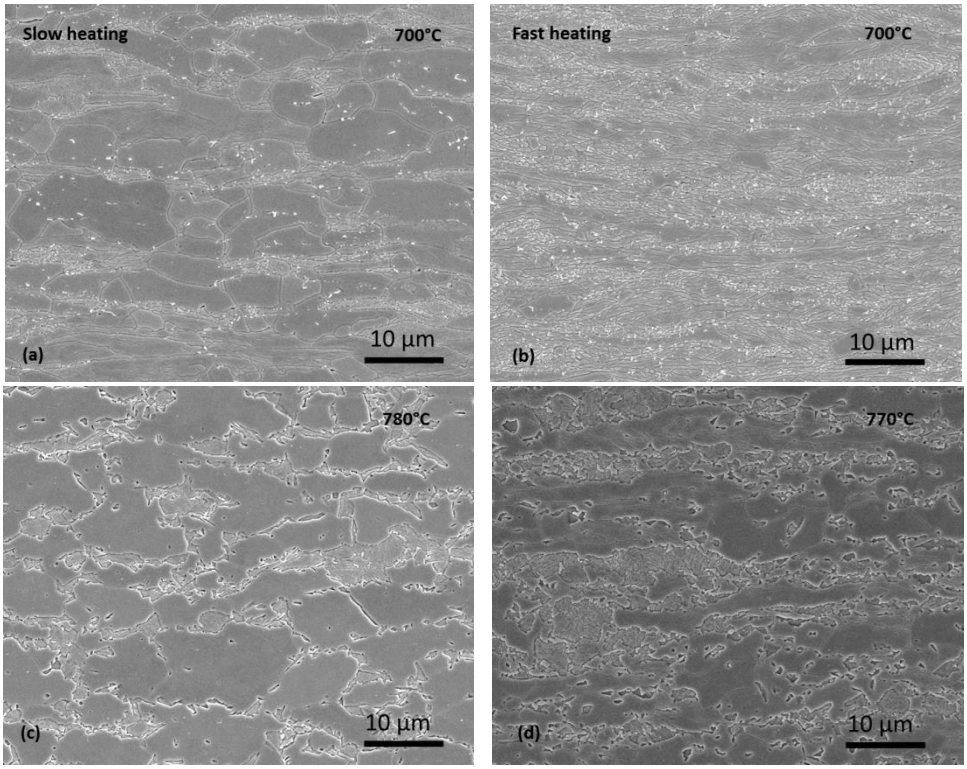

Figure 7: SEM micrographs after etching of the studied steel heated (a)-(b) up to 700°C and (c)-(d) up to 770°C at low (3°C.s^{-1}) and high (30°C.s^{-1}) heating rates and then quenched. Etchant reveal grain and sub-grains of the ferrite and martensite which reveals the presence of austenite at high temperature.

At 700°C, the etchant reveals carbides (clear contrast) but also sub-grains that are characteristic of non-recrystallized grains. At low heating rate, the sample is almost fully recrystallized at 700°C whereas the recrystallized process has not started at high heating rate. The presence of austenite grains at higher temperature is revealed by the presence of martensite which is also etched as in Figure 2. At 770°C, after slow heating, austenite grains are dispersed in the ferrite matrix whereas they show a clear banded organization after fast heating.

The effects discussed above depend also on carbide microstructure inherited from the hot-bands before continuous annealing, in particular as carbides are preferred nucleation sites for austenite. Many studies so far highlighted the dependence of the cementite Mn-enrichment on the dissolution kinetic, which in turns drives that of austenite. Figures 8 from the investigations of Gouné *et al.* [GOU'12] compares the austenite phase fraction transformed from the dissolution of Mn- poor/rich cementite in spheroidized/lamellar pearlite islands during heating and isothermal holding at 750°C, respectively. This study also highlights the key role of manganese in these steels that will be discussed in details in chapter 3 and 5.

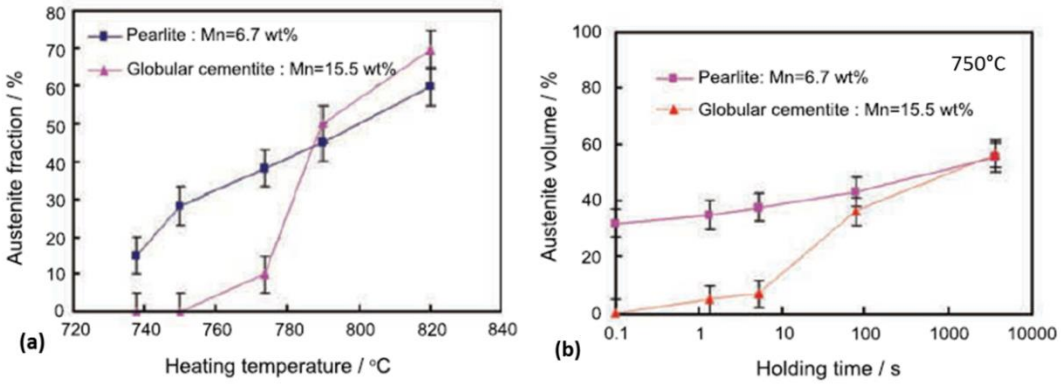

Figure 8: Comparison of the austenite phase fraction transformed from dissolution of poor and rich Mn cementite during heating (a) and time during isothermal holding at 750°C (b) [GOU'12].

III. Problematic and objectives of the thesis

All these examples highlight that numerous metallurgical mechanisms take place and interact during the annealing of deformed ferrite/pearlite microstructure, among them; cementite ripening (fragmentation, spheroidization, coarsening, and composition evolution), recovery/recrystallization and nucleation and growth austenite. This list must be complemented with different inheritance effects associated to hot-rolling, as Mn partitioning during pearlitic transformation and also to cold-rolling as the severe plastic deformation of phases or the mechanical fragmentation of carbides.

These mechanisms were all individually characterized in the past (a large literature is addressed throughout this work), but to date, there is no consensus of theirs possible interactions with the reverse austenite transformation.

In this work, we have thus tried to deconvolute experimentally the contributions of each mechanism by innovative experimental approaches, involving either microstructure observations at micro/nanoscale (by SEM/TEM) or *in situ* (by HEXRD) technics. We have then used and calibrated commercial thermo-kinetics local field models in order to understand the observed trends. In a third step, this knowledge has then served to develop our own physically-based CPU-efficient models for phase transformations and recrystallization. The stakes of this work are thus related to the real-time monitoring of DP production lines and an Industry 4.0 agenda.

IV. PhD manuscript's outlines

The manuscript is divided into 5 chapters. In this thesis report, we have made the original choice to present a dedicated literature review in each chapter. This is the reason why chapters 2, 3, 4 and 5 starts with a literature review focusing respectively on the different studied mechanisms.

Chapter 1 presents the steel investigated as well as the experimental and modeling technics employed in this work. We describe in particular how the samples has been prepared for metallographic observations, the operating conditions for electronic microscopy, how we have conducted our *in situ* High Energy X-Ray Diffraction (HEXRD) experiments on a synchrotron beamlines and post-treated the data. Commercial computational tools for phase transformation and thermodynamic databases used in this study (ThermoCalc and DICTRA) will also be presented briefly.

Chapter 2 proposes an overview of the microstructural morphogenesis from the Hot-Rolled state to the end of soaking as a function of the heating rates. The investigations have been conducted mainly by SEM on as-received samples and samples annealed at different temperatures along industrial-like annealing treatments. The evolution of carbide microstructure, the recrystallization state of ferrite and the nucleation and growth of austenite have been followed to highlight the possible interactions between these mechanisms and to show how the necklace and banded microstructures appear step by step. Our whole analysis sustains mainly the interpretation proposed by Li *et al.* in 2013 [LI'13] and reveals the essential role of some intergranular carbides on the austenite transformation kinetics and on the final topology of microstructures. This is the reason why we have proposed in chapter 5 a modeling strategy distinguishing the behavior of pearlitic islands and these carbides to calculate transformation kinetics.

Chapter 3 is dedicated to characterization of the chemical composition of carbides during the heating step before austenitization starts. The chemical composition of carbides during hot-rolling and after cold-rolling was also been studied to better understand the inheritance effects. The experimental part of this work has mainly been conducted by Transmission Electron Microscopy (TEM) to measure manganese composition field at the nanoscale in precipitates. Thermodynamical analyses and DICTRA simulations were employed to interpret the measured composition evolutions and in particular predict the manganese partition in cementite occurring during pearlite transformation. The DICTRA simulations have permitted to reassess the standard Mn diffusion coefficient available in commercial database. Finally, a predictive Finite Difference tool was built in order to reproduce the results of DICTRA. This chapter gave rise to a publication in Materialia [MOR'19].

As shown in Chapter 2, recrystallization governs the morphogenesis of DP structures. Chapter 4 is thus dedicated to the experimental characterization, modeling and coupling of recovery and recrystallization phenomena in ferrite. The experiments have consisted to follow both recovery and recrystallization during annealing schedules at different heating rates. This work has been conducted mainly by *in situ* HEXRD experiments. The evolution of the density dislocations (recovery) is determined by a conventional Williamson-Hall method. During the same experiment, the recrystallization kinetics is determined by the mean of an original method developed in the frame of this study. This new method was validated by direct SEM-EBSD observations on the studied steel and on modeling results from the literature. The experimental part of this chapter has been the subject of a recent publication [MOR'18]. Both recovery and recrystallization kinetics were then modeled by a physically-based mean-field approach inspired by Zurob *et al.* [ZUR'06] and Sinclair *et al.* [SIN'07]. The parameters and mobility functions have been calibrated to best reproduce experimental results. This model reproduces well the sensitivity of recrystallization kinetics to heating rates but also to cold-rolling ratios.

The last chapter aims at shedding in light the influence of the heating rate on the reverse austenite transformation. The reverse transformation has been surveyed via *in situ* HEXRD experiments to follow in real time the austenite phase fraction transformed as function of temperature and time during the heating

stage and the subsequent holding at 800°C. Fast acquisition mode has enabled (1 Hz) to follow the progress of the transformation with an excellent time resolution, even for high heating rates (3, 30 and 100°C.s^{-1}). An important part of the following investigation aimed at replicate the relation between heating rate and reverse transformation kinetic by simulation. For this purpose, a different approach from those reported in literature has been proposed. The dissolution of pearlite islands and of the intergranular cementite particles were studied separately (local fields). The global kinetic was thereafter re-build and compared to the experimental data. It has permitted to highlight that the reverse transformations of pearlite and isolated cementite particles have different behaviors which are tightly related to the heating rate. The influence of the Mn composition of cementite on the transformation kinetic regimes is well depicted, but this approach mainly permitted to identify which role plays recrystallization when the reverse transformation occurs in initial non-recrystallized ferrite-pearlite microstructures.

Finally, the main findings of this work are summarized and the outlooks of the study are evoked. In particular, we will suggest continuing the investigations about the formation of intragranular carbides in ferrite-pearlite microstructures. Their formations are still a debating question and represent surely an important outlook of this thesis.

REFERENCES

[AVR'09] Avramovic-Cingara, G., Ososkov, Y., Jain, M.K., Wilkinson, D.S., 2009. Effect of martensite distribution on damage behaviour in DP600 dual phase steels. Materials Science and Engineering: A 516, 7–16. https://doi.org/10.1016/j.msea.2009.03.055

[EEA'17] "Monitoring CO_2 emissions from new passenger cars and vans in 2017". https://doi.org/10.2800/74986

[HUA'04] Huang, J., Poole, W.J., Militzer, M., 2004. Austenite formation during intercritical annealing. Metallurgical and Materials Transactions A 35, 3363–3375. https://doi.org/10.1007/s11661-004-0173-x

[GOU'12] Gouné, M., Maugis, P., Drillet, J., 2012. A Criterion for the Change from Fast to Slow Regime of Cementite Dissolution in Fe–C–Mn Steels. Journal of Materials Science & Technology 28, 728–736. https://doi.org/10.1016/S1005-0302(12)60122-4

[LI'13] Li, P., Li, J., Meng, Q., Hu, W., Xu, D., 2013. Effect of heating rate on ferrite recrystallization and austenite formation of cold-roll dual phase steel. Journal of Alloys and Compounds 578, 320–327. https://doi.org/10.1016/j.jallcom.2013.05.226

[MAT'06] MATLOCK, D. K. et SPEER, John G. Design considerations for the next generation of advanced high strength sheet steels. In : *Proceedings of 3rd International Conference on Structural Steels*. 2006. p. 774-781.

[MOR'18] Moreno, M., Teixeira, J., Geandier, G., Hell, J.-C., Bonnet, F., Salib, M., Allain, S., 2018. Real-Time Investigation of Recovery, Recrystallization and Austenite Transformation during Annealing of a Cold-Rolled Steel Using High Energy X-ray Diffraction (HEXRD). Metals 9, 8. https://doi.org/10.3390/met9010008

[MOR'19] Moreno, M., Teixeira, J., Ghanbaja, J., Bonnet, F., Allain, S., 2019. Evolution of cementite composition along the processing of cold-rolled and annealed Dual-Phase steels. Materialia 6, 100179. https://doi.org/10.1016/j.mtla.2018.100179

[PIN'12] A. Pineau, materiaux et mobilité, Saint-Germain en Laye, 2012.

[SIN'07] Sinclair, C.W., Hutchinson, C.R., Bréchet, Y., 2007. The Effect of Nb on the Recrystallization and Grain Growth of Ultra-High-Purity α-Fe: A Combinatorial Approach. Metallurgical and Materials Transactions A 38, 821–830. https://doi.org/10.1007/s11661-007-9106-9

[TAS'14] Tasan, C.C., Hoefnagels, J.P.M., Diehl, M., Yan, D., Roters, F., Raabe, D., 2014. Strain localization and damage in dual phase steels investigated by coupled in-situ deformation experiments and crystal plasticity simulations. International Journal of Plasticity 63, 198–210. https://doi.org/10.1016/j.ijplas.2014.06.004

[ZUR'06] Zurob, H., Brechet, Y., Dunlop, J., 2006. Quantitative criterion for recrystallization nucleation in single-phase alloys: Prediction of critical strains and incubation times. Acta Materialia 54, 3983–3990. https://doi.org/10.1016/j.actamat.2006.04.028

Chapter 1

Experimental and Simulation Methods

This chapter presents the different experimental and simulation methods employed throughout this study. Their physical and operating principles will not be detailed. However, it will be explained how they were used for the specific needs of the study. The studied material and samples will be described in Chapter 2.

- **Castaing Microprobe** was used to measure the microsegregated state of the industrial steel. The results will be presented in Chapter 2.
- **Scanning Electron Microscopy (SEM)** after etching was employed to observe the microstructure evolution after heat treatments. To quantify these evolutions, microstructural features such as cementite particle size distribution or phase fractions were measured using an image analysis tool. The results will be presented in Chapter 2. The procedures to perform these measurements are detailed in this chapter. Some **Electron Back Scattering Diffraction (EBSD)** maps have also been produced to follow the recrystallization kinetics. The results will be presented in Chapter 4.
- **In situ high Resolution dilatometry** was also used to perform the thermal treatments on selected samples and follow the transformation kinetics. The results will be presented in Chapters 2 and 5.
- **Transmission Electron Microscopy (TEM)** has been used to measure the chemical composition of cementite along different heating stages. The results will be presented in Chapter 3.
- **In situ High-Energy X-Ray Diffraction (HEXRD)** experiments on a synchrotron beamline have been performed at DESY (Hamburg). They have permitted to follow the recrystallization and the phase transformation kinetics along different heating stages of the studied steel. The results will be presented in Chapter 4 and 5 respectively.
- **Commercial computational tools for phase transformation and thermodynamic databases** have been used to model the cementite ageing and phase transformation during the processing of the studied steels. The softwares (Thermocalc and DICTRA) and their references will be briefly described in this chapter. Nevertheless, the studied configuration will be described in Chapter 3 and 5 in more details.

Content

1.1 Studied material

The steel studied in this work serve to produce a DP-600 steel grade. The alloy composition is given in %mass in Table.

C	Mn	Cr	Si
0.1	1.91	0.195	0.205

The material has been provided under the as-hot-rolled state by the industrial partner (industrial semi-product). Cold-rolling has been simulated at the laboratory scale to reproduce two conventional rolling ratios (30 and 60%).

1.2 Electron Probe MicroAnalyser (EPMA)

The chemical homogeneity of our samples has been characterized using a CAMECA SX100 EPMA Castaing Microprobe. In this device, an electron beam is focused on the sample. The interaction between the beam and the atoms of the substrates provokes the emission of X-Rays, whose wavelengths depend on the exited chemical species. The X-Rays are analyzed with a Wavelength-Dispersive Spectrometer (WDS) to identify the nature and the local concentration of the chemical species. For one measure, the excited gauge volume is around 1 μm^3 (electron beam diameter = 1µm). For the present work, a spatial step of 1 µm was used, the accelerating voltage was set to 15 keV (current = 2µA). This work was carried out by Gerard Petitgand at ArcelorMittal Research center (Maizières-les-Metz).

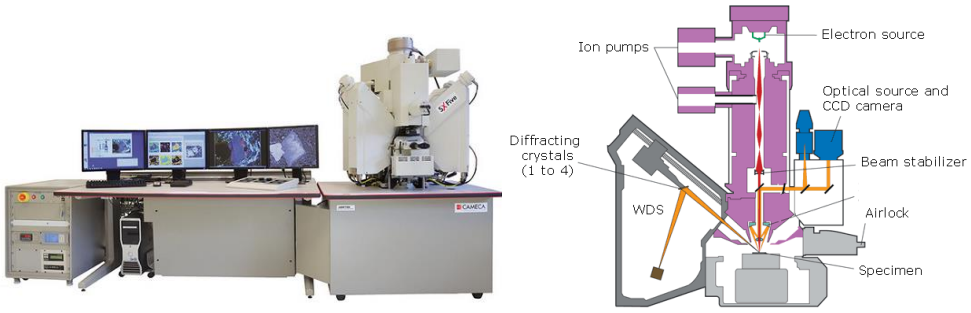

Figure 1.1: Commercial illustration of the CAMECA SX100 EPMA device [CAM'18] and schematic view.

1.3 Dilatometer trials

The heat treatments, presented in the following chapters, were performed on lamellar samples 10 x 5 x 1.2 mm^3, cut down from the industrial sheet. A high precision saw was employed with a slow advance in order to avoid possible sample deformation.

The thermal cycles at low temperatures (below Ac1) were realized using a vertical Rapid Cycle Dilatometer (RCD), developed in our laboratory. Since no phase transformation with large volume change occurs within this temperature range, the dilatometric signal was not exploited.

The treatments in the intercritical range were carried out using a Bähr DIL805 A/D dilatometer at ArcelorMittal Research Center. This device permits an accurate acquisition of the dilatometric signal for phase fractions quantification. These trials have been conducted by Carla Oberbillig.

In both devices, the temperature was measured in real-time using spot welded K-type thermocouples on the d_l slice of the lamellar samples (cf. Fig. 1.5). A brief presentation of the dilatometers is given below.

1.3.1 Rapid Cycle Dilatometer (RCD)

This rapid cycle dilatometer (shown in Figure 1.2) was developed by the engineers of IJL [SAL'15]. The heating is achieved thanks to a light bulb furnace (4 x 1000W) which enables top temperatures as high as 1200°C. The temperature is regulated via a Proportional Derivative Integral (PDI) system. Samples can be cooled by helium injection, whose flow is controlled by regulated modular valves. Maximum cooling rates as high as 70°C.s^{-1} are possible. Samples are installed into a sample holder made of silicon

rods having a weak thermal expansion coefficient (5 x 10^{-7} $^{\circ}C^{-1}$). Our experiments have been conducted under secondary vacuum (1 x 10^{-4} mbar).

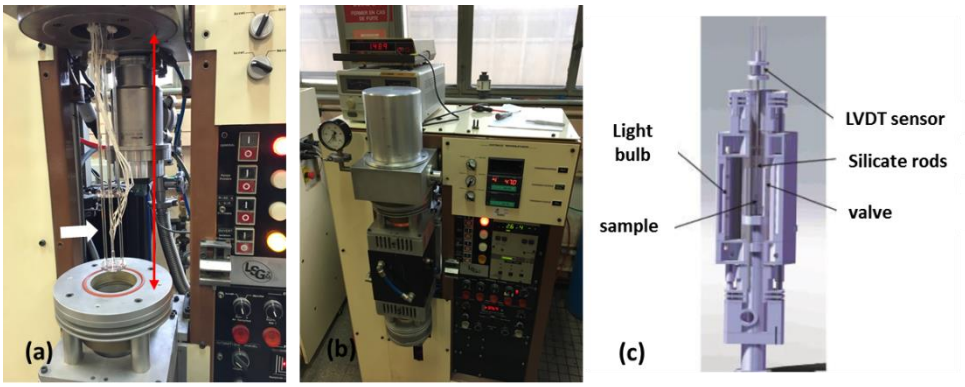

Figure 1.2: (a) open furnace with silicon sample holder in the middle (white arrow). (b) Furnace in operating position. (c) Schematic cross-section of the furnace showing the internal elements [SAL'15].

1.3.2 Bähr DIL 805

Commercial dilatometer Bähr DIL805 [TA'19], available at the ArcelorMittal Research Center and also at the DESY synchrotron facilities was employed to simulate the thermal cycles at high temperatures (interrupted for post-mortem characterization and in situ experiments). The sample is installed into a hermetic chamber where a secondary vacuum is realized. The sample holder is made of two quartz rods, whose one is mobile. The length variation is also measured from the mobile rods displacement via a Linear Variable Differential Transformer sensor (LVDT). Heating is achieved by induction (high frequency) while cooling is achieved by nitrogen or helium injection through the induction coil.

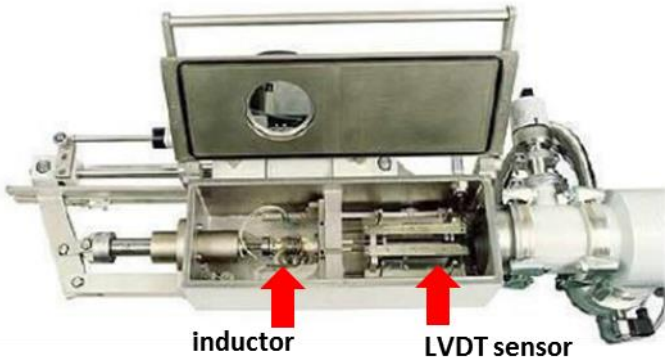

Figure 1.3: Overview of the sample environment in Bähr 805 dilatometer (opened position).

The length variations are captured in real time by a Linear Variable Differential Transformed (LVDT) sensor all along the heat treatment. These variations are due to the thermal expansions of the constituting phases, their change in chemical compositions and the possible volume change to phase transformations.

In the studied transformations, the signal is essentially due to the thermal expansions and to the phase transformations. To deconvolute the contributions, the classical tangent method has been used. For instance, the austenite phase fraction has been measured from the dilatometric curve (relative change in

length vs. time) in Figure 1.4.a. The slope of the upper tangent (blue dashed line) is related to the thermal expansion of ferrite/cementite (no austenite) and the lower tangent slope corresponds to the thermal expansion of austenite (full transformation). The experimental slope deviation from this trend around 720°C corresponds to the austenite transformation onset. Above the transformation onset, a lever rule is used to determine the fraction of austenite. The red segment shows for instance how the austenite volume phase fraction is calculated at 800°C. The fraction is proportional to the AB/AC ratio. The Figure 1.4.b finally represents the austenite transformation kinetics deduced from the dilatometric curves in the adjacent Figure. As heating is achieved by induction, a minor artefact is observed around 750°C (small hump on the dilatometer signal) due the Curie transitions of the alloy.

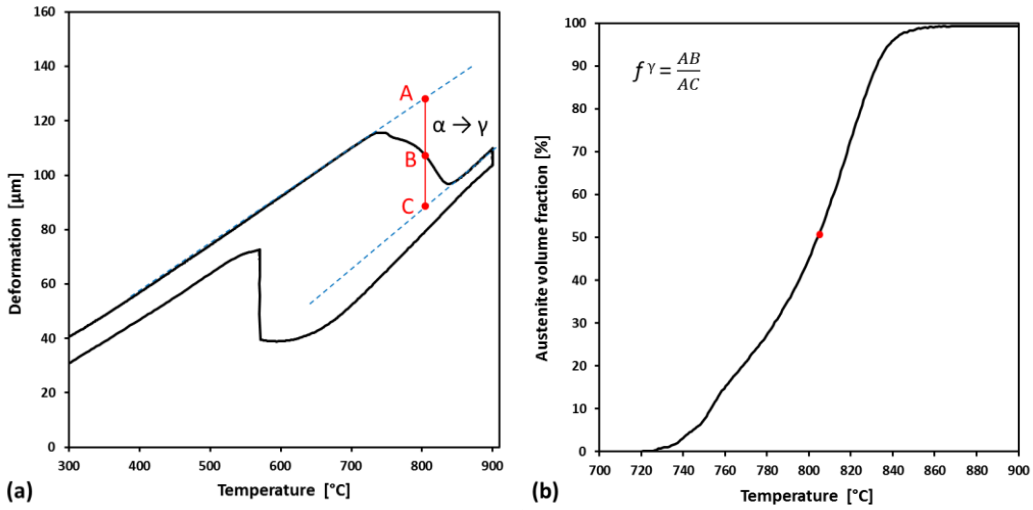

Figure 1.4: dilatometric curve measured during a thermal cycle performed in a Bähr dilatometer. (b) Austenite phase fraction as function of temperature, determined by application of the tangent rule.

1.4 Scanning Electron Microscopy

Scanning Electron Microscopy (SEM) was employed to characterize the microstructures of the studied steels after interrupted or complete heat-treatments.

1.4.1 Metallographic preparation

After heat treatment, the samples were coated with epoxy resin (sagittal cut) for manual polishing. The polishing procedure comprises three steps. First, the samples are polished with silicate grid paper down to 1µm. A second polishing using colloidal silica suspension solution was performed to remove the finest scratches. Finally, the samples were immersed in methanol and cleaned in an ultra-sonic bath (30 min) to eliminate small silica residues.

Two etchants have been used in this study. 2% Picral – 98% ethanol solution (called Picral etchant in the following) has been used to reveal carbide microstructure and a DINO solution has been used to reveal martensite islands (former austenite in fact) and carbide microstructure. DINO etchant is made of (for 250 ml):

- Distilled water (140 mL)
- Hydrogen peroxide (H_2O_2 30%) (100 mL)
- Oxalic acid (4 g)
- Sulfuric acid H_2SO_4 (2 mL)
- Fluorhydric acid HF (1.5 mL)

1.4.2 SEM microstructural observations

Two SEMs have been used in this study. The Phillips XL-30 FEG-SEM at IJL has been used to study carbide distribution after heat-treatment below Ac_1 (Picral etching) while a JEOL JSM-IT300 Tungsten SEM at AM have served to study microstructure after heat treatment below Ac1 (Dino etching).

In both cases, the micrographs were obtained using the Secondary Electron (SE) imagery mode. All samples were investigated at sheet quarter thickness, as illustrated in Figure 1.5.

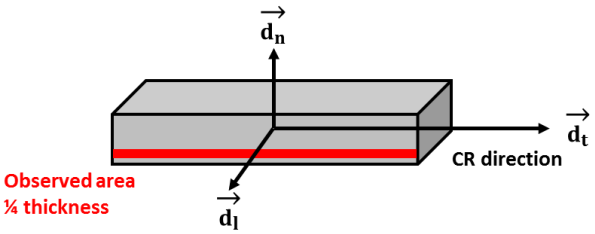

Figure 1.5: schematic representation of the lamellar sample orientations. The cold-rolling direction is denoted by the d_t vector. The systematic sample area investigated at the cold-rolled sheet quarter thickness is highlighted by the red area.

The observations using the JEOL JSM-IT300 Tungsten SEM were made using an acceleration tension of 15kV. The Working Distance (WD) was set to 9 mm. The micrographs were acquired randomly throughout the specimen quarter thickness at various magnifications (x2000, x5000 and x8000).

The set-up using Phillips XL-30 FEG-SEM was less conventional in order to ease the subsequent image analysis. The Working Distance was set so 5 mm using a magnification x10000 to obtain a good compromise between observed surface and resolution. The voltage was set to 5 kV. The micrographs were recorded according the layout displayed in Figure 1.6. 16 micrographs (4 x 4 grid) were realized in order to investigate a large continuous 92 x 120 μm^2 surface of the sample. This permits to account for several pearlite bands over a long distance.

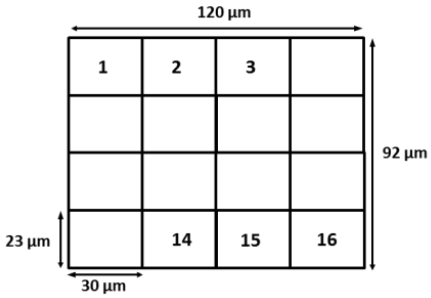

Figure 1.6: experimental layout for SEM micrograph obtention.

EBSD was employed to quantify the recrystallized state of a deformed and heated sample. This operation was realized by Mathieu Salib at ArcelorMittal Research Center. The device used was a FEG SEM JEOL 6500, equipped with the EBSD "Oxford Instrument" system. The post-treatment was done with the AZtec acquisition software. The used post-treatment algorithm will be discussed in chapter 2.

1.5 Image Analysis

SEM micrographs have been analyzed to quantify different microstructure features, such as the size of the constituents (pearlite islands, ferrite grain, and isolated cementite particles) and possibly their size distribution as well as their fractions. This work was accomplished either manually (intercept and point counting method) or using ImageJ software (particle size distribution) [IMJ'19].

1.5.1 Pearlite and ferrite grain size

Mean pearlite island and ferrite grain diameters were measured using the intercept method defined by the ASTM standard E112-96 procedure [ASM'04]. The reader is referred to the publications of Voort *et al.* [VOO'84, VOO'99] for a review and comparisons of the other available approaches. The grains at the micrograph edges were excluded from the analysis. 10 micrographs per investigated conditions were analyzed. 25 straight analyzing lines were randomly considered according 4 different directions, and the number of intersections between line and grain boundaries was rationalized over the total length of the lines. This method permits to erase the effect of moderately non-equiaxed morphologies [PAR'19].

1.5.2 Phase fraction

The quantification was performed by point counting, in accordance with the ASTM E565 standard [ASM'08], to estimate the austenite volume fraction after Dino etching (heat treatment above Ac_1) or Pearlite fraction after Picral etching (heat treatment below Ac1).

1.5.3 Carbide morphology and size

In this section, the procedure developed with ImageJ to prepare and analyze SEM micrographs for the characterization of carbide microstructure in the studied micrographs is explained.

The SEM micrographs are computer-generated greyscale images, where the value of each pixel is between 0 and 255. Figure 1.7(a) represents a typical SEM micrograph with the associated grey scale histogram. Low values represent the darkest contrast (0 = black) while the highest values correspond to bright contrast (255 = white). After Picral etching, ferrite appears in dark and cementite particle in bright. The distinction between ferrite and cementite is then possible by defining a threshold grey value above which the pixel will correspond to cementite (or conversely to ferrite). Once the threshold value is fixed, cementite can appear in white while the ferrite matrix can be transformed into a black background (cf. Fig. 1.7(b)). This key step is termed "binarization".

This operation may be the source of numerous errors since all the particles do not show a homogenous contrast and can show different morphology and topology. Specific routines were developed

in this study to avoid using classical morphological transformations as opening, eroding, closing which lead to biases. These routines permit a better control in the areas where particles of various shapes were close to each other. Moreover, in some cases, these operations are not sufficient to eliminate the grain boundaries, where an example is shown on Figure 1.7 (white arrows). For instance, the removal would require repeated operations, involving particles over-thickening. The treatment procedure is briefly described here:

(i) A median filter is applied to lower the noise and enhance the contrast.
(ii) Top-hat transformation with a circular kernel (radius 3 pixels) to increase locally the contrast around the cementite particle boundaries.
(iii) Detection of the particles intercepting grain boundaries. The grain boundaries are erased without eroding the particles via an algorithm.
(iv) Fill holes transformation.
(v) Despeckle operation to remove single pixels.

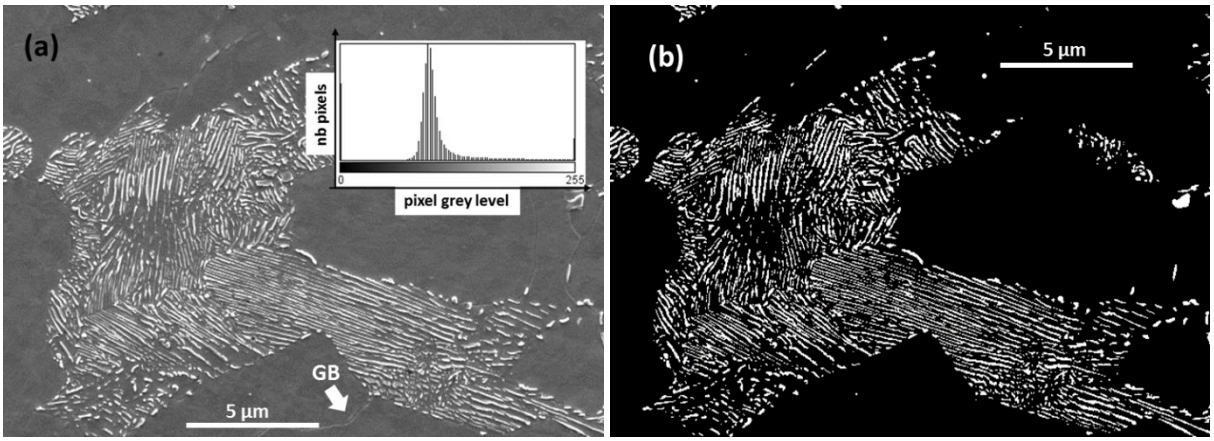

Figure 1.7: SEM micrograph of a pearlite colony. Cementite and ferrite appear in bright and dark contrast, respectively. (a) Original SEM picture with the distribution of the pixels as function of their grey level. (b) Image after standard binarization.

The estimation of the spheroidized state of the microstructure requires the separation of circular shaped particles from that having a longitudinal morphology. Usually, this is accomplished using the Aspect Ratio (AR) criterion [CHA'77, CHA'82, GUO'11]. A fictive box encloses the particles, and the width/length ratio determines if the particle is to be considered as a sphere (generally for AR lower than 3 or 5 according literature). In current case, the "circularity" criterion, defined such that circularity = $4\pi.\text{Area}/\text{Perimeter}^2$ [IMJ'19], was chosen because it seemed more reliable after careful examination. Figure 1.8 illustrates the outcome of the sorting procedure, where spheroids appear in red while lamellar and strongly anisotropic particles remain in black.

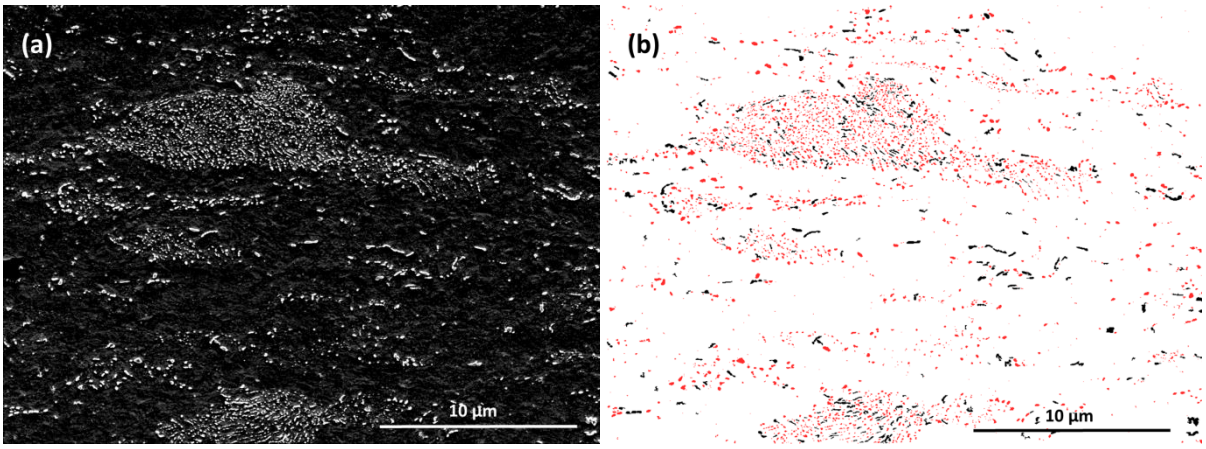

Figure 1.8: (a) original non-binarized SEM micrograph (b) Image after binarization (routine) and particles morphology sorting. Lamellar and spheroidal particle are colored in black and red, respectively.

The true diameters of the cementite particles as well as the size distribution were calculated from the application of the Johnson-Saltykov stereological correction [SAL'67]. The reader can find the detailed procedure here [RUS'12]. The interlamellar spacing in pearlite was measured and corrected in accordance with the method assessed by Ridley [RID'84]. Review and comparisons of various techniques are also reported in the latter article. The particles density was calculated separately in pearlite islands and in the ferrite matrix. Thereupon, the cumulated area occupied by the cementite was rationalized over the examined surfaces.

1.6 Transmission Electron Microscopy (TEM)

The TEM investigations have been conducted at IJL on the JEOL ARM 200F TEM device (Cold Field Emission Gun) with the support of Jaafar Ghanbaja. It has been used to measure in particular the local chemical compositions inside cementite particles.

1.6.1 Thin foil preparation

The thin foils were extracted from the samples after SEM investigations. The specimens were removed from the epoxy-resin shell and ground parallel to the initial faces of the flat products, down to a thickness of about 60 µm using grinding papers. Both sides of specimens were polished to remove possible decarburized layers, trying however to avoid the central segregation. After that, specimens were manually punched to obtain 3 mm diameter cylindrical samples. Finally, foils were drilled by electropolishing using 5% Perchloric - 95% Acetic acid solutions. The electrolytic solution was used at 18°C with a tension of 30V. Appropriate electropolishing parameters were sought to remove ferritic matrix while preserving cementite carbides. Before observations, foils were cleaned using a Precision Ion Polishing System (Gatan 691 PIPS).

1.6.2 Chemical Analysis of the cementite particle compositions

The TEM was operated at 200 kV. Composition measurements were performed with a BRUKER XFlash EDXS Silicon Drift Detector with a chemical resolution of 127 eV and a collector plate of 30 mm^2. The measurements presented in the following have been obtained with a probe size of 1 nm (1000 times finer than a conventional Castaing microprobe). Accounting for the thickness of the foil and contrary to SEM, there is no enlargement of the excitation volumes within the sample. The analyzed volume is thus limited to the probe size diameter.

EDXS measurements are by nature punctual, but repeating the measurements along lines and columns permits to reconstruct composition profiles or maps. A minimum spatial step of 5 nm was chosen to provide suitable compromise between spatial resolution and X-ray counts, in order to obtain statistically meaningful results in a reasonable period of time.

Detection of light chemical species like carbon is not possible by EDXS method because of the energy resolution. For this reason, it has been carried out only for major substitutional elements for Fe like Mn, Cr and Si. The measured concentrations are given by the Desktop Spectrum Analyzer (DTSA) in relative atomic site-fraction. As carbon is not considered in the balance, the measurements correspond to the u-fractions for each element. The typical relative error for measured substitutional concentrations was calculated using standard statistical techniques and does not exceed 5% (relative value). An Electron Energy Loss Spectroscopy (EELS) detector has also been used to estimate the local thickness of the foil. For each studied state, about 5 particles have been studied in detail (composition profiles). These particles were located in pearlite islands (not isolated at a ferrite grain boundary) to obtain a possible correlation with our thermodynamic prediction. However, it is not possible to tell with certainty that they are located in a microsegregated band.

1.7 High Energy X-Ray Diffraction (HEXRD)

1.7.1 Experimental set-up

In situ High Energy X-Ray Diffraction experiments have been conducted on Petra III-P07 line (EH3 hutch) at the Deutsches Elektronen SYnchrotron (DESY) facilities in Hamburg (Germany). The experimental configuration is schematized in Figure 1.9(a) and the experimental setup is illustrated in b and c. 63 in situ High Energy X-Ray Diffraction (HEXRD) experiments were carried out on lamellar samples 10 x 5 x 1.2 mm^3, cut down from the industrial cold-rolled ferrite pearlite DP600 product.

The monochromatic incident X-Ray beam is diffracted when passing through the lamellar sample (oriented perpendicularly to the beam, according the d_n vector, cf. Fig. 1.5). This technique permits to investigate in transmission larger volumes (700 x 700 x 1200 μm^3) compared to the microscopy technique detailed above. The high energy of the incident beam (wavelength λ=0.124 nm) produces low Bragg's diffraction angles. The fine grain size in the studied microstructures enables the production of continuous diffracted beam cones. These diffracted beams generate Debye Scherrer (DS) ring patterns on the planar CCD detector. The used Perkin Elmer detector shows a low ratio between background noise over signal intensity. The combination between the brightness of the beam, the energy and the quality of the detector has permitted to reach acquisition frequency rates up to 10 Hz.

The position of the detector relative to the samples was measured by laser and then determined precisely during the calibration procedure. This procedure consists in analyzing with Fit2D software a single diffraction pattern of LaB_6 powder. A capillary filled with strain-free powder is put at the place of the steel sample and a diffraction pattern is recorded. As the lattice parameter of the LaB6 is well known at room temperature, it permits to determine the exact position of the incident beam on the detector, its distance and also its parallelism. The values determined are then used to correct and interpret

systematically all the diffraction patterns obtained on steels. As explained below, the second interest of this calibration procedure is to estimate the natural broadening tendency of the set-up.

The heat treatments were performed by mean of a modified 805 A/D Bähr dilatometer as shown in Figure 1.10. The thermal schedules will be detailed in Chapter 4 and 5 respectively. As diffraction patterns can be obtained at the same time as the sample is heated, we are speaking about in situ experiments.

The temperature was measured in real time using K-type thermocouple that was spot welded on the d_l side (as shown in Figure 1.9). The intrinsic uncertainty on temperature measurement associated with such thermocouple is ±2.2°C and must be added to that due to thermocouple connectors (±1°C). An additional temperature uncertainty is induced with the fast acquisition mode due to their intrinsic response times (0.1ms). This uncertainty ΔT is then estimated as ΔT = ± 0.1 x heating rate [ESI'04, NAK'04]. For a heating rate of 30°C/s, the temperature uncertainty is thus about ± 3°C. These temperature uncertainties will be taken into account during the exploitation of the results.

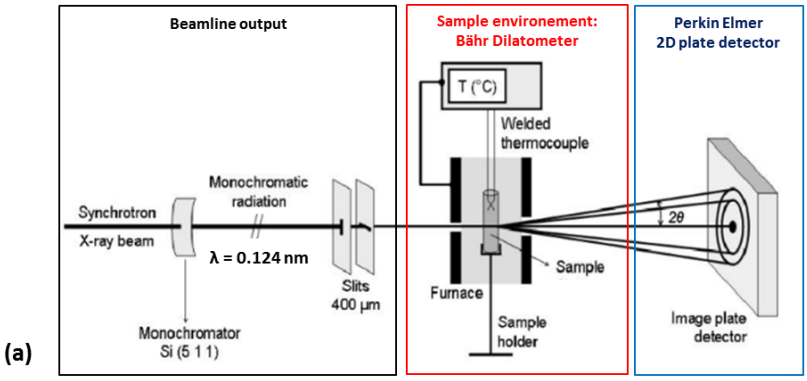

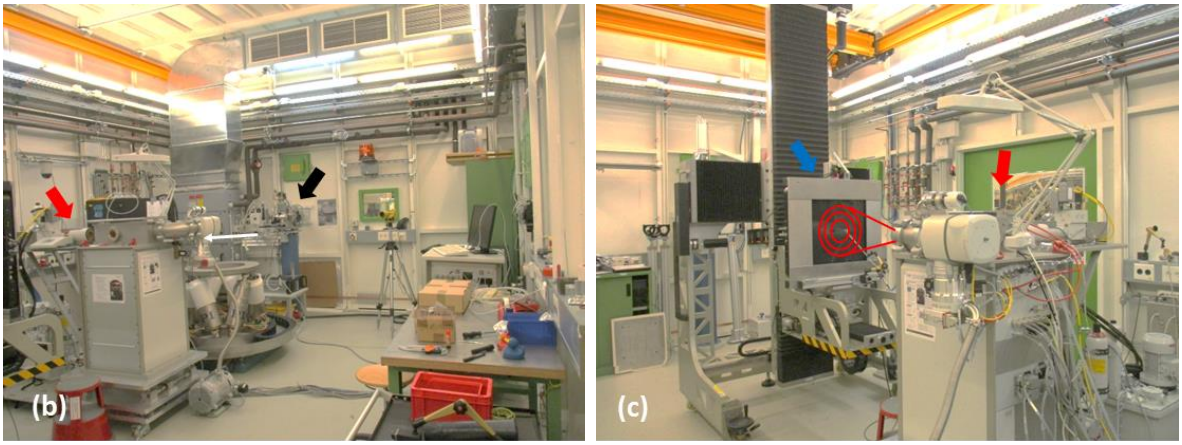

Figure 1.9: (a) scheme of the experimental setup. (b) Illustration of the beam output (black arrow) and of the Bähr dilatometer (red arrow). The beam direction is indicated by the white arrow. (c) 2D plate detector (blue arrow) from which the 2D patterns are recorded.

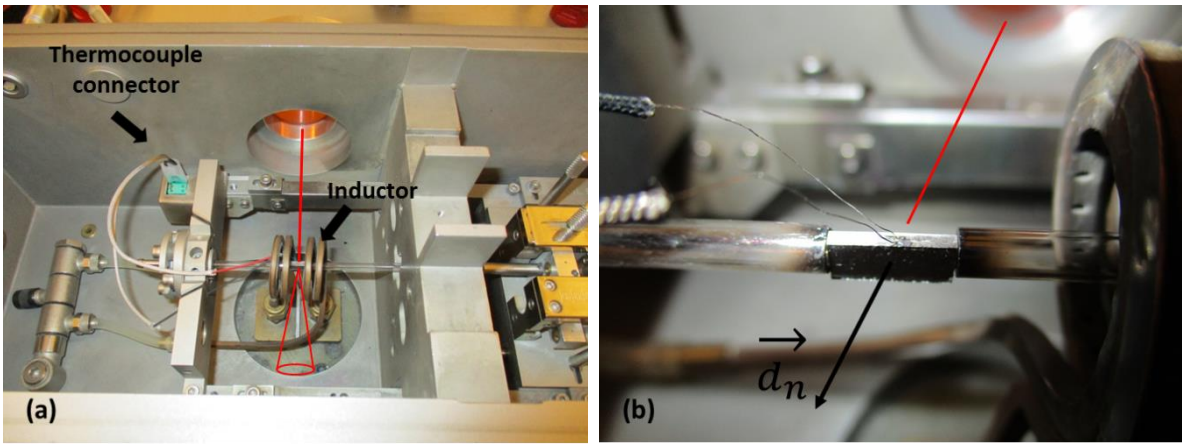

Figure 1.10: (a) Inner view of the sample enclosure inside the Bähr dilatometer. The beam input and the diffracted signal are represented in red. (b) Focus on the lamellar sample. The thermocouple is spot welded on the slice. The synchrotron beam passes through the sample according the d_n direction (cf. Fig. 1.4).

Not less than 7000 patterns were produced per experiment. The diffraction patterns have thus been analyzed using automated tools. In this Chapter, we will present the procedure which has been followed to perform our conventional Rietveld refinements (circular integration of DS rings and refinement). However, this analysis is not sufficient to obtain information about the recrystallization state of our material. A new analyzing technique has thus been developed and exploited. This latter will be discussed in Chapter 4.

1.7.2 Circular integration

When necessary, the intensity of the DS rings is integrated over the circular length of the rings (using Fit2D software) to produce 1D - 2θ intensity profiles (cf. Fig. 1.11). There are as many 1D-profiles produced as the number of recorded 2D patterns. Reliable integration requires an accurate instrumental calibration.

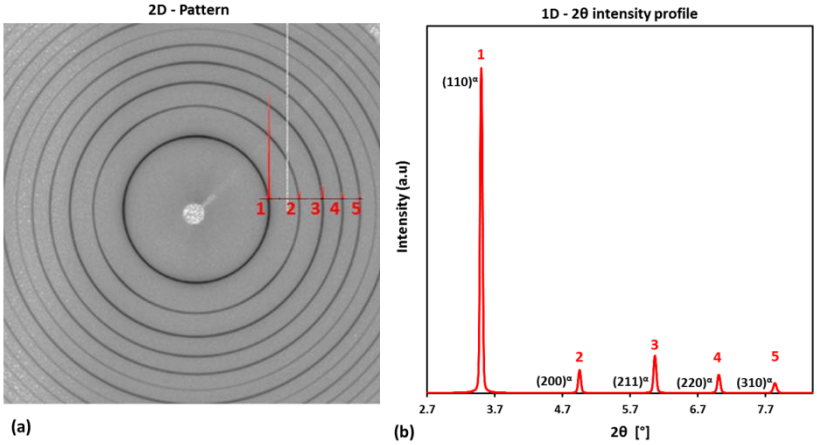

Figure 1.11: (a) 2D diffraction pattern where the Debye-Scherrer rings are produced by the diffraction of ferrite α. (b) 1D-2θ integrated intensity profile. The intensity peaks are identified by their corresponding *hkl* lattice index.

1.7.3 Phase quantification by Rietveld refinement

After circular integration, the patterns are analyzed by multiphase Rietveld refinement using the Fullprof software developed by Carvajal *et al.* [CAR'93]. The Rietveld approach consists in simulating theoretical 1D profiles, calculated from instrumental and structural parameters, to determine the phase fractions (in %weight). The simulated profiles are assessed upon minimizing the weight squared difference between the observed intensity $y_{i,exp}$ and the calculated one $y_{i,rietveld.}$ The function to be minimized is termed "chi-2", expressed by (1.1):

$$\chi^2 = w_i(y_{i,exp} - y_{i,rietveld})^2 \quad (1.1)$$

being w_i a factor inversely proportional to the variance, such that $w_i = 1 / \sigma_i^2$. Thus, the standard deviation σ_i permits to establish the phase fraction uncertainty (error bar). The reader is referred to the work of Rietveld [RIE'69] for a detailed description of the numerical approach which relates the phase fractions to the diffracted intensities.

In the present study, the 1D profiles were integrated in batch-mode within the 2.7 - 7.2° 2θ range, discretized in 0.003751° steps, in such a manner to include only full rings. The mathematical form chosen to reproduce the experimental peaks is based on pseudo-Voigt functions. The refinement worked on the following phase structural parameters: lattice parameters, scale factors, peak widths, strains and overall isotropic temperature factor. Figure 1.12 is a screenshot taken from manual refinement (ferrite + austenite), where the experimental profile is plotted in red while that obtained from refinement appears in black.

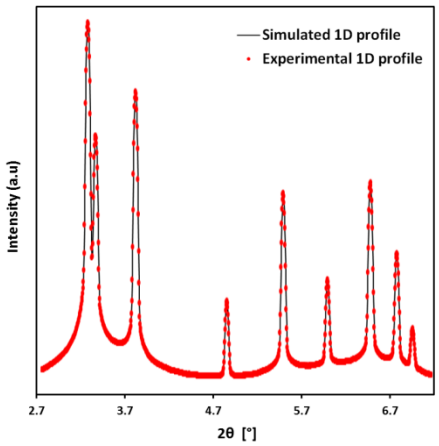

Figure 1.12: (a) Example of Rietveld refinement performed on a 1D profile, where ferrite and austenite diffract.

The adjustment of the experimental peak width is essential, since it results from different contributions that must be deconvoluted: experimental broadening and density of crystalline defects in particular. In the Rietveld numerical procedure, the Full Width Half Maximum (FWHM) is determined by the calculation of three variables denoted U, V, W, related to the FWHM (termed β_{hkl}) by the Caglioti formula (1.2):

$$\beta_{hkl} = \sqrt{U\,tan^2\theta + V\tan\theta + W} \quad 1.2)$$

where θ is the half 2θ angle and β_{hkl} the FWHM. As evoked previously, the LaB_6 calibration enables the instrumental peak broadening determination. This is due to a particular feature of the LaB_6 material: the

FWHM remains constant as function of the 2θ angle. The instrumental broadening in then subtracted from the experimental one using the relation (1.3):

$$\beta_{hkl} = \sqrt{{\beta_{exp}}^2 - {\beta_{inst}}^2} \tag{1.3}$$

being β_{exp} , β_{inst} the measured FWHM and the instrumental broadening measured with LaB_6 calibration. The exploitation of the peak widths is addressed in chapter 4.

An additional type of analysis was realized in frame of ferrite recrystallization *in-situ* characterization. The ring intensity of the $(200)^{\alpha}$ DS as function of the azimuthal angle ring was surveyed. The purpose of the method is presented in detail in the relevant Chapter 4, dedicated to recrystallization during heating.

1.8 Thermodynamic approach and Thermocalc/DICTRA modeling tool

1.8.1 Analytical treatment of diffusive and moving interface problems

In Fe-C-X steels, X being a substitutional alloy component, the phase transformation kinetics is simultaneously controlled by the solute diffusion inside the phases and the transfer of carbon and alloy elements at the interface. In many diffusive problems, the interface is reduced to a mathematical surface according the seminal work of Gibbs [GIB'48]. More complex models for the interface are possible (see e.g. [HIL'99, GOU'15]). The phase transformation taken as example for the following is austenite to ferrite. The interface migration rate *v* verifies the continuity equation [HIL'04]:

$$\frac{v}{V_m}(x_k^{\gamma} - x_k^{\alpha}) = J_k^{\gamma} - J_k^{\alpha} \tag{1.4}$$

where $x_k{}^{\alpha}$ and $x_k{}^{\gamma}$ stand for element k molar fraction at the interface at ferrite and austenite side, respectively, $J^{\phi}{}_k$ are the fluxes of k atoms in phase ϕ (α or γ) at the interface. V_m is the molar volume, considered the same for both phases α and γ.

Most frequently, one assumes that the thermodynamic equilibrium prevails locally at the α/γ interface [HIL'04, KIR'58]. The equality of the chemical potentials (1.5) provides the additional equations which enable the determination of a single solution.

$$\mu_k^{\gamma} - \mu_k^{\alpha} = 0 \qquad (k = 1, \dots, N) \tag{1.5}$$

The determination of the chemical potentials as function of phase compositions and temperature is made possible thanks to the CALPHAD method, detailed in the subsequent part.

1.8.2 CALPHAD method for calculation of thermodynamic equilibria

CALPHAD method (CALculation of PHAse Diagrams) consists in collecting and assessing all available experimental and theoretical information available on phase equilibria and thermochemical properties of the phases in a system. The thermodynamic properties of each phase are then described through the Gibbs free energy, which is represented by some mathematical function. Following this it is possible to recalculate the phase diagram, as well as the thermodynamic properties of all the phases and the system as a whole. Such calculations can be done with Thermocalc software.

The philosophy of the CALPHAD method allows to extrapolate the data established on binary, ternary or few higher-order systems to multicomponent systems. As the mathematical functions describing the Gibbs energies have some physical ground, these can also be extrapolated in temperature and composition domains without experimental and theoretical information. It also makes possible to predict metastable equilibria between phases, which are essential data to predict phase transformation kinetics.

1.8.3 Diffusive problem modeling with DICTRA

This section summarizes basic principles of DICTRA software, but more details can be found in the software's documentation and in [AND'02]. DICTRA software was intended primarily to solve numerically problems of diffusion but it was then extended to moving interface problems. It handles simple geometries (planar, spherical or cylindrical) reduced into a one-dimension (1D) problem with space variable *z*. According to Fick's first law, the fluxes J_k of atoms *k* used in the continuity equation introduced previously are written:

$$J_k = -\sum_{j=1}^{n} D_{kj} \frac{\partial c_j}{\partial z} \qquad 1.6)$$

where c_j is the molar concentration of solute *j*. D_{kj} is the inter-diffusion coefficient, whose element inter-dependence is written with equation (1.9):

$$D_{kj} = \sum_{i=1}^{n} L'_{ki} \frac{\partial \mu_i}{\partial c_j} \qquad 1.7)$$

The diffusion coefficients used in DICTRA are obtained by the product of a thermodynamic ($\partial\mu_i/\partial c_j$) and a kinetic factor, denoted L'_{ki}. It was demonstrated that the concentration gradient of one species may prompt other solutes to diffuse, as evoked by Darken [DAR'42] and experimentally evidenced by the same author [DAR'49]. The thermodynamic factor makes the diffusion coefficient proportional to the chemical driving force, which also accounts for the concentration of the other alloy components. L'_{ki} is computed consistently with the expression (1.10):

$$L'_{ki} = \sum_{j=1}^{n} (\delta_{jk} - c_k V_j) L_{ji} \qquad 1.8)$$

where δ_{jk} is the Kronecker symbol, V_j is the partial molar volume of the component j. DICTRA assumes a constant molar volume for all species, taken as $V_m = 10^{-5}$ $m^3.mol^{-1}$, per mole of substitutional species. L_{ji} is designated as the mobility of the component *i* within a *j* atomic lattice.

1.8.4 Mobility databases

Mobilities are stored in the databases rather than diffusion coefficients [BOR'00]. The mathematical functions giving the mobilities as a function of temperature and composition are written with the CALPHAD formalism, like for thermodynamic databases. The mobility terms are determined from experiments on binary alloys and few higher-order systems. The extension to multicomponent systems is then carried out by extrapolation. From an experimental point of view, the determination of diffusion coefficients is a long procedure. The assessment of experimental informations and the verification of the

model parameters to be included into the databases are time consuming [BOR'00]. Databases development is possible thanks to the collaboration between several research teams, like for instance in Europe within the Scientific Group Thermodata Europe community [SGT'94].
As illustrated by equations. (1.7) and (1.8), two databases are required to determine the diffusion coefficients: one for the thermodynamic data and the other for the mobilities. In this study, the TCFE9 and MOBFE2 [DIC'13] databases will be used.

REFERENCES

[AND'02] Andersson, J.-O., Helander, T., Höglund, L., Shi, P., Sundman, B., 2002. Thermo-Calc & DICTRA, computational tools for materials science. Calphad 26, 273–312. https://doi.org/10.1016/S0364-5916(02)00037-8

[ASM'04] AMERICAN SOCIETY FOR TESTING AND MATERIALS (FILADELFIA, PA.). ASTM E112-96., 2004 e2: Standard Test Methods for Determining Average Grain Size.

[ASM'08] Standard, A. S. T. M. "Standard Test Method for Determining Volume Fraction by Systematic Manual Point Count." *A STM E562-08*., 2008.

[BOR'00] Borgenstam, A., Höglund, L., Ågren, J., Engström, A., 2000. DICTRA, a tool for simulation of diffusional transformations in alloys. Journal of Phase Equilibria 21, 269–280. https://doi.org/10.1361/105497100770340057

[CAL'19] https://www.thermocalc.com/media/10884/DB-Overview_2013-12-05.pdf

[CAM'18] https://www.cameca.com/products/epma/sxfive

[CAR'93] Rodríguez-Carvajal, J., 1993. Recent advances in magnetic structure determination by neutron powder diffraction. Physica B: Condensed Matter 192, 55–69. https://doi.org/10.1016/0921-4526(93)90108-I

[CHA'77] Chattopadhyay, S., Sellars, C.M., 1977. Quantitative measurements of pearlite spheroidization. Metallography 10, 89–105. https://doi.org/10.1016/0026-0800(77)90044-1

[CHA'82] Chattopadhyay, S., Sellars, C.M., 1982. Kinetics of pearlite spheroidisation during static annealing and during hot deformation. Acta Metallurgica 30, 157–170. https://doi.org/10.1016/0001-6160(82)90055-4

[DIC'13] https://www.thermocalc.com/media/10884/DB-Overview_2013-12-05.pdf

[DIC'16]DICTRA Version 2016a User Notice. https://www.thermocalc.com/media/46093/Diffusion-Module-DICTRA-User-Guide-2016a.pdf

[ESI'14] Esin, V.A., Denand, B., Le Bihan, Q., Dehmas, M., Teixeira, J., Geandier, G., Denis, S., Sourmail, T., Aeby-Gautier, E., 2014. In situ synchrotron X-ray diffraction and dilatometric study of austenite formation in a multi-component steel: Influence of initial microstructure and heating rate. Acta Materialia 80, 118–131. https://doi.org/10.1016/j.actamat.2014.07.042

[GIB'48] Gibbs, J. W., 1948. The collected works of J. Willard Gibbs (No. 536.7092). Yale Univ. Press. n.d.

[GUO'11]Guo, W.Y., Li, J., Jiang, X.F., 2012. Subcritical Spheroidization of Medium-Carbon 50CrV4 Steel. Journal of Materials Engineering and Performance 21, 1003–1007. https://doi.org/10.1007/s11665-011-9957-5

[HIL'04] Hillert, M., Odqvist, J., Ågren, J., 2004. Interface conditions during diffusion-controlled phase transformations. Scripta Materialia 50, 547–550. https://doi.org/10.1016/j.scriptamat.2003.10.027

[HIL'80] Hillert, M., 1980. Empirical methods of predicting and representing thermodynamic properties of ternary solution phases. Calphad 4, 1–12. https://doi.org/10.1016/0364-5916(80)90016-4

[IMJ'12] ImageJ version 1.46r, User Notice. https://imagej.nih.gov/ij/docs/guide/user-guide.pdf

[KIR'58] Kirkaldy, J.S., 1958. DIFFUSION IN MULTICOMPONENT METALLIC SYSTEMS: II. SOLUTIONS FOR TWO-PHASE SYSTEMS WITH APPLICATIONS TO TRANSFORMATIONS IN STEEL. Canadian Journal of Physics 36, 907–916. https://doi.org/10.1139/p58-097

[NAK'04] Nakos, J.T., 2004. Uncertainty analysis of thermocouple measurements used in normal and abnormal thermal environment experiments at Sandia's Radiant Heat Facility and Lurance Canyon Burn Site. (No. SAND2004-1023, 918777). https://doi.org/10.2172/918777

[PAR'19] Paredes-Orta, C.A., Mendiola-Santibañez, J.D., Manriquez-Guerrero, F., Terol-Villalobos, I.R., 2019. Method for grain size determination in carbon steels based on the ultimate opening. Measurement 133, 193–207. https://doi.org/10.1016/j.measurement.2018.09.068

[RIE'69] Rietveld, H.M., 1969. A profile refinement method for nuclear and magnetic structures. Journal of Applied Crystallography 2, 65–71. https://doi.org/10.1107/S0021889869006558

[RID'84] Ridley, N., 1984. A Review of the Data on the Interlamellar Spacing of Pearlite. Metallurgical Transactions A 15, 1019–1036. https://doi.org/10.1007/BF02644694

[RUS'13] Russ, J.C., 2013. Practical stereology. Springer.

[SAL'15] M.Salib,. 2015. Étude cinétique et cristallographique de la précipitation de la phase α aux joints de grains β/β dans un alliage de titane. PhD report.

[SAL'67] Saltikov, S.A., 1967. The Determination of the Size Distribution of Particles in an Opaque Material from a Measurement of the Size Distribution of Their Sections, in: Elias, H. (Ed.), Stereology. Springer Berlin Heidelberg, Berlin, Heidelberg, pp. 163–173. https://doi.org/10.1007/978-3-642-88260-9_31

[SGT'94] *SGTE (Scientific Group Thermodata Europe´) Solution* 19, pp. 35-50. *Database of Jan. 1994*, B. Sundman, ed., Division of Computational Thermodynamics, Royal Institute of Technology, S-100 44 Stockholm, Sweden, e-mail: bosse@met.kth.se.

[SUN'85] Sundman, B., Jansson, B., Andersson, J.-O., 1985. The Thermo-Calc databank system. Calphad 9, 153–190. https://doi.org/10.1016/0364-5916(85)90021-5

[TA'19] https://www.tainstruments.com/products/dilatometers/quenching-dilatometers.

[VOO' 84] Vander Voort, G., 1984. Grain Size Measurement, in: Steele, J., McCall, J. (Eds.), Practical Applications of Quantitative Metallography. ASTM International, 100 Barr Harbor Drive, PO Box C700, West Conshohocken, PA 19428-2959, pp. 85-85–47. https://doi.org/10.1520/STP30216S

[VOO'99] Vander Voort, G.F., 1999. Metallography, principles and practice. ASM International, Materials Park, Ohio.

Chapter 2

Morphogenesis of ferrite-austenite microstructures during intercritical annealing

This chapter deals with the morphogenesis process of ferrite/austenite microstructure during the intercritical annealing of the cold-rolled ferrite-pearlite microstructure, i.e. the process explaining the morphology and topology (spatial distribution) of the phases after transformation. It addresses in fact the question of the interactions between austenite phase transformation and recrystallization processes. This is a key topic for steelmakers because industrial plant configurations are such that the interactions can be weak and strong depending on the heating technology. Ferrite/austenite microstructure presents a "necklace" configuration after slow heating whereas the microstructure is "banded" after fast heating. Our literature review shows that all the authors do not agree about the basic mechanisms behind these interactions (carbide ripening, nucleation and growth of austenite, nucleation and growth of recrystallized ferrite grains). Even recent full field simulations are not able to capture the main experimental observations about these interactions.

This is the reason why we have conducted our own systematic study of the microstructure evolutions all along continuous annealing cycles. This part of the study has been mainly conducted using Scanning Electron Microscopy (SEM) on representative samples and is essentially qualitative. First, the ferrite-pearlite microstructures obtained after hot-rolling and further cold-rolling are compared. This preliminary work is important as it serves to determine the main characteristics of the microstructure before annealing. In this section, a special attention has been paid to the carbide microstructure. The investigations of the annealing processes are conducted in two temperature ranges. The first studied range corresponds to the sub-critical domain up to 700°C in order to stay below Ac_1 temperature. In this range, some interactions are expected between recrystallization and carbide spheroidization. Then, the austenite transformation is studied in the intercritical range. All the experimental procedures deployed in this chapter have been described in previous chapter 1. Our whole analysis sustains mainly the interpretation proposed by Li *et al.* in 2013.

Content

2.1 Literature review: Morphogenesis of ferrite/austenite microstructures during annealing

This literature review is dedicated to the possible physical mechanisms explaining the interactions between carbide ripening, recrystallization and phase transformation (nucleation and growth) during the annealing of deformed ferrite/pearlite microstructures and leading to the typical "necklace" or "banded" microstructures.

2.1.1 Formation of cold-rolled ferrite-pearlite microstructures

Before discussing the physical mechanisms occurring during continuous annealing steels, the microstructure formation and evolution during hot-rolling and cold-rolling must be discussed.

2.1.1.a Microstructure evolution during industrial hot-rolling process

The hot-rolling of studied steels is conducted in industrial plants between 1250°C and 900°C typically. Slabs produced by continuous casting are heated first in a furnace at about 1250°C and then successively bloomed, edged and rolled (5 successive passes to reach a final thickness of about 3 mm). All these rolling operations are performed above 850°C in the austenitic state. After deformation in the last stand, the steel band is cooled by water spraying on a run-out-table. During cooling, when the temperature decreases below the A_{r3} temperature, austenite starts to decompose into pro-eutectoid ferrite. This ferritic transformation leads to progressive carbon enrichment in austenite. The precipitation of cementite particles at the pro-eutectoid grains/austenite boundaries is also possible.

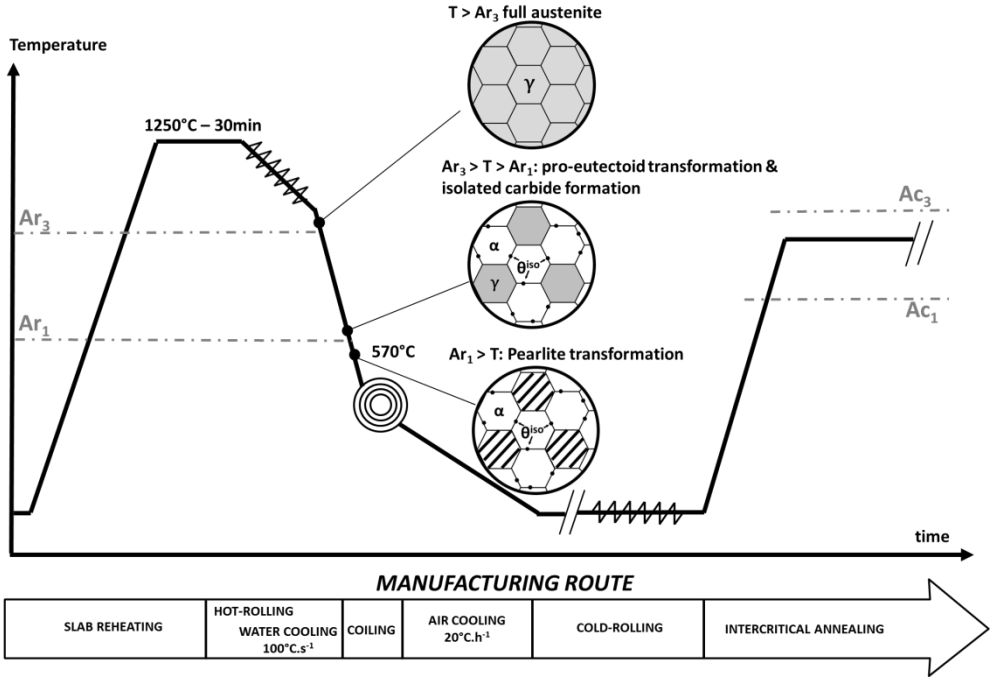

Figure 2.1: Austenite decomposition into a ferrite/pearlite microstructure along an industrial hot-rolling schedule. The studied steel is fully austenitic at the Finish Rolling Temperature (FRT). Ferrite transformation starts at Ar_3 and almost stops when austenite is sufficiently enriched in carbon. This condition is often reached just before coiling operation around 550°C.

At lower temperatures, the remaining austenite can transform into lamellar pearlite islands when carbon concentration is sufficiently high (around 570°C). This last transformation often occurs just before or after the coiling operation (550°C). These successive phase transformations, their thermodynamic conditions and their kinetics will be discussed in detail in chapter 3. Figure 2.1 illustrates the successive states of the microstructure and their respective temperature ranges.

2.1.1.b Precipitation of intergranular isolated cementite particles

Many authors report that they observe not only lamellar carbides in pearlite islands in as hot-rolled products but also carbides at ferrite grain boundaries. We will see in the following that these isolated carbides have a key role in the morphogenesis of ferrite/austenite microstructure as they act as preferential nucleation site for austenite transformation (chapter 2) and they control in large part the global transformation kinetics (chapter 5).

Lamellar pearlite transformation occurs mainly in enriched austenite grains and is a process studied for a while [JUD'69, SPE'69]. The presence of coarse intergranular cementite particles is also commonly observed on ferrite/pearlite grain boundaries. It is interpreted as the result of the Ostvald ripening of lamellar pearlite islands which occurs during prolonged heat treatments after pearlite formation.

On the contrary, the formation of isolated intergranular carbides between two ferrite grains is seldom discussed in literature [YAN'85, LEE'87, LEE'90, LEE'93, GRA'10]. These particles are sometimes simply ignored [OLL'17] or presented as the result of spheroidization process [TOM'18]. Lee *et al*. [LEE'87] on the contrary noticed the systematic formation of intergranular cementite particles in steels that are slowly cooled down from the austenitic domain. The same authors conducted experiments to

identify the temperature range in which precipitation occurs [LEE'90]. They concluded that these particles are formed in fact before pearlitic transformation. They also suspect that the presence of a cementite particle at a boundary between a ferrite grain and an untransformed austenite grain is necessary to trigger the formation of a pearlite island. After further TEM investigations, the latter authors proposed a mechanism to explain the formation of the intergranular carbides [LEE'93], which is schematized in Figure 2.2. During the pro-eutectoid ferrite transformation, several austenite pools can be trapped between two growing ferrite grains (cf. Figure 2.2(a)). The austenite nucleation at the austenite pool / ferrite grain triple junction is assumed possible (cf. Figure 2.2(b)). The carbide can grow by depleting the austenite pool in carbon and then transform the remaining pool into a ferrite grain, leaving a cementite particle or a group of small carbides on the grain boundary (cf. Figure 2.2(c)). Prolonged cooling permits coarsening and impingement of the cementite particles which leads to continuous layers of cementite along the grain boundaries.

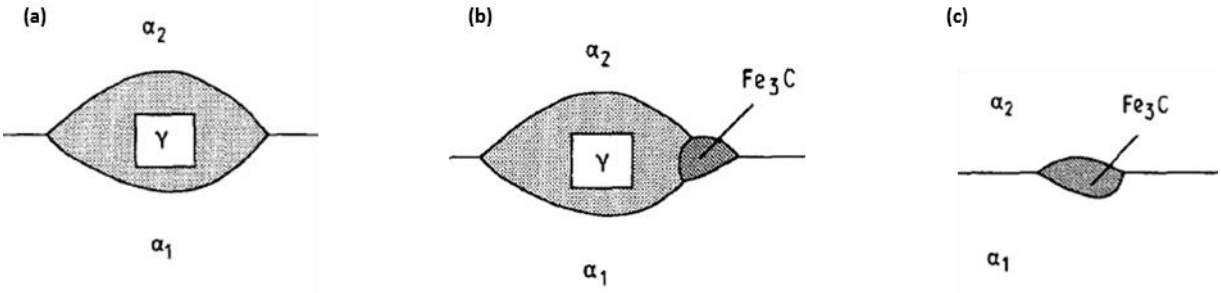

Figure 2.2: Schematized formation of intergranular cementite particles at ferrite grain boundaries. (a) Austenite pool is trapped between two growing ferrite grains. (b) A carbide nucleates at the ferrite / austenite triple junction. (c) The growing carbide depletes the remaining austenite pool in carbon [LEE'93].

More recently, Granbom [GRA'10a, GRA'10b] investigated the formation of these intergranular particles on different DP steel grades in industrial conditions. They report the presence of isolated carbides in products slowly cooled (2°C.s^{-1}) within the 710-760°C temperature interval confirming the prior works of Lee *et al.*. Nevertheless, they explain the precipitation of intergranular cementite by the carbon supersaturation in ferrite, which is possible only in case of slow heating.

The formation mechanisms of these carbides thus remain controversial in the literature and would deserve deeper study accounting their critical role in the austenite phase transformation. We will see however in chapter 3 that their precipitation temperature does not affect much their compositions.

2.1.1.c Microstructure evolution during CR

Cold-Rolling (CR) is a severe plastic deformation (SPD) process. In this thesis, two cold-rolling ratios have been studied (30% and 60%) but in this chapter, we will only consider steels deformed with the highest ratio. The equivalent plastic strain by rolling can be calculated with equation (2.1) [FRE'96]:

$$\varepsilon = \frac{2}{\sqrt{3}} . \ln(\frac{1}{1-R}) \quad (2.1)$$

where R is the cold rolling ratio.

The studied cold-rolling ratio (60%) corresponds to a severe plastic deformation of 106% in bulk. During such process, as pearlite shows a higher flow stress than ferrite, the local deformation is even higher in the ferritic matrix. The model proposed by Allain *et al*. [ALL'04] predicts such strain partitioning in both ferrite and pearlite and enables estimating the density of dislocations in ferrite after cold-rolling. For the studied case, the predicted deformation of ferrite and pearlite is about 120% and 67%

respectively. Ferrite and pearlite islands will thus be strongly elongated during the cold-rolling process. It is rather well established that pearlite islands buckle and undergo intense shear banding. Another interesting consequence of the rolling process is the decrease in the lamellar spacing of pearlite. The true interlamellar spacing can be calculated as follows:

$$S_\varepsilon = S_0 . \exp(-\frac{\varepsilon}{2}) \quad (2.2)$$

where S_ε is the interlamellar spacing after cold-rolling and ε is the equivalent plastic strain by rolling.

This rolling process leads to the fragmentation of the pearlite lamellar structures to the benefit of spheroidized particles. It is the reason why we will compare systematically the Hot-Rolled (HR) and Cold-Rolled (CR) microstructures. A particular attention is paid to the spheroidized particles because they are more favorable sites for the nucleation of austenite, as discussed in the following sections.

2.1.2 Interactions between recrystallization and austenitization

The interactions between recrystallization and austenitization of deformed ferrite-pearlite steels were the topic of numerous studies since the beginning of the 80's. Most of them were conducted during annealing at a constant heating rate of cold-rolled steels as these conditions are encountered in the production of low thickness advanced high strength steels (AHSS).

When considering the recent literature in this field, most of the authors agree on the following experimental facts:

- If the deformed ferrite-pearlite microstructure is annealed at a low heating rate, the resulting microstructure in the intercritical range presents a necklace topology, i.e. that recrystallized ferrite grains are bordered by a continuous layer of austenite. The recrystallization of ferrite is finished before austenite transformation and the interactions between mechanisms are "weak". Austenite transformation starts at temperature close to equilibrium conditions (Ac_1) and the transformation kinetics are fast.
- If the deformed ferrite-pearlite microstructure is annealed at fast heating rate, the interactions between the recrystallization process of ferrite and austenite transformation are "strong". The microstructures in the intercritical range show a banded topology, i.e. the austenite islands are aligned in the rolling direction and show an elongated morphology. Recrystallized ferrite grains are also elongated and founded in between austenite bands. Austenite transformation starts at temperature higher than equilibrium conditions and the transformation kinetics are affected by the heating rates. This banded structure is often correlated to Mn micro-segregations inherited from the manufacturing process.

Nevertheless, the physical mechanisms (nucleation and growth of austenite, nucleation and growth of recrystallized ferrite grains, diffusion of species and their various short-circuits) behind these experimental observations are still a bone of contention in the literature. In this section, we will briefly review the different physically-based explanations found in the literature in order to highlight their differences and similarities. In this chapter, we mainly focus on the morphological and topological organization of the microstructures after annealing, determined by nucleation and growth processes as a function of heating rates. The central questions of kinetics will be briefly addressed but will be more detailed in chapter 5.

2.1.2.a Huang *et al.*'s model 2004

Huang *et al.* [HUA'04] studied in 2004 the austenite transformation of non-deformed and deformed ferrite-pearlite microstructure at constant heating rates. Their investigations were conducted by dilatometry and optical microscopy mainly. Their main findings are summarized in Figure 2.3 (taken from their publication). They explain that when annealing a deformed (cold-rolled) ferrite-pearlite microstructure at a low heating rate (1°C.s^{-1} for the studied DP and TRIP steels), the austenite transformation process is similar to the one observed from a non-deformed isotropic microstructure (as hot-rolled for instance) because recrystallization of ferrite takes place before transformation. Nucleation of austenite occurs not only in pearlite islands but also on ferrite/ferrite grain boundaries. It is not clear in the paper whether nucleation on boundaries requires the presence of carbides or not. As a consequence, as pearlite islands are elongated after cold-rolling, the resulting austenite grains will show the same elongated morphology after annealing.

At high heating rate, when interactions are strong, the shape and topological arrangement of austenite is similar to those of pearlite islands. It is as if the nucleation process of austenite was suppressed on ferrite grain boundaries. The explanation given relies on the fact that nucleation can only occur on immobile recrystallized ferrite grain and conversely not possible on boundaries in motion when grains are recrystallizing. The banded structure is thus the consequence of the absence of recrystallization outside pearlite bands, thus more often in Mn depleted bands (no austenite transformation outside pearlite bands in Mn-rich bands). In terms of kinetics, the authors observed that the highest amount of austenite transformed at end of the heating stage is measured with the highest heating rate (100°C.s^{-1}).

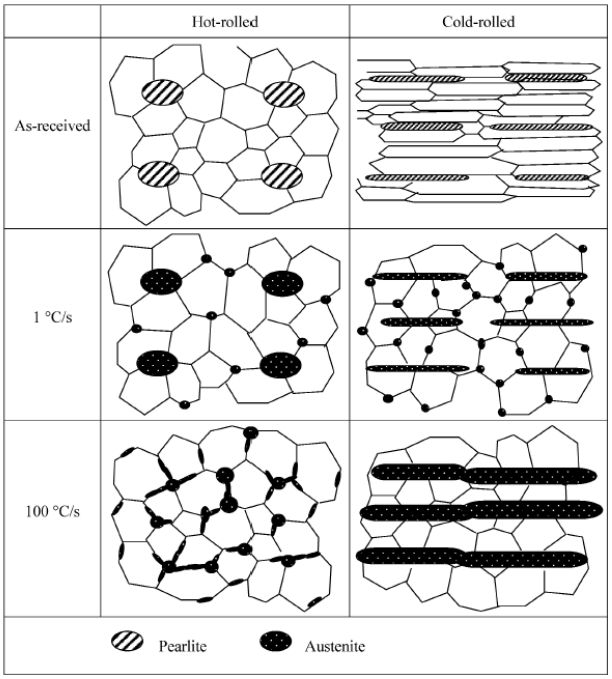

Figure 2.3: Model of Huang *et al.* [HUA'04] explaining the effect of deformation state prior to annealing and heating rates on the topology and morphology of ferrite/austenite microstructures in the intercritical range.

2.1.2.b Thomas *et al.*'s model 2018

The recent work of Thomas *et al*. [TOM'18] is also based on dilatometer trials and microstructure observations by SEM-EBSD. They investigated recrystallization and phase transformations during annealing of a cold-rolled steel and a tempered ferrite-pearlite steel. At low heating rate, they observed that nucleation of austenite occurs near carbides at recrystallized ferrite grain boundaries. Austenite then grows along the boundaries leading to the necklace microstructure. Contrary to the scheme proposed by Huang *et al*. [HUA'04], the presence of carbides is a necessary condition for austenite nucleation at boundaries. At high heating rate, they claim that nucleation of austenite occurs mainly in pearlite island. At intermediate heating, nucleation is favored also on ferrite subgrains, as observed sooner by Petrov *et al*. [POV'12]. The conclusions of Thomas and Petrov are in contradiction with the explanations of Huang *et al.* [HUA'04]. Thomas *et al.* claim that the banded structure appears due to the growth of austenite in recovered ferrite, which keeps an elongated morphology. However, in their analysis, the nucleation of austenite on isolated carbides is disregarded.

In Thomas *et al*.'s approach, the degree of banding is related to the heating rate because the formation of austenite is rapid within the elongated pearlite bands and occurs also at the boundaries of the recovered ferrite grains that keep their elongated shape in absence of recrystallization.

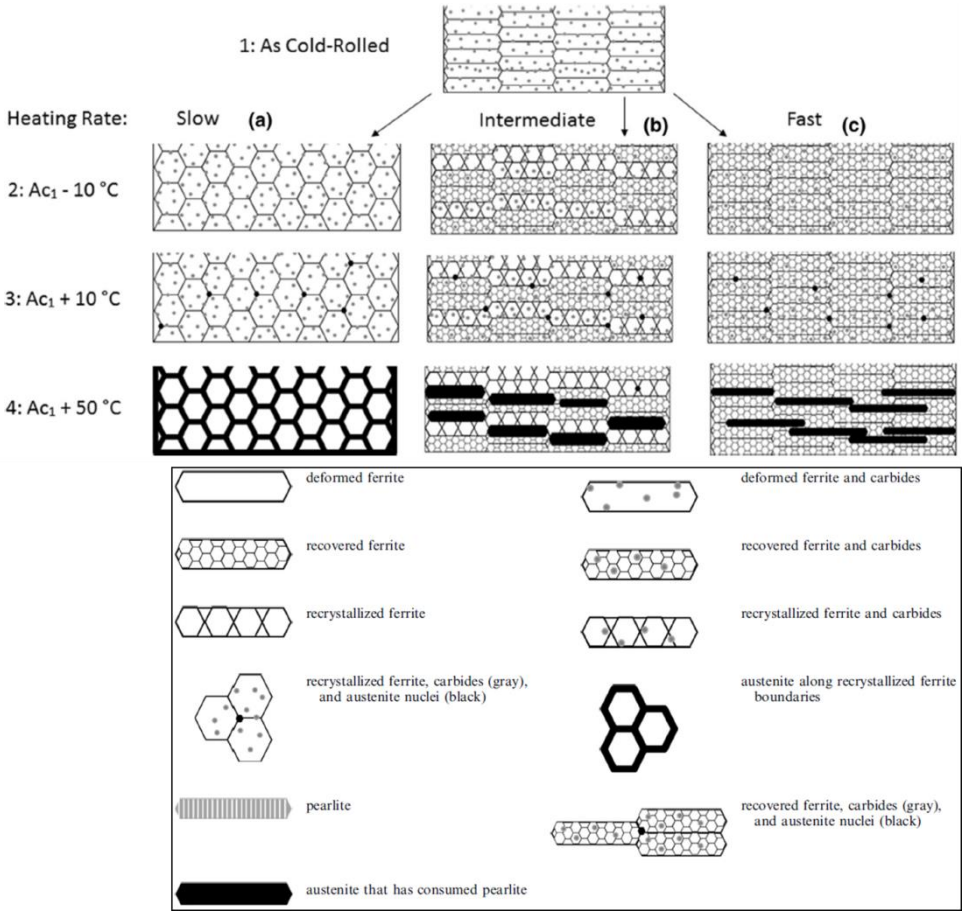

Figure 2.4: Model of Thomas *et al*. [TOM'18] explaining the effect of deformation state prior to annealing and heating rates on the topology and morphology of ferrite/austenite microstructures in the intercritical range.

2.1.2.c Chbihi *et al.*'s model 2014

The work of Chbihi *et al*. [CHB'14] in 2014 mainly consists of SEM-EBSD observations after thermal treatments. They measured the volume fraction of austenite by image analysis while recrystallization was quantified by hardness measurements and EBSD. The transformation kinetics were modeled using DICTRA while recrystallization was simulated using a morphological analysis tool. At low heating rate, when the interactions between recrystallization and phase transformation are weak, austenite nucleates on intergranular carbides at ferrite grain boundaries. For the authors, intergranular cementite particles likely block ferrite grain boundaries during recrystallization. Intragranular carbides can also serve as austenite nucleation sites but austenite growth is limited on these sites. On the contrary, austenite nuclei located on ferrite grain boundaries benefit from carbon atoms flux through the boundaries (as preferred diffusional path). Austenite then grows along ferrite grain interfaces and cover progressively all the boundaries. This scheme, depicted in Figure 2.5, is rather similar to the explanation given by Thomas *et al*. [TOM'18], but it neglects the possible nucleation in pearlite islands, as shown by Huang *et al*. [HUA'04]. The presence of Mn segregated bands is not revealed, except by limited local fluctuations of phase fractions. When interactions are strong, i.e. when phase transformation starts before full recrystallization, Chbihi *et al*. claim that nucleation of austenite takes place on the numerous carbides present in deformed ferrite, in agreement with Andrade-Carozzo [AND'07] or Barbier *et al*. [BAR'14]. Hence, they suggested that higher heating rates shift the nucleation from recrystallized ferrite boundaries to recovered or deformed ferrite boundaries. In Chbihi *et al*.'s scenario, austenite also grows in non-recrystallized bands which coincide with Mn-rich bands. The banded structure does not result from a direct effect of the local chemistry fluctuation. Recrystallization process is in turn limited in term of kinetics and of available space. Austenite nuclei occupying subgrain boundaries reduce the number of potential sites for recrystallization and new recrystallized ferrite grains are forced to grow in between austenite bands. Again, the proposed scenario shows similarities with the work of Thomas *et al*., but contrary to the two discussed works, the role of the elongated pearlite islands is not highlighted.

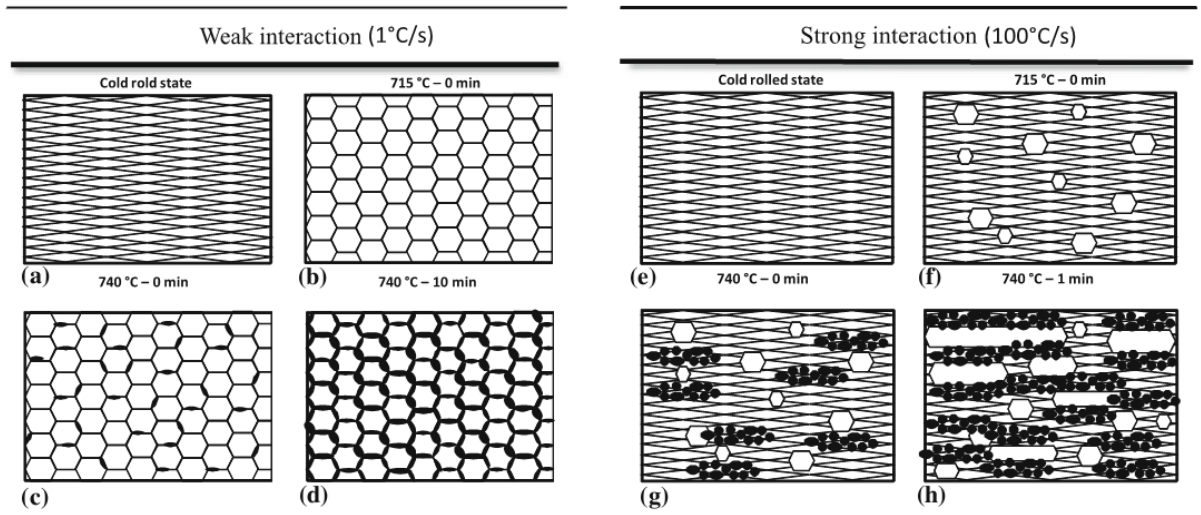

Figure 2.5: Model of Chbihi *et al*. [CHB'04] explaining the effect of deformation state prior to annealing and heating rates on the topology and morphology of ferrite/austenite microstructures in the intercritical range.

2.1.2.d Li *et al.*'s model 2013

The approach proposed by Li *et al*. [LI'13] is summarized in Figure 2.6. This interpretation was mainly built from microstructure observations by optical microscopy, SEM and TEM and dilatometric measurements.

Contrary to the aforementioned authors, Li et al. noticed the presence of isolated intergranular cementite particles. Figure 2.6 highlights that the microstructure in the cold-state contains not only elongated pearlite islands but also numerous isolated carbides located mainly at former ferrite grain boundaries.

At low heating rate, Li *et al*. show of course that recrystallization occurs before austenite transformation. As recrystallization process is hindered by isolated carbides, numerous carbides are found at new and immobile ferrite grain boundaries. Li *et al*. considered that austenite nucleation occurs systematically on cementite particles at boundaries (as diffusion short-circuits). As a consequence, the events take place simultaneously in pearlite islands and at ferrite boundaries. The growth of austenite is fast in pearlite islands. Austenite first consumes the pearlite islands and then grows at the expense of neighboring ferrite grains. Growth of austenite between ferrite grains occurs mainly along the boundaries and creates the austenite network which is characteristic of the necklace microstructure.

At very high heating rates, nucleation of austenite is supposed to occur again on pearlite islands and isolated carbides between deformed grains. As recrystallization process is not started, the density of intergranular isolated carbides, and thus of austenite nuclei is high. As a consequence, austenite grains are all aligned along former ferrite grain boundaries and formed the band structure inherited from pearlite islands.

As Thomas *et al*. [TOM'18], Li *et al*. propose an additional scenario for medium heating rates in which recrystallization and phase transformation occur at the same time. The authors pointed out a delay of the transformation kinetics relative to those observed with slow heating rates. They explained this retardation by an unfavorable nucleation of austenite at moving ferrite boundaries (no carbides available). In such scenario, austenite nucleates either on recrystallized grain boundaries or on deformed grains. As the nuclei are less numerous, the austenite network around recrystallized grains cannot be created and few austenite bands on former deformed grains can develop. As recrystallization is delayed by Mn solute-drag, such minor austenite bands are often observed in Mn-rich segregated bands.

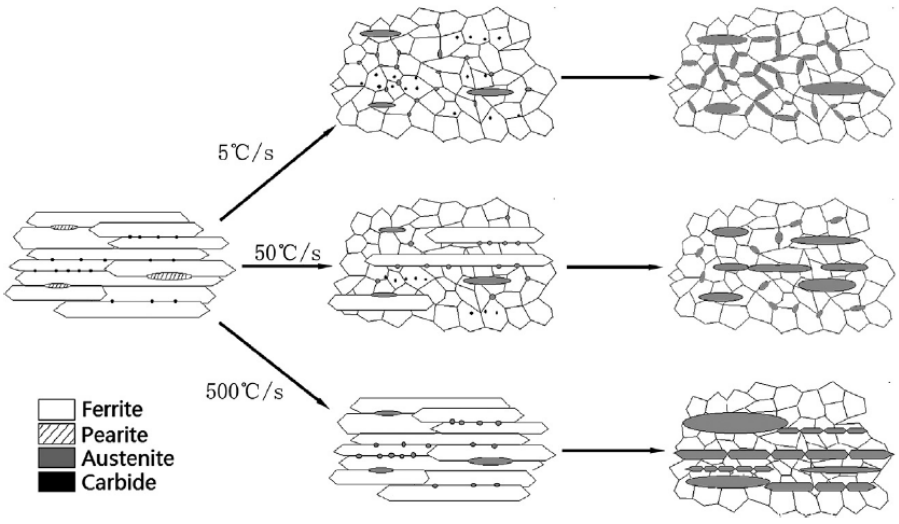

Figure 2.6: Model of Li *et al.* [LI'13] schematizing the effect of deformation state prior to annealing and heating rates on the topology and morphology of ferrite/austenite microstructures in the intercritical range.

2.1.2.e About full-field simulations

Recently, Zheng *et al*. [ZHG'13] developed a full-field simulation chain at the scale of a Representative Volume Element (RVE) of the microstructure, to model the heterogeneous deformation of the ferrite-pearlite microstructure as well as the competitive austenite phase transformation and ferrite recrystallization processes thanks to a cellular automaton (CA). The model predicts realistic final

microstructures and is clearly sensitive to annealing temperatures. Nevertheless, as their models consider that the initial microstructures are made of polygonal grains surrounded by pearlite, they are not able to predict realistic spatial distribution of nuclei. As a consequence, their model is not enough sensitive to heating rates. The limitation of the approach is also related to the choice of a CA model which is not able to deal with fine interface conditions (NPLE/PLE transitions for instance).

To overcome these limitations, Zhu *et al*. [ZHU'15b] have developed a 2D phase field modeling. Their model is able to capture rather well their experimental transformation kinetics as a function of the heating rate, even though they did not include cementite dissolution. They also claimed to reproduce the necklace to banded transitions. However, their resulting RVEs shown in Figure 2.7 to sustain this result are clearly not convincing, despite a large number of calibration parameters. Regardless of the heating rate, pearlite islands are transformed rapidly into elongated austenite bands. At low heating rate, small austenite grains have a sufficient time to grow along boundaries, whereas their growths are inhibited with high heating rate. Microstructures are finally very similar, despite the large difference in heating rates ($1°C.s^{-1}$ or $100°C.s^{-1}$). The "banded" structure is thus explained by a pure diffusion effect, without involving strong interactions with recrystallization. This work is however interesting since it highlights the role of the elongated pearlite islands in the whole process. Rudnizki *et al*. [RUD'11] realized a similar 2D phase field model. The same conclusions can be drawn from this work, except that they modeled pearlite dissolution prior to austenite growth. Hence, the two stages of the austenite growth (pearlite transformation and further austenite growth in the ferritic matrix) were modeled according a two-step sequence without any interactions.

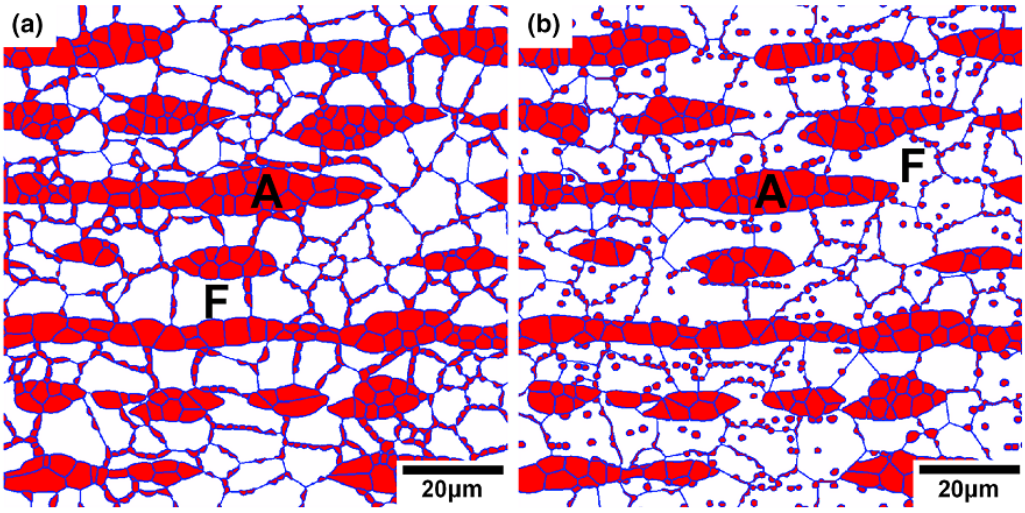

Figure 2.7: Phase field simulation results taken from Zhu *et al*. [ZHU'15b] REV at 800°C after phase transformation and full recrystallization after 300s at 770°C after an heating sequence (a) at $1°C.s^{-1}$ and (b) at $100°C.s^{-1}$. ferrite (F) appears in white and austenite (A) is in red. Blue lines indicate phase boundaries.

2.1.3 Discussion: austenite nucleation and growth

2.1.3.a Austenite nucleation sites

In a ferrite-pearlite microstructure, the austenite nucleates and grows from two main sites: the boundaries of the pearlite domains and intragranular isolated carbides located at the ferrite / ferrite grain boundaries. Most efficient nucleation sites are located at the boundaries of pearlite islands [GAR'81, SAV'07], at the triple junction with pearlitic ferrite and cementite [GOT'11a, GOT'11b]. These sites combine a carbon source and a high-energy defect. According to most studies, austenite grows then

extremely fast into the pearlite, because the pearlite/austenite interface provides a fast diffusion path for carbon (e.g. [SPE'81]) and the diffusion distance is reduced to the interlamellar spacing. The cementite can also dissolve in front of the approaching austenite interface [LI'11], involving fast carbon diffusion in ferrite. However, pearlite dissolution is not always fast. It remains sluggish [SPE'81, GAR'81, LI'11] at temperature close to Ae_1. Also, the cementite may be "left behind" the austenite interface [NEM'77, LI'11] and in such case, it will dissolve more slowly.

Carbides located at ferrite / ferrite grain boundaries are also efficient nucleation sites, but less than pearlite boundaries. For instance, according to [GAR'81, YAN'85, LI'13], nucleation on these sites occurs on heating at higher temperature than at pearlite boundaries, meaning that more driving force is required. Regarding austenite growth from these sites, it is not clear in all studies whether austenite then grows along the ferrite grain boundaries or equiaxially.

Higher heating rate favors nucleation on pearlite boundaries to the detriment of ferrite boundaries. Indeed on fast heating, less-efficient nucleation-growth sites have less time to be active. For example, in [AZI'11], comparing heating at 1 and 300°C.s^{-1} in the same steel, nucleation occurs both at fragmented pearlite and ferrite grain boundaries at 1°C.s^{-1}. At 300°C.s^{-1}, only the former nucleation sites are active. Accordingly, [SAV'07] established that at slower heating rate (0.05°C.s^{-1}) austenite nucleation has time to occur on ferrite grain boundaries, whereas at faster heating rate 20°C.s^{-1}, nucleation is restricted to pearlite island boundaries. The reason would be that the carbon has not enough time to diffuse towards the austenite over long distances, at 20°C.s^{-1}.

Regardless of the nature of the nucleation sites, increasing the heating rate increases the number density of austenite nuclei, as the transformation is shifted to higher temperatures where diffusivity and driving force are higher. This is well put into evidence in [AZI'11] by comparing the microstructure after fast or slow heating (1°C.s^{-1} or 300°C.s^{-1}) of the same HR microstructure.

Lower-efficiency nucleation sites have also been reported. These have little influence on the transformation kinetics and the austenite morphogenesis. These are:

- Ferrite / ferrite grain boundaries (without intergranular cementite carbide) [SAV'07, SAV'10, OFF'02]. Carbon is supplied to austenite from cementite by long range diffusion through ferrite or fast diffusion paths [OFF'02].
- Interior of pearlite islands, at ferrite/cementite interfaces, in non-spheroidized pearlite [SHT'99] or in spheroidized pearlite [AZI'11].
- Intragranular cementite particles [YAN'85, AZI'11].

2.1.3.b Austenite nucleation rate

There are few reported measurements of nucleation rate, which is obviously due to experimental difficulties. In [ROO'83], quantitative metallography was done to estimate the austenite nucleation in an eutectoid plain carbon steel during isothermal annealing. Austenite nucleation is progressive, meaning that the nucleation sites are not quickly saturated. The nucleation rate is correlated with the lamellar spacing of the colonies. It increases with increasing temperature, leading to finer microstructure, in accordance with [AZI'11]. Savran and Offerman [OFF'02, SAV'10] measured the nucleation rate (reported in Figure 2.8) of austenite by *in situ* 3D synchrotron XRD during continuous heating at 10°C.min^{-1} of C22 and C35 steels. Austenite nucleation occurs quickly with fast saturation of available sites at pearlite and more progressively at ferrite boundaries. Also, in C35 steel, because of the higher driving force, nucleation is restricted to pearlite and it occurs faster.

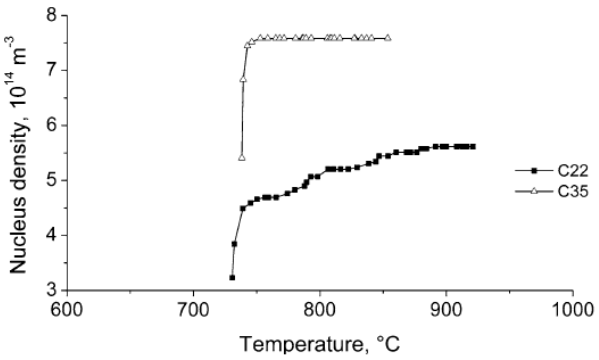

Figure 2.8: Densities of austenite nucleus as function of temperature measured by Savran [SAV'10] for C22 and C35 steels).

2.1.4 Effect of cold-rolling and recrystallization

The cold-rolling and subsequent heating modify the initial microstructure by introducing deformed ferrite grains with high density of defects and recrystallized ferrite grains (depending on heating rate). The pearlite colonies become fragmented and spheroidized.

The boundaries of spheroidized/fragmented pearlite islands remain the most efficient nucleation sites [AZI'11, SAN'08, KUL'13, MOH'11]. Austenite then still grows extremely fast into the pearlite island. Compared to lamellar pearlite, dissolution of fragmented/spheroidized pearlite is faster. According to [NEM'77], the cementite plates of pearlite would represent obstacles to the austenite growth.

New potent nucleation sites are the boundaries of recrystallized ferrite grains, especially if there is an isolated cementite particle located on the grain boundary [HUA'04, YAN'85, AZI'11, MOH'11, LI'13, KUL'13].

Regarding the non-recrystallized and highly-defected ferrite grains, it is not clear from the literature whether or not they accelerate the austenite nucleation. There are few observations of austenite nucleation inside non-recrystallized ferrite grains [YAN'85, KUL'13]. In contradiction with these studies, it is stated in [HUA'04] that austenite nucleation inside recrystallizing ferrite would be difficult, because the ferrite/ferrite interfaces are moving. As for austenite growth, quantitative microstructure characterizations of [CHB'14, BAR'14] strongly suggest that the austenite grows preferentially into non-recrystallized ferrite. According to Kulakov *et al.*, austenite growth would be enhanced by the presence of defects. Other studies report conversely that the austenite grows preferentially along ferrite grain boundaries, recrystallized or not [HUA'04, LI'13].

The interaction between recrystallization and phase transformation of cold-rolled transformation thus remains a hot topic for the community and difficult to address as the processes are difficult to observe in situ. As shown recently by Lai *et al*. [LAI'16] and Ollat [OLL'17], this question is especially important to predict the final morphology and spatial distribution of phases. It is possible to address only kinetic aspects by considering sub-systems representative of both pearlite islands and isolated carbides. This is also the strategy applied in this thesis.

2.2 Microstructure characterization

The objective of this chapter is to assess the validity of explanations detailed above about studied steels and to prepare the reader for the detailed discussion in following chapters about carbide ripening (chapter 3), recrystallization (Chapter 4) and austenite transformation kinetics (chapter 5) respectively.

2.2.1 Sample preparation and nomenclature

In this chapter, the microstructures are characterized by means of SEM in the as hot-rolled and subsequent cold-rolled states and along different continuous annealing schedules. The samples have been prepared using a dilatometer to reproduce interrupted thermal schedules. Two constant heating rates have been investigated; a slow one (3°C.s^{-1}) and a medium/fast one (30°C.s^{-1}) which are often encountered in industrial plants.

In the following, HR and CR refer to samples extracted from the as-received Hot-Rolled and Cold-Rolled specimens, respectively. The label of the annealed samples is composed with the stop temperature (up to 800°C) and the annealing heating rate (H3 or H30 corresponding to respectively 3 and 30°C.s^{-1}, respectively). Sample 710H30 corresponds for instance to a CR sample heated up to 710°C at a constant heating rate of 30°C.s^{-1} and then quenched. In such samples, since austenite transformed into martensite during quenching, martensite reveals the presence of austenite at the stop temperature. The progression of the austenite transformation is also studied during isothermal holding at 800°C for 60 and 600s. Consistently, these specimens are designated with the holding duration followed by the heating rate employed. For instance, ISO60H3 corresponds to a sample heated at 3°C.s^{-1} and hold for 60s before quench.

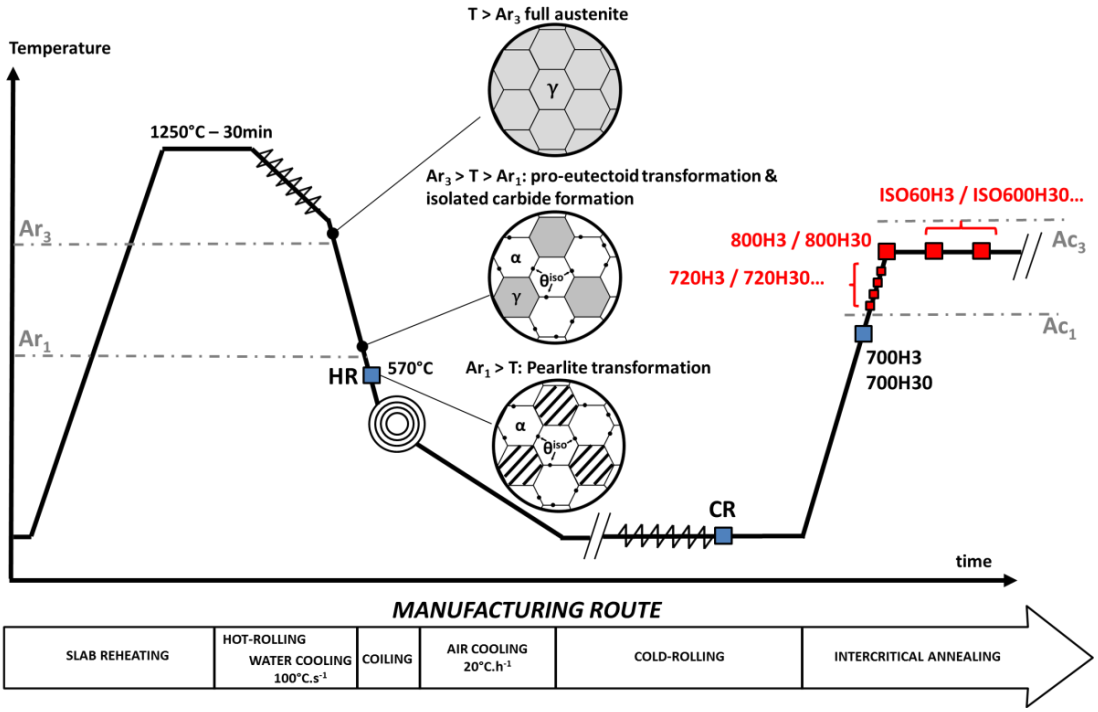

Figure 2.9: Key stages of DP steel manufacturing studied in the present work. The corresponding sample designations are indicated (HR, CR, 700H3, .ISO600H30).

The following experimental study is divided into five sections. The two first ones are dedicated to the detailed characterization of the HR and CR microstructures prior to annealing and their comparison. We will show in particular how cold-rolling alter the as-hot-rolled ferrite/pearlite microstructure. The third section aims at discussing the mechanisms operating during sub-critical annealing up to 700°C, i.e. mainly carbide ripening processes and recrystallization, which are both highly sensitive to the heating rates. Then, the microstructure evolutions are characterized as function of the temperature during heating and as function of the holding time at 800°C for both heating rates. Finally, the experimental results are discussed at the light of the literature. A special attention will of course be paid to the Mn segregation of studied steels, the evolution of carbide microstructure (below and above Ac_1), i.e. pearlite islands and isolated carbides, nucleation sites of austenite, recrystallization states of ferrite and growth modes of austenite and transformation kinetics.

2.2.2 Characterization of the HR state before cold-rolling

2.2.2.a Ferrite and carbide microstructures in the as-hot-rolled state

Figure 2.10(a) shows the hot-rolled microstructure of the studied steel observed by SEM after etching. As expected, the microstructure is essentially made of polygonal ferrite and islands of lamellar pearlite. Pro-eutectoid ferrite grains appear in dark contrast. They are equiaxed and their mean radius is estimated to 5 μm. Cementite appears in clear contrast on the contrary.

The pearlite islands consist of groups of parallel cementite lamellae without any preferential orientation. Their true interlamellar spacing is S_0 = 82 nm according to our measurement using a planar intercept method and Ridley's stereological corrections [RID'84]. Nevertheless, the structure is not ideally fully lamellar. Several lamellae localized on the pearlite / ferrite grain boundaries show some rounded extremity and rounded shape carbides can be found in the islands.

The fraction of lamellar pearlite has been determined by image analysis with a manual delimitation of pearlite islands. Figure 2.10(b) shows the result of the image analysis procedure applied to (a) as explained in chapter 1. Carbide in pearlite islands appears in white and isolated carbides have been colored artificially in red. Using such procedure, the volume fraction of pearlite islands is estimated at $16\%_{vol}$. Considering the nominal alloy carbon balance, $25\%_{vol}$ of pearlite was however expected by the prevailing thermodynamic conditions during the transformation (see chapter 3 for more details). The same differences between expected and measured pearlite fraction were reported by Rudnizki and Kulakov [RUD'11, KUL'13]. Thus, the whole carbon content of the studied steel ($0.46\%_{at}$) is not exclusively found in pearlite islands. A mass balance (detailed in Chapter 3) shows that, consistently with the measured fraction of pearlite, only $0.29\%_{at}$ of the carbon is found in pearlite. This finding is sustained by the presence of an important number of cementite films and isolated carbides on the ferrite/ferrite grain boundaries (artificially colored in red in Figure 2.10(b)). They mainly have a long and thick rectilinear morphology, but some of these have a rounded shape. These shape and localization are consistent with the interpretation of Lee *et al*. [LEE'93] discussed above. As very few intra-granular particles can be observed, it is likely that the remaining carbon ($0.46\%_{at}$ - $0.29\%_{at}$ = $0.17\%_{at}$) contributes to the formation of those isolated carbides.

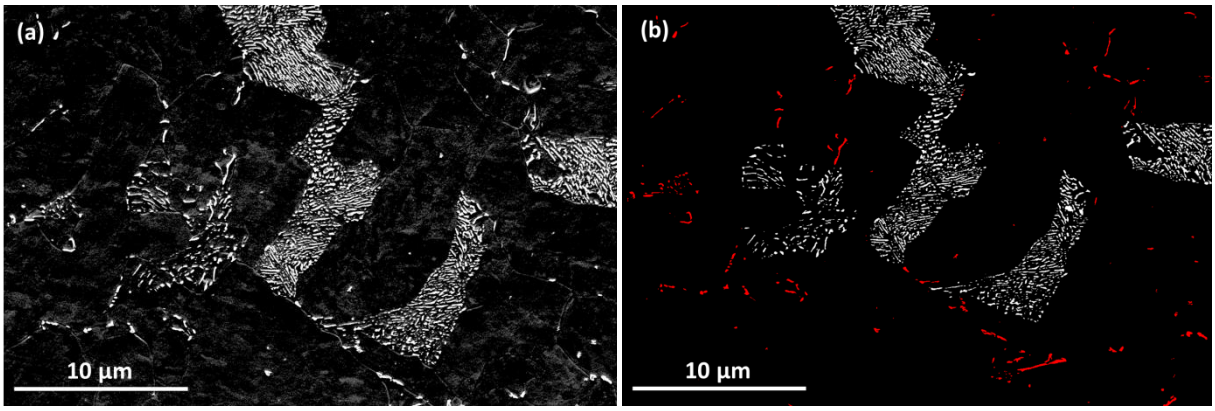

Figure 2.10: (a) SEM micrograph of the Hot-Rolled material. (b) Same micrograph after binarization. Cementite particles are colored and have been sorted depending on their localization on ferrite grain boundaries (red) or in pearlite islands (white).

2.2.2.b Mn segregations

When observing HR microstructure at a larger scale, it clearly appears that pearlite islands are topologically organized in bands. Figure 2.11(a) highlights the microstructure organization.

Pearlite bands (in bright contrast) are 20 µm distant from each other and have an average thickness of 7 µm. The band morphology is caused by local Mn depletions which promote transformation of pro-eutectoid ferrite. Last austenite to transform at coiling temperature shows then a banded morphology [DES'76]. These local Mn depletions and enrichments are called micro-segregations and are due to a partition processes occurring during solidification of slabs. During Hot-Rolling, the segregations are oriented with respect to the rolling direction [FLE'06]. Figure 2.10(b) is a Mn WDS map from another study, realized by Castaing microprobe on the DP600 steel at the cold-rolled state [CHB'14]. The Mn segregation bands are 7 µm large in average. In present study, WDS measurements were also carried out along the thickness (d_l side, see Figure 1.5) by Castaing microprobe. It was established that the Mn concentration measured at quarter-thickness of specimen is varying between 1.83 (depleted band) and 2.02%$_{wt}$ (enriched band).

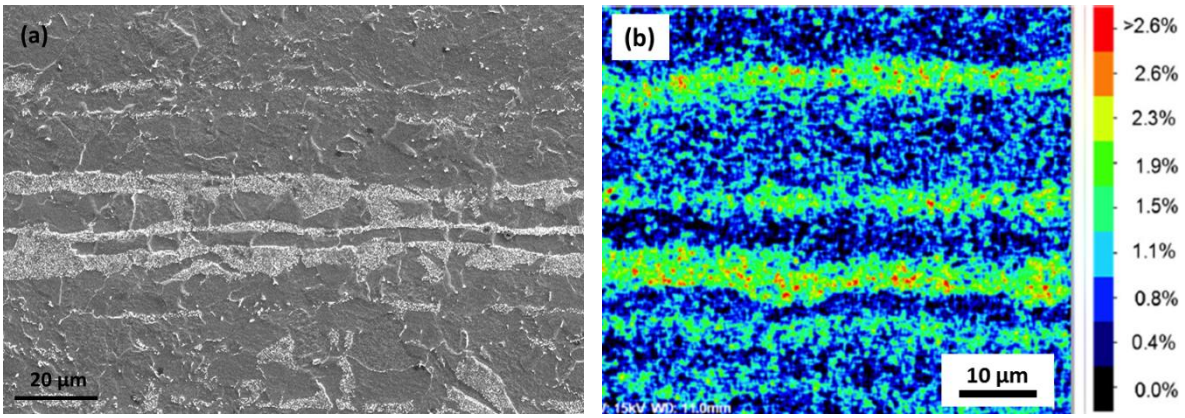

Figure 2.11: (a) SEM micrograph of the studied steel in hot-rolled state (HR). The large pearlite bands are located on the central macro-segregation. (b) WDS mapping of the Mn through the thickness of a cold-rolled DP600 specimen [KUL'13].

2.2.3 Characterization of the CR state prior to annealing

2.2.3.a Evolution of the Ferrite and carbide microstructures after cold-rolling

The consequences of the Cold-Rolling process on the initial HR microstructure are shown in Figure 2.12. The Figures compare the microstructures before and after CR at low magnification or focusing on pearlite islands and isolated cementite particles.

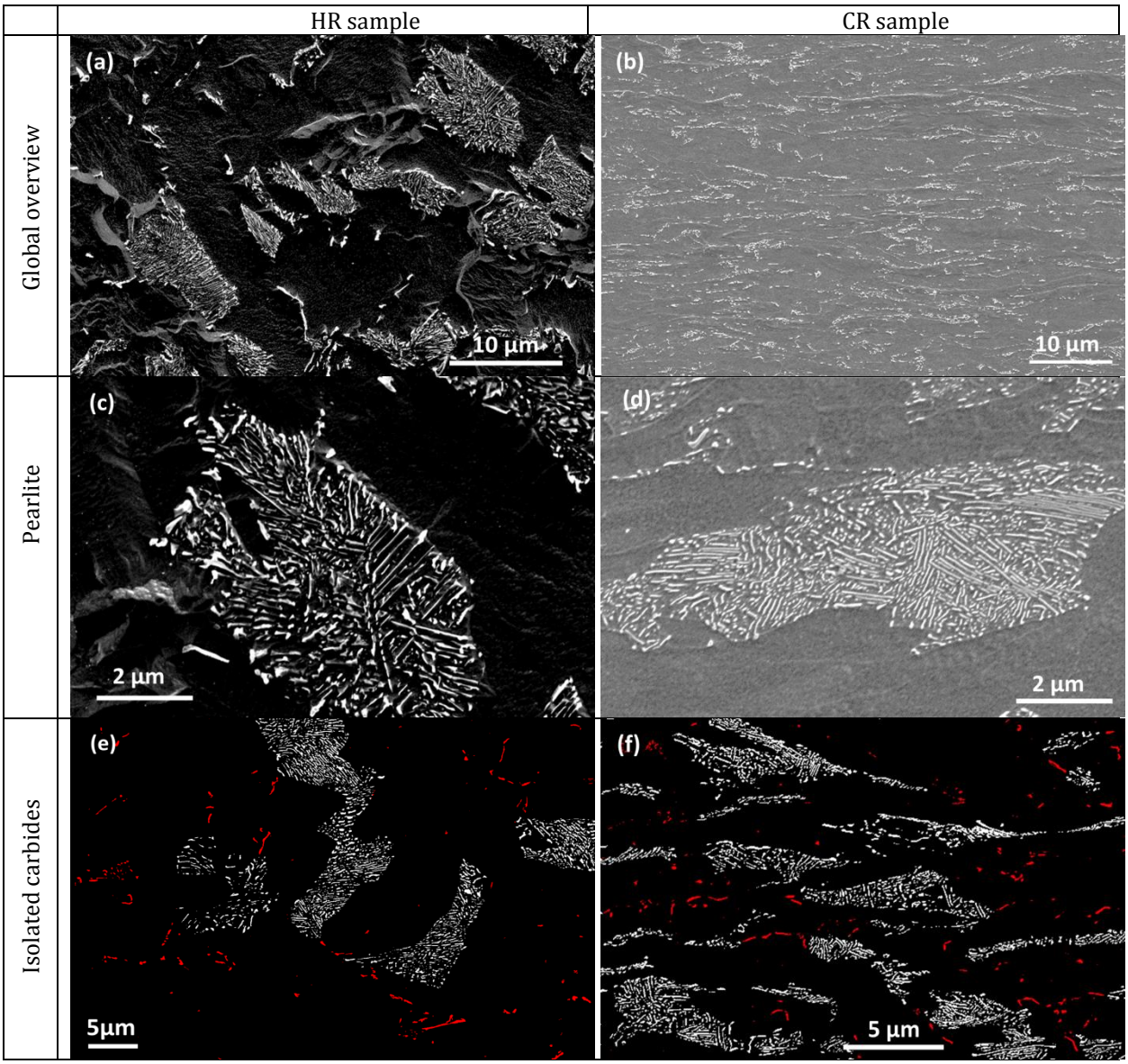

Figure 2.12: SEM micrographs after etching representative of the HR and CR microstructures respectively. (a) and (b), at low magnification, (c) and (d) focusing on pearlite islands, (e) and (f) after image analysis highlighting isolated carbides in red.

The micrographs reflect well the deformation induced by the rolling process. Both pearlite and ferrite grains are elongated in the rolling direction. Pearlite bands as well as ferrite grains are now 3 µm thick, with a large scattering in terms of length. Some cementite lamellae remain relatively undamaged while others are fragmented owing to the high deformation. The true interlamellar spacing is significantly

reduced down to S_0 = 47 nm (measured by the same method as previously, but with a lower confidence level).

Dealing with isolated cementite particles, the high deformation presumably caused the displacement and the fragmentation of the large particles localized on ferrite boundaries. This fragmentation produces thin cementite clusters oriented toward the rolling direction (as shown by Li *et al*. [LI'13] for instance). A higher number of intergranular cementite particles are thus observed on grain boundaries. Some intergranular cementite films are still present, but appear to have been bent. Almost no intra-granular carbides are observed in ferrite.

2.2.3.b Morphology and size evolution of the carbide microstructure

As individual carbides can act as potential nucleation sites for austenite, a quantitative analysis of the carbide microstructure (size, density, morphology) was conducted. Between HR and CR states, it seems that pearlite lamellae as well as cementite films at boundaries were fragmented by mechanical deformation. It is thus expected an increase in the density of particles as well as an increase in the proportion of particles with a rounded shape at the expense of lamellar shaped carbides.

This work was conducted by detecting and analyzing systematically all particles in our image processing, as explained in chapter 1. Our particle counting method in surface will be used to compare different microstructure states in a relative way. It must be stressed that the following microstructure quantifications in 2D cannot be extended with confidence to 3D (number of particles per volume unit for instance).

A distinction is again made between pearlite and isolated carbides. The cementite particles were sorted into two categories to discriminate spheroidized from non-spheroidized particles

The calculated SPHeroidization ratio (SPH ratio) is defined as the cumulated area of spheroidized cementite particles over the cumulated area of all cementite particles. The density (being the ratio of the number of particles over the area observed) in pearlite was calculated by considering uniquely the cumulated area of all surveyed pearlite islands. Nonetheless, the isolated particle density was calculated over the whole area (the particles counted from pearlite were of course deduced). Table 2.A compares the spheroidization ratio, the densities and the mean equivalent radius of the spheroidized particles between HR and CR states. Figures 2.13(a) and (b) compare the equivalent radius size distribution for pearlite and isolated particles, respectively. The volume of cementite represented for each particle size class is rationalized over the total volume of cementite. The total volume of cementite represents the amount of cementite contained in the single pearlite in a first hand, or solely the isolated carbides in the other hand.

	Sample	Density (part.µm^{-2})	SPH ratio (%)	Equivalent radius (nm)
Pearlite island	HR	26.6	42	83
	CR	29.8	68	75
Isolated carbide	HR	0.4	43	90
	CR	1.8	69	94

Table 2.A: Density, degree of spheroidization (SPH) and mean equivalent radius of the spheroidized cementite particles in pearlite or within the matrix in HR and CR samples.

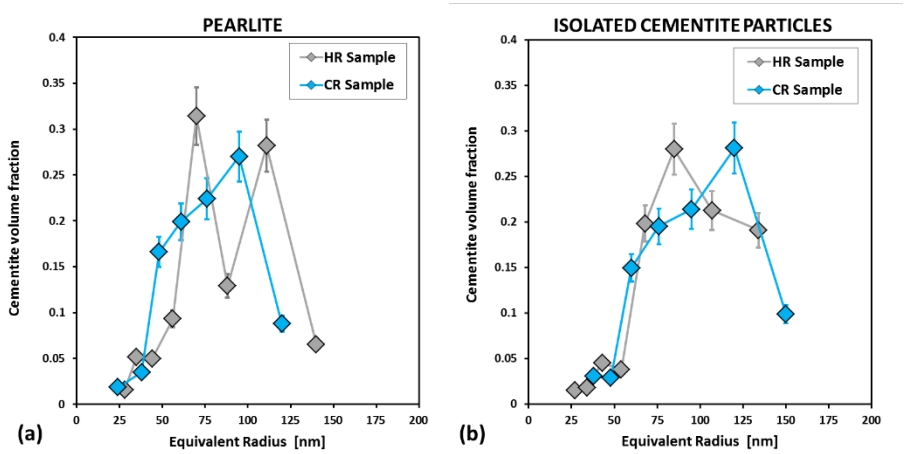

Figure 2.13: Size distribution of spheroidized carbides (a) in pearlite islands and (b) in the matrix (isolated) in CR and HR microstructures.

Isolated carbides are coarser than particles found in pearlite. After cold-rolling, the density of carbides in pearlite remains constant but is multiplied by four for the isolated carbides. Their mean equivalent diameter is reduced within pearlite and barely augmented for the isolated carbides in the matrix. The spheroidization ratio is increased from ca. 40 to 70% for both carbide categories. In pearlite, the size distribution is moved toward smaller sizes (90 nm down to 75 nm in average). The size distributions of isolated particles are rather comparable.

2.2.3.c Conclusion

The HR microstructure is made of large and equiaxed ferrite grains and pearlite islands containing lamellar and almost non-fragmented cementite. The cold-rolling process induces a strong deformation of ferrite grains and pearlite colonies, which become elongated parallel to the rolling direction. The pearlite lamellae are often fragmented. Consistently with the higher number of particles, the spheroidization ratio increases up to 70%. The mean radius of the spheroidized particles is reduced from 90 to 75 nm in pearlite islands.

Dealing with the isolated carbides, the mean radius is stable, while the spheroidization ratio is strongly raised. In fact, some intergranular films are broken or bent during the CR process. The carbides are now found aligned according to the deformed ferrite grain boundaries. Very few intra-granular particles have been observed inside ferrite grains.

2.2.4 Microstructure evolution during heating below Ac1

As explained, CR samples were heated in order to characterize the microstructure evolution during annealing in the sub-critical and in the intercritical range, i.e. before and after austenitization starts. Two heating rates, 3 and 30°C.s^{-1} have been considered. It appears that austenitization starts at 710°C for the slow heating rate and at 720°C for the fast heating rate. Studying the microstructure at 700°C in both cases is thought to be representative of microstructure evolutions in the sub-critical range, just before austenitization.

The evolution of microstructures is represented in Figure 2.14. As in previous Figure 2.12, a special attention is paid to the structure of the ferritic matrix and the states of pearlite islands and isolated carbides.

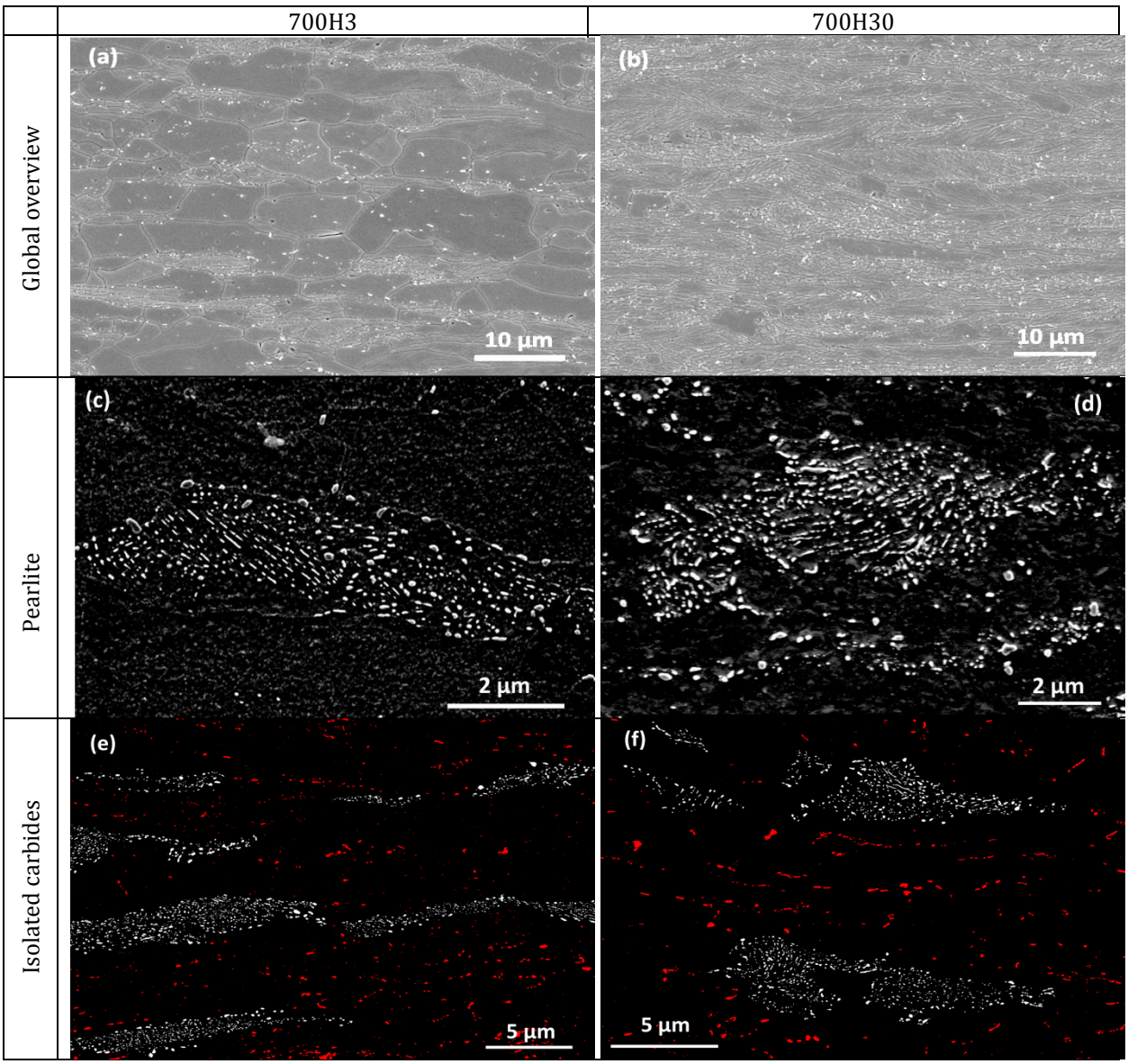

Figure 2.14: SEM micrographs representative of the slow and fast heated samples (700HR3 and 700HR30). (a) and (b), at low magnification, (c) and (d) focusing on pearlite islands, (e) and (f) after image analysis highlighting isolated carbides.

2.2.4.a Recrystallization as a function of the heating rates

When considering only the ferritic matrix, a fully recrystallized state is clearly observed after slow heating whereas after fast heating, the matrix is obviously non-recrystallized at 700°C. In Figure 2.14(a), the ferrite grains, initially elongated in the rolling direction at the CR state, are large and equiaxed with a mean radius estimated to 6 µm. On the contrary, in Figure 2.14(b), after fast heating, the matrix contains a large number of sub-grains highlighted by etching with a mean radius of 0.5 µm.

This observation is in good agreement with studies found in literature. Mohanty *et al.* [MOH'11] or Huang *et al.* [HUA'04] identified a threshold heating rate of 10°C.s^{-1} above which recrystallization does

not occur in their cold-rolled DP780 steel grades. Similar investigations were made for the current cold-rolled DP600 material by Kulakov *et al.* [KUL'13]. They reported that the microstructure was more or less recrystallized at 700°C for heating rates greater than 3°C.s^{-1}. Below this heating rate, the microstructure was systematically recrystallized. Ollat *et al*. [OLL'17] did not observe recrystallization as well for heating rates higher than 3°C.s^{-1} on a similar CR ferrite-pearlite steel (DP780) having the same cold-rolling reduction rate. The kinetics of recrystallization will be studied in detail in chapter 4.

2.2.4.b General evolution of carbide microstructure

Pearlite islands have evolved in the same manner, whatever the heating rates, as shown in Figures 2.14(c-d). The former pearlite colonies contain now fragmented lamellae. Almost all cementite lamellae have disappeared to the profit of cementite particles with a spheroidal shape. The fragments with a spherical shape are aligned, indicating the position of the former lamellae. Some fragments can keep also a slightly rectilinear shape.

On the contrary, the evolution of isolated precipitates on ferrite grain boundaries depends on the heating rate. The initial rectilinear films found in the CR state have been fragmented, like the lamellae in pearlite islands, and now consist of clusters of spherical particles for both heating rates. However, in the case of slow heating, a high number of small particles are now trapped inside the large recrystallized ferrite grains. This leads to a quite homogeneous distribution of cementite particles throughout the matrix. The larger precipitates are localized on ferrite grain boundaries while the smallest are localized inside the grains. After fast heating, no intra-granular particles can be observed. Cementite particles throughout the ferrite matrix are thus not distributed homogeneously. The carbides are only found on the deformed ferrite grain boundaries. As a consequence, they are distributed along linear arrays between the pearlite islands and along the elongated ferrite grain boundaries, consistently with the cold-rolling direction. These observations are rather consistent with the scheme proposed by Li *et al.* [LI'13].

2.2.4.c Morphology and size evolution of the carbide microstructure

The particle density, i.e. the ratio of the number of all particles observed (pearlite + isolated carbides) over the whole sample area investigated is significantly increased from 1.8 to 2.6 particles.µm^{-2} after slow heating (700H3). On the opposite, it is barely modified after fast heating (700H30) for which a density of 1.9 particles.µm^{-2} is observed. Specific investigation of pearlite islands reveals that the carbide densities are surprisingly similar. After slow and fast heating, densities are respectively equal to 189.1 and 176.4 particles.µm^{-2}.

Spheroidization degree and averaged particle sizes as a function of the heating rates are summed-up in Table 2.B. The size distribution of cementite particles is represented in Figures 2.15(a) and (b) for carbides inside the pearlite and isolated carbides, respectively.

In pearlite islands, the degree of spheroidization does not seem to depend on the heating rate. All heated microstructures are spheroidized to ca. 85%. The average equivalent radius in pearlite is the same after heating (ca. 75 nm), regardless the heating rate. The widths of size distributions are rather similar even though the distribution for slow heating seems bimodal. This result clearly evokes that remaining lamellae have been fragmented by a ripening process. However, as the mean size of precipitate did not evolve significantly, it means that coarsening is not really operative in pearlite islands (except marginally in the case of the slow heating rate).

	Sample	Density (part.µm^{-2})	SPH ratio (%)	Equivalent radius (nm)
Pearlite	CR	29.8	68	75
	700HR3	189.1	89	74
	700HR30	176.4	84	72
Isolated cementite	CR	1.8	69	90
	700HR3	2.6	83	111
	700HR30	1.9	83	73

Table 2.B: Density, degree of spheroidization (SPH) and mean equivalent radius of the spheroidized cementite particles in pearlite or within the matrix in CR, 700H3 and 700H30 samples.

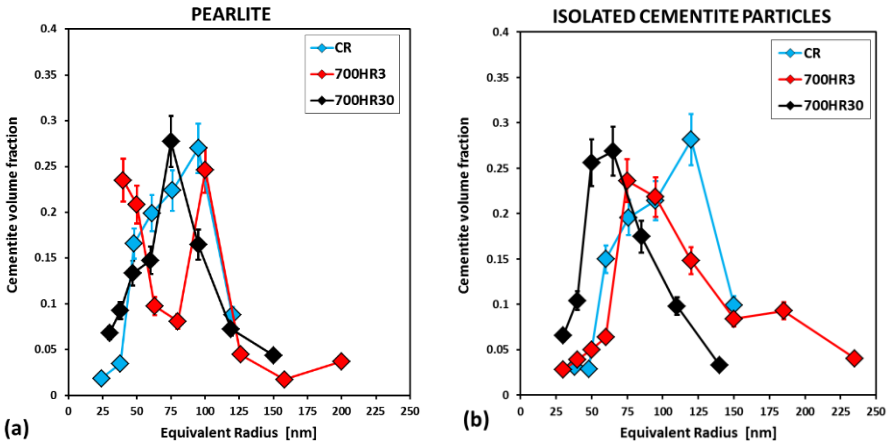

Figure 2.15: Size distribution of spheroidized carbides (a) in pearlite islands and (b) in the matrix (isolated) in CR, 700HR3 and 700HR30 samples.

The proportion of spheroidized isolated particles in the matrix increases after heating and achieves the same degree of spheroidization, regardless the heating rates. Both microstructures are highly spheroidized (85%) at 700°C as for pearlite islands. The effect of the heating rate on the mean sizes and size distributions is obviously more pronounced. The mean radius is increased from 90 to 111 nm after slow heating, while it is lowered to 73 nm after fast heating. The widths of size distribution after slow and fast heating are also different. The distribution is shifted to the low values for the high heating rate while the size distribution for low heating rate shows an extended tail in the direction of large particles.

As for pearlite islands, these results evoke a ripening process which leads to the fragmentation of lamellar structures (more particles, higher degree of spheroidization) and the coarsening of spheroidized particles. Here again, coarsening is only seen after slow heating and is revealed by the extended tail of the size distribution.

2.2.4.d Discussion: Evolution of carbide microstructure in pearlite islands

The fragmentation mechanism of cementite lamellae during annealing is achieved at the same degree of completion at 700°C, independently of the heating rate (same density inside pearlite islands, same spheroidization ratio). The ripening process is thus fast.

The seminal works of Chattopadhyay *et al.* highlighted the contribution of prior deformation to enhance fragmentation kinetics [CHA'77, CHA'82]. More recently, it was established that the

fragmentation mechanism is fast when the deformation exceeds 30% [SHN'01] which is the case of the studied steel (local deformation in pearlite estimated around 70%). The fragmentation process is observed at temperatures as low as 450°C and is extremely fast near 600°C [SHN'01]. The severe plastic deformation process induces defects inside the cementite platelets [ETO'08, YIN'18]. According to the mechanism detailed by Mahlzahn and Kampe [MAL'89], during recovery, some dislocations migrate and gather to form a subgrain on the cementite surface. The Gibbs-Thomson effect is active on the two edges of the subgrain and then promotes carbon diffusion which broadens the sub-grain. Progressively, the subgrain forms a groove which moves deeper until the separation of a cementite rod from the platelet. With longer time, rods are then fragmented into spheroids [ARR'14]. The mechanism of fragmentation is depicted in Figure 2.16. The combination of both cold-rolling deformation and high annealing temperature thus contributes to a fast spheroidization, independently of the heating rate.

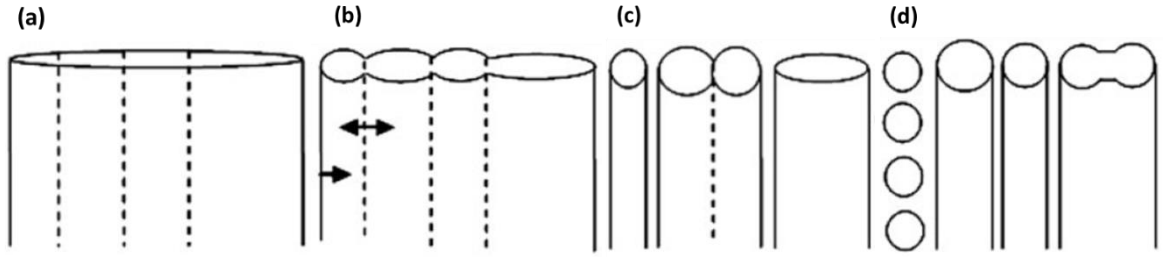

Figure 2.16: Schematic representation of the successive steps leading to the fragmentation of a cementite platelet into spheroidal particles. (a) Dislocation sub-grains induced by a prior deformation in cementite. (b) Carbon diffusion from the groove edges toward flat surfaces. (c) Separation of rods from the parent platelets (d) Fragmentation of rods into spheres [MAL'89].

The particle size distribution in pearlite shows a single peak located at about 75nm for the 700H30 sample while it appears to be bimodal for the 700H3 specimen. The first peak corresponds to carbides smaller than 50 nm while the second accounts for those larger than 100 nm. This split-up indicates that the coarsening mechanisms was shortly active during slow heating, but did not have sufficient time to occur during fast heating. It is in agreement with the usual durations found in the literature for cementite coarsening [GAN'09, SU'15, MAT'17].

2.2.4.e Discussion: Evolution of isolated carbides in the ferritic matrix

The slow heating permits a significant increase from 90 to 110 nm in the mean equivalent radius of isolated carbides. Coarsening is expected to have sufficient time to proceed and is promoted by the enhanced solute diffusion through the grain boundaries [GAR'81]. At the same time, the particles density is considerably increased from 1.8 to 2.6 (part.μm^{-2}). This important evolution is not only explained by the fragmentation of the cementite intergranular films. The micrographs in Figure 2.14(c) reveal in fact many small precipitates inside the ferrite grains.

One reported interpretation suggests that during the recrystallization process, ferrite grain boundaries can overcome the pinning force of the smallest precipitates, leaving some particles inside ferrite grains. The particles left behind the moving boundary will finally dissolve to the benefit of those localized on the grain boundaries [KUL'13, LAI'16]. In fact, this mechanism should result in a decrease in carbide density.

On the contrary, Shin *et al.* [SHN'01, SHN'03] observed the dissolution of intergranular carbide films and the precipitation of isolated carbides within the matrix during isothermal annealing of highly deformed ferrite-pearlite. This process is made possible thanks to the increase in solubility of carbon in the ferrite matrix due to the deformation state. For the authors, the mechanism can be active at

temperature as low as 400°C. Nevertheless, the nucleation sites of the newly precipitated particles are not discussed.

In fact, to our best knowledge, these intergranular carbides appearing during heating have already been observed but the mechanism explaining their presence is far from being clear. Nevertheless, we will see in the following, that these intragranular carbides do not play a major role in the morphogenesis of ferrite/austenite microstructure contrary to intergranular carbides.

2.2.4.f A summary so far

The consequences of the heating rates on the microstructures before the austenitization were observed and discussed in this section. For both heating rates, spheroidization of the carbide microstructure is almost complete (85%). The heating rate does not affect the spheroidization of pearlite islands. The radius of cementite particles generated by the fragmentation of the lamellae is about 75 nm in both cases. During slow heating, the coarsening process which follows the fragmentation of the cementite lamellae remains moderate.

For intergranular isolated precipitates in the ferritic matrix, coarsening is enhanced by the faster diffusion of the elements along the grain boundaries. After slow heating, a consequent mean size of 110 nm is achieved while the initial size was initially 90 nm in the CR state. Slow heating condition leads also to the presence of inter-granular carbides. The mechanisms behind are worth being investigated. With fast heating, the mean equivalent cementite radius is lowered to 75 nm, since only fragmentation of the cementite intergranular films occurs. As a result, the intergranular carbides remain distributed in arrays arranged linearly along the elongated ferrite grain boundaries, in accordance with Li *et al.* [LI'13] (cf. Fig. 2.6).

Recrystallization is possible only in case of slow heating. The initial elongated ferrite grains become equiaxed and large (R=4 μm). After fast heating, the highly-deformed matrix did not evolve and was still composed of small ferrite subgrains (R=0.5 μm).

2.2.5 Austenite transformation

2.2.5.a Introduction

The effect of the heating rate on austenite transformation has been extensively discussed in past and recent literature. Global kinetics can be explained by some empirical models (see chapter 5 for more details) but the resulting spatial distributions and morphologies are not well understood. As shown in the bibliographic survey, fast heating leads to banded configuration while slow heating produces a necklace configuration. One objective of the thesis was to propose a consistent approach to explain the morphogenesis of the ferrite/austenite microstructure at the light of the existing literature and systematic microstructure observations.

For this purpose, different specimens were heated between 700 and 800°C (with a 10°C temperature step) and quenched. In this manner, the first stages of the austenite formation can be characterized. Special attention was paid to the study of austenite nucleation sites in order to decide if the austenite nucleates exclusively on carbides as claimed by [LI'13, LAI'16, OLL'17, TOM'18], or whether austenite can also nucleate on ferrite grain boundaries and grow by long range diffusion of carbon [KAL'98, SAV'07, GOT'11a].

The samples used for the SEM observations were etched by DINO etchant, which preferentially attacks martensite (former austenite) to obtain a good contrast between martensite and ferrite. A

supplementary advantage of the DINO etchant is that the ferrite grain boundaries are revealed as well. One important drawback of DINO is however to leave residual particles that look like cementite particles on flat surface. In this section, cementite particles (sometimes redeposited particles due to DINO) appear in bright contrast on SEM micrographs, while martensite appears in darker contrast. Owing to the small size of the austenite nuclei at the beginning of transformation, austenite is colored artificially in red on certain micrographs to improve its visibility. Slow and fast heating conditions are successively detailed. The resulting austenite transformation kinetics will be briefly discussed at the light of direct measurements on SEM micrographs (using a point counting method) and dilatometry experiments. We will show that both measurements lacks of reliability compared HEXRD detailed in chapter 5 but provide already interesting trends.

2.2.5.b Slow heating: SEM characterization of the microstructure evolution

Figures 2.17 show the SEM micrographs of the samples heated at 3°C.s^{-1} and quenched at different temperatures in the range of 710°C - 800°C with a 10°C step. The different figures correspond respectively to samples 710H3, 720H3, 730H3, 740H3, 750H3, 780H3 and 800H3. For each sample, two micrographs are presented corresponding to two different magnifications, at the segregated structure scale and at a single pearlite island scale.

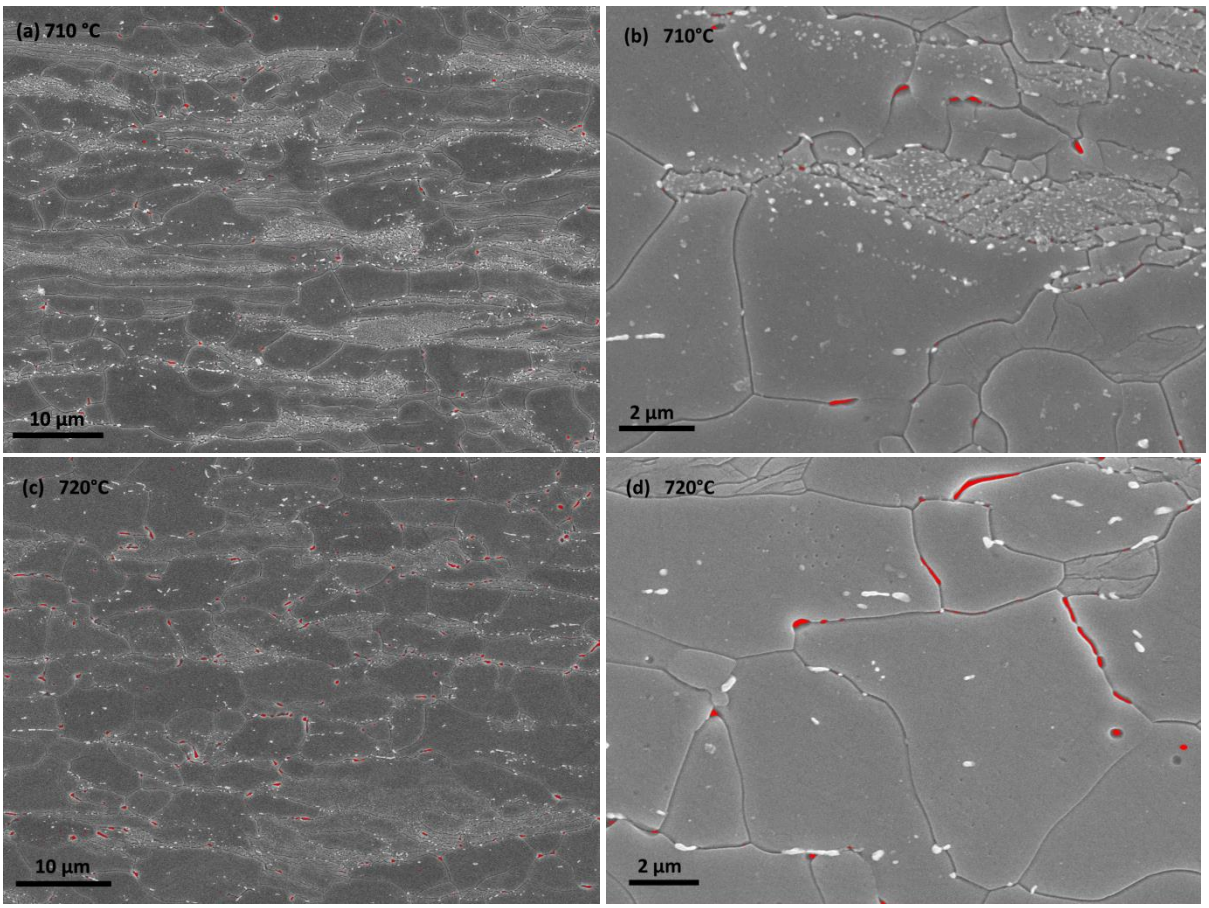

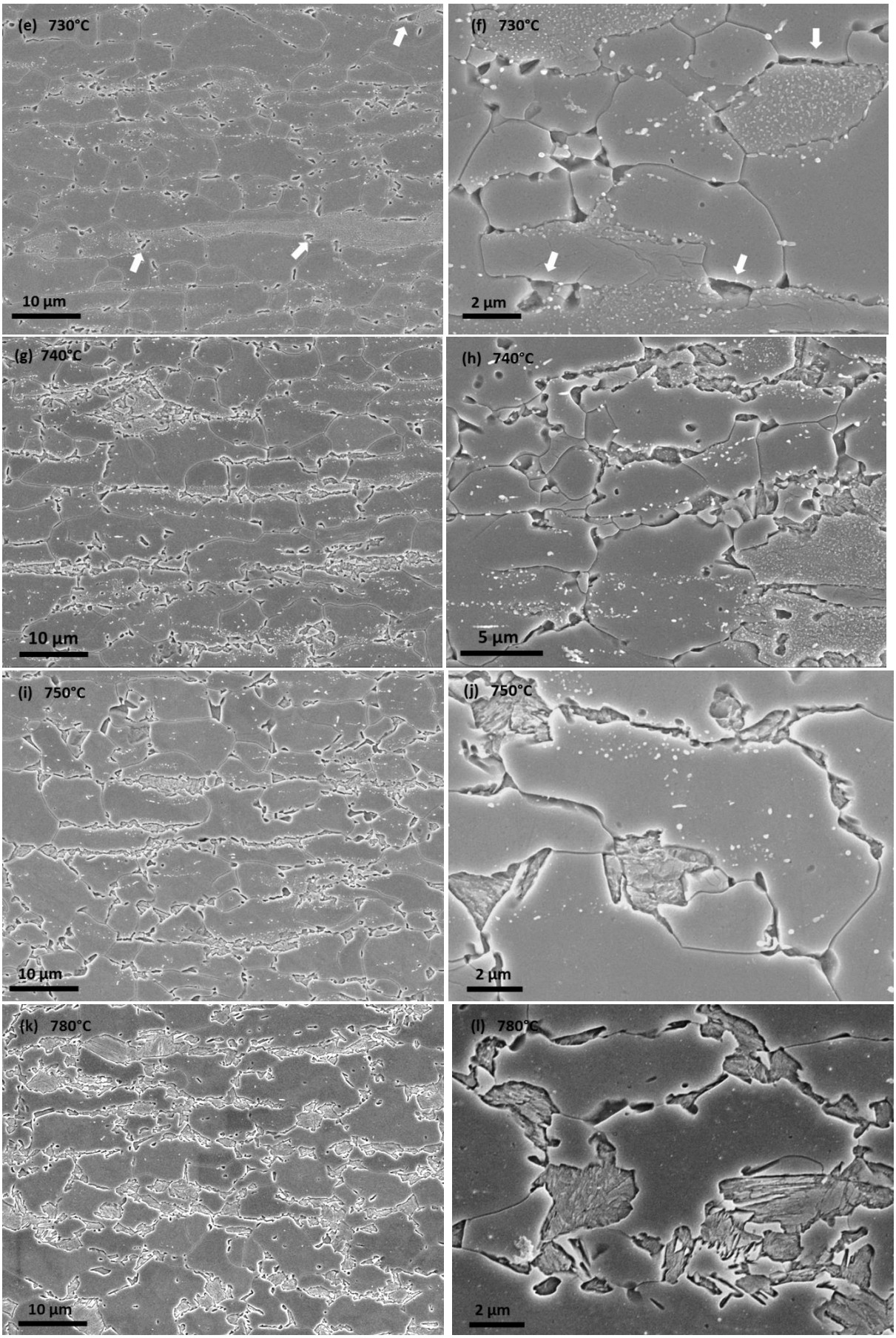
(e) 730°C
10 µm
(f) 730°C
2 µm
(g) 740°C
10 µm
(h) 740°C
5 µm
(i) 750°C
10 µm
(j) 750°C
2 µm
(k) 780°C
10 µm
(l) 780°C
2 µm

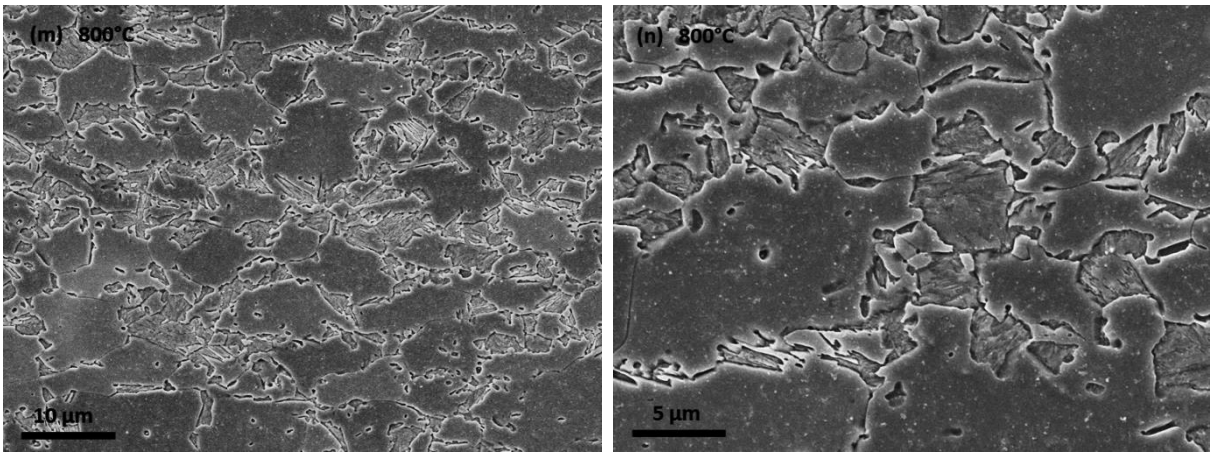

Figure 2.17: SEM micrographs of samples heated at 3°C.s^{-1} at different temperatures in the range of 710°C - 800°C and quenched. (a)-(b): 710°C (sample 710H3). The smallest austenite grains are colored in red for a better visibility. (c)-(d): 720°C (sample 720H3). (e)-(f): 730°C (sample 730H3). (g)-(h): 740°C (sample 740H3). (i)-(j): 750°C (sample 750H3). (k)-(l): 780°C (sample 780H3). (m)-(n): 800°C – 0s (sample 800H3). For each sample, two micrographs are presented corresponding to two different magnifications, at the segregated structure scale and at a single pearlite island scale.

- 710-720°C (710H3 and 720H3 samples): The ferritic matrix is almost fully recrystallized but pearlite islands still contain sub-grains revealing the absence of recrystallization in this domain. Austenite nucleates first around recrystallized ferrite grains. Small austenite grains present two distinct morphologies. Most of them have a spheroidal shape. These ones are principally localized at the triple-junctions of ferrite grains (between ferrite grains or between ferrite grains and pearlite islands) [GOT'11b]. The other morphology consists of austenite films (typically 100 nm thick) positioned on ferrite grain boundaries. The morphology of these new austenite grains is presumably due to the enhanced boundary diffusion as proposed by [LI'13]. It may be also due to percolation of austenite grains. Intra-granular nuclei are rare despite numerous intragranular carbides (see section 2.1.1.b). As pearlite colonies remain untransformed, austenite nucleation is highly heterogeneous below 720°C and the austenite growth is limited.

- 730°C (730H3): The austenite grains (films or sphere) between ferrite grains or between ferrite/pearlite islands have grown significantly and have adopted almost spheroidal shape (0.7µm as mean diameter). At this temperature, the number of new austenite grains observed around pearlite islands (few configurations are highlighted by arrows in Figures 2.17(e)-(f)) is in fact limited. No austenite grains are observed inside decomposed pearlitic islands. Rare intra-granular austenite grains do not evolve between 720°C and 730°C. The austenite fraction is estimated around 3.5%$_{vol}$.

Deeper investigations were carried out to verify if undissolved carbides can be observed inside newly formed austenite grains (the smallest austenite grains) at ferrite boundaries. In most of the cases, a white particle can be observed (Figures 2.18(a)-(b) and (c)) whatever the boundary configuration (plane or triple-point). Nevertheless, this observation is not systematic (Figures 2.18(d)-(e) and (f)) whatever the configuration and the size of the austenite grain. As a consequence, it has not been possible to conclude definitively about the nature of intergranular nucleation sites of austenite (systematic heterogeneous nucleation on the carbide). However, it seems statistically obvious that a very close carbide is required to act as a carbon source (dissolution). The absence of carbide can be interpreted either as a sign of a complete dissolution or because the carbide is not localized on the observed sample section.

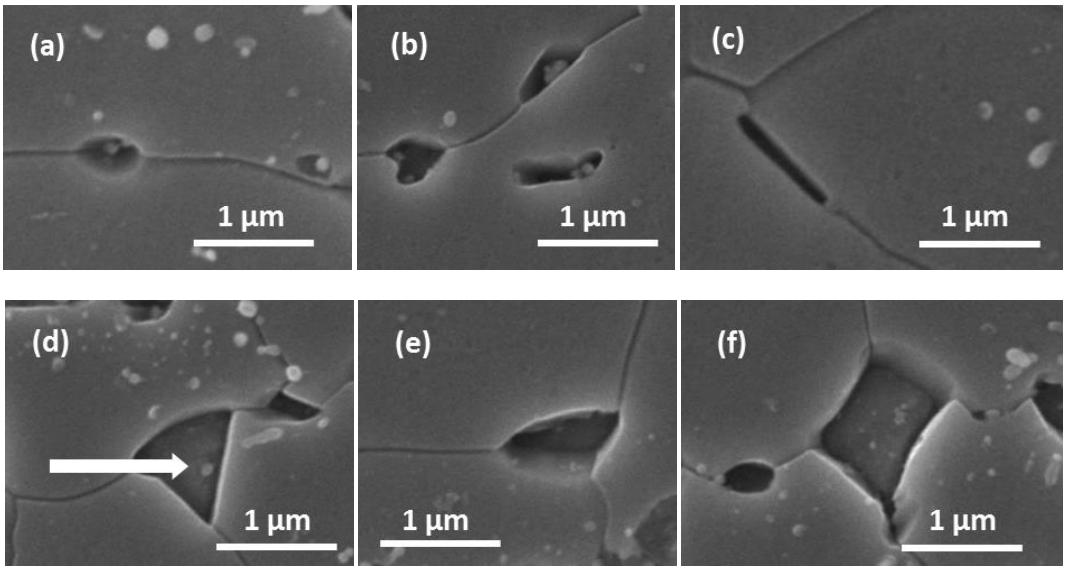

Figure 2.18: SEM micrographs at high magnification of sample 730H3 focusing on austenite nuclei localized (a),(b) and (c): on ferrite grain boundaries or (e), (f) and (g): at triple-junctions.

- 740°C (740H3): The ferritic matrix is now fully recrystallized. Between 730°C and 740°C, numerous austenite grains appear at pearlite island boundaries. These new grains grow rapidly in this stage and have almost consumed all pearlite islands at 740°C. Only larger pearlite islands with their aligned spheroidized carbides are still visible. The transformation of pearlite islands is the most important phenomenon observed in this temperature range.
  The grains at the triple-junctions seem to grow faster than those located along boundaries. Their typical diameter is estimated around 0.85 µm. In fact, the sizes of austenite grains are highly scattered. Austenite films reported at 720°C have barely thickened (0.22 µm thick). In some cases, the films and the spheroidal austenite grains are impinging and are forming the first continuous austenite layer along ferrite grain boundaries. As reported at lower temperature, rare intra-granular austenite grains kept their size, their growth being apparently stopped. The austenite volume fraction reaches about $8\%_{vol}$.

- 750°C (750H3): The austenite volume fraction is about $10\%_{vol}$. Pearlite islands are now fully transformed into austenite at this temperature. It is worth noting that each former pearlite island has been replaced by different austenite grains. The corresponding transformed volume inherits the thickness of the former pearlite (typically 2 µm width). The austenite grains localized on the triple-junctions are growing in the surrounding ferrite grains and reach a mean diameter of 2 µm. A significant proportion of the ferrite grain boundaries are thus decorated by austenite (around 50% of the linear boundary length) thanks to the growth of austenite grains located on ferrite grain boundaries.

- 780°C (780H3): The austenite volume fraction reaches $26\%_{vol}$. The large austenite domains which result from the dissolution of pearlite are expanding into the surrounding ferrite and their thickness is comprised between 3 and 8µm. The majority of the ferrite grain boundaries are decorated by austenite, leading to a microstructure made of austenite rings around the ferrite grain boundaries and large austenite islands at the place of former pearlite islands. This configuration is characteristic of the "necklace microstructure". The austenite films which are already percolated are now growing further into the ferrite grains and become thicker (500 nm thick). Again, the intra-granular austenite grains do not evolve.

- 800°C (800H3): The austenite volume fraction increases significantly between 780°C and 800°C (about 37%$_{vol}$ is now transformed at 800°C). The evolution seems mainly associated with the growth of former pearlite bands whereas the microstructure evolution in between (necklace structure) seems limited. It is however difficult to be definitive and quantitative as austenite network is now highly percolated.

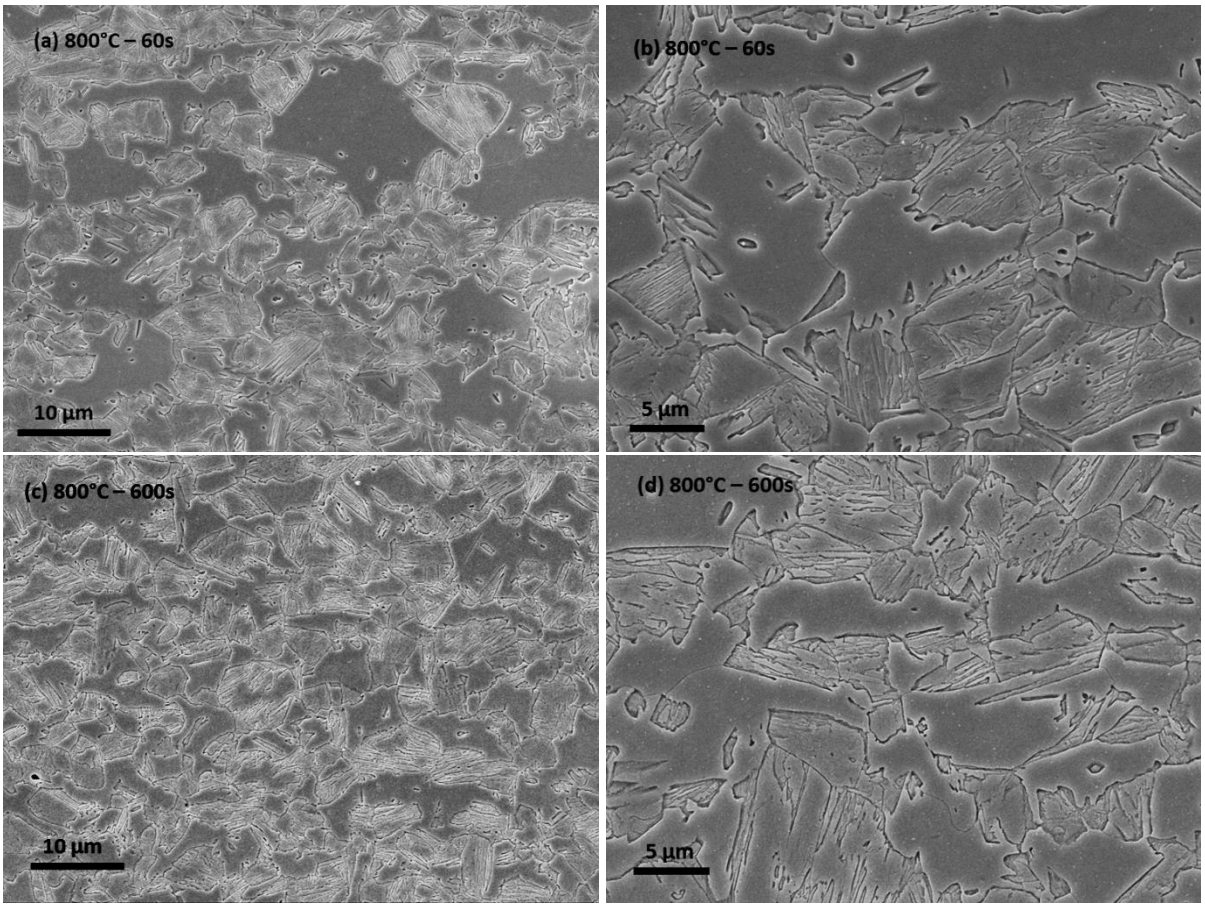

Figure 2.19: SEM micrographs of samples heated at 3°C.s^{-1} at 800°C, hold during (a)-(b) 60s (ISO60H3) and (d)-(d) 600s (ISO600H3) and quenched. For each sample, two micrographs are presented corresponding to two different magnifications, at the segregated structure scale and at a single pearlite island scale.

- 800°C – 60s (ISO60H3): The austenite volume fraction is 45%$_{vol}$. The necklace morphology obtained at end of the heating step (800H3) is disappearing due to the growth of austenite grains (around ferrite grains and austenite stemming from pearlite islands). Hence, the smallest ferrite grains are almost fully transformed into austenite and only the larger ferrite grains remain visible.

- 800°C – 600s (ISO600H3): At end of the holding stage, the amount of austenite reaches 57%vol, i.e. twice the value estimated at the beginning of the stage. The austenite distribution looks homogeneous and only the largest ferrite grains remain.

2.2.5.c Fast heating: SEM characterization of the microstructure evolution

Figures 2.20 show the SEM micrographs of the samples heated at 30°C.s^{-1} and quenched at different temperatures in the 720 - 800°C range with a 10°C step. The different figures correspond

respectively to samples 720H30, 730H30, 740H30, 750H30, 760H30, 770H30 and 800H30. For each sample, two micrographs are presented corresponding to two different magnifications, at the segregated structure scale and at a single pearlite island scale.

The microstructures are studied in this section above 720°C as the microstructure at 710°C (710H30) is strictly identical to the one of sample 700H30 (no transformation, no recrystallization). The first events of phase transformation / recrystallization were observed at 720°C by SEM. For 720H30, 730H30 and 740H30 samples, the densities of austenite grain and mean equivalent diameters calculated from the size distributions are given to highlight the nucleation process. The fractions of austenite transformed were measured again by a point counting method.

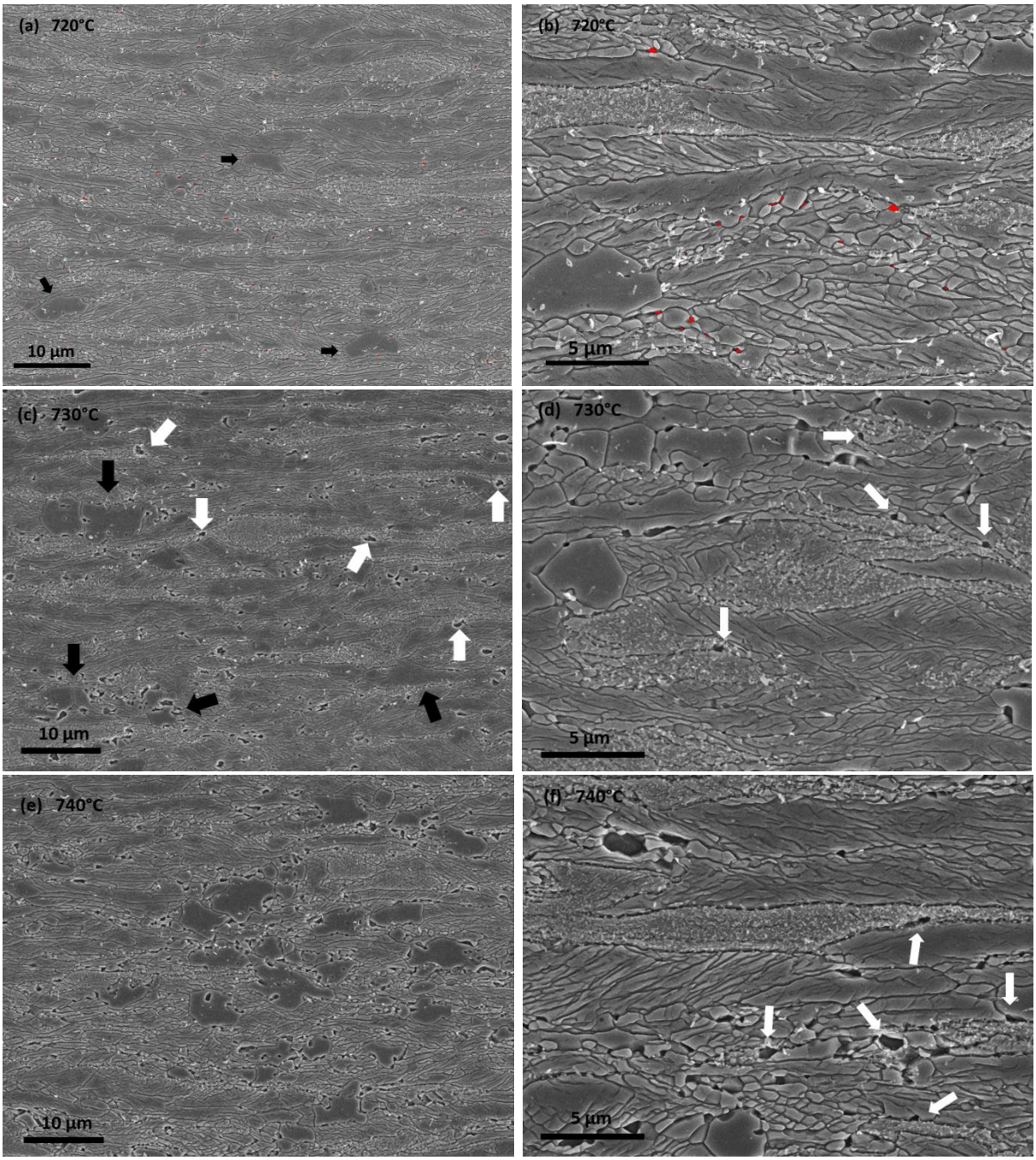

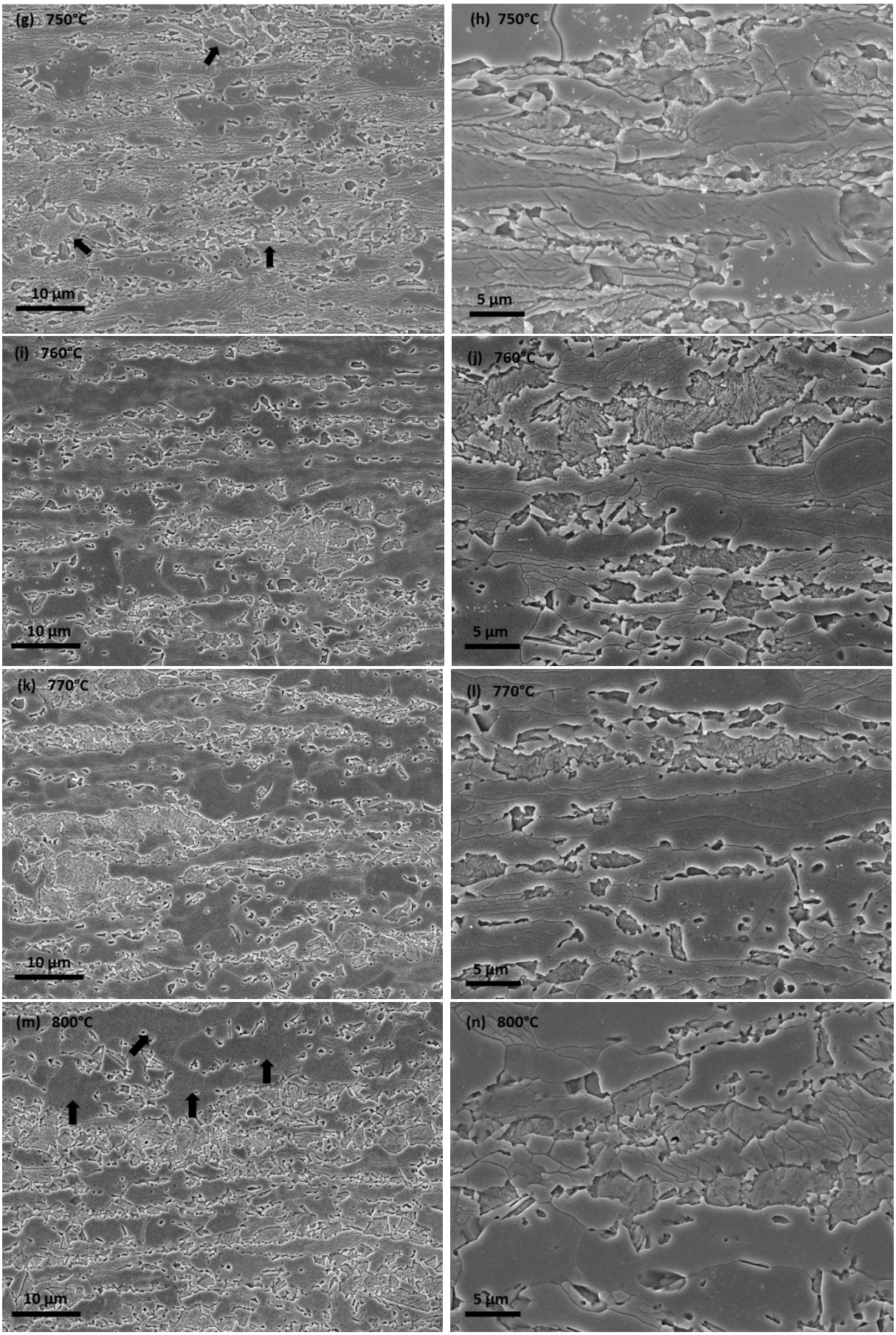
(g) 750°C
10 µm
(h) 750°C
5 µm
(i) 760°C
10 µm
(j) 760°C
5 µm
(k) 770°C
10 µm
(l) 770°C
5 µm
(m) 800°C
10 µm
(n) 800°C
5 µm

Figure 2.20: SEM micrographs of the samples heated at 30°C.s^{-1} at different temperatures in the range of 720°C - 800°C and quenched. (a)-(b): 720°C (sample 720H30). The small austenite grains are colored in red for better visibility. (c)-(d): 730°C (sample 730H30). (e)-(f): 740°C (sample 740H30). (g)-(h): 750°C (sample 750H30). (i)-(j): 760°C (sample 760H30). (k)-(l): 770°C (sample 770H30). (m)-(n): 800°C (sample 800H30). For each sample, two micrographs are presented corresponding to two different magnifications, at the segregated structure scale and at a single pearlite island scale.

- 720°C (720H30): The ferrite matrix is almost not recrystallized as in sample 700H3, (cf. Fig 2.17). The ferrite sub-grains are put into evidence by etching and their mean radius does not exceed 0.5 µm. The morphological texturing due to cold-rolling is still clearly observable. Very few large recrystallized grains (indicated by black arrows in Figure 2.20(a)) are however visible, meaning that recrystallization has just started at this temperature. At the same time, a significant number of small austenite grains (diameter in the order of 0.1µm, colored in red in Figures 2.19) is observed on deformed former ferrite boundaries, as highlighted by [LI'13] and excluding the interpretations of Huang *et al*. [HUA'04], Thomas *et al*. [TOM'18] or Chbihi *et al*. [CHB'14]. As for slow heating conditions, austenite nucleates first thus on the ferrite grain boundaries. The contrasts due to sub-grains inside non-recrystallized prevent from observing any intra-granular austenite grains.

- 730°C (730H30): Qualitatively, the density of austenite nuclei seems relatively similar to the one observed at the same temperature in slow heating conditions (cf. Figures 2.17(c)-(d)). New austenite grains seem to nucleate preferentially on deformed non-recrystallized ferrite grain boundaries and on recrystallized ferrite grain boundaries and seem to grow rapidly (austenite grains present in fact a typical size of about 1 µm). Pearlite dissolution is initiated from the pearlite/ferrite boundaries (white arrows on Figure 2.20(d)), analogously to slow heating condition for the same temperature. The recrystallization of the ferrite matrix proceeds concomitantly but remains moderate.

- 740°C (740H30): austenite nuclei are far more numerous but mainly all located around recrystallized ferrite grains due to the extent of the recrystallization. Very few of them are located on former pearlite islands. Rare intra-granular nuclei can also be now observed. At 740°C, contrary to the case of slow heating, austenite grows systematically in an isotropic way (no preferential growth of austenite films as observed sometimes in slow heating conditions). Pearlite dissolution remains very limited (cf. white arrows on Figure 2.20(f)), suggesting that the austenite transformation in pearlite start also at about 740°C, as for slow heating conditions. The fraction of austenite reached now 3%$_{vol}$. Between 730°C and 740°C, the recrystallized fraction has increased (about 5%) and the mean size of new ferrite grains has increased from 2 to 4 µm.

- 750°C (750H30 sample): The number of new austenite grains has not increased significantly and the austenite phase fraction is estimated to about 5%$_{vol}$. However, most austenite grains reach diameter greater than 2 µm. The transformation of pearlite islands has started at 740°C and most of pearlite islands are transforming at 750°C, even though the dissolution is obviously not complete at this temperature. Large recrystallized ferrite grains (up to 10 µm long in the rolling direction) are found between dissolving pearlite islands. They seem to inherit the elongated shape of the deformed ferrite grains.

- 760°C (760H30 sample): Between 750°C and 760°C, the austenite fraction increases rapidly, to reach a value of 15%$_{vol}$ at 760°C. This rapid increase is due to the complete transformation of pearlite islands and the growth of the resulting austenite grains. Figure 2.20(i) shows austenite grains, 20 µm long and 10 µm thick in average, resulting from the transformation of former pearlite islands and inheriting from their banded morphology. Many sub-grains are still visible in the ferritic matrix showing that the recrystallization process is far from being achieved.

- 770°C (770H30 sample): The large austenite grains inherited from pearlite island dissolution keep growing and are extended through the ferrite matrix in the cold-rolling direction. They are more than 20 µm long and their width is comprised between 6 and 12 µm. The space between the former pearlite bands reaches 15 µm in average, consistently with the distribution of Mn microsegregated bands. The austenite grains at the grain boundaries do not seem to grow significantly in this temperature range but are still aligned in the rolling as they have nucleated on deformed grains. The combination of elongated austenite grains inherited from pearlite islands and isolated grains aligned at ferrite grain boundary conducts to the formation of the so-called "banded" microstructure at 770°C. At 760°C; the austenite phase fraction is about 23%$_{vol}$ and the recrystallization of the ferritic matrix is not over.

- 800°C (800H30): The austenite volume fraction is now 40%$_{vol}$. Former pearlite bands are about 13 µm large, revealing that austenite coming from the dissolution of pearlite continues to grow into the surrounding matrix. The nucleation and growth of austenite also continue at ferrite grain boundaries, so that continuous films of austenite grains aligned in the cold-rolling direction are produced reinforcing the banded topology. Between 720°C and 800°C, rare intragranular austenite particles remain very small and represent a negligible part of the global austenite transformed. The recrystallization process has significantly proceeded and large recrystallized ferrite grains can be observed (black arrows, cf. Figure 2.20(m)) between austenite grain bands. It must be noted that the process is however not finished at 800°C.

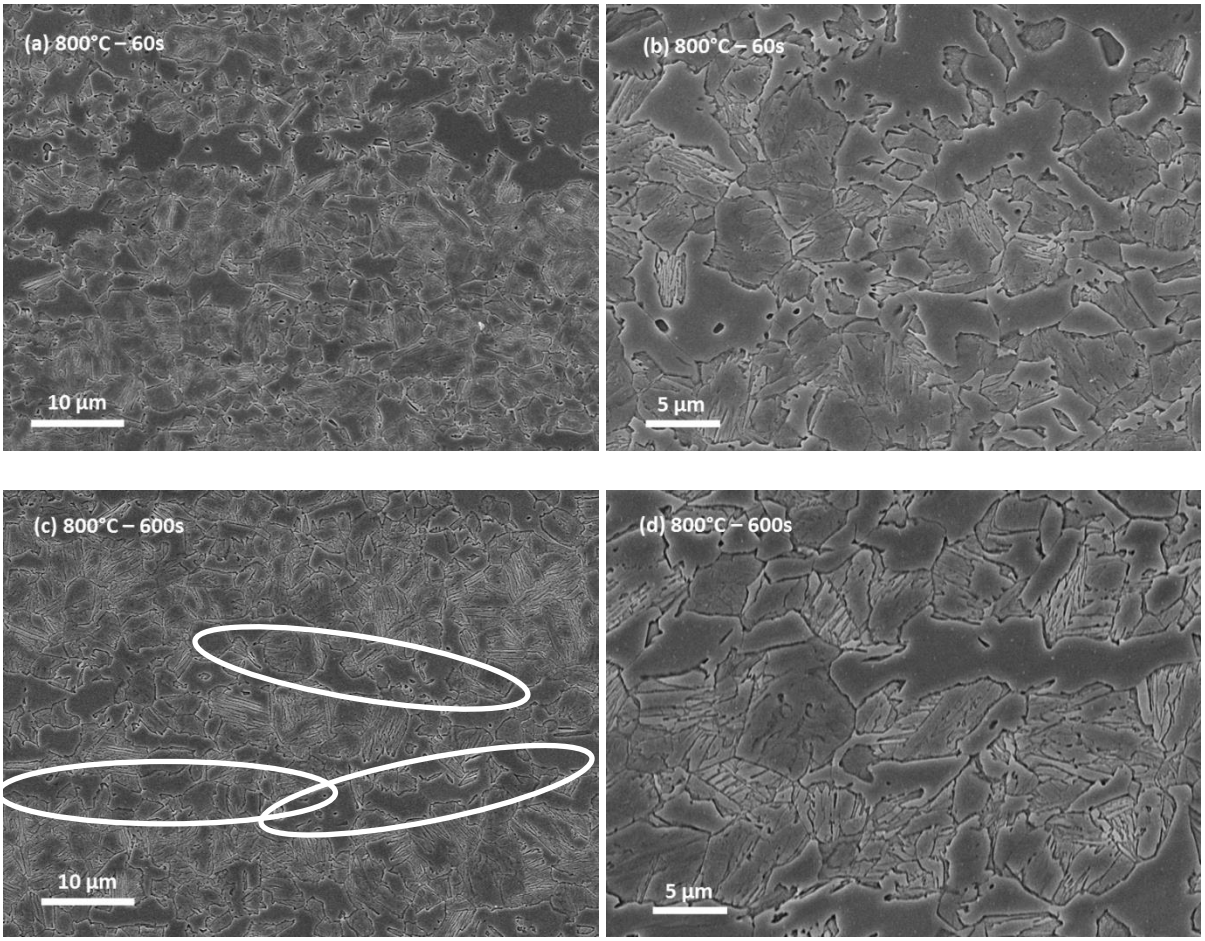

Figure 2.21: SEM micrographs of the samples heated at 30°C.s^{-1} at 800°C, hold during (a)-(b) 60s (ISO60H30) and (d)-(d) 600s (ISO600H30) and quenched. For each sample, two micrographs are presented corresponding to two different magnifications, at the segregated structure scale and at a single pearlite island scale.

- 800°C – 60s (ISO60H30): The transformation proceeds mainly by the growth of austenite grains which in turn consume ferrite grains. The recrystallization is now finished and only the larger recrystallized ferrite grains remain with a typical size of 10 µm. At 800°C, the austenite phase fraction approaches 60%$_{vol}$. The volume fraction is so high that the banded topology is disappearing to the profit of a homogenous distribution.

- 800°C – 600s (ISO600H30): At the end of the isothermal holding, the transformed fraction reaches a value of 70%$_{vol}$. The mean ferrite grain size is about 7µm. The microstructure looks homogeneous except the presence of aligned and elongated ferrite grains (probably in poor Mn segregated bands) which are the sole traces of the banded structure (highlighted by the white ellipses).

2.2.5.d Phase transformation kinetics

In this section, austenite transformation kinetic was determined thanks to two conventional techniques: a point counting method applied to SEM micrographs and the double-tangent method applied to dilatometer measurements. The latter experiments have been obtained during our *in situ* experiments on the synchrotron beamline. The method is described in chapter 1 (cf. Fig 1.11 and 1.12) and has been calibrated knowing the fraction of austenite measured by HEXRD at the end of the treatment (after 600s at 800°C for both heating rates). The phase fractions determined as a function of temperature during the heating stages are reported in Figure 2.22.

When comparing the phase fractions measured with the same technique, the evolutions of the phase fractions are very similar between both heating schedules. However, a significant gap exists between both techniques within the 710-780°C temperature range (about 10% difference). At the end of the heating step, the estimates show on the contrary a relatively good agreement.

These differences are not necessarily surprising as dilatometry signals raises different issues:

- Dilatometry is known to be insensitive to very low transformed fractions. It is the reason why we can observe first austenite grains on SEM micrographs without any deviation on the dilatometer signal.
- The heating system of the dilatometer used for the experiments is based on induction and is thus sensitive to the magnetic state of the material. This is the reason why we observe artefacts on the dilatometer signal when reaching the Curie point of the steel (745°C).
- The determination of the austenite phase fraction would have required taking into account cementite (pearlite islands and isolated carbides) to calculate the initial slope in the low temperature range.
- Contrary to SEM observations and HEXRD measurements (cf. Chapter 5) which are conducted just below the thermocouples driving the heating devices, dilatometer signal accounts for possibly large temperature heterogeneities over the whole sample.

The values produced by image analysis in the heating stage (on SEM micrographs) are in excellent agreement with the reference values determined by HEXRD. Nevertheless, the values given during the holding sequence at 800°C are lower than the value given HEXRD probably (57% for ISO600H3 and 70% for ISO600H30 samples compared to about 80% determined by HEXRD for both heating rates). This underestimate can have two reasons:

- DINO etchant is sensitive to carbon content of phases. As a consequence, when the transformed volume is high, the carbon content in austenite is low which can lead to difficulty in distinguishing martensite and ferrite after etching. This etching bias can be observed for instance in Figure 2.19 (d).

- Ferrite transformation during quenching: It is also not completely excluded that a certain fraction of ferrite can appear during quenching, especially when the carbon content in austenite is also low.

This is the reason why these measurements were considered with care and assumed that the new *in situ* HEXRD method was the most reliable means to measure the transformation kinetics.

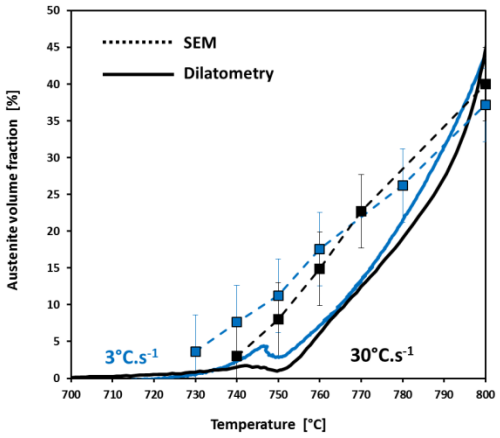

Figure 2.22: Austenite phase fraction as function of the temperature measured using SEM micrographs and dilatometry for slow (blue) and fast (black) annealing schedules.

Regardless of the quantification method, both heating rates produce comparable austenite phase fractions as function of temperature. At end of the heating stage, the microstructure is half austenitic whatever the heating rate. The fact that the phase fractions remain similar as function of the temperature while the fast heating rate is ten times higher than the slow one shows that the transformation kinetic is much more fast during fast heating.

2.3 Summary and discussion

An extensive SEM observation campaign was carried out to follow the evolution of the reverse austenite transformation during slow and fast heating up to 800°C. Our investigations were performed from 700 to 800°C with a 10°C temperature step. In addition, the microstructure evolution was also studied during the subsequent holdings for 600s.

2.3.1 Summary

As widely shown in the literature, our microstructure observations conclude that slow heating conditions produces necklace microstructure in the studied steel while fast heating results in a banded microstructure. The differences between the observed microstructures nevertheless vanished when the transformation rate is high (after long holdings at high temperature). The first differences in microstructure evolution appear in fact before the austenitization starts.

- Slow heating leads to a fully recrystallized ferrite matrix. The grain boundaries are impeded by the largest carbides which are the carbon source for future austenite nucleation. Isolated carbides have enough time to coarsen and achieve a mean radius greater than 100 nm. They are systematically found on the equiaxed ferrite grain boundaries. At the same time, decomposition / re-precipitation of cementite introduced small carbides within the ferrite grains (R < 15 nm). The cementite particle

density is almost doubled relative to the CR state and the particles are homogeneously spread in the microstructure.

- Rapid heating does not let time for recrystallization to occur. The ferrite matrix is made of sub-grains (diameter 0.5 μm). The density of carbides is very close to that measured on the CR sample. Clusters of cementite particles in matrix did not coarsen and remain aligned along the former grain boundaries oriented parallel to the rolling direction. The number of intra-granular particles is negligible.

Our observation of austenite microstructure sustains in fact the approach suggested by Li *et al.*, our studied cases corresponding respectively to the slow and medium heating rates of their models (full recrystallization before austenite transformation and concomitant mechanisms) as shown in Figure 2.6. The sole difference is that we observe that austenite nucleates first on ferrite boundaries and not in pearlite. Our study also does not clearly highlight a difference in nucleation flux between both scenarios.

In the studied case of slow heating, austenite nucleation starts first on isolated carbides at ferrite boundaries (mainly triple-points in our case). The enhanced solute diffusion through the grain boundaries promotes the continuous layer of austenite grains which progressively impinge, producing an austenite network covering the ferrite grain boundaries in the matrix between two pearlite bands. Transformation of pearlite islands occurs rapidly. Elongated pearlite islands parallel to the cold-rolling direction are transformed into large austenite grains. When the pearlite dissolution is complete, carbon -rich austenite continues to grow in the surrounding matrix. The necklace configuration is thus explained by austenite nucleation on isolated carbides. These carbides have thus a key role in the morphogenesis of ferrite/austenite microstructures.

Fast heating hinders ferrite recrystallization as well as coarsening of the isolated precipitates before austenitization. The ferrite grains are highly elongated according to the cold-rolling direction and fragmented into sub-grains. Clusters of aligned carbides, inherited from the CR microstructure are found along these grain boundaries. Thus, the particle alignments are in most of the cases parallel to the deformed structure. When the transformation temperature is achieved, the inter-granular carbides dissolve, giving place to austenite nuclei which prevent any movement of ferrite interfaces (ferrite recrystallization). Therefore, to recrystallize between two aligned clusters of nuclei, the ferrite sub-grains have no other alternative than merge according to the cold-rolling direction. It is confirmed by the large elongated ferrite areas seen on Figure 2.17. As in the case of slow heating, elongated pearlite islands transform into austenite grains (cf. Fig. 2.14). The newly formed austenite grains expand in the surrounding matrix; up to achieve austenite band 14 μm broad. Those dimensions correspond to the Mn-rich segregated bands illustrated in Figure 2.11 [CHB'14].

2.3.2 Discussion

2.3.2.a Isolated carbides at ferrite boundaries

Our observations have confirmed the key role played by isolated carbides. Like different authors from the literature, our observations seem to confirm that they are nucleation sites for austenite and at least close carbon sources for austenite nuclei on ferrite grain boundaries. For both studied heating rates, austenite transformation starts on ferrite grain boundaries (either recrystallized or still deformed) at close temperature (710°C and 720°C for slow and fast annealing schedules respectively). One can stress out that this result is in contradiction with many studies from the literature that report that nucleation starts at pearlite island boundaries, while ferrite grain boundaries would be less efficient nucleation sites [AZI'11, SAV'07].

For both heating rates, the austenite grains inherited from these isolated carbides seem to grow rapidly once formed up to about 750°C. Above this temperature, their growth rate appears to be limited.

2.3.2.b Intragranular carbides

The intra-granular carbides seem not to be favorable austenite nucleation sites. Rare intergranular austenite grains can be observed at the very beginning of transformation but they do grow and dissolve at higher temperature. This is presumably due to the lower diffusion coefficient of carbon in bulk compared to diffusion along grain boundaries. The higher diffusion coefficient on grain boundaries also explains the film morphology of certain austenite grains observed at low heating rates.

2.3.2.c Pearlite islands

Interestingly, the temperatures for pearlite start / complete dissolution are identical, regardless the heating rates. The dissolution is triggered near 730°C and achieved close to 750°C. This observation is well captured by the model developed in chapter 5 and is explained by the narrow distribution of cementite in pearlite islands which permits fast local transformation kinetics at island scale. As will be reminded in Chapter 5, austenite nucleation at pearlite island boundaries is frequently reported to occur with fast saturation of the nucleation sites (see e.g. [OFF'02]).

In contrast, the subsequent growth of the former pearlite bands (being now austenite) shows a difference in terms of kinetics. The growth appears to proceed faster during the fast heating when comparing with the slow one. At 760, 770 and 800°C (0s) the former pearlite bands are 3, 5 and 10μm thick during slow heating and respectively 10, 12 and 14 μm thick after fast heating. In fact, the pearlite bands progressively adopt the width of the Mn-rich bands. This difference in growth kinetics has been explained by our model in chapter 5.

2.3.2.d Global Transformation kinetics

A first look was given to transformation kinetics with the help of dilatometry and SEM micrographs. It appears that they are similar whatever the heating rate in the heating stage. This observation is consistent with the effect of heating rates reported by Li *et al.* [LI'13] (a similar temperature of 20°C is reported for slow and medium heating rates) or Huang *et al.* [HUA'04] for instance.

As the kinetic are similar whereas the high heating rate is ten times higher than the slow one, it suggests that the transformation kinetic is much faster when the heating rates are high. Our HEXRD in situ will reveal that will be also the case during the holding stage. The final transformed fractions after 600s will however be similar (typically 80 %).

2.3.2.e Topology after holdings

Our observations reveal in fact that the necklace and banded microstructures can be observed only if the transformation rate is limited in the studied steels (below 50%). After a 600 s holding at 800°C, the microstructures look similar whatever the heating rate. The sole difference is maybe the presence of few alignments of elongated ferrite grains for the high heating rate.

2.4 Conclusion

In this chapter, the evolution of the microstructure of the studied steel was characterized by means of electronic microscopy from as hot-rolled state to the end of the intercritical soaking in conventional annealing lines.

The hot-rolled material presents large equiaxed ferrite grains and pearlite islands. The volume fraction of pearlite is lower than expected by thermodynamic calculations (16% instead of 25%). A significant part of the carbon is trapped between pro-eutectoid ferrite grains in the forms of isolated intergranular carbides (films or particles). Cold-Rolling leads to a severe deformation of both pearlite islands and ferrite grains and conduct to a new distribution of cementite in the ferrite matrix (fragmentation and shuffling). The number of isolated cementite precipitates inside the matrix increase significantly as a consequence. These particles are found to be aligned on the deformed ferrite grain boundaries parallel to the cold-rolling direction.

The heating rate affects the dynamic balance between concomitant metallurgical mechanisms occurring during annealing, as cementite ripening and recrystallization, which in turn plays a key role on the spatial distribution of austenite. Our observations have confirmed essentially the scenario proposed by Li et al. to explain the morphogenesis of austenite microstructure during intercritical annealing. We have also shown that the different topologies produced during heating can vanish when the transformation fractions are high.

When the deformed ferrite/pearlite microstructure is heated at slow rate ($3°C.s^{-1}$), the recrystallization precedes phase transformation. Austenite nucleation starts on intergranular carbides found on the recrystallized matrix. The further growth of these austenite grains enhanced by boundary diffusion produces continuous layers which form the necklace microstructure. Transformation of pearlite islands starts at slightly higher temperature and produces elongated austenitic structure which cannot be neglected.

When the deformed ferrite/pearlite microstructure is heated at fast rate ($30°C.s^{-1}$), the recrystallization starts concomitantly to the phase transformation. As at low rate, austenite nucleation starts on intergranular carbides. The sole difference is that these carbides are aligned and found on the deformed grains. The further growth of these grains produces aligned austenite structure. This process is reinforced by the transformation of pearlite islands which produced elongated austenitic structure. Both mechanisms thus contribute to the formation of the banded structure.

In this study, we have highlighted the particular role of intergranular carbides on the final topology and transformation kinetics. This is the reason why we have proposed in chapter 5 a modeling strategy distinguishing the behavior of pearlitic islands and these carbides. The mechanisms behind the formation of these carbides are still a debating question and represent an important outlook of this thesis.

REFERENCES

[ALL'04] Allain, S., Chateau, J.-P., Bouaziz, O., Migot, S., Guelton, N., 2004. Correlations between the calculated stacking fault energy and the plasticity mechanisms in Fe–Mn–C alloys. Materials Science and Engineering: A 387–389, 158–162. https://doi.org/10.1016/j.msea.2004.01.059

[AND'07] Andrade-Carozzo, V., Jacques, P.J., 2007. Interactions between Recrystallisation and Phase Transformations during Annealing of Cold Rolled Nb-Added TRIP-Aided Steels. Materials Science Forum 539–543, 4649–4654. https://doi.org/10.4028/www.scientific.net/MSF.539-543.4649

[ARR'14] Arruabarrena, J., López, B., Rodriguez-Ibabe, J.M., 2014. Influence of Prior Warm Deformation on Cementite Spheroidization Process in a Low-Alloy Medium Carbon Steel. Metallurgical and Materials Transactions A 45, 1470–1484. https://doi.org/10.1007/s11661-013-2066-3

[CHA'77] Chattopadhyay, S., Sellars, C.M., 1977. Quantitative measurements of pearlite spheroidization. Metallography 10, 89–105. https://doi.org/10.1016/0026-0800(77)90044-1

[CHA'82] Chattopadhyay, S., Sellars, C.M., 1982. Kinetics of pearlite spheroidisation during static annealing and during hot deformation. Acta Metallurgica 30, 157–170. https://doi.org/10.1016/0001-6160(82)90055-4

[CHB'14] Chbihi, A., Barbier, D., Germain, L., Hazotte, A., Gouné, M., 2014. Interactions between ferrite recrystallization and austenite formation in high-strength steels. Journal of Materials Science 49, 3608–3621. https://doi.org/10.1007/s10853-014-8029-2

[DAN'98] Danoix, F., Julien, D., Sauvage, X., Copreaux, J., 1998. Direct evidence of cementite dissolution in drawn pearlitic steels observed by tomographic atom probe. Materials Science and Engineering: A 250, 8–13. https://doi.org/10.1016/S0921-5093(98)00529-2

[DES'76] Desforges, C.D., Duckworth, W.E., Ryan, T.F.J.N., 1976. Manganese in ferrous metallurgy. Manganese Centre, Neuilly-sur-Seine (191 Av. Charles de Gaulle, 92521).

[DIN'10] Dini, G., Ueji, R., Najafizadeh, A., Monir-Vaghefi, S.M., 2010. Flow stress analysis of TWIP steel via the XRD measurement of dislocation density. Materials Science and Engineering: A 527, 2759–2763. https://doi.org/10.1016/j.msea.2010.01.033

[ENO'18] Enomoto, M., Li, S., Yang, Z.N., Zhang, C., Yang, Z.G., 2018. Partition and non-partition transition of austenite growth from a ferrite and cementite mixture in hypo- and hypereutectoid Fe-C-Mn alloys. Calphad 61, 116–125. https://doi.org/10.1016/j.calphad.2018.03.002

[ESI'14] Esin, V.A., Denand, B., Le Bihan, Q., Dehmas, M., Teixeira, J., Geandier, G., Denis, S., Sourmail, T., Aeby-Gautier, E., 2014. In situ synchrotron X-ray diffraction and dilatometric study of austenite formation in a multi-component steel: Influence of initial microstructure and heating rate. Acta Materialia 80, 118–131. https://doi.org/10.1016/j.actamat.2014.07.042

[ETO'08] Etou, M., Fukushima, S., Sasaki, T., Haraguchi, Y., Miyata, K., Wakita, M., Tomida, T., Imai, N., Yoshida, M., Okada, Y., 2008. Super Short Interval Multi-pass Rolling Process for Ultrafine-grained Hot Strip. ISIJ International 48, 1142–1147. https://doi.org/10.2355/isijinternational.48.1142

[FLE'06] Flemings, M.C., 2006. Solidification Processing, in: Cahn, R.W., Haasen, P., Kramer, E.J. (Eds.), Materials Science and Technology. Wiley-VCH Verlag GmbH & Co. KGaA, Weinheim, Germany. https://doi.org/10.1002/9783527603978.mst0173

[FRE'96] Freshwater, I.J., 1996. Simplified theories of flat rolling—I. The calculation of roll pressure, roll force and roll torque. International Journal of Mechanical Sciences 38, 633–648. https://doi.org/10.1016/S0020-7403(96)80006-3

[GAR'81] Garcia, C.I., Deardo, A.J., 1981. Formation of austenite in 1.5 pct Mn steels. Metallurgical Transactions A 12, 521–530. https://doi.org/10.1007/BF02648551

[GAN'09] Gang, U.G., Lee, J.C., Nam, W.J., 2009. Effect of prior microstructures on the behavior of cementite particles during subcritical annealing of medium carbon steels. Metals and Materials International 15, 719–725. https://doi.org/10.1007/s12540-009-0719-3

[GOU'12] Gouné, M., Maugis, P., Drillet, J., 2012. A Criterion for the Change from Fast to Slow Regime of Cementite Dissolution in Fe–C–Mn Steels. Journal of Materials Science & Technology 28, 728–736. https://doi.org/10.1016/S1005-0302(12)60122-4

[GOT'11a] Lischewski, I., Gottstein, G., 2011. Nucleation and variant selection during the α–γ–α phase transformation in microalloyed steel. Acta Materialia 59, 1530–1541. https://doi.org/10.1016/j.actamat.2010.11.017

[GOT'11b] Zhao, B., Gottstein, G., Shvindlerman, L.S., 2011. Triple junction effects in solids. Acta Materialia 59, 3510–3518. https://doi.org/10.1016/j.actamat.2011.02.024

[GRA'10a] Granbom, Y., 2010. Structure and mechanical properties of dual phase steels an experimental and theoretical analysis. KTH, Stockholm.

[GRA'10b] Granbom, Y., Ryde, L., Jeppsson, J., 2010. Simulation of the Soaking and Gas Jet Cooling in a Continuous Annealing Line using Dilatometry. steel research international 81, 158–167. https://doi.org/10.1002/srin.200900097

[HON'99] Hong, M.H., Hono, K., Reynolds, W.T., Tarui, T., 1999. Atom probe and transmission electron microscopy investigations of heavily drawn pearlitic steel wire. Metallurgical and Materials Transactions A 30, 717–727. https://doi.org/10.1007/s11661-999-0063-3

[JUD'69] Judd, R. R., & Paxton, H. W. (1968). Kinetics of austenite formation from a spheroidized ferrite-carbide aggregate. *TRANS MET SOC AIME*, *242*(2).

[KAL'98] Kaluba, W.., Taillard, R., Foct, J., 1998. The bainitic mechanism of austenite formation during rapid heating. Acta Materialia 46, 5917–5927. https://doi.org/10.1016/S1359-6454(98)00210-9

[KUL'13] Kulakov, M., Poole, W.J., Militzer, M., 2014. A Microstructure Evolution Model for Intercritical Annealing of a Low-carbon Dual-phase Steel. ISIJ International 54, 2627–2636. https://doi.org/10.2355/isijinternational.54.2627

[LAI'16] Lai, Q., Gouné, M., Perlade, A., Pardoen, T., Jacques, P., Bouaziz, O., Bréchet, Y., 2016. Mechanism of Austenite Formation from Spheroidized Microstructure in an Intermediate Fe-0.1C-3.5Mn Steel. Metallurgical and Materials Transactions A 47, 3375–3386. https://doi.org/10.1007/s11661-016-3547-y

[LAN'97] Languillaume, J., Kapelski, G., Baudelet, B., 1997. Cementite dissolution in heavily cold drawn pearlitic steel wires. Acta Materialia 45, 1201–1212. https://doi.org/10.1016/S1359-6454(96)00216-9

[LEE'87] Lee, J.-W., Howell, P.R., 1987. Microstructural development in non-oriented lamination steels: Part 1 The nature of ferrite/pearl ite aggregates in continuously cooled low-carbon steels. Journal of Materials Science 22, 3631–3641. https://doi.org/10.1007/BF01161471

[LEE'90] Lee, J.-W., Thompson, S.W., Howell, P.R., 1990. Microstructural development in non-oriented lamination steels: Part 2 Isothermal transformation studies. Journal of Materials Science 25, 1699–1710. https://doi.org/10.1007/BF01045373

[LEE'93] Lee, J.W., Thompson, S.W., Varughese, R., Howell, P.R., 1993. The interaction between proeutectoid ferrite and austenite during the isothermal transformation of two low-carbon steels ? a new model for the decomposition of austenite. Journal of Materials Science 28, 4571–4577. https://doi.org/10.1007/BF00414244

[LI'13] Li, P., Li, J., Meng, Q., Hu, W., Xu, D., 2013. Effect of heating rate on ferrite recrystallization and austenite formation of cold-roll dual phase steel. Journal of Alloys and Compounds 578, 320–327. https://doi.org/10.1016/j.jallcom.2013.05.226

[LI'16] Li, Z.-D., Miyamoto, G., Yang, Z.-G., Furuhara, T., 2011. Kinetics of Reverse Transformation from Pearlite to Austenite in an Fe-0.6 Mass pct C Alloy and the Effects of Alloying Elements. Metallurgical and Materials Transactions A 42, 1586–1596. https://doi.org/10.1007/s11661-010-0560-4

[MAL'89] Courtney, T.H., Kampe, J.C.M., 1989. Shape instabilities of plate-like structures—II. Analysis. Acta Metallurgica 37, 1747–1758. https://doi.org/10.1016/0001-6160(89)90060-6

[MAT'17] Matusiewicz, P., Augustyn-Nadzieja, J., Czarski, A., Skowronek, T., 2017. Kinetics of pearlite spheroidization. Archives of Metallurgy and Materials 62, 231–234. https://doi.org/10.1515/amm-2017-0034

[MOH'11] Mohanty, R.R., Girina, O.A., Fonstein, N.M., 2011. Effect of Heating Rate on the Austenite Formation in Low-Carbon High-Strength Steels Annealed in the Intercritical Region. Metallurgical and Materials Transactions A 42, 3680–3690. https://doi.org/10.1007/s11661-011-0753-5

[NEM'77] Nemoto, M., 1977. The formation of austenite from mixtures of ferrite and cementite as observed by HVEM. Metallurgical Transactions A 8, 431–437. https://doi.org/10.1007/BF02661753

[OFF'02] Offerman, S.E., van Dijk, N.H., Sietsma, J., Grigull, S., Lauridsen, E.M., Margulies, L., Poulsen, H.F., Rekveldt, M.T., van der Zwaag, S., 2002. Grain Nucleation and Growth During Phase Transformations. Science 298, 1003–1005. https://doi.org/10.1126/science.1076681

[OLL'17] Ollat, M. 2017. Characterization and modeling of microstructural evolutions during the thermal treatment of cold-rolled Dual-Phase steels. PhD report. https://tel.archives-ouvertes.fr/tel-01920855

[POV'12] Petrov, R.H., Sidor, J.J., Kaluba, W., Kestens, L., 2012. Grain Refinement of a Cold Rolled TRIP Assisted Steel after Ultra Short Annealing. Materials Science Forum 715–716, 661–666. https://doi.org/10.4028/www.scientific.net/MSF.715-716.661

[RID'84] Ridley, N., 1984. A Review of the Data on the Interlamellar Spacing of Pearlite. Metallurgical and Materials Transactions A 15, 1019–1036. https://doi.org/10.1007/BF02644694

[RUD'11] Rudnizki, J., Böttger, B., Prahl, U., Bleck, W., 2011. Phase-Field Modeling of Austenite Formation from a Ferrite plus Pearlite Microstructure during Annealing of Cold-Rolled Dual-Phase Steel. Metallurgical and Materials Transactions A 42, 2516–2525. https://doi.org/10.1007/s11661-011-0626-y

[SAV'07] Savran, V.I., Van Leeuwen, Y., Hanlon, D.N., Kwakernaak, C., Sloof, W.G., Sietsma, J., 2007. Microstructural Features of Austenite Formation in C35 and C45 alloys. Metallurgical and Materials Transactions A 38, 946–955. https://doi.org/10.1007/s11661-007-9128-3

[SAV'10] Savran, V.I., Offerman, S.E., Sietsma, J., 2010. Austenite Nucleation and Growth Observed on the Level of Individual Grains by Three-Dimensional X-Ray Diffraction Microscopy. Metallurgical and Materials Transactions A 41, 583–591. https://doi.org/10.1007/s11661-009-0142-5

[SCH'01] Shin, D.., Kim, Y.-S., Lavernia, E.., 2001. Formation of fine cementite precipitates by static annealing of equal-channel angular pressed low-carbon steels. Acta Materialia 49, 2387–2393. https://doi.org/10.1016/S1359-6454(01)00165-3

[SCH'03] Shin, D.H., Park, K.-T., Kim, Y.-S., 2003. Formation of fine cementite precipitates in an ultra-fine grained low carbon steel. Scripta Materialia 48, 469–473. https://doi.org/10.1016/S1359-6462(02)00512-2

[SHT'99] Shtansky, D.V., Nakai, K., Ohmori, Y., 1999. Pearlite to austenite transformation in an Fe–2.6Cr–1C alloy. Acta Materialia 47, 2619–2632. https://doi.org/10.1016/S1359-6454(99)00142-1

[SPE'69] G. R. Speich and A. Szirmae, with Appendix by G. R. Speich and M. J. Richards,*Trans. TMS-AIME*, 1969, vol. 245, pp. 1063–74.

[SU'15] Su, Y., Morooka, S., Ohnuma, M., Suzuki, J., Tomota, Y., 2015. Quantitative Analysis of Cementite Spheroidization in Pearlite by Small-Angle Neutron Scattering. Metallurgical and Materials Transactions A 46, 1731–1740. https://doi.org/10.1007/s11661-014-2737-8

[TAK'10] Takebayashi, S., Kunieda, T., Yoshinaga, N., Ushioda, K., Ogata, S., 2010. Comparison of the Dislocation Density in Martensitic Steels Evaluated by Some X-ray Diffraction Methods. ISIJ International 50, 875–882. https://doi.org/10.2355/isijinternational.50.875

[TOM'18] Thomas, L.S., Matlock, D.K., 2018. Formation of Banded Microstructures with Rapid Intercritical Annealing of Cold-Rolled Sheet Steel. Metallurgical and Materials Transactions A 49, 4456–4473. https://doi.org/10.1007/s11661-018-4742-9

[YAN'85] Yang, D.Z., Brown, E.L., Matlock, D.K., Krauss, G., 1985. Ferrite recrystallization and austenite formation in cold-rolled intercritically annealed steel. Metallurgical Transactions A 16, 1385–1392. https://doi.org/10.1007/BF02658671

[YIN'18] Yin, Y., Sun, J., Zhao, A., Gou, J., 2018. Ultra-low-carbon steel spheroidization and torsion. Journal of Iron and Steel Research International 25, 968–974. https://doi.org/10.1007/s42243-018-0137-9

[ZHU'15b] Zhu, B., Militzer, M., 2015. Phase-Field Modeling for Intercritical Annealing of a Dual-Phase Steel. Metallurgical and Materials Transactions A 46, 1073–1084. https://doi.org/10.1007/s11661-014-2698-y

Chapter 3

Evolution of cementite composition along the processing of cold-rolled and annealed Dual-Phase steels

As shown in previous Chapter 2, carbide microstructure evolves significantly. This ripening process is accompanied by a composition evolution. Understanding and modeling this evolution is one of the keys to understand carbide dissolution processes and henceforth the austenitization kinetics. As discussed in introduction, high cementite Mn composition may for instance considerably delay this last phase transformation.

The first part of the chapter will be dedicated to the experimental characterization of the chemical composition of carbides during DP steel manufacturing prior to austenization, i.e. from hot-rolled state to continuous annealing. Specimens were produced to replicate the material state at three key stages of the manufacturing route and investigated by Transmission Electron Microscopy (TEM) as described in Chapter 1. The initial composition of cementite directly after pearlite transformation was first examined to serve as reference. A second specimen, taken from the cold-rolled state (as-received material) permits to quantify the Mn diffusion during the slow cooling from coiling stage to room temperature. The third studied state corresponds to an annealing sequence interrupted before austenitization starts. Different samples have been produced as function of the heating rate (samples already studied in Chapter 2). This experimental study reveals that carbides are already enriched homogeneously in manganese just after pearlite transformation and that diffusion profiles appear in carbides during coiling. During further annealing, these composition profiles are maintained at high heating rate and suppressed at low heating rate as the kinetics conditions are so that the thermodynamic equilibrium is almost reached.

In the last part of this chapter, thermodynamical analyses and DICTRA simulations will be employed to interpret the measured composition evolutions with an emphasis on Mn. A thermodynamic analysis based on Hutchinson *et al*. [HUT'04] will be used and improved to predict successfully the cementite composition when the pearlite transformation occurs. DICTRA simulations will serve to calculate the evolution of composition profiles during both coiling and annealing. In the course of this study, it has been necessary to reassess the Mn diffusion coefficient of the MOBFE2 database based on experimental results.

Finally, a simplified calculation module, working by Finite Difference resolution, will be built on the basis DICTRA simulations in order to reproduce the experimental results and provide an operational predictive tool in view of industrial implementation (product line management).

Content

3.1 Experiments: TEM observations and compositions measurements

3.1.1 Sampling plan

The production of thin sheets of DP steels requires complex thermomechanical schedule as the one represented in Figure 3.1. Along this treatment, the carbide microstructure (lamellar pearlite and isolated carbides) forms below Ar_1 after hot-rolling and then undergo a ripening process during coiling and further annealing. In this section, the carbide microstructures and their compositions will be studied by the mean of TEM coupled with an EDXS as explained in Chapter 1 at different critical stages of this schedule. These particular steps are indicated in Figure 1 by blue squares.

The sample designation is the same as the one used in Chapter2. FP stands for the material state just after ferrite-pearlite transformation at 570°C, HR designates the ferrite-pearlite microstructure at end of the coiling step, CR after cold-rolling, while 700H3/700H30 correspond to slow and fast heated specimens to 700°C at 3 and 30°C.s^{-1}, respectively and quenched.

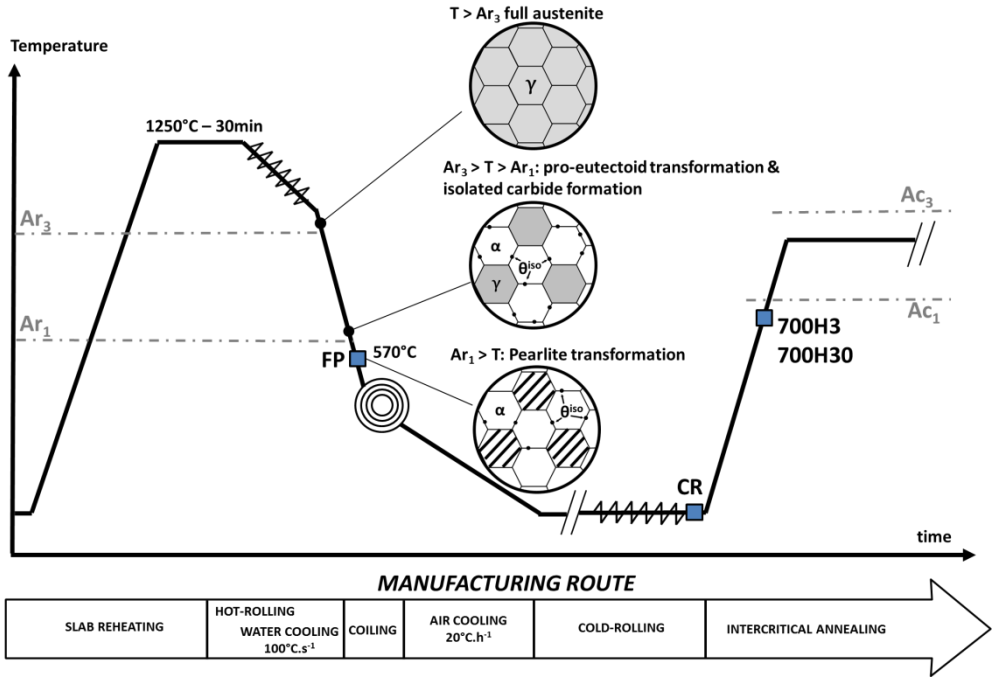

Figure 3.1: Scheme of the DP steel manufacturing route, from the slab re-heating to the end of the intercritical annealing. The blue squares indicate the microstructure states investigated in this chapter.

3.1.2 TEM observations conditions

TEM samples corresponding to the studied states have been prepared according to the process described in Chapter 1. It has been decided to observe carbide microstructures in the ferritic matrix to be able to measure composition gradients outside precipitates, to observe their neighborhood and to detect their possible localization in a Mn segregated band. The technique of extractive replicas has not been used accordingly.

This choice however could lead to biases. In fact, to perform reliable EDXS measurements, the height of studied cementite lamella or particle must exceed the thickness of thin foil. The latter was verified by Electron Energy Loss Spectroscopy (EELS). The measurements were carried out on the areas bordering the central hole of the thin foils to minimize the matrix thickness. In this manner, electronic beam surely goes through cementite only. If not, the measurement can be affected by the presence of ferrite above or below the cementite particle and thus lead to underestimated manganese enrichment in cementite. Moreover, it is not possible to guaranty that the interfaces of cementite lamellae are always strictly parallel to the incident beam. Measurements close to the interfaces must thus be considered with care as the slightly tilted lamella can also hide the presence of ferrite under the beam. This is the reason why on the composition profiles presented below we will systematically highlight the measurement points that can be affected by such tilting issue.

For each studied state, about 5 particles have been studied in detail (composition profiles). These particles were located in pearlite islands (not isolated at a ferrite grain boundary) to obtain a possible correlation with our thermodynamic prediction (cf. section 2 of this chapter). However, it is not possible to tell with certainty that they are located in a microsegregated band. The studied pearlite colonies were selected close to the hole of the thin foils, in order to minimize the dilution effect. The three results shown in this chapter correspond to representative cases for each step.

To verify the statistical validity of our approach, we have conducted in parallel systematic EDX punctual measurements on a large number of particles. These results are not shown here as they are more

difficult to interpret. In these additional observations, cementite particles are often embedded in the matrix, which biases the measured Mn u-fraction by a dilution effect.

3.1.3 Carbide composition after pearlite transformation (HR sample)

To investigate this particular state, a sample was specially prepared to reproduce as faithfully as possible the conditions under which pearlite is formed. Samples cut down from the industrial products were re-austenitized at 900°C for 30 min to ensure complete cementite dissolution. The specimen was then rapidly cooled (30°C.s^{-1}) to 570°C and maintained 30 min before helium quench. Figure 3.2 is a TEM Bright Field (BF) micrograph representative of the pearlite transformation at about 570°C during the hot-rolling process. Similarly to the SEM micrographs presented in the previous Chapter (HR state), it consists mainly of lamellar pearlite colonies (cementite appears in dark contrast) surrounded by large pro-eutectoïd ferrite grains (bright contrast). Isolated cementite particles are also present on the latter ferrite grain boundaries (black arrows).

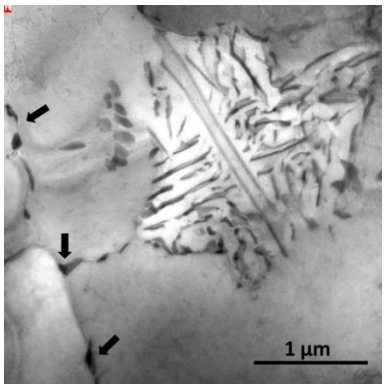

Figure 3.2: BF TEM micrograph of a lamellar pearlite island formed at 570°C. The latter is surrounded by large pro-eutectoid ferrite grains. Intergranular carbides are found along the grain boundaries (indicated by the arrows).

Figure 3.3(a) shows an example of composition measurement inside a cementite lamella. The etching depth difference between the lamella and its matrix is about 25 nm, according to the EELS signal. Investigated lamella appears in dark contrast and the surrounding ferrite in bright. An EDXS profile was obtained thanks to 10 aligned punctual measurements (10 nm step size) and is represented in Figure 3.3(b).

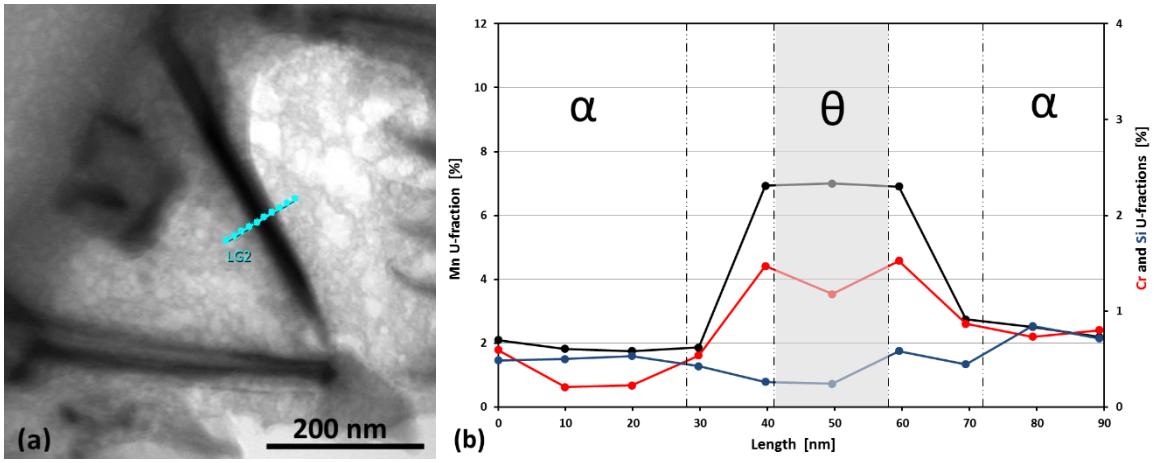

Figure 3.3: (a) TEM BF micrograph of cementite lamella (dark contrast) emerging from the thin foil and its surrounding matrix (bright contrast) in the FP sample. The aligned blue points correspond to the positions of EDXS measurements to establish a composition profile across the carbide and its surrounding matrix.

The composition profile within the cementite lamella is flat and reveals a significant enrichment up to U_{Mn} = 7 %. The Mn composition in the matrix is uniform and similar to the nominal one (U_{Mn} = 1.94 %) meaning that the observed pearlite aggregate is not located inside a Mn microsegregated region. The Cr concentration in the matrix is close to the nominal one, while an enrichment up to U_{Cr} = 1.5 % is observed inside the lamella. On the contrary to Mn and Cr, Si shows a constant profile through the matrix and the lamella, which corresponds to the nominal composition (U_{Si} = 0.41 %).

Our systematic investigations on other adequate configurations confirm systematically Mn enrichment in cementite between 6 and 8%. This result confirms that pearlitic transformation at 570°C in studied steels occurs with a partition of Mn and Cr, in accordance with the works of Al-Salman *et al.* [SAL'79], Chance and Ridley [CHA'81] or Hutchinson [HUT'04].

3.1.4 As received state (CR sample)

As for FP sample, different cementite particles have been studied by TEM with the experimental limitations discussed previously. Figure 3.4 shows for instance a fragment of cementite lamella with a suitable thickness (20 nm thicker than the foil). Therefore, the carbide (clear contrast) arises surely from the matrix. The concentration measurements measured along the blue line are reported in Figure 3.4(b)

Mn concentration in ferrite in the studied field is about U_{Mn} = 4%. This value is significantly higher than the nominal one, meaning that this cementite particle is located in a Mn microsegregated band. In cementite, a U-shape concentration profile of Mn is observed, bringing to light a significant Mn concentration gradient at interface, extended over about 15 nm. This profile reaches a maximum Mn concentration in cementite near U_{Mn} = 10% at interface cementite / ferrite, while a slight depletion is visible in surrounding matrix (only on the right side). A minimum value of U_{Mn} = 6% is observed in the middle of the U-shape profile. Cr concentration in cementite is also not uniform and shows an average value of 0.5%, which is two times higher than the nominal composition. Si seems to be rejected from cementite into the surrounding ferrite (two times higher than the nominal value) as expected from the observations of many authors [OWE'54, MIY'07, JAN'09].

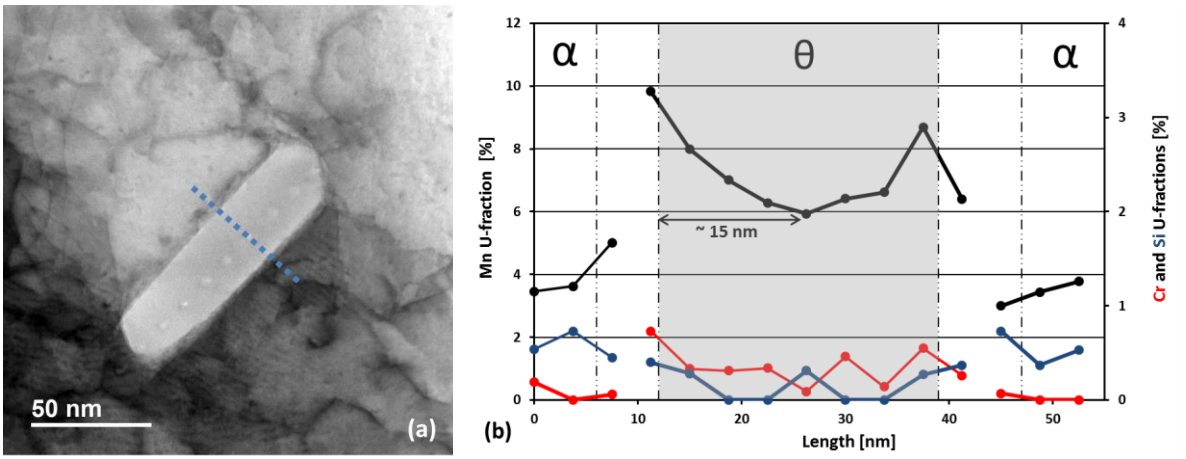

Figure 3.4: (a) TEM BF micrograph of cementite lamella (object with the brightest contrast) emerging from the thin foil and its surrounding matrix in CR sample. The aligned blue points (step size = 5 nm) correspond to the positions of EDXS measurements to establish a composition profile across the carbide and its surrounding matrix. (b) Mn (black), Cr (red) and Si (blue) u-fraction profiles. The areas bounded by the dashed lines indicate spots where the TEM beam could cross simultaneously ferrite and cementite at interface due to a possible tilting issue.

Figure 3.5(a) shows a cementite lamella undergoing a ripening process as its extremity is rounded. This bulging process, as described by Tian and Kraft [TIA'87], is made possible by the coiling operation after hot rolling which corresponds in fact to a long cooling stage after the pearlitic transformation. As for the previous studied cases, the compositions measured along the line in former Figure are reported in Figure 3.5(b) with a step size of 17 nm.

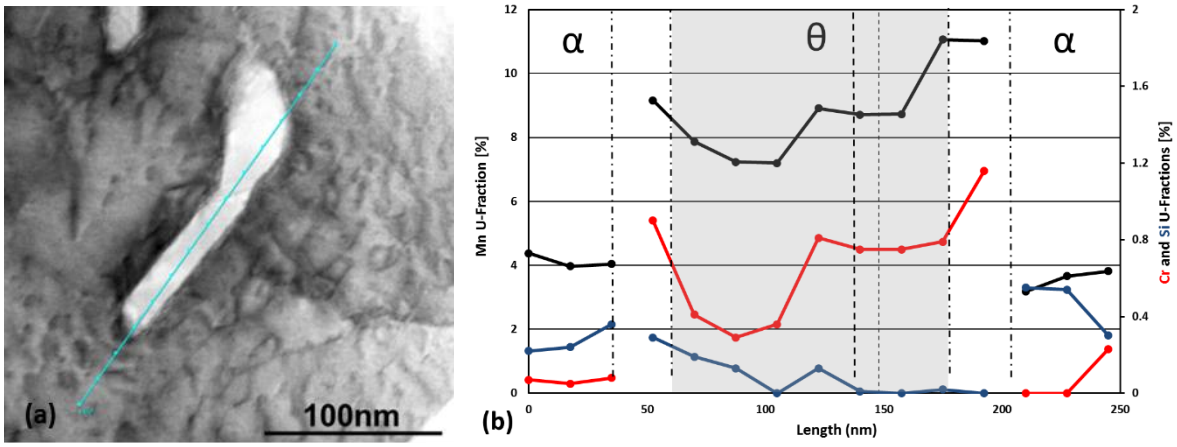

Figure 3.5: (a) TEM BF micrograph of second cementite lamella (dark contrast) emerging from the thin foil and its surrounding matrix (bright contrast) in the CR sample. The aligned blue points (step size = 17 nm) correspond to the positions of EDXS measurements to establish a composition profile across the carbide and its surrounding matrix. (b) Mn (black), Cr (red) and Si (blue) u-fraction profiles. The dashed line indicates the position of the sub-grain separating the straight and the bulged part of the particle. The areas bounded by the dot-dashed lines indicate spots where the TEM beam could cross simultaneously ferrite and cementite at interface due to a possible tilting issue.

The composition profiles also reveal U-shape concentration profiles of Mn and Cr in the straight part of the particle, with a Mn concentration at interface similar to the previous case (cf. Fig. 3.4), close to 10%, but with slightly more extended gradients (about 2 step sizes). At the deepest point of the U-shape profile, the u-fraction of Mn is about 7%, as in the preceding case. The u-fraction of Cr is about 1% at the ferrite / cementite interface and about 0.4% approximatively at the center of the lamella. Si is rejected into the ferritic matrix. In the rounded bulb, a significant enrichment in Mn and Cr is also measured. Mn and Cr concentrations reach 11 and 1.3% at the interface. Therefore, partitioning of substitutional elements is even higher in carbide undergoing a ripening process.

When studying other precipitates, we measured concentrations between 6 and 12%. We thus confirmed that Mn and Cr concentrations in cementite continue to increase during coiling, i.e. after pearlite transformation, but at temperature lower than 550°C. Nevertheless, their repartitions are not uniform. U-shape composition profiles are observed, whose gradients are extended over few tens of nm. At the interface, the u-fractions of Mn are close to 12%, whereas in the middle of particles, local compositions remain similar to those observed in the FP sample. During this long cooling stage (20°C.h^{-1}), cementite lamellae undergo also a ripening process (fragmentation and bulging) but this process is limited as pearlitic structures are still mainly lamellar, as shown in Figure 3.5(a) and in Figure 2.11(a).

3.1.5 Heating to 700°C

3.1.5.a Slow heating (700H3 sample)

Subsequent observations have been made on the 700H3 sample, heated slowly (3°C.s^{-1}) to 700°C after hot-rolling and cold-rolling. Figure 3.6 shows a TEM BF micrograph of the microstructure at low magnification. Numerous carbides (dark contrast) can be observed, which are mostly embedded in the ferritic matrix. Compared to Figure 3.2, the morphology of the precipitates has evolved significantly. Cementite lamellae are fragmented and remnants are round-shaped. This observation is consistent with those reported at SEM scale (cf. Fig. 2.13). For more details, please refer to [ALL'15].

To obtain a statistical overview of composition distribution inside spheroidized carbides and matrix, punctual measurements have been performed. Red and blue crosses represent EDXS spots for cementite carbides (isolated and lamellae) and ferrite respectively. Mn measurements are reported in Figure 3.6(b)

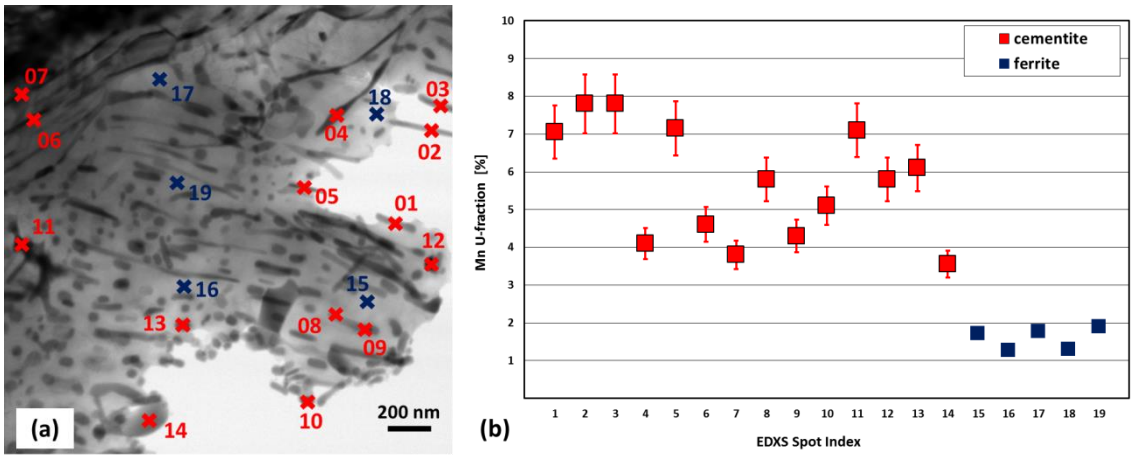

Figure 3.6: (a) TEM BF micrograph of the of the ferrite / pearlite microstructure after heating to 700°C. Carbides appear in dark contrast. (b) Mn (red) measurements corresponding to the spot in (a).

Mn concentrations in ferritic matrix are close to the nominal one, indicating that observed zone is outside a microsegregated band of Mn. However, cementite carbides show a strong enrichment in Mn around 8%, particularly for lamellae outside the matrix (corresponding to spot index 1, 2, 3 and 5). An important scattering of measured values for cementite carbides is noticeable. It can be explained by the fact that cementite carbides are embedded in ferritic matrix, such that EDXS measurements are lowered randomly by dilution effect.

To obtain exploitable and more detailed results, a cementite lamella has been carefully selected, as the one corresponding to spot index 2 in Figure 3.6(a). It is suspended into vacuum by one extremity, hindering dilution effects. Figure 3.7 shows an enlargement of Figure 3.6(a) to observe this particular cementite lamella. Figure 3.7(b) shows the composition measured along the line in Figure 3.7(a) (step size about 5 nm).

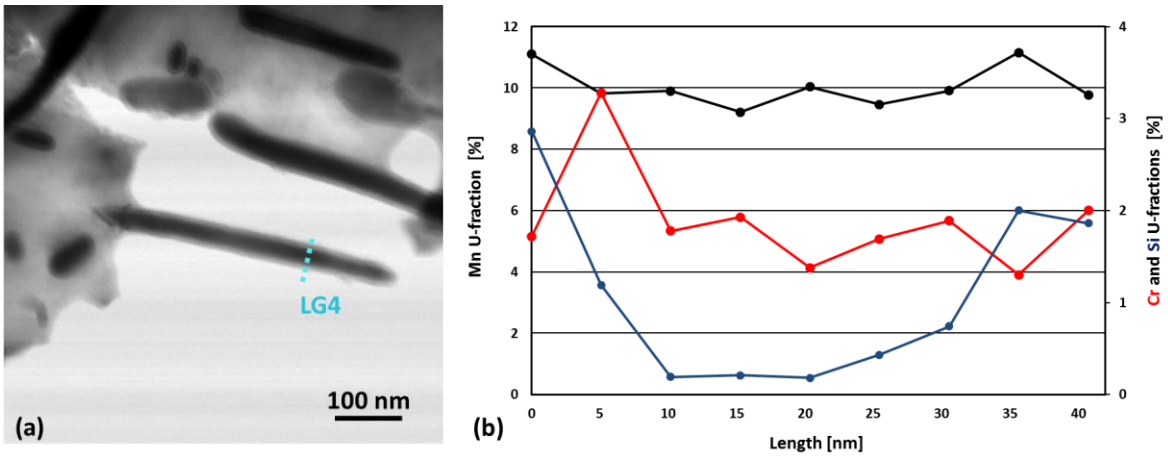

Figure 3.7: (a) TEM BF micrograph of cementite lamella (dark contrast) suspended into vacuum by one extremity emerging in sample 3. The aligned blue points (step size = 5 nm) correspond to the positions of EDXS measurements to establish a composition profile across the carbide and its surrounding matrix. (b) Corresponding Mn (black), Cr (red) and Si (blue) u-fraction profiles.

After heating to 700°C at 3°C.s^{-1} (700H3 sample), Mn and Cr show an important partition up to respectively 11 and 1.8% inside cementite. The obtained profiles are homogenous and flat, indicating that a particular composition has been achieved, likely consistent according to thermodynamical conditions within this temperature range. The compositions remain unchanged in the matrix.

3.1.5.b Fast heating (700H30 sample)

About 15 cementite particles were investigated for this condition. Figure 3.8(a) shows one of the best studied configurations. A long lamella (1.2 µm and 30 nm thick) is localized at the vicinity of the hole and exceeds the foil thickness by 15 nm (EELS measurement). The lamella edges are not straight in comparison with the previous samples and reveal successive spheroidized portions. Fragmentation process has presumably started but remains unachieved due to the fast heating.

Figure 3.8(b) shows the solute profiles across the lamella (20 spots) and in the surrounding matrix. The Mn profile (black curve) is flat and remains close to U_{Mn}=7%. There is no sharp composition gap between cementite and ferrite at the interfaces, but it may arise from the position of the EDXS spots, not sufficiently close to the α/θ interface to reflect possible higher interfacial concentrations. The left side matrix shows high concentration (more than 4%) instead of the expected depletion. On the right side, the Mn composition decreases before reaching a value equivalent to the nominal one (U_{Mn}=1.94%). At both sides, the rounded edges seem to contain less Mn (ca. U_{Mn}=5%) than in the bulk lamella. This is possibly due to tilting issues (the lamella may be inclined). Cr is also found in higher concentration within cementite but remains lower than 0.9%. In the matrix, its concentration is close to the nominal one (U_{Cr}=0.2%). Dealing with Si, the profile is homogeneous in ferrite and cementite and remains comparable to the nominal concentration (U_{Si}=0.41%).

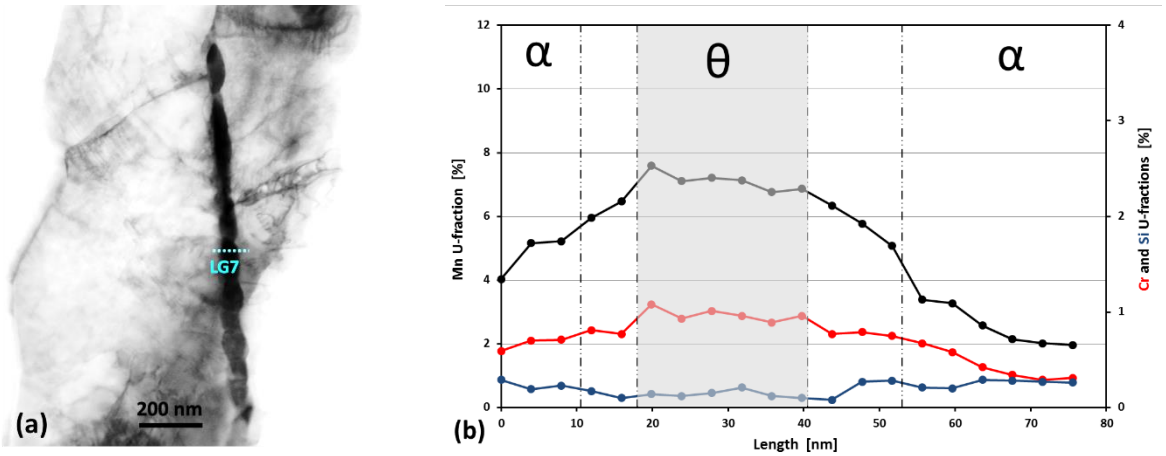

Figure 3.8: (a) TEM BF micrograph of cementite lamella (dark contrast) localized in the vicinity of the thin foil hole in sample 700H30. The aligned blue points (step size = 4 nm) correspond to the positions of EDXS measurements to establish a composition profile across the carbide and its surrounding matrix. (b) Corresponding Mn (black), Cr (red) and Si (blue) u-fraction profiles.

A second example supports the aforementioned measurements. Figure 3.9(a) shows another lamella very close to the hole and surrounded by a thin layer of ferrite. The Mn profile shows a slight U-shape profile inside the lamella, where the composition is close to U_{Mn}=7% in the middle and reaches 9% near the interfaces. Again, the positions of the measuring spots possibly not permit to reflect the possible higher concentrations at the α/θ interfaces. Cr has a linear profile where the mean value is U_{Cr}=1.3%. Si is also homogeneous and remains equal to the nominal composition, i.e. U_{Si}=0.41%

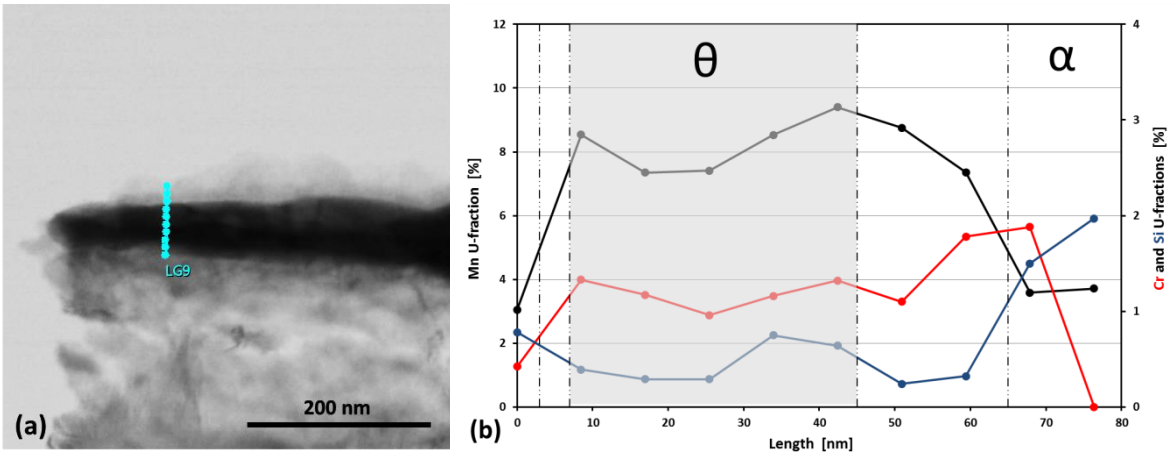

Figure 3.9: (a) TEM BF micrograph of cementite lamella (dark contrast) localized in the vicinity of the thin foil hole in sample 700H30. The aligned blue points (step size = 8.5 nm) correspond to the positions of EDXS measurements to establish a composition profile across the carbide and its surrounding matrix. (b) Corresponding Mn (black), Cr (red) and Si (blue) u-fraction profiles.

3.1.6 Intermediate conclusion

The experiments reveal that pearlite transformation at 570°C in the studied steel (FP sample) occurred with a noticeable partition of Mn between ferrite and cementite. The homogenous concentration in Mn is about 7% in cementite. In contrast, Si concentration remains uniform through cementite and matrix and corresponds to the nominal value. During coiling, i.e. the slow cooling down to room

temperature (20°C.h^{-1}, CR sample), the Mn bulk composition of cementite does not evolve, but strong gradients, about 10-30 nm wide are found at interfaces with interfacial concentration at about 11%. The initial partition due to the transformation condition is thus reinforced during coiling by diffusion. However, the observed composition gradients are the proof that cementite is far from being at equilibrium in the CR state. This enrichment prior annealing is often neglected in most of the studies dedicated to the annealing of ferrite-cementite microstructures. After slow heating at 700°C (sample 700H3), Mn seems more homogenously distributed in cementite with an average composition of about 10%. In contrast, fast heating (700H30 sample) reduces the time which enables diffusion of the substitutional solutes, whose composition profiles remain similar to that measured on the CR sample.

In the following part, thermo-chemical and diffusion analysis will be thus performed to interpret the above EDXS measurements.

3.2 Discussion and modeling

This discussion will be divided into two parts. In the first part, the combined findings of Hillert and Pandit *et al.* [HIL'82, PAN'11] are rationalized in order to predict thermodynamically the composition of the pearlite's constituents and thus explain the measured compositions inside cementite in the as-transformed state (FP sample). To our knowledge, we are the first to bring experimental evidence of the validity of such a thermodynamical prediction for hypoeutectoid steels in anisothermal condition. In the second part, the composition evolution in cementite during coiling and annealing will be modeled with DICTRA software, in order to explain composition gradients in the CR sample and in annealed samples (700H3 and 700H30, respectively). This work has required reassessing the standard Mn diffusion coefficient of the commercial MOBFE2 database. Coupling the model for phase transformation and diffusion calculations thus permits to predict the local Mn composition field in cementite particles all along steel manufacturing.

3.2.1 Manganese partition during pearlite transformation

3.2.1.a Pro-eutectoid transformation prior formation of pearlite

The ferrite-pearlite microstructure obtained after hot-rolling is the product of a two-step decomposition of austenite. The pro-eutectoid ferrite transformation occurs first in recrystallized austenite. The pro-eutectoid transformation temperature in the studied steel has been measured using a dilatometer around 685°C for the studied cooling condition (20°C.s^{-1}) (neglecting possible interactions with austenite deformation). This temperature is far below the NPLE (negligible partitioning local equilibrium)/PE (Para Equilibrium) transition temperature determined by Zurob around 825°C [ZUR'08]. Ferrite transformation in the studied steel occurs thus under para-equilibrium conditions, in accordance also with the work of Chen *et al.* [CHN'16]. It thus means that the substitutional solute composition of untransformed austenite remains constant during ferritic pro-eutectoid transformation. Only its carbon concentration increases progressively. It is generally admitted that the pearlitic transformation then occurs when the carbon concentration is high enough, i.e. when the local composition in untransformed austenite reaches the extrapolated Acm boundary below the eutectoid point. This criterion, named Hultgren criterion, permits to determine the pearlite transformation start temperature and is detailed in the following.

3.2.1.b Pearlitic transformation temperature

In a first approach, the "TACSI" software, developed by ArcelorMittal [IUG'03, PER'05] was employed to calculate this transformation condition in industrial conditions.

TACSI is an in-house software developed by ArcelorMittal for intelligent manufacturing, able to simulate the phase transformations occurring during hot-rolling of conventional high strength steels, considering complex thermomechanical schedules. The predicted microstructures (phases, size, precipitation state …) then serve to predict the mechanical properties of the steels using micromechanical approaches. When linked to sensors on industrial plants, TACSI is used to drive the industrial production and is able to predict the local mechanical properties on coils. The model is thus calibrated on large industrial and laboratory databases.

The theoretical background of TACSI is briefly detailed here. In the phase transformation model, the ferrite and pearlite transformations occur in two successive steps. First, the ferrite transformation is calculated thanks to a physically based nucleation and growth approach. The Classical Nucleation Theory [ENO'86a, ENO'86b, ENO'86c] is used to compute nucleation flux considering nuclei with pillbox shapes. The model is essentially based on the original work of Tanaka *et al*. [TAN'95]. Ferrite growth is governed by a mixed-mode model (cf. Chapter 5). The progress of the ferrite transformation permits to calculate mean carbon enrichment in remaining austenite. The assumption is thus made that the pearlite transformation is triggered when the carbon concentration of remaining austenite exceeds a modified Hultgren criterion calibrated on a large database. When this criterion is reached, ferrite transformation is inhibited. For studied steels and cooling conditions, it has been established that pearlite transformation starts at 570°C.

This value has been confirmed by analyzing the interlamellar spacing in the as-received state using the procedure detailed in Chapter 2 (cf. section 2.1.1.c). The mean interlamellar spacing measured by the planar intercept method is 48 nm. After stereological correction and accounting for the cold-rolling ratio, the true interlamellar spacing is about 82 nm after transformation. The upper Ae_1 temperature of the studied steel is 682°C according THERMOCALC (TCFE9 database). Inverting Marder's relationship [MAR'75] gives then a transformation temperature of 585°C, very close to the predicted one.

3.2.1.c Hultgren criterion and austenite carbon composition

Knowing the pearlite transformation temperature, the carbon composition of austenite is deduced using the Hultgren extrapolation of the A_{cm} line to avoid the use of TACSI, alternative solutions exists as the empirical equation giving the Acm temperature as function of the composition proposed by Lee *et al.* [LEE'14] :

$$\begin{aligned} A_{cm}(°C) = \; & 297.5 + 655C\,(1 - 0.205C) \\ & + 13.3Mn - 13.3Ni\,(1 - 0.06Ni) \\ & + 6.5Mo - 16.6Cu + 79.8Cr\,(1 + 0.055Cr) \\ & - C\,(4.7Mn - 25.6Si - 9.6Ni + 36.7Cr - 8.7\,Cu) \end{aligned} \tag{3.1}$$

where the compositions are given in %weight.

The carbon composition of the austenite which is transformed into pearlite is predictable from the new calculated Acm phase boundary at 570°C, as illustrated in Figure 3.10. A carbon composition of $1.78\%_{at}$ is found ($\approx 0.39\ \%_{wt}$). The application of the lever rule yields a theoretical pearlite fraction of $25\%_{vol}$, which is consistent with our experimental observations (16% considering only well delimited pearlite islands), bearing in mind that isolated carbides present in the microstructure are not taken into account and represent a large fraction of cementite.

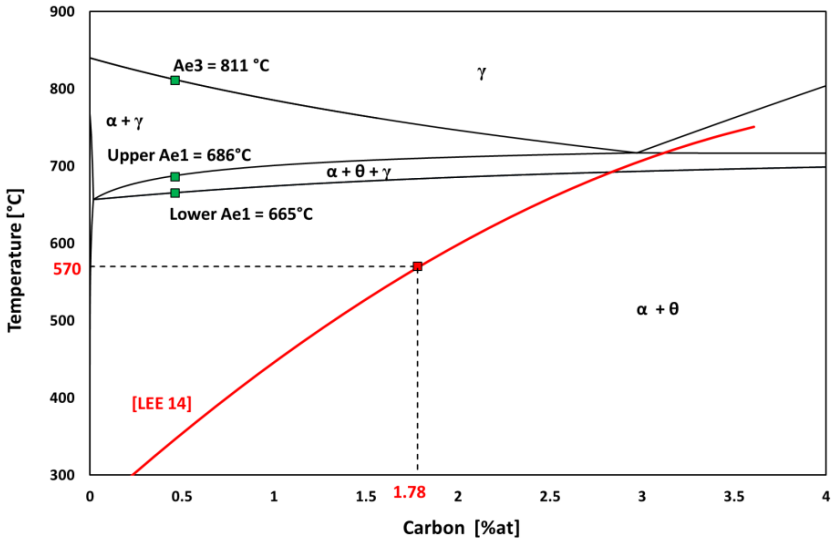

Figure 3.10: Isopleth diagram of DP600 alloy, for the full nominal composition (TCFE9 Database). The red continuous line is the A_{cm} phase boundary calculated from the relation established by [LEE'14]. The green dots indicate the temperature of interests relative to the alloy nominal composition (X_C=0.46%$_{at}$).

3.2.1.d Interface conditions for pearlite transformation

The pearlite transformation in austenite at the A_{cm} point involves two phases growing in a cooperative manner and sharing a common front with the remaining austenite. Since the substitutional species diffuse far slower than carbon, the growth mode of pearlite could induce or not a partition of alloying elements between ferrite and cementite.

Early studies of Razik *et al.* on Fe-C-Mn and Fe-C-Cr [RAZ'74, RAZ'76] steels claim that below about 650°C, no partition is observed. However, the comparisons of experimental growth kinetics with those calculated from the former assumption are in complete disagreement. Al-Salman *et al.* [SAL'79] observed manganese partitioning in Fe-C-Mn-Cr steel at temperatures down to 600°C, but were unable to identify a threshold temperature between growth modes with or without partition. Chance and Ridley [CHA'81] extended this finding by observing partition for temperatures as low as 550°C. The fact that partition was detected at such low temperatures despite of the weak diffusivity of substitutional elements suggested for the first time that diffusion occurred not only by bulk diffusion. An interfacial diffusion must in fact be considered to maintain a local equilibrium at the interface. More recently, Hutchinson [HUT'04] reported again a manganese partitioning in strongly alloyed steels (up to U_{Mn} = 6.8% at 625°C). The experimental results to date from the literature lead to conclude that substitutional elements do partition at any temperature where pearlite is known to grow [PAN'11]. Hillert [HIL'82] developed an interesting framework to estimate the composition of growing cementite and ferrite in ternary alloys, successfully applied by Hutchinson *et al.* [HUT'04]. The approach is based on two important assumptions:

(1) Local Equilibrium (LE) conditions prevail at the two γ / α and γ / θ interfaces

(2) Carbon diffuses much faster than Mn. Therefore, the carbon activity is assumed uniform in the vicinity of the growing fronts as well as in the bulk austenite.

Consistently, it involves that a single carbon iso-activity line passes through the bulk composition and intercepts both γ / α+γ and γ+θ / θ phase boundaries. Figure 3.11 shows the carbon iso-activity line of the austenite bulk composition in an isotherm section of Fe-C-Mn ternary diagram at 570°C calculated with Thermocalc. This black dotted-dashed line passes through the blue dot representing the initial bulk composition. The red and black continuous lines represent respectively the α+γ / γ and γ / γ+θ boundaries.

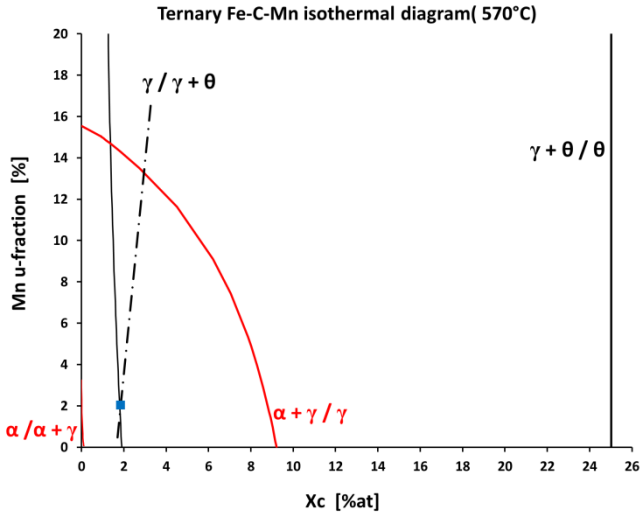

Figure 3.11: Isothermal section of the Fe-C-Mn diagram at 570°C. The dotted-dashed line represents the carbon iso-activity determined from the austenite bulk composition. The two domains delimited by the red and black boundaries represent respectively the α + γ and θ + γ two-phase fields.

The interception of the carbon iso-activity line with the phase boundaries indicates the compositions prevailing at the γ side at the γ / α and the γ / θ interfaces respectively. The corresponding LE tie-lines can then be calculated to deduce the compositions of the growing ferrite and cementite.

For the current study, Thermocalc calculations give in austenite U_{Mn} = 13.3 % at the α / γ interface and U_{Mn} = 1.6 % at the θ / γ interface. The two corresponding configurations are represented separately in Figures 3.12(a) and b (for α and θ, respectively). In both cases, the dotted-dashed line still represents the carbon iso-activity line and the dashed lines represent operating tie-lines at θ / γ and α / γ interface respectively. For the studied configuration, the Mn composition predicted in cementite and ferrite are U_{Mn} = 6.05 and 2.33 %, respectively.

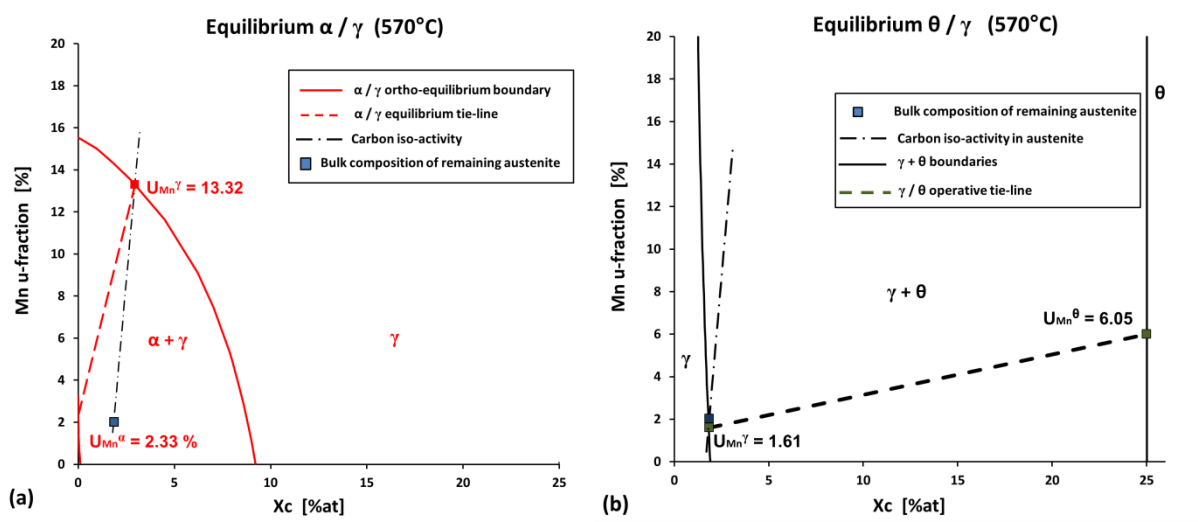

Figure 3.12: Isothermal section of equilibrium Fe-C-Mn diagram for (a) θ / γ and (b) α / γ metastable equilibrium. The dotted dashed line is the carbon iso-activity line that is used to find the composition of austenite, cementite and ferrite at the θ / γ and α / γ interfaces. It enables the calculation of the effective tie-lines relative to each equilibrium and thus to deduce the Mn compositions of the growing phases.

The predicted Mn compositions of cementite and ferrite (respectively U_{Mn} = 6.05 and 2.33%) are in excellent agreement with TEM measurements of FP sample (U_{Mn}= 6.6 and 1.90 %), supporting the assumption of a partitioned growth of pearlite with local specific equilibria at γ/α and γ/θ interfaces. One emphasizes that the composition in cementite would be significantly different if an equilibrium α / θ had been considered at 570°C (U_{Mn} = 19 %).

However, the previous thermodynamic prediction does not satisfy *a priori* the Mn solute molar balance, such that:

$$f_M^\theta . X_{Mn}^\theta + f_M^\alpha . X_{Mn}^\alpha = X_{Mn}^0 \qquad (3.2)$$

where X_{Mn}^0 is the nominal atomic Mn composition of γ. X_{Mn}^θ and X_{Mn}^α are the atomic Mn compositions of cementite and ferrite respectively, determinated with the latter approach. f_M^θ , f_M^α are the molar fractions of cementite and ferrite respectively. At 570°C, assuming a nominal atomic carbon composition X_c = 1.78 % (0.39%$_{wt}$) in austenite at the beginning of the transformation and a negligible content in ferrite, the lever rule imposes a molar fraction of cementite of 7.10 % in pearlite. Therefore, assuming that the Mn compositions inside cementite and ferrite are those determined by the thermodynamic approach, the overall manganese atomic composition (2.46 %) should have been higher than the nominal atomic composition (1.94 %). This purely thermodynamic approach thus does not permit to verify a correct molar balance in the studied case.

This unsatisfactory situation has been avoided by Pandit and Bhadeshia [PAN'11] who in fact recommend first to calculate the γ / θ tie-line from the uniform carbon activity assumption. Once the Mn composition inside cementite is determined, they establish a new tie-line starting from this composition and passing through the bulk composition (It is not an equilibrium tie-line). The corresponding Mn composition inside the growing ferrite is then deduced by extending this tie-line to the α / α + γ phase boundary. Figure 3.13 shows the approximation of Pandit and Bhadeshia [PAN'11] for the current steel. Mn composition in ferrite determined under this approximation is U_{Mn} = 1.80 % which is even closer to our TEM measurement in ferrite. In that case, the solute molar balance is verified.

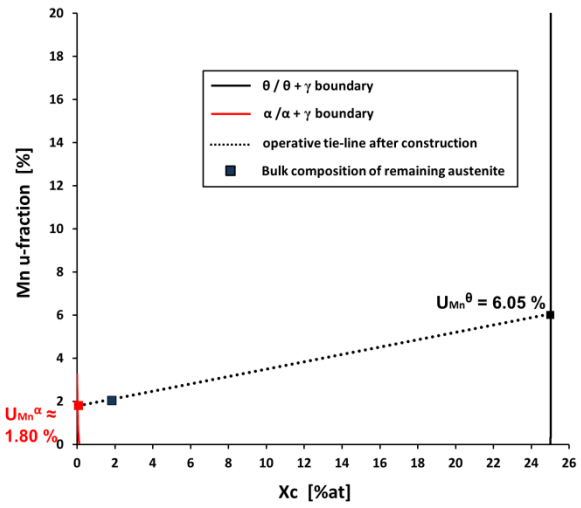

Figure 3.13: Isothermal section of the Fe-C-Mn ternary diagram at 570°C. The α+γ and α+θ two-phase domains are delimited by the red and black continuous lines respectively. The remaining austenite initial composition is represented by the blue dot. The black dotted represents the approximation of Pandit and Bhadeshia [PAN'11].

The proposed thermodynamic approach using the carbon iso-activity is thus a convenient tool for the prediction of the solute composition within pearlite constituents (ferrite and cementite). However, this kind of approach is rarely used, even in the most recent investigations on pearlite. To our knowledge, only Pandit and Bhadeshia [PAN'11] have attempted to apply this reasoning to explain successfully the experimental results of Razik and Ridley. These investigations have been carried out on eutectoid steels in frame of isothermal treatments only. The present work seems to be the first to date to investigate with this model the pearlite transformation conditions after a pro-eutectoid transformation and thus at very low temperature.

As discussed in Chapter 2, the formation of the isolated cementite particles is suspected to occur between 710 and 760°C (cf. Chapter 2, section 2.1.1b). The carbon concentration of austenite varies between 3.9 and 4.1 $\%_{at}$ within this temperature range, according thermodynamic calculations. Reproducing the previous approach predicts a narrow Mn concentration interval in cementite being U_{Mn}^{θ} = 5.10 – 5.5%, i.e. slightly lower than that predicted for the lamellar perlite transformed at 570°C.

3.2.2 Ripening process of cementite during coiling and annealing

3.2.2.a Basic thermodynamic and diffusion analysis

We have seen in the previous sections that the phase compositions inherited from the transformation conditions are far from the local equilibrium conditions (considering the local carbon composition in pearlite X_c = 1.78 $\%_{at}$). The differences are even higher at room temperature (even if the thermodynamic databases at such low temperatures should be considered carefully). The equilibrium composition in Mn and Cr at room temperature in cementite are U_{Mn} = 36% and U_{Cr} = 4%. The measurements of the CR sample are far lower revealing that the diffusivities of substitutional solutes are too low below coiling temperature range to obtain a uniform equilibrium composition profile through cementite. As central composition of cementite has not evolved, it means that substitutional solutes had even not the time to diffuse from the interfaces to the middle of cementite particles. Composition gradients from interfaces are thus observed over a limited distance (about 15-30 nm).

Mn composition profile measured in cementite after slow heating up to 700°C (700H3) are almost flat and the constant value (about U_{Mn} = 10.0% in the CR sample) is approaching the equilibrium composition (U_{Mn} = 13.36%). It leads to the conclusion that, during heating, above a certain temperature, the Mn diffusivity is sufficient to permit the homogenization of Mn close to the equilibrium composition within a short period of time. Cr equilibrium composition (U_{Cr} = 2.7%) is nevertheless not reached, as 1.7% is measured in the cementite in the 700H3 sample owing to a lower diffusivity. Similar observations were reported by Baltazar *et al.* [BAL'11] or by Phillipot *et al.* [PHI'15] who studied the Mn enrichment in cementite after heating up to 700°C at 1°C.s^{-1} of a 0.37C-2.53Mn steel (%weight). They measured Mn concentration in cementite by atom probe tomography close to 11 $\%_{wt}$ (U_{Mn} = 12%) in good agreement with our own observations. As in the studied case, Cr does not reach equilibrium after heating. On the contrary, the solute profiles measured after fast heating remain analogous to that measured on the CR sample. It evidences that rapid heating does not permit the solute to diffuse out and modify the cementite composition.

Mn diffusion lengths in cementite for both cooling from 570°C down to room temperature at 20°C.h^{-1} and heating up to 700°C at 3°C.s^{-1} were estimated using the sole diffusion coefficient of Mn in cementite found in literature. D^{θ}_{Mn} has been extracted from the MOBFE2 and TCFE9 databases of DICTRA and Thermocalc. For the sake of simplicity, isothermal holdings at 570°C and 700°C, during t = 24 h and t = 200 s were considered to estimate a first order upper value of $\sqrt{Dt}$. In both cases, diffusion lengths did not exceed 2 nm. This is far lower than our observations (about 15-30 nm in the first case and larger than cementite half width in the second case).

Since D^{θ}_{Mn} provided by DICTRA software is obviously too weak, it must be reassessed, as did e.g. Song [SON'14]. This author proposes to multiply D^{θ}_{Mn} by 5 in order to better calibrate its own experiments. Luo *et al.* also [LUO'16] needed to multiply it by 72 to make its DICTRA simulations consistent with their own experimental data. More recently, a deeper investigation was performed by Wu *et al.* [WU'18] on cementite coarsening in a wide range of Fe-C-Mn alloys, whose one is equivalent to the current studied steel. Numerous Mn composition profiles were measured by TEM inside cementite for temperatures ranged between 400 and 600°C. They established a new diffusion coefficient of Mn within cementite, being roughly equivalent to 7500 times the standard coefficient of DICTRA. In the present study, we also need to reassess D^{θ}_{Mn} on the basis of our own experimental results. These diffusion coefficients are compared and discussed in Appendix. As done by Luo, simulations of Mn diffusion in pearlite will be conducted using the DICTRA software.

3.2.2.b DICTRA Simulations

A model ternary Fe-C-Mn system is considered for the phase transformation calculations with DICTRA software (2017a version, TCFE9 and MOBFE2 databases). Our equilibrium calculations have shown that other alloying elements (Si and Cr) do not affect significantly the chemical compositions of the phases and transformation temperatures. For this reason, the following DICTRA simulations do not deal with the latter species.

A planar configuration representing a lamellar pearlite structure (half ferrite lamella in contact with a half cementite lamella) has been considered for the sake of simplicity, even if our observations are not all obtained in such simple geometrical configurations. Half-lamellar spacing and lamella thickness have been set respectively to 340 and 20 nm in accordance with our observations. The considered volumes are consistent with equilibrium calculations at 570°C (94.2 and 5.8 $\%_{vol}$ of ferrite and cementite respectively).

Three successive thermal treatments have been simulated. The first one corresponds to the cooling treatment (composition evolution from FP to CR sample). Initial Mn concentrations profiles in cementite and ferrite for coiling simulation have been considered uniform and set to U_{Mn} = 6.25% in cementite and U_{Mn} = 1.70% in ferrite, as observed experimentally in the FP sample (cf. Fig. 3.3(b)). The second and third one corresponds to the slow (3°C.s^{-1}) and the fast (30°C.s^{-1}) heating to 700°C (corresponding 700H3 or 700H30 samples). Phase and composition fields resulting from the first simulated treatment are used as initial conditions for these latter heating simulations by a field transfer in DICTRA.

Modeling space is discretized using unidimensional grids. 50 grid nodes have been distributed in both ferrite and cementite following a geometrical progression in both phases with ratio 0.98 and 1.02 respectively, in order to get a finer mesh near α/θ interface. Both time and spatial discretization have to be optimized in order to reduce computation time without losing accuracy. Inappropriate simulation parameters could induce a significant decrease of the overall Mn concentration in the system. One points out that of curvature effects (Gibbs Thompson), morphological evolutions or interaction between particles (coarsening) were disregarded in our simulations. These contributions could be nonetheless taken into account to explain the significantly higher compositions measured inside the spheroidized extremity of the lamella shown in Figure 3.5. However, such a deeper investigation lies beyond the scope of this PhD.

The activation energies and the pre-exponential factors calculated with DICTRA for ferrite and cementite are summarized in Table 3.A. To obtain these values, the composition of the austenite at 570°C have been considered (X_c = 1.78%$_{at}$, U_{MN} = 1.94%). In the case of ferrite, both parameters vary significantly with the temperature. An Arrhenius plot was drawn from data tabulated from Thermocalc to deduce the values shown in Table 3.A.

	Pre-exponential factor	Q (kJ.mol^{-1})
Cementite θ	1.05 x 10^{-5}	286.0
Ferrite α	0.127	272.2

Table 3.A: pre-exponential factor and activation energies of the Mn diffusion coefficient in cementite and ferrite, respectively.

Mn diffusion coefficient in cementite has been adjusted to best reproduce our experimental observations. In this procedure, only pre-exponential term has been modified so far (not the activation energy) and multiplied by 2000. This value is consistent with Luo and Wu [LUO'16, WU'18]. Mn diffusion coefficient in ferrite has been taken from the database and has not been modified, since it is considered well validated.

3.2.2.c Simulation results

Figure 3.14 shows the composition profiles simulated in pearlite during coiling (a) and annealing at low (b) and high rates (c) respectively. The simulated profiles are systematically compared to the corresponding experimental measurements. For simulated annealing, the expected equilibrium Mn composition at 700°C (considering Fe-C-Mn alloy) is represented by a dotted line. It corresponds to the partition expected in the sole pearlite sub-system.

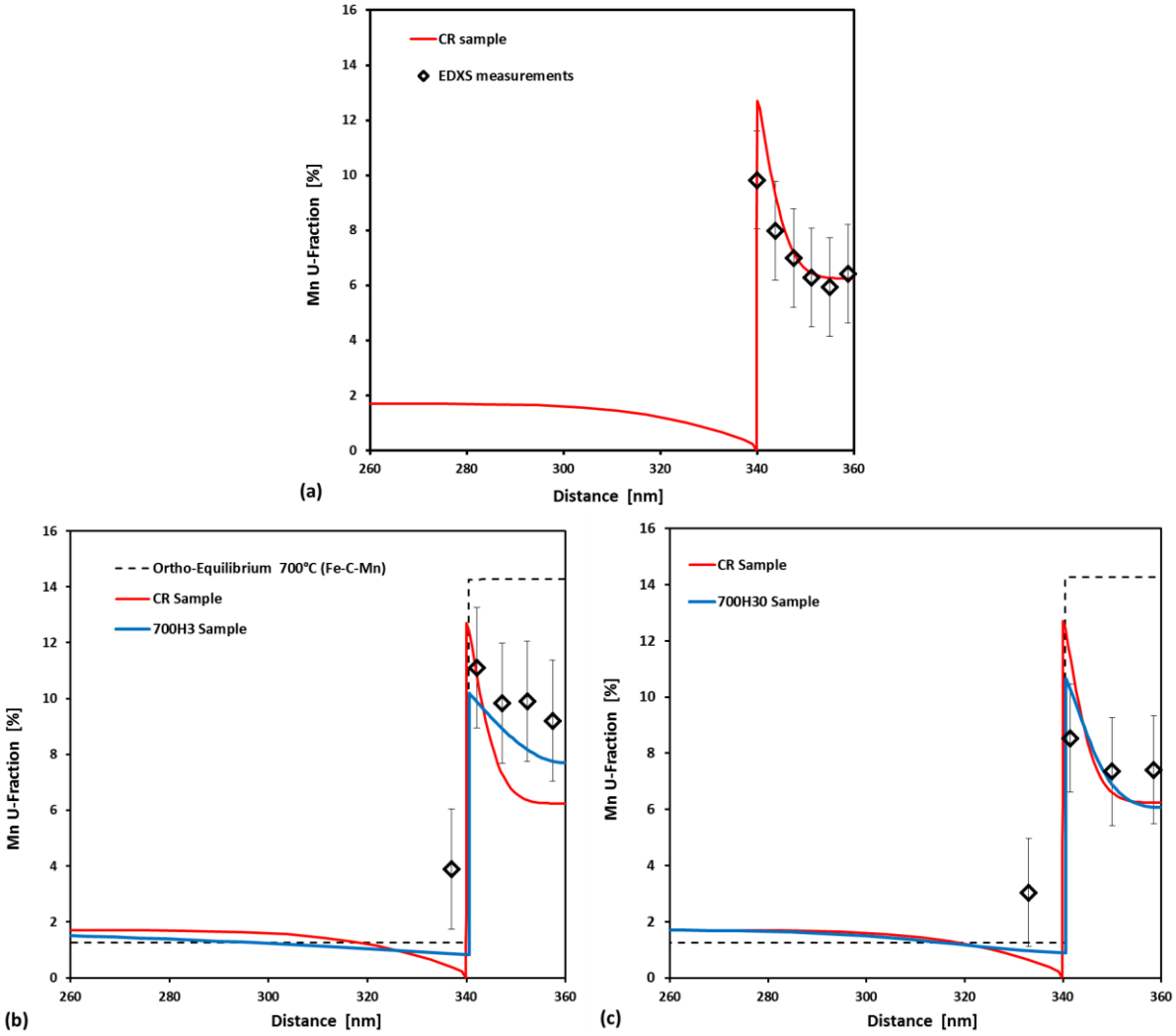

Figure 3.14: Comparison between the DICTRA simulations of the various thermal cycles with the compositions measured by TEM. Simulated profiles are reported by the blue lines. The continuous red line indicates the initial composition profile at the onset of the simulations. The dots reflect the experimental measurements. (a) Cooling from 570°C down to room temperature at 20°C.h^{-1}. The experimental measurements are those reported in Fig. 3.4(b). (b) Slow heating (3°C.s^{-1}) to 700°C. The measurements correspond to that Fig. 3.7(b). (c) Fast heating (30°C.s^{-1}) to 700°C, compared with the profile shown in Fig.3.9(b).

It should first be emphasized that in all cases, interface remains fixed during the inter-diffusion process as carbon solubility in ferrite and in pearlite does not vary much with temperature. In Figure 3.14(a), the composition profile shows a steep gradient in cementite at the interface (extended over about 15 nm) whereas the middle of the cementite particle is not enriched (still at 6.25%). Mn interfacial composition predicted by DICTRA is U_{Mn} = 12.7 %, that is far lower than that equilibrium composition expected at room temperature ($U_{Mn} \approx 36\%$) consistently with the low Mn diffusivity in this temperature range (T < 570°C). The Mn composition profile inside ferrite shows a depletion over 40 nm from the interface, similarly to the TEM measurements, except that particle studied in the CR sample is located in a Mn microsegregated band (cf. Fig. 3.4 and 3.5), involving a Mn concentration twice higher ($U_{Mn} \approx 4\%$). It is the reason why the experimental Mn profile is higher than the simulated one in the ferrite matrix. Hence, calibrating Mn diffusion coefficient in cementite has permitted to reproduce consistently our experimental observations.

The reliability of our reassessment was confirmed by simulating the composition evolution in cementite during reheating to 700°C. Figure 3.14(b) shows that the calculated profile after slow heating is far flatter than after coiling. Low calculated composition gradients are in excellent agreement with our experimental observations. Only interface compositions are slightly lower than observed experimental values. The Mn profile is not affected after fast heating, as shown in Figure 3.14(c). The Mn composition profile obtained after fast heating is very similar to that found in the simulated coiling. The U-shape profile is preserved; the concentration in the middle of the lamella is barely changed while the interfacial composition is slightly decreased. The agreement with experiment is however less good than in the case of the slow heating rate.

Our DICTRA simulations show that it is possible to explain and predict experimental Mn concentration profiles inside cementite during coiling and heating by simple diffusion calculations with local equilibrium at ferrite/cementite interface. When using MOBFE2 and TCFE9 databases, Mn diffusion coefficient in cementite (pre-exponential factor) has to be multiplied by a factor 2000 to obtain consistent composition profiles and gradients. Nevertheless, this rough reassessment considering the sole pre-exponential factor is surely not sufficient for accurate prediction.

3.3 Finite Difference (FD) model

According to industrial practices, a typical annealing schedule takes about 15 minutes. The DICTRA simulations require about 20 min to converge for a complete annealing simulation. The in-line use of DICTRA for phase prediction is thus ludicrous. This is the reason why a Finite Difference model for Mn diffusion in pearlite has been developed and calibrated to predict the observed enrichments. This simplified model aims at reproducing DICTRA results with drastically reduced calculation costs.

3.3.1 FD Model's description

A classical finite difference model for Mn diffusion in lamellar pearlite has thus been developed. The basis has been inspired by the work of Santofimia *et al.* [SAN'08] who investigated the carbon diffusion during partitioning of Q&P steels. Originally, the model accounts for a mobile interface. In present case, the application of the model is easier since the α/θ interface is considered as immobile.

The model is based on four main assumptions:

- Diffusion calculations are restricted to Mn (no interdiffusion, considering an apparent diffusion coefficient) by a simple Fick's law (based on atomic concentrations),
- Mass balances are used to calculate evolution of Mn concentration in cells,
- Local equilibrium is assumed at ferrite/cementite interfaces but operative tie-lines are to be determined by the model,
- Interface mobility is neglected as molar volumes of both phases are hardly affected by their Mn compositions.

The modeling space is divided into cells with a 1D planar configuration similar to the DICTRA simulations. The diffusion is solved by finite difference procedure, as illustrated in Figure 3.15. Each cell i contains a control point at position z_i at which the mean concentration in Mn of the cell $x^k(z_i, t)$ is evaluated at a given instant t. The Mn evolution in each single phase is calculated by a simple mass balance. The accumulation (resp. depletion) of Mn depends on the flux of Mn coming (resp. escaping) from the neighboring cells that is estimated a simple Fick law (flux). Mn concentration in cell i in phase k at $t + dt$ is modeled by Equation (3.3):

$$x^k(z_i, t+dt) = x^k(z_i, t) + r^k\left(x^k(z_{i-1}, t) - 2x^k(z_i, t) + x^k(z_{i+1}, t)\right) \quad (3.3)$$

where x^k is the atomic fraction of the control point of the cell located at position z_i, belonging to the phase k.

A schematic representation of the solving strategy is given in Figure 3.15 with three cells called x_1, x_2, x_3 . It explains how the Mn flux between cells (x_1, x_2) and (x_2, x_3) and the mass balance in cell x_2 are calculated. For the sake of simplicity, it is assumed that at considered instant t, $x_{1,t}(z_1, t) > x_{2,t}(z_2, t) > x_{3,t}(z_3, t)$.

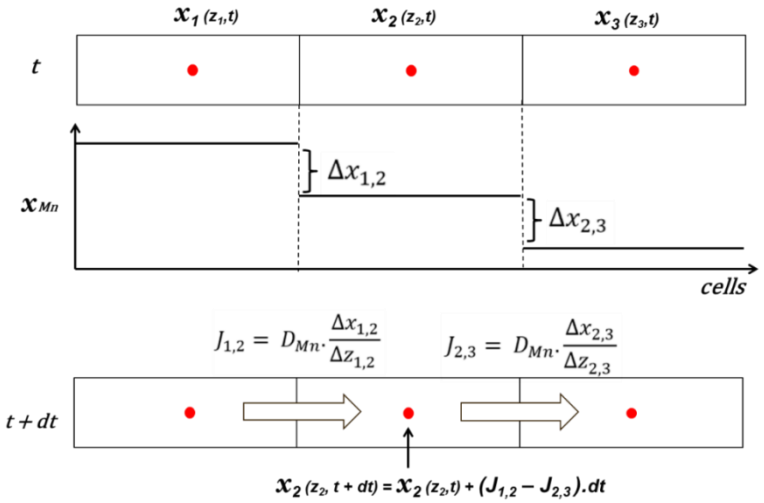

Figure 3.15: Explicit resolution scheme for the diffusion process in the Finite Difference model. Concentration gradients present at instant t produce solute fluxes. In a given cell, the evolution of the mass is related to the difference between incoming/outcoming fluxes.

The solving scheme is thus purely explicit. The parameter r^k, given by Equation (3.4) according to Fick's second law, is set to 0.5. This permits to select spatial and time steps which ensure the stability of the numerical calculation [CRA'75] by limiting the error accumulated after successive iterations.

$$r_k = \frac{D^k \Delta t}{(\Delta z^k)^2} \quad (3.4)$$

Δz^k is the constant spatial step size in the phase k (ferrite or cementite). D^k is the Mn diffusion coefficient of the considered phase. Time is also discretized with a constant time increment Δt.

3.3.2 Interface modeling

In Finite Difference models, an interface must be located at control point, separating the considered cell in two domains, as schematized in Figure 3.16. In the present case, the interface is immobile and lies in a fixed cell which binds ferrite and cementite phases. On both sides of the interface, one domain behaves as ferrite and the other as cementite with thus two different r^k values. The respective manganese compositions in ferrite or cementite domains are called $x_{Mn}^{\alpha,IF}$ and $x_{Mn}^{\theta,IF}$.

Local Equilibrium (LE) is assumed at the interface. Thus, at any instant, $x_{Mn}^{\alpha,IF}$ and $x_{Mn}^{\theta,IF}$ correspond to a given equilibrium tie-line. The tie-lines were tabulated from Thermocalc at different temperatures. For each temperature, an empirical law was calibrated to relate the compositions given by the extremities of the tie-lines. As a first guess, a 5th degree polynomial function was adjusted to reproduce Thermocalc data and giving $x_{Mn}^{\alpha,IF} = f(x_{Mn}^{\theta,IF})$. Empirical laws were calculated for temperatures ranging from 20 to 700°C, with a temperature step of 20°C. A matrix temperature / polynomial coefficients was built with MATLAB to produce an expression which includes the temperature, such that $x_{Mn}^{\alpha,IF} = f(x_{Mn}^{\theta,IF}, T)$.

The LE condition is used to calculate the composition of Mn in ferrite half-cell and a simple mass balance, according the expression (3.5). Thus, a natural gradient is set at the interface, imposing equal fluxes in both phases, as illustrated in Figure 3.16.

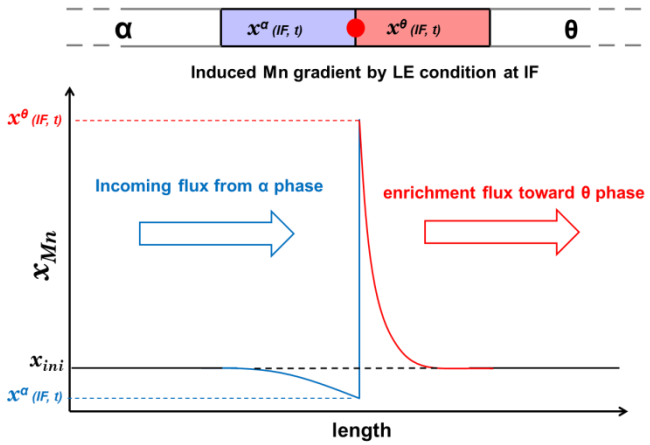

Figure 3.16: Calculation strategy for interface cells. The LE condition is used to calculate the composition of Mn in ferrite half-cell (blue) and a simple mass balance is used to calculate the composition in cementite half-cell (red).

The particular mass balance equation for cementite half-cell is given by Equation (3.5):

$$x^{\theta,IF}(t+dt) = x^{\theta}(t) + r^{\alpha}\left(x^{\alpha}(z_n,t) - x^{\alpha,IF}(t)\right) + r^{\theta}\left(x^{\theta}(z_n,t) - x^{\theta,IF}(t)\right) \quad (3.5)$$

At the first time increment, the composition in ferrite will be imposed by the LE considering nominal Mn values without any gradient in cementite. During the next increments, the flux calculations will naturally lead to Mn enrichment in cementite.

It should be mentioned that this explicit resolution scheme can induce a direct loss of Mn in the calculations during the first time increment. The cause is illustrated in Figure 3.17. In fact, when applying the LE in ferrite and maintaining a constant Mn profile in cementite at very beginning of the calculations, the ferrite half-cell are depleted in Mn without any mass transfer in cementite (case 1) due to the explicit solving scheme. To neutralize this artifact, the amount of Mn lost in ferrite is transferred into cementite at the interface (case 2). This "artificial" transfer is applied only during the first time step dt. It may be applied optionally as the Mn lost during this operation is however limited.

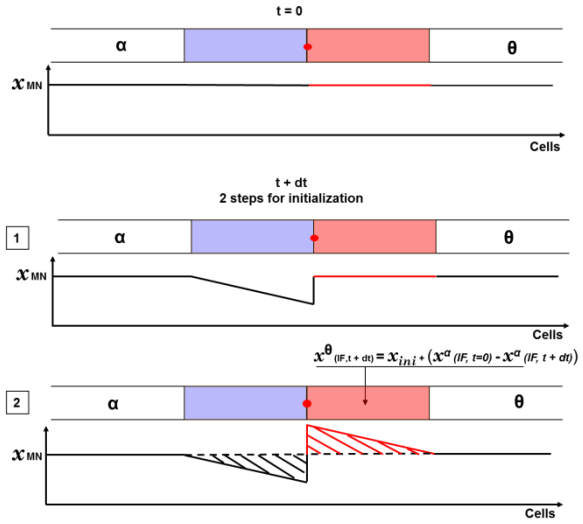

Figure 3.17: Illustration of the Mn loss mechanism for the first time increment. After initialization (no-partition for the reference state), when applying the LE in ferrite and maintaining a constant Mn profile in cementite at very beginning of the calculations, the ferrite half-cells are depleted in Mn without any mass transfer in cementite (case 1). To neutralize this effect, the amount of Mn lost in ferrite is transferred into cementite at the interface (case 2).

This approach permits locally to ensure consistence with local equilibrium conditions and mass balances at the same time (absolute loss of 0.13%, higher than with DICTRA calculations but considered as negligible). The sizes of the cells and calculation conditions have thus been adjusted to obtain the lowest Mn mass loss.

3.3.3 Calibration of the model and initialization of the calculation

The model has been assessed and calibrated taking into account the chemical initial condition considered for DICTRA calculations; flat Mn profile within ferrite and cementite at 1.7 and 4.75 $\%_{at}$ consistently with the U-fractions given in Figure 3.3(b)

For the calibration, i.e. the determination of reliable spatial and time steps, simple isothermal calculations were carried out (isothermal treatments during 200s at 700°C). Same geometrical configurations have been considered. Namely the considered interlamellar spacing and lamella half-thickness were set to 340 and 20nm, respectively. The Mn diffusion coefficient in ferrite and cementite are those calculated by DICTRA, presented in Table 3.A after optimization for current alloy composition (considering a simplified Fick's law).

Many conditions have been tested until equilibrium is completed at the end of the isothermal treatment at 700°C. After investigations, a spatial step of 1 nm and a time step of 5.10^{-3} s have been set in order to obtain the lowest mass loss of Mn. Smaller time step leads to higher time consuming calculations, whereas higher spatial step increases the mass loss of Mn.

3.3.4 Results

Figure 3.18 represents the Mn concentration profile obtained using the FD model after reproducing the annealing simulations. The diffusion coefficient has been multiplied by 2000, consistently with the calibration carried out during the DICTRA analyses. The FD model reveals to be in excellent agreement with both DICTRA simulations, since obtained profiles are very similar. The mass loss detected is inferior to 0.13 $\%_{at}$ relative to the nominal composition, which is less than expected.

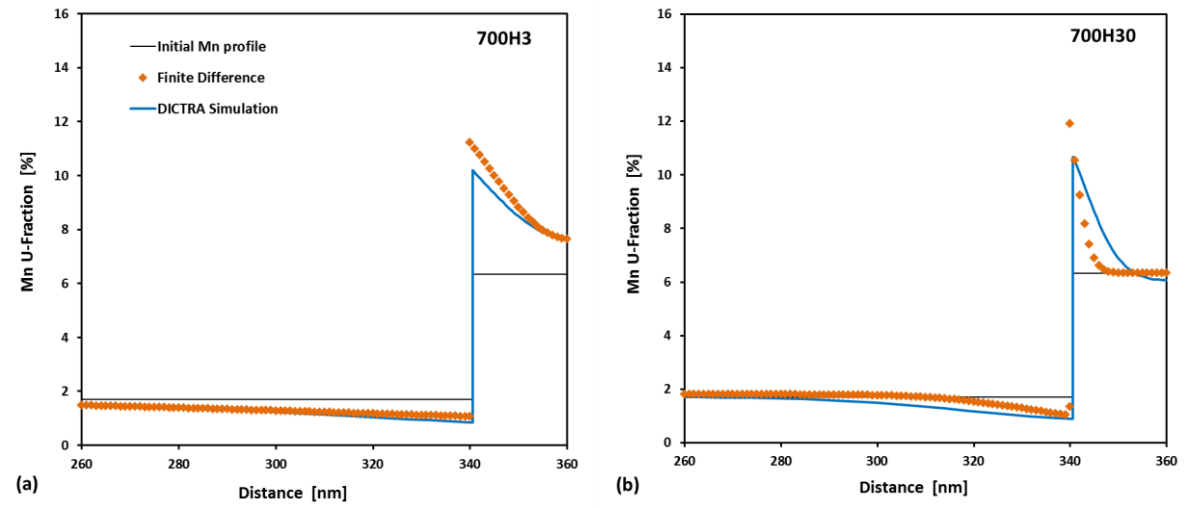

Figure 3.18: Comparison of the Mn concentration profiles calculated with the FD model with the previous DICTRA simulations (see Fig 3.14.b and c) for a heating from room temperature to 700°C. The black profile shows the initial concentration profile introduced in the VF model. Blue lines and orange dots represent the DICTRA simulations and the results of the FD model, respectively: (a) after slow (3°C.s^{-1}) and (b) fast heating (30°C.s^{-1}).

3.3.5 Discussions

The FD model reproduces faithfully the DICTRA simulations in term of kinetics and final states for after slow and fast heating treatments to 700°C, even though the initial gradients obtained after slow cooling were not introduced. To achieve the reproduction of the profiles acquired with DICTRA, the same multiplying factor was employed (2000).

In conclusion, the FD model offers a good alternative relative to DICTRA simulations. It enables quick calculations (~ 2 s with an excel macro) and is easier to configure. The implementation in a suitable language for intensive calculations (FORTRAN) should permit to obtain very short CPU times.

Indeed, using DICTRA, a lot of settings must be investigated (accuracy of calculation's algorithms, number of grid points, etc.) before to obtain reliable simulations. In current state, only equilibrium tie-lines obtained using Thermocalc and diffusion's coefficient of Mn in ferrite and cementite from MOBFE2 database were needed to run the FD model. Of course, it remains valid as long as the modeled system has a simple geometry with immobile interfaces and that only one alloy component is investigated.

3.4 Conclusion

The Mn enrichment of cementite throughout the manufacturing route was surveyed by TEM from the pearlite transformation at 570°C occurring just before coiling process from the heating to 700°C, just below the Ac_1 temperature:

- During pearlite transformation at 570°C, the cementite is found to have an initial homogeneous composition U_{Mn}=6.5%. A thermodynamic analysis assuming LE compositions at the θ/γ interface during the growth agrees very satisfyingly with the latter measurements.

- Along the slow air cooling which follows to room temperature, Mn has sufficient time to partition further inside cementite. The TEM investigations explicitly highlighted the diffusion of Mn from ferrite to cementite. Depletions over 40 nm were observed in ferrite in contact with the cementite lamellae. High concentrations (around U_{Mn}=12%) are generated at the α/θ interfaces, consistently with the LE compositions excepted within this low temperature range. However, the sluggish Mn diffusivity does not permit to establish a homogeneous flat profile. Sharp gradients were found over 15 nm, from the interface to the middle of the lamella, where the Mn composition remained comparable to that measured after pearlite formation.

- Slow heating (3°C.s^{-1}) from room temperature to 700°C permitted to achieve a flat Mn profile inside cementite, being remarkably consistent with the ortho-equilibrium composition at 700°C, calculated for the full alloy chemistry.

- Fast heating, on the contrary, does not let time to Mn for further partition. The measured profiles do not show any evolution relative to that measured after pearlite formation at room temperature (cooling succeeding the coiling process). The Mn profiles examined by TEM remains relatively flat around U_{Mn}=7% while the interfacial concentration is slightly higher, around U_{Mn}=9%.

DICTRA simulations were carried out to correlate the evolution of the Mn profiles to the thermodynamic and diffusive conditions which prevailed during the various heat treatments. First, the formation of the U-shape gradient produced during slow air cooling is faithfully replicated. However, the standard Mn diffusion coefficient of Mn inside cementite contained in the MOBFE2 database required a consequent increase. To this end, the coefficient was multiplied by 2000.

The validity of the re-assessment was confirmed with the simulations dealing with the slow and fast heating to 700°C. In former case, the Mn enrichment up to values close to the equilibrium was well captured. In the latter one, the Mn profile remained very similar to that measured at room temperature after cold-rolling.

A simplified 1-D Finite Difference module was developed in order to reproduce the results obtained from DICTRA with a smaller calculation time. The subjacent objective is to build an efficient tool, tractable in industrial context. The module provided reliable results, in remarkable agreement with the DICTRA simulations with negligible mass losses.

REFERENCES

[ALL'15] Allam, T., Abbas, M., 2015. Mechanical Properties, Formability, and Corrosion Behavior of Dual Phase Weathering Steels Developed by an Inter-Critical Annealing Treatment. steel research international 86, 231–240. https://doi.org/10.1002/srin.201400033

[SAL'79] Al-Salman, S.A., Lorimer, G.W., Ridley, N., 1979. Pearlite growth kinetics and partitioning in a Cr–Mn eutectoid steel. Metallurgical Transactions A 10, 1703–1709. https://doi.org/10.1007/BF02811704

[BAL'11] Baltazar Hernandez, V.H., Nayak, S.S., Zhou, Y., 2011. Tempering of Martensite in Dual-Phase Steels and Its Effects on Softening Behavior. Metallurgical and Materials Transactions A 42, 3115–3129. https://doi.org/10.1007/s11661-011-0739-3

[CHA'81] Chance, J., Ridley, N., 1981. Chromium partitioning during isothermal transformation of a eutectoid steel. Metallurgical Transactions A 12, 1205–1213. https://doi.org/10.1007/BF02642334

[CHN'16] Chen, H., van der Zwaag, S., 2016. The Effect of Interfacial Element Partitioning on Ferrite and Bainite Formation. JOM 68, 1320–1328. https://doi.org/10.1007/s11837-016-1848-7

[CRA'75] Crank, J., 2009. The mathematics of diffusion, 2. ed., reprinted. ed, Oxford science publications. Oxford Univ. Press, Oxford.

[ENO'86a] Enomoto, M., Aaronson, H.I., 1986. Nucleation kinetics of proeutectoid ferrite at austenite grain boundaries in Fe-C-X alloys. Metallurgical Transactions A 17, 1385–1397. https://doi.org/10.1007/BF02650120

[ENO'86b] Enomoto, M., Aaronson, H.I., 1986. On the critical nucleus composition of ferrite in an Fe-C-Mn alloy. Metallurgical Transactions A 17, 1381–1384. https://doi.org/10.1007/BF02650119

[ENO'86c] Enomoto, M., Lange, W.F., Aaronson, H.I., 1986. The kinetics of ferrite nucleation at austenite grain edges in Fe-C and Fe-C-X alloys. Metallurgical Transactions A 17, 1399–1407. https://doi.org/10.1007/BF02650121

[HIL'81] Hillert, M., Aaronson, H. I., Laughlin, D. E., Sekerka, R. F., & Wayman, C. M. (1982). Solid-Solid Phase Transformations, n.d.

[HUT'04] Hutchinson, C.R., Hackenberg, R.E., Shiflet, G.J., 2004. The growth of partitioned pearlite in Fe–C–Mn steels. Acta Materialia 52, 3565–3585. https://doi.org/10.1016/j.actamat.2004.04.010

[IUG'03] Iung, T., Kandel, M., Quidort, D., de Lassat, Y., 2003. Physical modelling of phase transformations in high strength steels. Revue de Métallurgie 100, 173–181. https://doi.org/10.1051/metal:2003105

[JAN'09] Jang, J.H., Kim, I.G., Bhadeshia, H.K.D.H., 2009. Substitutional solution of silicon in cementite: A first-principles study. Computational Materials Science 44, 1319–1326. https://doi.org/10.1016/j.commatsci.2008.08.022

[LEE'14] Lee, J.W., Thompson, S.W., Varughese, R., Howell, P.R., 1993. The interaction between proeutectoid ferrite and austenite during the isothermal transformation of two low-carbon steels ? a new model for the decomposition of austenite. Journal of Materials Science 28, 4571–4577. https://doi.org/10.1007/BF00414244

[LUO'16] Luo, H., Liu, J., Dong, H., 2016. A Novel Observation on Cementite Formed During Intercritical Annealing of Medium Mn Steel. Metallurgical and Materials Transactions A 47, 3119–3124. https://doi.org/10.1007/s11661-016-3448-0

[MAR'75] Marder, A.R., Bramfitt, B.L., 1975. Effect of continuous cooling on the morphology and kinetics of pearlite. Metallurgical Transactions A 6, 2009–2014. https://doi.org/10.1007/BF03161825

[MIY'07] Miyamoto, G., Oh, J., Hono, K., Furuhara, T., Maki, T., 2007. Effect of partitioning of Mn and Si on the growth kinetics of cementite in tempered Fe–0.6 mass% C martensite. Acta Materialia 55, 5027–5038. https://doi.org/10.1016/j.actamat.2007.05.023

[OWE'54] OWEN, W. S. The effect of silicon on the kinetics of tempering. Transactions of the American Society for Metals, 1954, v, n.d.

[PAN'11] Pandit, A.S., Bhadeshia, H.K.D.H., 2011. Diffusion-controlled growth of pearlite in ternary steels. Proceedings of the Royal Society A: Mathematical, Physical and Engineering Sciences 467, 2948–2961. https://doi.org/10.1098/rspa.2011.0165

[PER'05] Perlade, A., Grandemange, D., Iung, T., 2005. Application of microstructural modelling for quality control and process improvement in hot rolled steels. Ironmaking & Steelmaking 32, 299–302. https://doi.org/10.1179/174328105X45893

[PHI'15] Philippot, C., Hoummada, K., Dumont, M., Drillet, J., Hebert, V., Maugis, P., 2015. Influence of a 2-D defect on the partitioning during the formation of a cementite particle in steels. Computational Materials Science 106, 64–68. https://doi.org/10.1016/j.commatsci.2015.04.020

[RAZ'74] Razik, N.., Lorimer, G.., Ridlel, N., 1974. An investigation of manganese partitioning during the austenite-pearlite transformation using anallticaI electron microscopl. Acta Metallurgica 22, 1249–1258. https://doi.org/10.1016/0001-6160(74)90138-2

[RAZ'76] Razik, N.A., Lorimer, G.W., Ridley, A.N., 1976. Chromium partitioning during the austenite-pearlite transformation. Metallurgical Transactions A 7, 209–214. https://doi.org/10.1007/BF02644458

[SAN'08] Santofimia, M.J., Zhao, L., Sietsma, J., 2008. Model for the interaction between interface migration and carbon diffusion during annealing of martensite–austenite microstructures in steels. Scripta Materialia 59, 159–162. https://doi.org/10.1016/j.scriptamat.2008.02.045

[SON'14] Song, W., Choi, P.-P., Inden, G., Prahl, U., Raabe, D., Bleck, W., 2014. On the Spheroidized Carbide Dissolution and Elemental Partitioning in High Carbon Bearing Steel 100Cr6. Metallurgical and Materials Transactions A 45, 595–606. https://doi.org/10.1007/s11661-013-2048-5

[TAN'95] Tanaka, T., Aaronson, H.I., Enomoto, M., 1995. Nucleation kinetics of grain boundary allotriomorphs of proeutectoid ferrite in Fe-C-Mn-X2 alloys. Metallurgical and Materials Transactions A 26, 547–559. https://doi.org/10.1007/BF02663905

[TIA'87] Tian, Y.L., Kraft, R.W., 1987. Mechanisms of Pearlite Spheroidization. Metallurgical Transactions A 18, 1403–1414. https://doi.org/10.1007/BF02646654

[WU'18] Wu, Y.X., Sun, W.W., Styles, M.J., Arlazarov, A., Hutchinson, C.R., 2018. Cementite coarsening during the tempering of Fe-C-Mn martensite. Acta Materialia 159, 209–224. https://doi.org/10.1016/j.actamat.2018.08.023

[ZUR'08] Zurob, H.S., Hutchinson, C.R., Béché, A., Purdy, G.R., Bréchet, Y.J.M., 2008. A transition from local equilibrium to paraequilibrium kinetics for ferrite growth in Fe–C–Mn: A possible role of interfacial segregation. Acta Materialia 56, 2203–2211. https://doi.org/10.1016/j.actamat.2008.01.016

Chapter 4

Recovery and Recrystallization

Recovery and recrystallization are two important microstructural evolutions occurring in the deformed ferritic matrix of cold-rolled ferrite pearlite steels when annealing. The phenomena are governed by the same driving force, i.e. the decrease in the elastic and surface energy due to defects in the deformed microstructure. They hence enter in competition during the annealing process and both can strongly affect the morphogenesis of the ferrite/austenite microstructure, as shown in chapter 2.

This chapter is dedicated to experimental characterization, modeling and coupling of recovery and recrystallization phenomena. The first part of this chapter is dedicated to a bibliographic study about the investigation methods and the modeling approaches of both metallurgical mechanisms. In the present study, *in situ* characterizations were mainly conducted by HEXRD. The experimental results, presented in the second part, were obtained during an experimental campaign at the DESY synchrotron. Recovery was tracked using a conventional Williamson-Hall approach while the recrystallization kinetics was determined by mean of an original method developed in the frame of this study. This new method was validated by direct SEM-EBSD observations on the studied steel and modeling results from the literature. The last section of this chapter is dedicated to the modeling of both phenomena using a physically based mean-field approach inspired by literature models. The model was calibrated on available experimental results (kinetics and size measurements) and permits to simulate the recovery/recrystallization kinetics of the studied steel during the continuous annealing at slow and fast heating rates (as in chapter 2). Once adjusted and coupled with a micromechanical model for cold-rolling, it was employed to predict accurately the effect of cold-rolling ratio on the recrystallization kinetics.

4.1 Bibliographic study

4.1.1 Recovery

4.1.1.a Definition

Recovery is a metallurgical process by which a deformed crystalline structure reduces its elastic stored energy, either by rearranging or by annihilating lattice defects. These defects are often statistical stored dislocations (perfect or partial) inherited from the deformation process. Their rearrangement leads to the formation of low-angle low energy sub-boundaries (subgrain) which evolves as function of time, temperature and initial deformation state [NES'95]. Contrary to recrystallization, recovery occurs without the migration of a high angle grain boundary [DOH'97]. Figure 4.1 shows for instance the schematic evolution of the deformation substructure of a polycrystalline metal as a function of annealing conditions and initial deformation states.

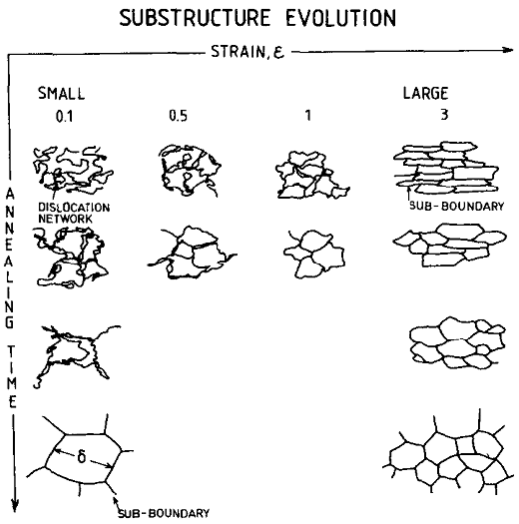

Figure 4.1: Schematic evolution of the deformation substructure of a polycrystalline metal as a function of annealing conditions and initial deformation states [NES'95].

During recovery, the decrease in dislocations densities combined with the increase in the mean subgrain size leads to a decrease in both strength and hardness of the studied material. Recovery generally occurs during a thermal treatment at temperature that permits the thermally activated gliding (dynamical recovery) or climb of dislocations under residual stresses (static recovery). This process is thus highly sensitive to the temperature and to the density of defects.

4.1.1.b Investigation methods

Different experimental methods enable to investigate recovery kinetics. In most studies, only the decrease in dislocations density is described, whereas the evolution of sub-grains microstructures can have a sense as they both can interfere with a further possible recrystallization process [REH'13, DOH'97]. In the SIBM theory [BAI'62, FAI'79], subgrains serve for instance as nucleation site for recrystallization [REH'13]. Moreover, according to Nes *et al*. [NES'95], this sub-grain growth in steels during recovery is partially responsible from the decrease in hardness.

The most used characterizing method to assess the density of defects in a polycrystalline and deformed sample consists in studying the shape, the width, the tails and the asymmetry of its X-Ray diffraction peaks [WIH'53, PES'03, RIB'04, RIB'10, KHR'11, UNG'14, SAL'14]. The evolution of dislocation densities can be followed in real time if the experiments are conducted *in situ* (for instance on synchrotron beamlines) or *ex situ* after various heat treatments. The results of these methods depend strongly on how the physical models correlate the presence of defects to the diffracted beam. Since the pioneer work of Williamson and Hall [WIH'53], many approaches were proposed. They rely either on the Full Half Width Maximum (FHWM) of the diffractions peaks or their breadth (Williamson and Hall method) or Fourier's coefficients of the profiles (Warren–Averbach method) [SAL'14]. Ungar's group [UNG'14, RIB'11] provided the most advanced works in this field, in which the whole diffraction patterns are deconvoluted by Convolutional Multiple Whole Profile fitting (CMWP).

Another option is to measure the decrease in the macroscopic mechanical properties caused by the recovery process and to relate it to the decrease in dislocation density. The latter is estimated via a micromechanical model. Verdier *et al*. [VER'98] for instance carried out tensile tests at room temperature after annealing treatments on Al-Mg alloys and have studied the evolution of their yield strengths as a function of the severity of the thermal treatments. The model proposed by these authors links interestingly the thermal activated relaxation of the internal stresses to the density of dislocations. The

use of hardness measurements (which requires smaller samples) remains hence the preferred experimental method [PER'10]. These mechanical tests must however be considered with care when recrystallization occurs, as recovery and recrystallization may concomitantly contribute to the decrease in hardness.

Alternatively, recovery kinetics can be studied indirectly by following other physical properties also affected by the defect density (as magnetism or electric conductivity). For instance, Gurruchaga [GUR'10] identified recovery and recrystallization temperature ranges using the Barkhausen's noise while Khodabakhshi *et al.* [KHO'11] used the electric resistivity to determine the dislocation density and the grain size of their steels.

The very last option to study recovery is to observe and characterize directly the dislocation microstructures by microscopy. Accounting for the high density of dislocation in cold-rolled ferrite-pearlite steels, TEM is seldom used and allow studying only dislocation organization (sub-grains and cells) [VER'98]. SEM-EBSD mapping are often preferred even though it does not permit an absolute measurements of dislocation densities [CHB'14]. Radwański [RAD'15] recommended the use of the Quality Index mapping to reveal various levels of recovery between different grains. This technic does not permit on the contrary to compare different states. The evolution of sub-grains can be revealed by studying the disorientations of sub-boundaries (below 1.5°) but it requires EBSD setup with an improved angular resolution [SLA'18]. Finally, it should be emphasized that some authors used the density of subgrains revealed by ESBD to track the elastic stored energy [LIU'16] and thus to estimate the driving force for recrystallization.

In this PhD study, the Williamson-Hall methodology was utilized on *in situ* experiments conducted on synchrotron beamlines. The principle of this method is detailed in the next section.

4.1.1.c Williamson-Hall Theory

As strains and defects distort atomic lattices of crystalline structures of the microstructure, they affect in turn the diffraction patterns. The diffraction conditions for an infinite perfect crystal given by the Bragg's law are no more perfectly fulfilled. It explains why diffraction peaks are enlarged compared to the perfect case. This enlargement depends on the mean size of the perfect crystallites able to diffract and on the mean deformation of the structure. In the Williamson-Hall method, this enlargement is measured on the Full Width Half Maximum (FWHM) of diffraction peaks.

For a given Bragg's diffraction angle θ, Equation (4.1) permits to correlate the FWHM of diffraction peaks to parameters ε and *D*, being the mean deformation of the material the crystallite size, respectively [WH'53, ZAK'10, KOH'11, SAL'14]:

$$\mathrm{FWHM}(\theta).\cos\theta = \frac{K.\lambda}{D} + 4.\sin\theta.\varepsilon \qquad (4.1)$$

K is a constant, set to 0.9 and λ is the wavelength of incident monochromatic beam. The first term depending on the crystallite size is known as the Scherrer's term while the second refers to the pioneer work of Stokes and Wilson. The reader is referred to [WH'53] for more details.

Once strain parameter ε and crystallite size D are known for a given diffraction pattern, the dislocation density ρ (m^{-2}) can be estimated thanks to the Smallman's formula (4.2) [SMA'57]:

$$\rho = \frac{3\sqrt{2\pi}\varepsilon}{bD} \qquad (4.2)$$

where b is the Burger vector of perfect dislocations in ferrite ($b = 2.5x10^{-10}$ m in our case, neglecting the effect of the temperature).

4.1.2 Recovery modelling

In the literature, two types of model can be found, either purely phenomenological (mathematical functions adjusted on experimental data) or physically based mean field models trying to describe the mechanisms at dislocations scale (climb, network annihilation, subgrain growth).

4.1.2.a Phenomenological approaches

Yunning Wang proposed a recovery model in frame of martensite tempering [WAN'06]. The density of dislocations was supposed to evolve as a function of temperature and time according to the following empirical equation (4.3) inspired from JMAK formalism:

$$\rho=\rho_0 \exp\left(-C_1 \exp\left(-\frac{Q}{RT}\right) t+C_2\right) \quad (4.3)$$

with Q an apparent activation energy of the process and R the perfect gas constant. ρ_0, C_1, C_2 are parameters that must be calibrated on experimental results. Senuma *et al*. [SEN'08] proposed also very similar empirical equation for austenite recovery at high temperature:

$$\rho=\rho_0 \exp\left(-90 \exp\left(-\frac{8000}{T}\right) t^{0.7}\right) \quad (4.4)$$

In both cases, such purely mathematical approaches show good performances once adjusted. Nevertheless, they lack of generality and do not provide reliable predictions outside their calibration domains.

4.1.2.b Physically based mean field approaches

The field of recovery modeling was reviewed in 1995 by Nes [NES'95]. The original goal pursued by the author was in fact to establish the relative contributions of dislocation and subgrain substructures in the decrease in the mechanical properties of metals during annealing. For the case of high purity steel, he succeeds to demonstrate that the mechanical recovery is due in fact to both annihilation of dislocations and subgrain growth.

Most of models for dislocation annihilation are inspired from the seminal work of Friedel [FRI'64]. He proposed to describe the logarithmic relaxation of internal stress σ_i during annealing in alloys at a given temperature T according the relation (4.5):

$$\frac{d\sigma_i}{dt} = -K\exp\left(\frac{-U(\sigma_i)}{kT}\right) \quad (4.5)$$

being K a parameter, U the apparent activation energy of the process and k the Boltzmann constant. The internal stress σ_i can be related to the density of dislocations such that:

$$\sigma_i = \alpha M \mu b \sqrt{\rho} \quad (4.6)$$

and the apparent activation energy can be related to the internal stress as follows:

$$U(\sigma_i) = U_0 - V\sigma_i \quad (4.7)$$

with α a term related to the dislocation forest strengthening, M a Taylor factor and V the apparent activation volume of individual recovery processes. This set of equations describes well dislocation annihilation by climb, in particular in fcc alloys.

This model was further improved by Verdier *et al*. [VER'98] for instance by introducing a mobility equation for dislocation and by detailing K parameter thanks to Orowan relationship. This latter development was extensively employed by Zurob *et al*. in their works for austenitic steels [ZUR'02, REH'13]. In our work, accounting for the incertitude on our experimental measurements, we decided to use the original Friedel's model [FRI'64].

Many models also exist for the evolution of the low-angle boundaries substructure [LI'62, NES'95, FUR'95]. Furu *et al*. [FUR'95] proposed for instance to write the increase in subgrain radius r as:

$$\frac{dr}{dt} = C_1 \sinh\left(\frac{C_2}{rkT}\right) \quad (4.8)$$

where C1 and C2 are two parameters. This formalism can provide an adequate description of subgrain growth once adjusted. However, it hides the fact that subgrain growth also depends on the surrounding dislocation structure. This is a reason why we preferred in our development to consider the work of Rehman *et al*. [REH'13] who describe the growth of sub-grains in the frame of a SIBM growth. This model will be detailed in the modeling section of this chapter.

In conclusion, it appears that recovery was extensively studied since the 50's, but remains an active research field. It comprises in fact many physical mechanisms which are highly coupled (annihilation of dislocations by climb and subgrain-growth). Most of studies focus often uniquely on the evolution of the dislocation density. However, this literature review outlines the interest of describing also the substructure evolution for modeling recrystallization.

4.1.3 Recrystallization

4.1.3.a Introduction

The recrystallization is defined as follows in the reference review of this field [DOH'97]: "The authors have agreed that recrystallization is the formation of a new grain structure in a deformed material by the formation and migration of high angle grain boundaries driven by the stored energy of deformation. High angle grain boundaries are those with greater than a 10–15° misorientation. Grain coarsening can, in turn, be defined as processes involving the migration of grain boundaries when the driving force for migration is solely the reduction of the grain boundary area itself."

This definition excluded thus recovery processes which only describe the rearrangement of low angle boundaries, even though their driving forces are the same and also grain coarsening whose driving forces are of different nature (decrease in grain boundary energy).

The recrystallization process occurs by nucleation and growth. Since the pioneer work of Cahn [CAH'50], it is well established that the nuclei are in fact not exactly new grains constructed atom by atom. On the contrary, they are in fact small sub-grains or dislocation cells, already present in the recovered structure. This selective process, far from randomization, explains why recrystallized crystallographic textures strongly depend on the original texture and the anisotropy of the deformation process.

This recrystallization process as recovery will strongly depends on the temperature since nucleation and growth are both thermally activated mechanisms and on the initial deformation state (texture, density of defects and grain substructure). Figure 4.2(a) shows for instance EBSD maps of a cold-rolled ferrite-pearlite steel, annealed at different temperatures. The progression of recrystallization is revealed by a suitable kernel post-treatment (new recrystallized grain in red). The most convenient way to characterize the extent of recrystallization in alloys consists in measuring the volume (surface) fraction of recrystallized grains in the microstructure. Figure 4.2(b) shows the corresponding as a function of the annealing temperature.

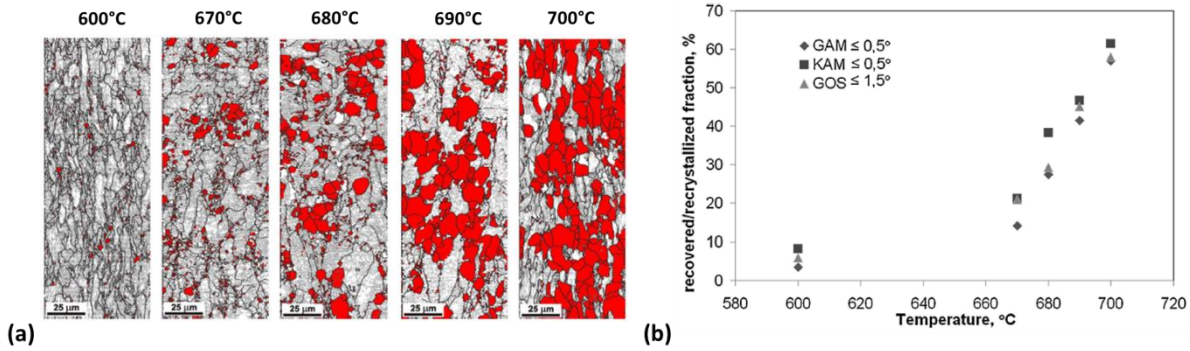

Figure 4.2: (a) EBSD maps of s cold-rolled ferrite-pearlite steel annealed at different temperatures, by Radwański [RAD'15]. Recrystallized grains appear in red. (b) Associated recrystallization kinetics.

4.1.3.b Investigation methods

As for recovery, studying the extent of recrystallization requires often tedious post mortem (*ex situ*) experiments on samples after interrupted thermal treatments. In the literature, the methods employed are either based on the mechanical behavior (hardness measurements) [HUA'04, LI'13, CHB'14] and/or on microscopic observations (optical, Scanning Electron Microscopy - SEM, Electron Back-Scattered Diffraction - EBSD, more rarely, and Transmission Electron Microscopy - TEM) [HUA'04, YE'02, PER'10, LU'11, CHB'14, ZHA'14b, LIU'16]. These techniques are time consuming and lack of accuracy to determine the recrystallization start temperature (detection of very first recrystallization processes, cf. Fig. 4.2(b)). The measurement based on hardness evolutions are also often biased, as the reported decrease in hardness can also be partially due to a concomitant recovery process.

Radwański [RAD'15] showed that the combination of EBSD technics as Grain Orientation Spread representation (GOS), Kernal Average Misorientation (KAM) or Grain Average Misorientation (GAM) permits an accurate characterization of the recrystallized state of steels (cf. Fig. 4.2(a)) [AYA'11, ZHA'14b]. These technics require to detect first the boundaries of deformed and recrystallized grains and to calculate a scalar value representative of the local misorientation angle with respect to a mean value

inside each studied grain. GOS is for instance the standard deviation of crystallographic misorientation inside the studied grain knowing its mean orientation. Thus, the higher the GOS value, the more the grain is deformed. Radwański consider that a grain is non-recrystallized if its GOS value is higher than 1.5°. This threshold value was also considered to estimate the mean unrecrystallized volume fraction in this work. The threshold value of the pixel-to-pixel misorientation to define a grain boundary was set to 5°.

Recently, Juul Jensen's group [LAU'03, LAU'06, POU'11] showed that recrystallization kinetics of individual grains in deformed aluminum or copper can be followed in real-time using 3D-XRD tomography. In the proposed experiments, each individual diffraction spot emerging from Debye-Scherrer (DS) rings is followed assuming that it corresponds to a newly recrystallized grain. As the intensities of the spots are supposed to be proportional to the volumes of the studied new grains, growth kinetics of individual grains as well as precise nucleation conditions can be determined from few *in situ* experiments. At the same time, the position and local crystallographic orientations of new grains can be tracked in bulk. A mean recrystallization kinetics can be deduced, but without guaranty of its statistical representativeness on larger volumes (low number of considered grains). Moreover, as 3D-XRD cannot be applied reasonably to grains smaller than 5 μm, the case of industrial steels discussed above cannot be dealt.

Inspired by these prior 3D-XRD investigations, the present work proposes a new *in situ* method based on HEXRD experiments to determine mean recrystallization kinetics in bulk, considering a large number of grains. It will be illustrated with a study on ferrite-pearlite steels but remains general and applicable to other metals. In the studied case, it will be shown that *in situ* HEXRD permits in fact to study simultaneously recovery, recrystallization and phase transformation.

4.1.4 Recrystallization modeling

4.1.4.a Global approaches

Recrystallization is characterized by 3 stages (nucleation/growth/abnormal growth), similarly to solid-state phase transformations. Thus, many authors applied the JMAK formalism to model the recrystallized volume fraction (often designated by X) [LIU'16]:

$$X = 1 - \exp\left(-b_0 \exp\left(-\frac{Q}{RT}\right) t^n\right) \tag{4.9}$$

being b_0 a pre-exponential factor, Q an apparent activation energy and n a parameter which depends on the nucleation processes. In principle, previous equation (4.9) is dedicated to follow transformations in isothermal conditions and must be calibrated in the same manner. It should not be used to follow recrystallization during continuous annealing. Li *et al*. [LI'13] thus proposed an integrated version, assuming the validity of JMAK equations during infinitesimal small isothermal steps along a continuous annealing at constant heating rate:

$$X = 1 - \exp\left(-\frac{n}{\beta^n}\int_{T^*}^{T} b_0 \exp\left(-\frac{Q}{RT}\right)(T - T^*)^{n-1} dT\right) \tag{4.10}$$

with T* the temperature start of recrystallization process and β the constant heating rate.

In literature, the values reported to describe recrystallization in cold-rolled steels are generally small (lower than 3), indicating that the nucleation is inhomogeneous (n = 1.7 after 50% cold-rolling for Zhu *et al*. [ZHU'12], n = 1 for Huang *et al*. [HUA'04], n=1.7 for Kulakov [KUL'13]). The activation energies are generally higher than the one for alpha iron bulk diffusion as the mobility of the interfaces can be controlled by substitutional elements. Huang *et al*. [HUA'04] for instance took Q = 350 kJ.mol^{-1}. This value

is similar to the one used by Zhu *et al*. [ZHU'12] to model the interface mobility in the phase field approach (360 kJ.mol^{-1}), but far lower than the one proposed by Kulakov (581 kJ.mol^{-1}). We will evidence in the following that such models can show good predicting performances but are never predictive as they do not describe well incubation and nucleation processes (prediction of T* for instance).

4.1.4.b Physically based mean-field approaches

Contrary to global JMAK approaches, more sophisticated physically based mean-field models aim at describing the sequential nucleation, growth and grain coarsening processes of recrystallization with coupled equations. However, few frameworks are available for steels in the literature and most of them are derived from the work of Zurob *et al*. [ZUR'02, ZUR'06, REH'13].

Latter authors developed for years a complete framework for austenite recrystallization. It takes into account the nucleation sites at localized on the former austenite grain boundaries (SIBM theory) as well as the mobility of the new grain boundaries. Their models permit to better understand the solute-drag effect of Niobium delaying the recrystallization (dynamical and static) of austenite at high temperature during hot rolling. However, it cannot be applied to our case. Firstly, the grain nucleation in bcc iron is not limited by the same interactions. Secondly, the interface mobility is not limited by the substitutional alloy components. Sinclair *et al*. [SIN'07] also developed a model in which the grain growth is controlled by a mobility parameter. The main drawback of the approach is that it does not propose any nucleation model (instantaneous nucleation site saturation) and it considers a constant driving force for the normal/abnormal grain growth. The common thread between these models is to represent the growth process with mobility equations of isolated new grains and capture the whole kinetics with the extended volume theory. In this work, we will propose an original model to describe recrystallization process in our deformed ferrite-pearlite steels which combines the nucleation theory from Zurob *et al*. [REH'13, ZUR'06] and the simplified growth model from Sinclair *et al*. [SIN'07]). The equations chosen to build the model are presented in section 3.

4.1.4.c Full field approaches

Miodownik [MIO'02] has reviewed the full field numerical approaches permitting to simulate at REV scale the topology and network connectivity of evolving grain and subgrain structures during recrystallization, grain normal and abnormal growth. Advantages and drawbacks of numerous types of model are discussed: Vertex, Monte Carlo Potts, Phase-Field [ZHU'12, ZHU'15b] and Cellular Automata [MAD'13, HAL'14, ZHG'13]. The metallurgical ingredients of such models are essentially the same than the mean field approaches; except that they reproduce more conveniently the impingement mechanisms (precipitates and second phases) and local relations (texture prediction for instance). Thus, it requires the setting of local rules which depends on numerous physical variables as: driving forces, interface energies, mobility equations, etc. In term of kinetic prediction, their performances are rather similar to that of the mean field approaches. Figure 4.3 gives different examples of full-field models applied to ferrite/pearlite steels taken from in literature.

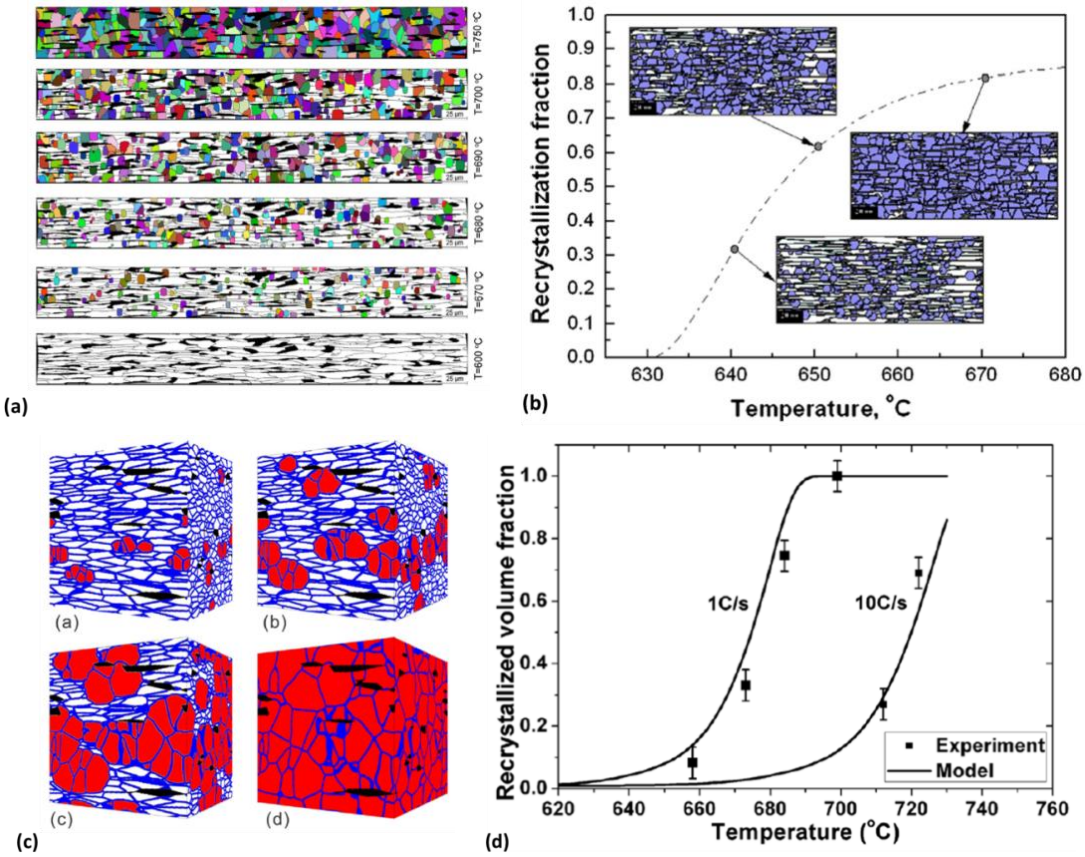

Figure 4.3: Recrystallization processes modeled in a cold-rolled ferrite-pearlite steels (a,b) by cellular automata after [MAD'13, ZHG'13] and (c,d) by phase field after [ZHU'12]. (a,b,c) corresponds to the full field calculations at the REV scale in 2D or 3D. (b,d) corresponds to the predicted global kinetics during continuous annealing schedules.

As recovery, recrystallization of steels is the topic of many applied and fundamental researches due to its high technological importance. In fact, the prediction of grain sizes is one of the pillars of microstructure design.

4.2 Experimental Results

4.2.1 Introduction

Series of *in situ* investigations on synchrotron beamline were conducted at DESY facilities. These *in situ* experiments permitted to follow recovery and phase transformation upon annealing a deformed ferrite/pearlite microstructure. These experiments are in fact complementary to the *ex situ* characterizations presented in Chapter 2.

This chapter is restricted to the characterization of recovery and recrystallization. Phase transformation will be considered in next Chapter 5. The FWHM, relevant for the current investigation of recovery were obtained during the post-treatment procedure by Rietveld refinement, as detailed in chapter 1 (cf. section 1.6.2). In parallel to this conventional treatment, we developed an original method inspired from the Jensen *et al.*'s works to follow recrystallization kinetics. This new method is based on the systematic detection of the appearing diffraction spots directly on the Debye-Scherrer rings, assuming they are related to newly recrystallized grains.

Two types of annealing schedules have been conducted on cold-rolled samples (CR state – 61% cold-rolling); ideal annealing schedules consisting in isothermal steps at different temperatures (at 450°C, 550°C, 650°C, respectively during 10 min after a fast heating at 100°C.s^{-1}) and annealing schedules at 800°C during 10 min after heating at constant rates (3° and 30°C.s^{-1}, respectively). The ideal schedules aim mainly at studying recovery within the 450 - 650°C temperature range and recrystallization (near 650°C) processes in isothermal conditions.

As the procedure developed to follow recrystallization is original, our HEXRD results were compared to conventional SEM-EBSD investigations. GOS mapping was carried out to measure recrystallized fraction on samples after interrupted schedules (for instance 700H3 and 710H3 samples already characterized by conventional SEM in Chapter 2).

4.2.2 Recovery

As explained in Chapter 1, all 2D diffraction patterns acquired during *in situ* experiments have been integrated circularly to obtain 1D pattern on which a Rietveld analysis has been conducted by Fullprof software. The Full Widths at Half Maximum (FWHM) of each 1D integrated diffraction peak of ferrite of each diffraction pattern have been determined using Caglioti's coefficients (U, V, W) determined in the refinement procedure. The FWHM obtained from the 1D-2θ profiles then serve to make a Williamson-Hall plot ($FWHM_{hkl}(\theta).cos(\theta)$ as a function of $sin(\theta)$), from which the mean deformation ε and the crystallite size D are calculated by linear regression. Thus, the application of equation (4.2) for each diffraction pattern enables the time-resolved quantification of the dislocation density all along studied thermal schedule and the characterization of recovery as a function of time and temperature.

For the annealing schedule at constant heating rates, the procedure was applied to all recorded patterns up to Ac_1, when the austenite transformation starts. In this manner, the overlap of the diffraction peaks of ferrite and austenite which occurs above this temperature is avoided. This overlapping would lead to a decrease in the confidence index of the refinement procedure. The Ac_1 temperatures were set to 710°C and 730°C for the slow and fast heating rates, respectively, in accordance to the metallographic observations of Chapter 2.

4.2.2.a Isothermal condition: results and interpretation

Figure 4.4 represents the evolution of the strain parameter ε and crystallites size D as a function of time along the ideal annealing schedules. It appears that in all studied conditions, only the strain parameter ε decreases while the evolutions of crystallites size D are similar, whatever the tested temperatures. Both evolutions are consistent with a recovery process.

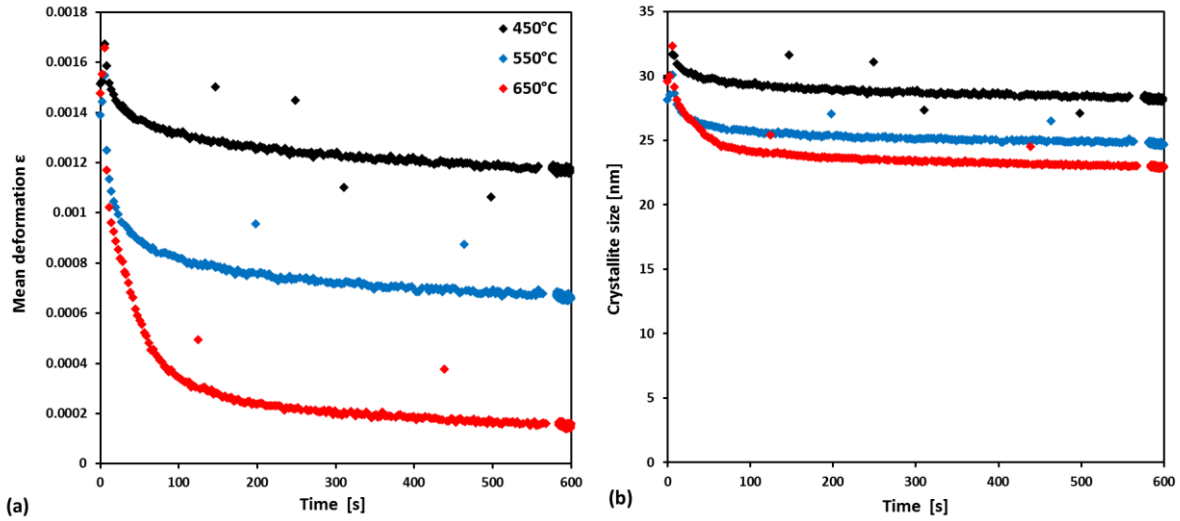

Figure 4.4: Evolution of (a) strain parameter ε and (b) crystallites size D as a function of time along the isothermal holdings at 450°C (black curves), 550°C (blue curves) and 650°C (red curves) respectively.

The evolution of estimated dislocation densities along the ideal annealing schedules are represented in Figure 4.5. Even though the accuracy and the validity of the equation (4.2) can be discussed, it sheds in light the major evolutions in the studied material. As expected for a recovery process, for all studied conditions, the density of dislocations decreases first rapidly and then seems to reach a stagnant regime. The fast regime spans over about 200s, whatever the temperature. The absolute decrease is on the contrary highly sensitive to the isothermal holding temperature. The higher the temperature, the higher the drop is, as expected for a thermally activated process. At 450°C, the relative decrease is 15% after 600s whereas it reaches 92% at 650°C. We will see in the following section after analyzing recrystallization process (formation of new defect grains) that the sharp decrease in dislocation density at 650°C can be also attributed to recrystallization, which is not the case at 550°C and at 450°C *a fortiori*. At this point, the recrystallization process cannot be identified when investigating solely these dislocation densities or the crystallite sizes.

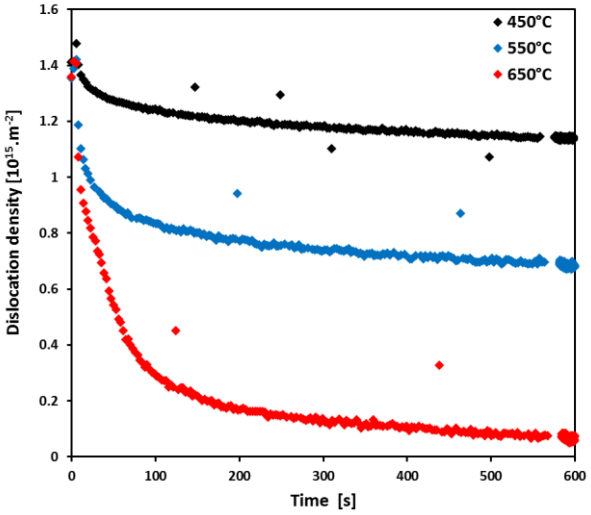

Figure 4.5: Evolution of dislocation densities deduced from equation (4.2) as a function of time along the isothermal holdings at 450°C (black curve), 550°C (blue curve) and 650°C (red curve), respectively.

It is worth noting that, whatever the trial, the procedure permitted to determine the same initial dislocation density of $1.4x10^{15}$ m^{-2}. This value is close to that determined by the micromechanical model of Bouaziz *et al*. [BOU'02], used in Chapter 3 to calculate the strain partitioning between pearlite and ferrite in the studied steel ($2.2x10^{15}$ m^{-2} in ferrite, see also the modeling section of this chapter for more details).

4.2.2.b Continuous heating: results and interpretation

The evolution of strain parameter ε, crystallite size D and dislocation densities ρ during slow and fast continuous heating is reported in Figure 4.6.

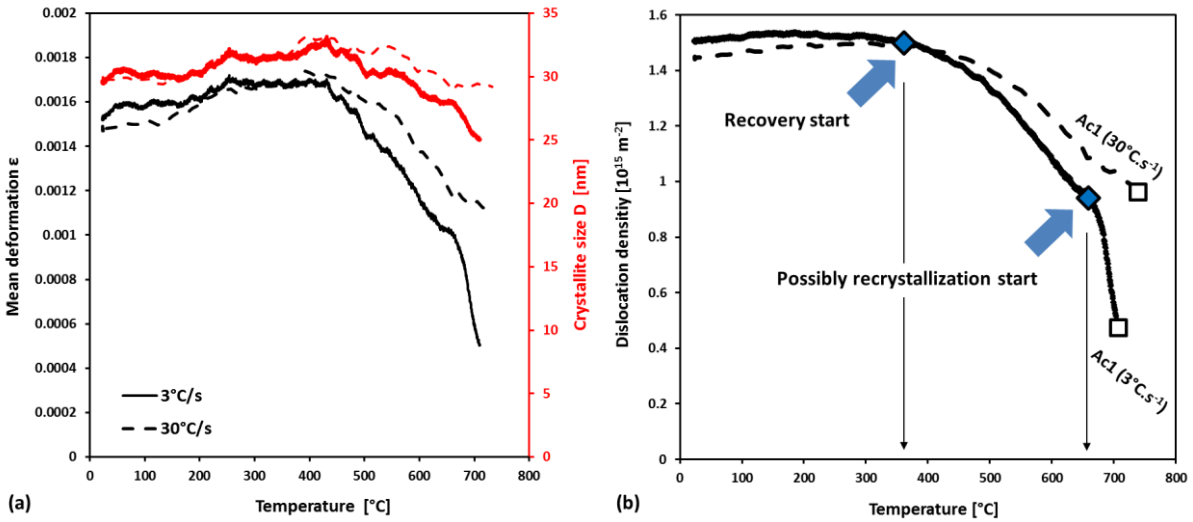

Figure 4.6: Evolution of (a) strain parameter ε, crystallites size D and (b) dislocation density ρ as a function of temperature during continuous heating at slow (continuous line) and fast rate (dashed line), respectively.

As during isothermal holdings, the measured crystallite sizes do not evolve much during annealing, whatever the heating rate, even though recrystallization appears to be finished at 700°C at low heating rate. On the contrary, the strain parameter ε and the deduced dislocation densities decrease obviously during the annealing. The decrease starts in both cases around 350°C. For high heating rate, the relative decrease in dislocation density is about 30%, whereas it attains 70% with the low heating rate. At low heating rate, the reduction occurs in two successive stages. Between 350°C and 650°C, the slope is weak and rather similar to that observed for the high heating rate. This stage is likely due to conventional recovery. Above 650°C, the slope increases suddenly. As we will show later, this sudden decrease can be associated to the recrystallization process, which ends up at 700°C. As recrystallization starts concomitantly to austenite formation at high heating rate, no sudden drop in dislocation density is observed for this heating condition. In addition, Figure 4.6(b) clearly highlights that at high heating rate, recovery is delayed, but the difference for a given temperature in the absence of recrystallization remains limited (about $0.2x10^{15}$ m^{-2}).

The Williamson-Hall method thus enables the start/end temperature detection for recovery of the ferrite matrix with a good precision and provides a reasonable estimate of the decrease in dislocation density. It seems also possible from this analysis to infer a possible start temperature for recrystallization if it occurs below Ac_1.

4.2.3 Recrystallization

As discussed in introduction, measuring recrystallization using *ex situ* experiments (interrupted thermal schedule) is a tedious process. We thus proposed a new methodology based on the *in situ* HEXRD experiments exploitation.

4.2.3.a Methodology for *in situ* characterization of recrystallization

The detailed observations of DS rings during continuous annealing experiments reveal the appearance of individual diffraction spots all along the rings. Figures 4.7(a), (b) and (c) show for instance the 2D diffraction pattern images captured at 25 and 700°C (full scale and magnified views). During the slow heating experiment ($3°C.s^{-1}$), the image contrast is improved to distinguish the individual spots despite the high intensity of the DS rings. These spots are presumably related to the new recrystallized grains and consistently, their kinetics of apparition should be related to the recrystallization kinetics. Jensen *et al*. [LAU'03, LAU'06, POU'11] showed that it is possible to compare the recrystallization processes upon following these individual diffraction spots for different initial grain orientations. Savran *et al*. [SAV'10] proposed an experiment based on a similar idea to measure the nucleation rate of austenite in low carbon steel. Nevertheless, from our best knowledge, these individual spots have never been exploited to quantify bulk recrystallization kinetics, whereas the density of spots is presumably correlated to the density of new recrystallized grains.

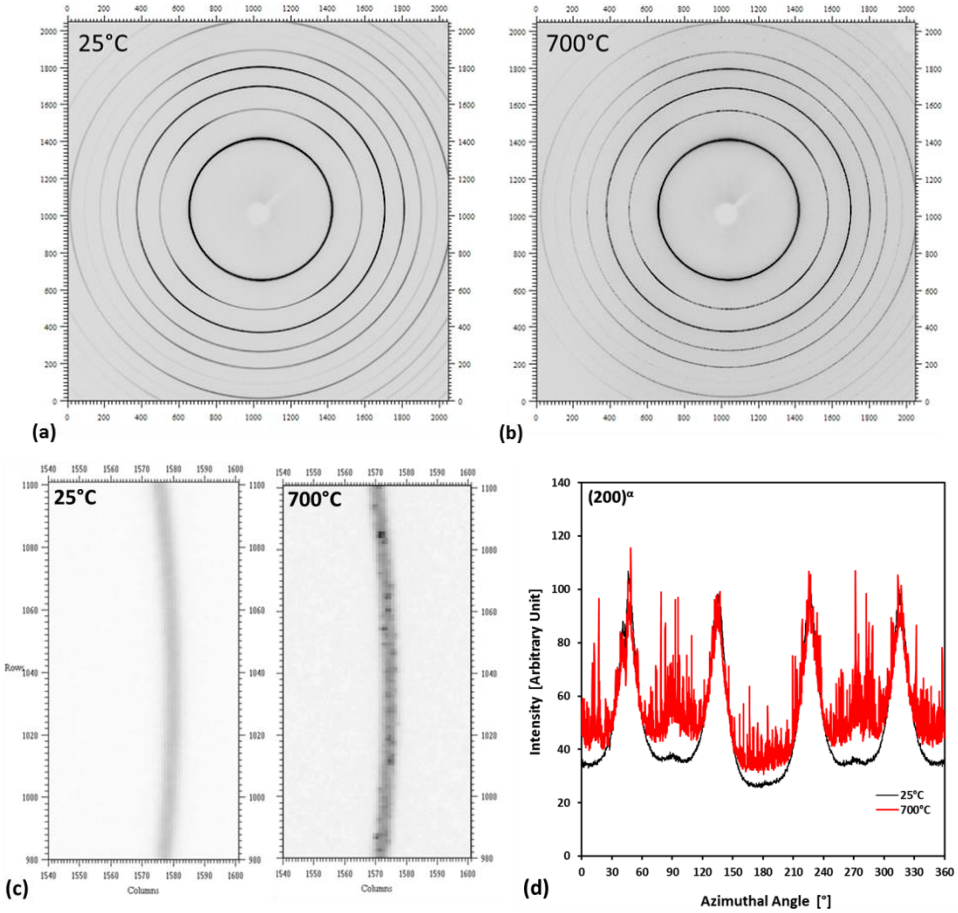

Figure 4.7: (a) and (b) full diffraction patterns obtained at 25 and 700°C, respectively, during the heating sequence (the intensities are given in arbitrary unit). The clear shadow in the center corresponds to the beam stop. Black rectangles correspond to the fields of the magnified views in Figure (c). (c) Magnifications of the $(200)^{\alpha}$ DS ring of ferrite at 25°C and 700°C, respectively during the heating sequence. The recrystallization peaks correspond to the individual dark spots seen at 700°C on DS rings. (d) Intensities of the $(200)^{\alpha}$ Debye-Scherrer rings as function of the azimuthal angle at 25°C (black curve) and 700°C (red curve).

It however supposes that the gradient of misorientations inside the new recrystallized grains is weak to observe concentrated spots and to be able to deconvolute these spots from the continuous diffraction rings of the studied phase. So, following the inspiring works of Jensen *et al.*, we developed an original method to estimate bulk recrystallization kinetics, depicted in the following section.

4.2.3.b Post-treatment procedure with Fit2D software

In practice, our method, illustrated in Figure 4.8, first consists in integrating radially the DS rings at each azimuthal position as it is more convenient without dedicated software to work in 1D than trying to detect individual spots in 2D images, close to intense DS rings. In the studied case, the $(200)^{\alpha}$ rings have been investigated in detail as it permits to avoid possible overlap with austenite above Ac_1 (for continuous annealing experiments). The integration has been made using Fit2D software in between an inner and an outer circular bound to produce a closed area embedding the whole studied DS rings. The width between inner and circular bounds corresponds to about 4 times the FWHM of the considered ring. The latter area is then divided into angular sectors. The number of sectors actually determines the angular resolution of the azimuthal integration. The binning rate has been set to 2575 bins in Fit2D software for the treatment of $(200)^{\alpha}$ ring. This value has been chosen according to the resolution of the detector (2048x2048 pixels) to a have coincidence between 1 bin and 1 pixel along the studied ring, i.e. guarantying the highest possible resolution.

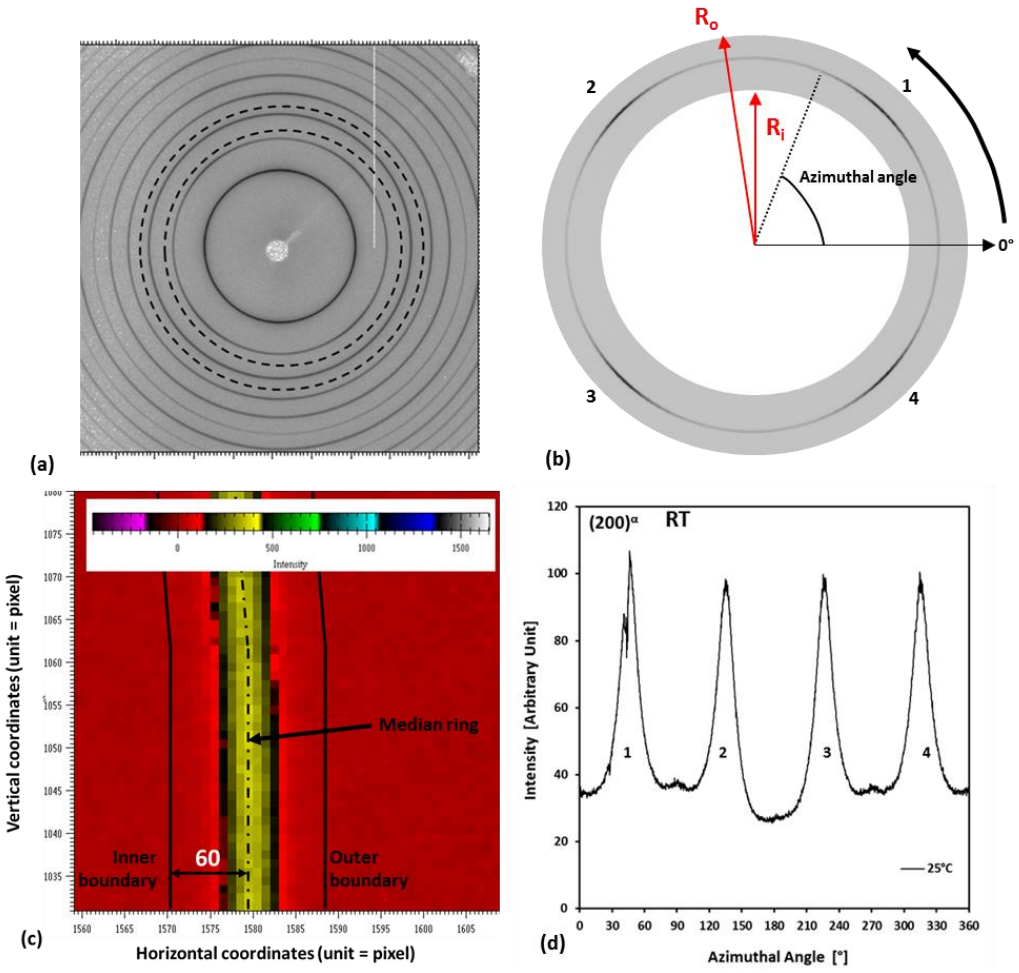

Figure 4.8: (a) 2D pattern recorded at room temperature. The boundaries enclosing the $(200)^{\alpha}$ ring are schematized by the black dashed lines. The curved arrow indicates the integration direction. (b) Schematic representation of the azimuthal integration method. Ri and Ro stand for the inner and outer radius, respectively, which delimit the area in which the ring intensity is integrated, respectively. Numbers 1 to 4 indicate local high intensities caused by the texture

effect induced during cold-rolling. (c) High magnification of the 2D pattern, focused on the $(200)^{\alpha}$ ring, with a modified color shade to highlight the intensity value difference among the pixels which constitute one ring. (d) Plot of the ring intensity as function of the azimuthal angle. The four numbered peaks are caused by the texture induced by the cold-rolling.

The ring is integrated in the angular range 0-360°, 0° corresponding to the horizontal axis of 2D diffractograms. Figure 4.8(d) represents the integrated intensity of the $(200)^{\alpha}$ DS at room temperature (black) and at 700°C (red), respectively during continuous annealing experiment ($3°C.s^{-1}$). The profile at room temperature shows four periodic main peaks due to the cold-rolling texture. In the following, these main variations of intensity with azimuthal angle will be called "texture peaks". Apart from texture peaks, the profile is relatively smooth with limited statistical fluctuations. On the contrary, the profile at 700°C still shows the four texture peaks but also numerous small fluctuations. The highest fluctuations are found in the vicinity of the 90° and 270° positions. These fluctuations are due to the individual diffraction spots observed in DS rings. In the following, those individual intensity fluctuations will be designated as "recrystallization peaks".

After azimuthal integration, the number of recrystallization peaks on the considered ring is counted on each 1D diffractogram similar to Figure 4.7(d). To this end, a specific algorithm was developed to identify each recrystallization peak from mean textured diffraction signal. The procedure is based on local rules without interpolation functions permitting to detect possible recrystallization peaks independently from texture peaks. The algorithm first detects all fluctuations on 1D azimuthal intensity profiles by searching points having lower intensity values on its left and right sides (finally an upward segment followed by a downward segment along the profile) and measure the total height of the detected fluctuation (difference between the maximum intensity value and the lowest value detected on its sides). Fluctuations are then numbered and the statistical distribution of their heights is calculated. A threshold value has also been considered in the algorithm to avoid counting statistical fluctuations of the signal (background noise). This value was calibrated in order to avoid 90% of statistical fluctuations recorded at room temperature, i.e. in the absence of recrystallization peaks. In such a manner, the purely statistical fluctuations are excluded from recrystallization peaks counting. As a consequence, the method is sensitive to the angular resolution chosen for azimuthal integration. It is thus impossible to interpret the absolute number of detected peak because one recrystallization peak does not necessarily correspond to one new single grain. However, the relative evolution of recrystallization peak number is believed to be representative of the bulk recrystallization kinetics.

As the sample was not rotated during the experiment, it is impossible to get diffraction signals from all newly recrystallized grains. As a consequence, new grains from certain texture fibers will never be in diffraction conditions. To reduce the associated bias, we have conducted our analysis systematically on different rings below Ac_1. In the studied steels, it happens that the evolutions of recrystallization peak densities deduced from these rings remain similar. DP steels are in fact known to show very limited recrystallization textures contrary to fully ferritic steels or aluminum alloys [PER'10, RAY'85, KAN'11]. As a consequence, this source of uncertainty is neglected in the present work, but this question is certainly worth to be investigated and this bias to be quantified in the future using more complex diffraction set-ups.

4.2.3.c Isothermal condition: results and interpretation

The recrystallization peak counting method detailed above was utilized to estimate recrystallization kinetics during isothermal holdings and during continuous annealing at constant heating rate, as detailed in introduction. Only the isothermal treatment at 650°C will be considered in the

following, since no evolution was detected at 450°C and 550°C (suggesting the absence of recrystallization at such low temperatures).

Figure 4.9(a) displays the evolution of the counted recrystallization peaks as function of the time (black dots) on recorded $(200)^{\alpha}$ DS rings during the isothermal treatment at 650°C. With the procedure described above, the number of detected peaks remains close to zero up to 30s and increases rapidly to a maximum value of approximatively 130 peaks after 150s. The evolution shows a sigmoidal shape with a saturation plateau after 150s. The weak scattering of the experimental values around the mean evolution clearly sustains our approach. The same work was conducted on other rings with similar conclusions (same relative trends but not same absolute numbers of peaks).

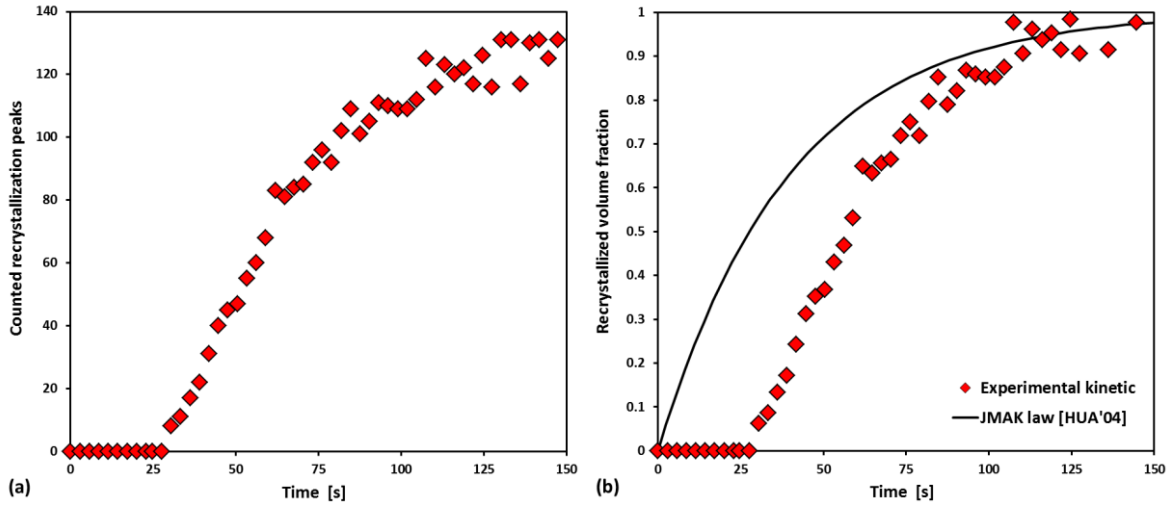

Figure 4.9: (a) Counted recrystallization peaks as function of the time (black dots) on recorded $(200)^{\alpha}$ DS rings during the isothermal treatment at 650°C (b) Deduced recrystallization kinetics assuming that full recrystallization is achieved when saturation value is reached in Fig. 4.9(a). The JMAK equation from Huang *et al.* [HUA'04] is plotted for the sake of comparison (black curve).

The evolution of the absolute number of new individual spots on diffraction rings can only be *stricto sensu* related to the nucleation process of new recrystallized grains, as shown by Savran *et al.* [SAV'10] when studying the early stages of ferrite to austenite transformation. This is also implicitly the hypothesis made by Jensen et al. [LAU'03, LAU'06, POU'11]. However, if one considers as a first estimate that the growth of new recrystallized grains is limited and hence, that the recrystallization kinetic is dominated by nucleation, then the relative evolution of new recrystallization peaks is directly correlated to the recrystallized fraction of the studied phase. The assumption that the growth of recrystallized grains is limited in the studied case is confirmed by our SEM observations presented in chapter 2, as well by the fact that the shapes of the individual spots do not evolve on successive 2D diffraction patterns during heating revealing the absence of lattice curvatures in new grains. However, we will discuss this assumption at the light of our modeling's results. As a recrystallization peak cannot be attributed to a single grain with certainty because of our counting procedure, it is not possible to keep track of the intensity of a single grain.

The number of counted peaks has thus been divided by the value found on the plateau after 150s (supposed fully recrystallized ferrite state) to provide a normalized density representative of the bulk recrystallization progress. The evolution deduced from HEXRD measurements is represented in Figure 4.9(b). The deduced function shows a sigmoidal shape as expected from recrystallization kinetics.

This recrystallization kinetics is in agreement with the calibrated JMAK equation proposed by Huang *et al.* [HUA'04] for Mo-free Fe-C-Mn-Si alloys (n = 1, Q = 350kJ.mol^{-1}, b_0 = 1.6x10^{18} s^{-1}), reported in

Figure 4.9(b) for the sake of comparison. Except that the model does not predict any incubation time, the slopes of sigmoidal shape kinetics are essentially the same. Applying the same empirical model at 550°C leads to final recrystallized fraction of less than 5% after 600s, which is also consistent with our experiments (no spots detected at 550°C on the DS rings and thus almost no recrystallization).

4.2.3.d Continuous heating: results and interpretation

Figure 4.10(a) shows the evolution of the counted recrystallization peaks as function of the temperature on recorded $(200)^{\alpha}$ DS rings for slow (blue dots) and fast heating (black dots) experiments. For the low heating rate, the number of detected peaks remains close to zero up to 670°C and suddenly increases to a maximum value of approximatively 225 peaks at 720°C. The increase shows a sigmoidal shape with a saturation plateau after 720°C. Above 740°C, the number of detected peaks decreases again. The first significant recrystallization peak appears at 670°C, when the dislocation density drops rapidly (cf. Fig. 4.6(b)). The concomitance between both events is noteworthy and thus provides a convincing and precise measure of the recrystallization start temperature for the studied steel relative to the studied heating conditions (670°C at $3°C.s^{-1}$). Above 740°C, Figure 4.10(a) shows that the number of recrystallization peaks on DS rings decreases. For the high heating rate, a similar evolution is observed, except that the first peaks are detected around 740°C and the plateau is reached at 780°C.

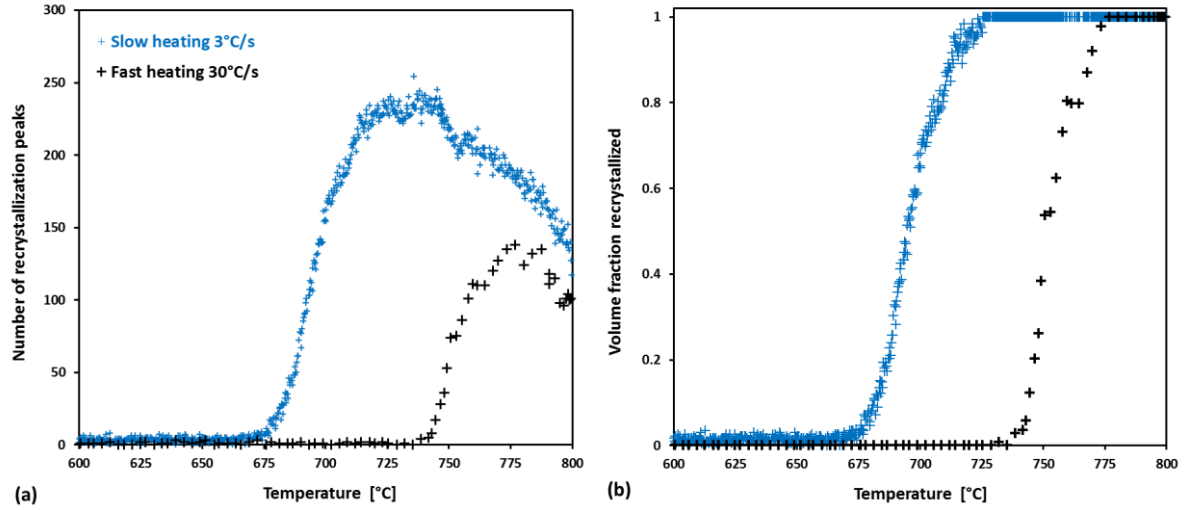

Figure 4.10: (a) Evolution of the number of recrystallization peaks as a function of temperature on recorded $(200)^{\alpha}$ DS rings during low (blue) and fast heating (black), respectively (b) Deduced recrystallization kinetics for both cases.

Considering the reasoning conducted in the previous section, recrystallization kinetics have been determined from these measurements, assuming that fully recrystallization is achieved when the plateau value is reached (at 730°C at $3°C.s^{-1}$ and at 780°C at $30°C.s^{-1}$). The curves are presented in Figure 4.10(b) for both continuous annealing schedules. At low heating rate, the austenite transformation starts nearly 10°C before the full completion of recrystallization, meaning that the interaction between recrystallization and phase transformation is negligible. On the contrary, at high heating rate, they are concomitant, confirming our SEM experiments presented in chapter 2. This result is also in good agreement with numerous previous reports on similar steels under similar heating conditions [HUA'04, KUL'13, FON'15,

ALL'15, ZHG'13]. The same work was conducted on other rings with similar conclusions (same relative trends but not same absolute numbers of peaks), as shown in Figure 4.11.

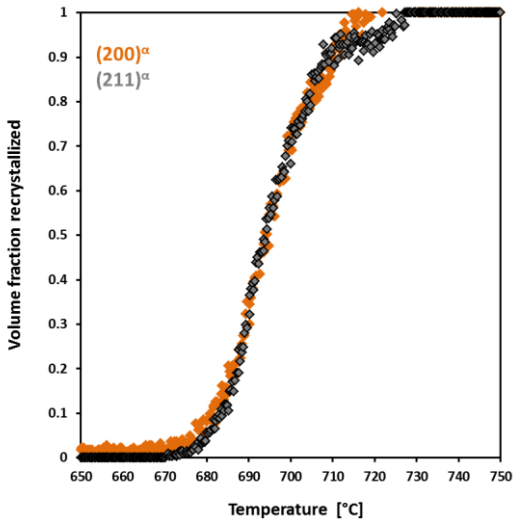

Figure 4.11: Recrystallization kinetics determined applying the spot counting method on (200)α and (211)α DS rings, colored in orange and grey, respectively.

The observed decrease in the number of peaks after saturation is probably due to the austenite transformation onset that broadens the individual diffraction spots, making them less as detectable as the recrystallization peaks. Consequently, the number of diffraction peaks must be considered with caution above Ac_1 (risk of underestimation).

Nonetheless, to assess the validity of our determination method, we have compared our experimental kinetics to the prediction of the calibrated JMAK law from Huang *et al*. [HUA'04] for Mo-free Fe-C-Mn-Si alloys considering the integration scheme of Li *et al*. [LI'13]. Figures 4.12(a) and (b) shows the performances of the model when considering the experimentally measured recrystallization start temperatures (670°C and 730°C for the low and high heating rates) or adjusted recrystallization start temperatures to get the best fit (680°C and 740°C for the low and high heating rates). The correlation between the empirical model and the experimental results is noteworthy confirming here the global validity of our experimental development. The extent of the temperature ranges for both heating conditions (about 50°C) is in particular well reproduced. The calibrated JMAK framework of Huang *et al*. is thus an interesting solution to model recrystallization kinetics of the studied steels in isothermal and continuous annealing conditions. This is the modeling strategy for instance followed by Ollat [OLL'17b], Li [LI'13]. However, as it does not describe the nucleation process properly, it remains not predictive and must be calibrated for each studied steels, particularly if specific alloy components delaying recrystallization are present (Mo for instance). For this reason, we have preferred instead to develop our own physically based model, inspired from Zurob *et al*. [ZUR'06].

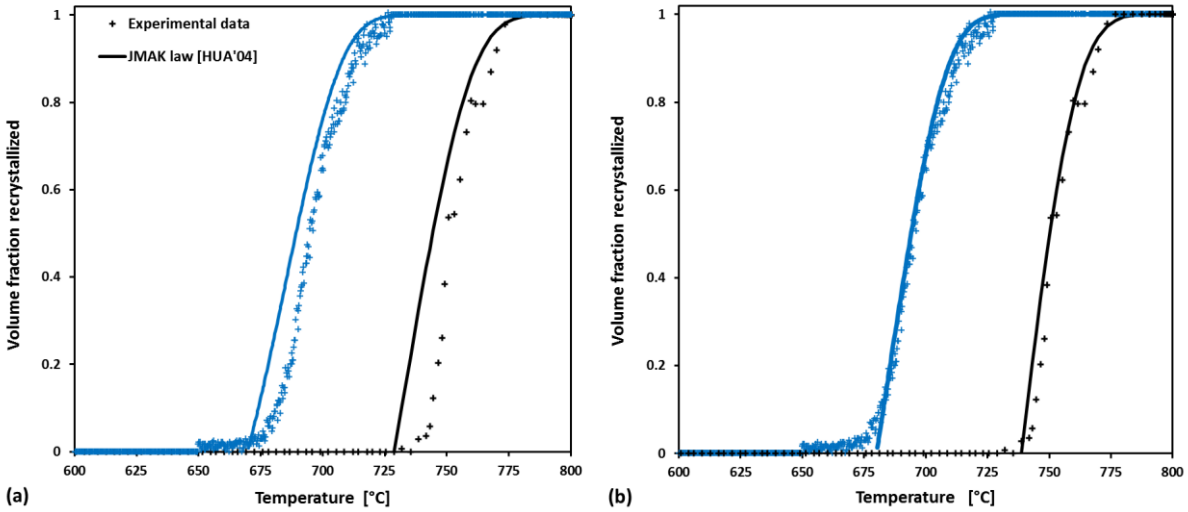

Figure 4.12: Comparison between the experimental recrystallization kinetics and the calibrated JMAK law from Huang *et al*. [HUA'04] for Mo-free Fe-C-Mn-Si alloys when: (a) imposing the measured start temperatures (670°C and 730°C for the low and high heating rates) or (b) adjusting recrystallization start temperatures T* to get the best adjustment (680°C and 740°C for the low and high heating rates respectively).

4.2.4 Discussions

In this section, our HEXRD measurements are confronted to direct SEM observations of partially recrystallized microstructures. Figures 4.13 (a)-(b) show the EBSD maps obtained on 700H3 and 710H3 samples, respectively. ESBD map have been post-treated to highlight the Grain Orientation Spread (GOS). As noticed by Radwański [RAD'15], non-recrystallized domains (in green and in red, GOS value higher than 1.5°) present a higher spread than recrystallized grains (in blue, GOS value lower than 1.5°). At 700°C, the microstructure is still obviously non-fully recrystallized. The recrystallized volume fraction is about 73%. At 710°C, the same method illustrated in Figure 4.13(b) gives a recrystallized fraction of 87%. These values given by EBSD appear to be in a good agreement with those determined by HEXRD. The careful investigations of a supposed fully recrystallized state at 720°C by SEM (cf. Fig. 2.8(c-d)) of the previous chapter, 720H3 sample) show also large non recrystallized domains.

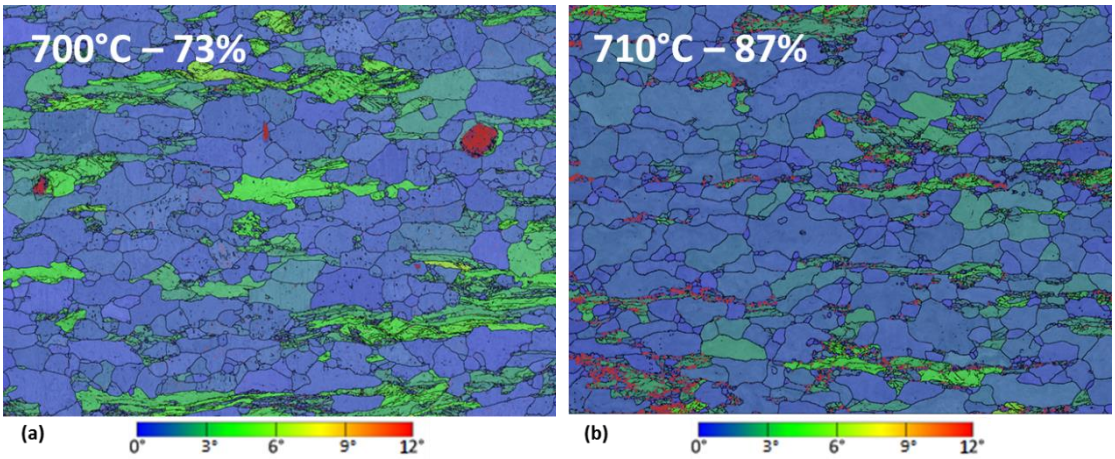

Figure 4.13: EBSD maps of the Grain Orientation Spread (GOS) of samples (a) 700H3 and (b) 700H30 respectively. The estimated volume fractions of recrystallized ferrite are 73 and 87%.

A detailed observation of microstructures reveals that the non-recrystallized domains in fact correspond systematically to the former lamellar pearlite islands. It is likely due to the presence of fragmented carbides which delay the recrystallization of ferrite in these islands. When observing the microstructures even above Ac_1, it appears that the former pearlite islands are never recrystallized prior to austenite transformation. As a consequence, it may be expected that the kinetics deduced from our HEXRD experiments corresponds solely to the recrystallization state of the ferritic matrix. The recrystallized fraction provided by our EBSD measurements must in fact be corrected with respect to the fraction of ferrite (84% before austenite transformation). As a consequence, the relative recrystallized fractions are thus 87% at 700°C and 100% at 710°C, respectively.

This conclusion is reinforced when studying the microstructures of the steels heated at $30°C.s^{-1}$. Even if no EBSD observations were conducted on samples heated at $30°C.s^{-1}$, the recrystallized fractions were roughly estimated by point counting on the SEM micrographs presented in chapter 2 (on a single low magnification micrograph). The measurements are reported in Table 4.A. As austenite transformation is concomitant to recrystallization, the total fraction of remaining ferrite (total ReX fraction) was also estimated as well as the relative recrystallized fraction (relative ReX fraction). In this particular case, the relative recrystallized fractions (recrystallization state in the ferritic matrix only) measured by SEM are close to the values determined by HEXRD.

Sample	T°C	Total ReX fraction	Fraction of Ferrite	Relative ReX fraction
700H3	700	0.73(GOS)	0.84	0.87
710H3	710	0.87(GOS)	0.84	1.00
740H30	740	0.17(SEM)	0.84	0.20
750H30	750	0.26(SEM)	0.84	0.31
760H30	760	0.32(SEM)	0.82	0.39
770H30	770	0.41(SEM)	0.76	0.54

Table 4.A: Total and relative recrystallized volume fraction. This latter correspond in fact to the recrystallized fraction in the sole ferrite matrix taking into accounting pearlite islands and/or austenite. The experimental method used to determine the total fraction is indicated into brackets.

For both heating rates, these relative recrystallized fractions were compared to the fractions determined with our new procedure in Figure 4.14. It appears that the agreement is rather satisfying, justifying that the measurement provided by our new method is representative of the recrystallization state of the sole ferritic matrix. In fact, the same discussion probably holds for recovery processes which occur both in ferritic matrix and in pearlitic islands. Recovery process is likely slower in pearlitic islands than in the ferritic matrix, meaning that measured recovery is essentially due to that occurring in ferrite.

These conclusions have two important consequences: first, the data provided by HEXRD can be directly reproduced by a model for fully ferritic steels (neglecting in fact the presence of pearlite). Second; the method can be applied regardless the initial faction of pearlite (recovery and recrystallization).

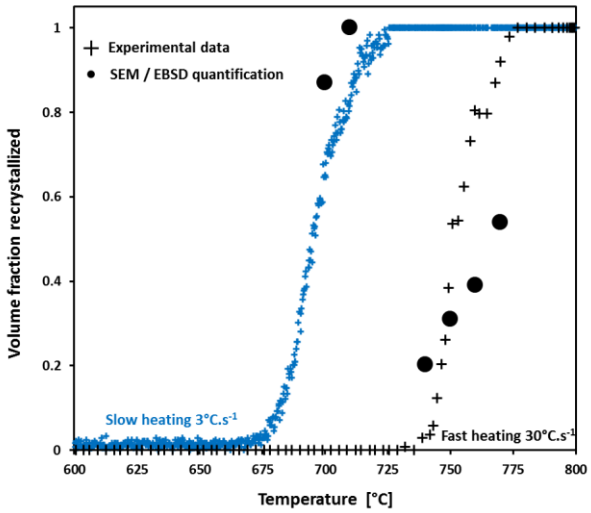

Figure 4.14: Comparison between the recrystallization kinetics deduced from our HEXRD measurements and relative recrystallized fractions (recrystallization state of the sole ferritic matrix) measured by SEM-EBSD (data from Table 4.A) (black circles)

4.3 Modeling

In this third section of chapter, we will present a new modeling approach developed in the frame of the PhD to predict coupled recovery and recrystallization processes in the studied steels.

All the physical models for recrystallization estimate the driving force G for the growth of new grains thanks to the stored energy in the deformed structure [HUM'04]. This stored energy is directly proportional to the density of dislocations ρ:

$$G = \frac{1}{2}\mu b^2 \rho \tag{4.11}$$

with μ the shear modulus and b the Burgers vectors. The estimation of the dislocation density during annealing, hence the recovery, is thus a prerequisite to model recrystallization.

4.3.1 Recovery

As shown in the literature review, different equations are proposed in literature to model the evolution of the dislocation density ρ as a function of time t and temperature T. The empirical equations of Senuma *et al*. [SEN'08] do not permit to reproduce the experimental trends observed in our work and in particular the rapid initial stage in isothermal conditions during the first 200s at 450°C and 550°C even after calibration (cf. Fig. 4.15). The model developed by Verdier *et al*. [VER'98] was able to reproduce some trends but not enough to get a perfect agreement despite its complexity. This is the reason why we have preferred to use the original relaxation model of Friedel *et al*. [FRI'64], even though the final agreement is not perfect:

$$\frac{d\rho}{dt} = -K\exp\left(\frac{-U_0 + V\alpha M\mu b\sqrt{\rho}}{kT}\right)\frac{2\sqrt{\rho}}{\alpha M\mu b} \tag{4.12}$$

U_0, V and K have been considered as calibration parameters and adjusted to best reproduce not only the recovery process under isothermal conditions (450 and 550°C, mainly) but also during continuous

annealing. α was set to 0.15, M to 3, b to 2.5 10^{-10} m. The model of Ghosh and Olson [GSH'02] was employed to model the evolution of the elastic constants as a function of the temperature:

$$\mu(T) = 8.407\left(1 - 0.48797\left(\frac{T}{1043}\right)^2 + 0.12651\left(\frac{T}{1043}\right)^3\right) \times 10^{10}\ N/m^2 \qquad (4.13)$$

The results of the model with U_0=180 kJ.mol^{-1}, V = 30 b^3 and K = 10^{13} Pa are compared to the previous experimental results in Figure 4.15. The model does not achieve a perfect agreement with the experimental data, except in the case where both activation energy and volume are considered temperature-dependent. The introduction of such dependence as suggested by Verdier *et al.* [VER'98] requires additional parameters which do not improve significantly the performance of the associated recrystallization model. However, it reproduces well the observed experimental trends, namely the rapid recovery which occurs during the first 200s and the sensitivity to both temperature and heating rate. Thus, the model is considered as satisfying, even though the recovery at 650°C is underestimated. This difference likely arises from the recrystallization process which took place during the first 150s. Because Friedel's model [FRI'64] only considers that relaxation is due to the dislocation density diminution, the dilution effect to new defect-free grains induced by recrystallization is not modeled. This difference is also observed during continuous annealing at low heating rate (cf. Fig. 4.16(a)) when recrystallization occurs at 650°C.

The values of physical parameters retained for the simulations are consistent with those found in literature. The activation energy (180 kJ.mol^{-1}) is a fraction of the one for bulk iron diffusion (2/3). It could be consistent with a pipe diffusion process (150 kJ.mol^{-1} or 174 kJ.mol^{-1} for dislocation core diffusion according Stechneur and Nes, respectively [NES'95, STE'14]). The activation volumes are also similar to the ones proposed by Verdier *et al.* (about 40 b^3 in Al at 120°C) [VER'98] and by Zurob *et al.* (35 b^3 in austenite at high temperature) [ZUR'06].

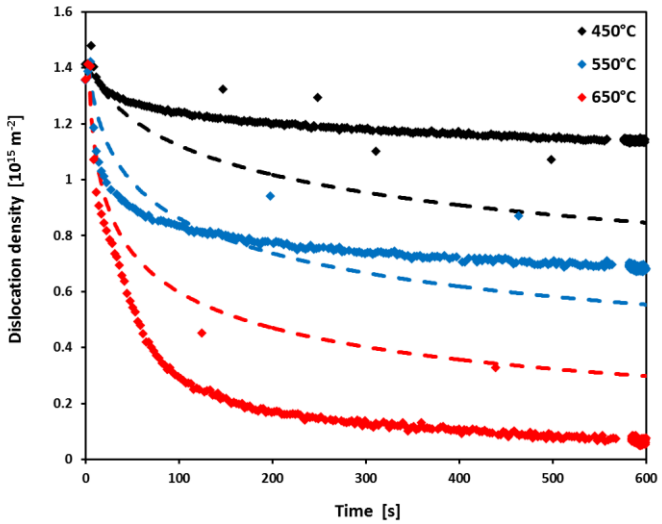

Figure 4.15: Comparison between experimental data of Fig. 4.6 and Friedel's recovery model (dashed lines) for the isothermal treatments. Black, blue and red curves correspond to holdings at 450, 550 and 650°C, respectively.

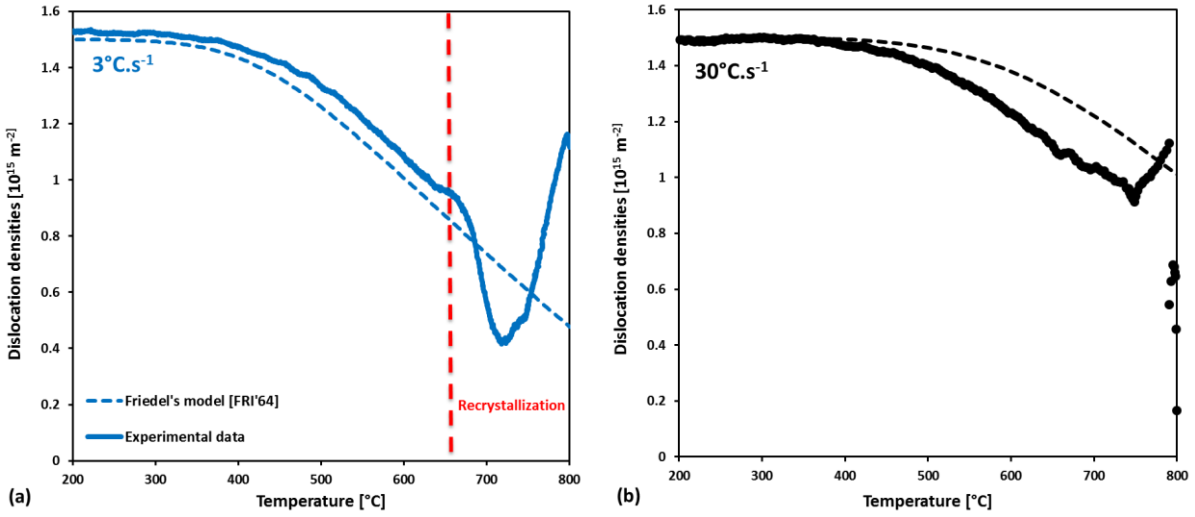

Figure 4.16: Comparison between experimental data of Figure 4.6 and Friedel's recovery model (dashed lines) for continuous heatings: (a)-(b) slow heating treatment (3°C.s^{-1}) and fast heating experiments (30°C.s^{-1}), respectively.

4.3.2 Recrystallization

4.3.2.a Constituting equations

The proposed modeling is largely adapted from Zurob *et al*. [ZUR'06, REH'13]. It first describes nucleation flux considering that only the largest sub-grains can evolve into a new recrystallized grain (according to the SIBM theory). The probability of this nucleation event depends on a critical radius r_c, calculated according the Classical Nucleation Theory. Contrary to the scheme of Zurob *et al*., our nucleation sites are well isolated (cf. SEM observations made in chapter 2). Our nuclei do not enter in competition contrary to austenite recrystallization. Hence, all the active nuclei grow independently (no site saturation around a former deformed grain). This simplification permits to apply the extended volume framework proposed by Sinclair *et al*. [SIN'07]. For more details about the origin of these equations, please refer to the original work of Zurob and Sinclair.

The first step of the model consists in calculating the subgrain size in non-recrystallized ferrite. These subgrain structures are also revealed by chemical etching, as seen in Figure 2.19(a-b) for fast heating experiments (cf. chapter 2). Their typical radius is of the order of the micrometer. It is in fact difficult to provide more precise measures due to their anisotropy, the possible 3D shapes and because they are not systematically revealed by chemical etching. The boundaries of such cells are characterized by low angle misorientation. Zurob *et al*. [ZUR'06] assumed that their mean radius was governed by both the mobility of their interface and by the density of defects as follows:

$$\langle r(t)\rangle = r_0 + \int_0^t \frac{2}{L} D_{Fe}(T) \sinh\left(K_{ad}\frac{\sigma b^2 L}{kT}\right) dt \qquad (4.14)$$

with r_0 the initial size of sub-grain structure inherited from cold-rolling process. K_{ad} is a calibration parameter (value in the order of the unity). L is the net spacing of dislocation pinning centers [REH'13], calculated using relation (4.15):

$$L = \frac{1}{K_1\sqrt{\rho}} \qquad (4.15)$$

where K_1 is a parameter close to unity. σ is a function accounting for a forest-type dislocation storage [SAA'60], such that:

$$\sigma = \alpha M \mu b \sqrt{\rho} \tag{4.16}$$

with M is the Taylor factor equal to 3.1 for fcc and bcc phases [ZUR'06], b the burger's vector and α a constant equal to 0.15.

D_{Fe} is the bulk self-diffusion of ferromagnetic bcc iron. In this work we used the value proposed by Stechneur *et al*. (in $m^2.s^{-1}$) [STE'14]:

$$D_{Fe}(T) = 6 \times 10^{-4} \exp\left(-\frac{285000}{RT}\right) \tag{4.17}$$

The same activation energy was employed by Nes [NES'95] (280 $kJ.mol^{-1}$) and suggested for ferromagnetic ferrite by Kučera [KUC'82] (292 $kJ.mol^{-1}$). These values are also similar to those reviewed by Zhang in 2014 [ZHA'14a]. The whole model is extremely sensitive to the choice of this diffusion coefficient which in fact controls nucleation process.
The critical radius for nucleation r_c is given by:

$$r_c = \frac{2\gamma}{\frac{1}{2}\Delta\rho\mu b^2} \tag{4.18}$$

with γ the interfacial energy of high angle boundary (surface energy of the new recrystallized grains) and Δρ the difference in dislocation density and the recovered grain. This is the size that a sub-grain must reach to possibly become a new grain. If we assume that new grains are defect-free, it comes: Δρ=ρ. This dislocation density is given by the recovery model detailed above. As the density of dislocations decreases along the thermal treatment, the driving forces for recrystallization decreases while the critical radius increases in turn.

The main innovation brought by Zurob *et al*. [ZUR'06] model is to introduce the distribution subgrain size knowing its mean value <r>. Such a distribution follows a Rayleigh law. Hence the fraction of subgrain having a size greater than the critical radius r_c is given by:

$$f(t) = \int_{\frac{r_c}{\langle r \rangle}}^{+\infty} \frac{\pi}{2} \frac{r}{\langle r \rangle} \exp\left(-\frac{\pi}{4}\left(\frac{r}{\langle r \rangle}\right)^2\right) d\left(\frac{r}{\langle r \rangle}\right) \tag{4.19}$$

This integral can be calculated analytically, yielding to:

$$f(t) = \exp\left(-\frac{\pi}{4}\left(\frac{r_c}{\langle r \rangle}\right)^2\right) \tag{4.20}$$

This equation tells for instance that if the critical radius is twice higher than the mean subgrain size, then the probability to find a cell larger than this critical value is less than 5%. In contrast, if the mean subgrain size is equal to the critical size, the probability increases up to 46%. Figure 4.17 shows for instance the evolution of calculated r_c and <r> during a continuous annealing after calibration of the model. The orders of magnitude are consistent with the SEM observations of previous chapter 2. Above 650°C, as <r> increases faster than r_c with the temperature, the number of subgrains with a size above r_c will statistically increase and thus the number of available nuclei will increase in turn. This increase will therefore occur as soon as the derivative of function *f* becomes positive (start of recrystallization process).

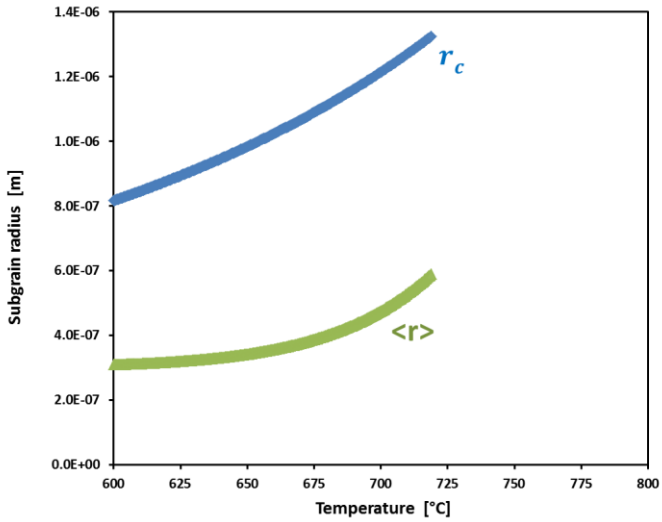

Figure 4.17: Evolution of r_c and <r> during the continuous annealing after calibration of the model (3°C.s^{-1}).

Zurob *et al.* [ZUR'06] established that the increase in the number of the active nucleus N is directly proportional to the increase in f. It describes in facts the competition between the decrease of the recrystallization driving force due to recovery and the thermally activated motion of low angle boundaries. Since nucleation event takes place at former grain sizes (under the assumption of SIBM), the nucleation flux will also depend on the available sites on deformed ferritic grain. Nevertheless, as new grains do not seem to enter in competition, we did not introduce the function F_n proposed by Zurob to describe the saturation of available nucleation sites. This simplification leads to:

$$\frac{dN}{dt} = \frac{df}{dt}\frac{S_v}{A_c} \tag{4.21}$$

with S_v the surface of deformed ferritic grain per volume unit and A_c the actual surface of critical nuclei. S_v is given by an empirical equation as a function of the applied strain ε and initial ferritic grain size D:

$$S_v = \left(\frac{24}{\pi D}\right)(0.491e^{\varepsilon} + 0.155e^{-\varepsilon} + 0.143e^{-3\varepsilon}) \tag{4.22}$$

and A_c is given by (4.23):

$$A_c = \pi(r_c)^2 \tag{4.23}$$

Once the nucleation flux is known, the extended recrystallized volume X_{ext} corresponds to number of active nuclei multiplied by the mean volume of recrystallized grains $\bar{R}$ (4.24):

$$X_{ext} = N\frac{4}{3}\pi\bar{R}^3 \tag{4.24}$$

The evolution of the radius R of a given grain is governed by a mobility equation (4.25):

$$\frac{dR}{dt} = M_{HAB}G \tag{4.25}$$

with M_{HAB} the mobility of high angle boundary and G the driving force of recrystallization, i.e. the energy stored in dislocation structures, given by (4.26):

$$G = \frac{1}{2}\mu b^2 \Delta\rho \tag{4.26}$$

As the new recrystallized grains are formed progressively as function of time, it produces a size distribution *f*. To avoid the tedious calculation of the evolution of the distribution function, only the mean radius $\bar{R}$ of the size distribution *f* was tracked. At a given time step, it must account concomitantly for the increase of the radius of ever nucleated grains and also that of the newly nucleated ones during the previous time step. These new grains will of course contribute to slow down the evolution of the mean radius $\bar{R}$. It thus comes:

$$\frac{d\bar{R}}{dt} = M_{HAB}G + \frac{dN}{Ndt}(r_c - \bar{R}) \tag{4.27}$$

This equation, used by [LAN'12] to deal with precipitation, permits to avoid the manipulation of explicit size distribution functions. The increase in mean radius $\bar{R}$ can be then integrated step by step, assuming that the initial grain size of the first nucleated grains is r_c.

The key of such model is the calibration of the equation describing the interface mobility M_{HAB}. Figure 4.18 illustrates a comparison between the thermally activated models with interface mobilities found in literature. For pure iron, the calibrated reference equation (4.28) was proposed by Hillert in 1975 [HIL'75]:

$$M_{Hillert} = 0.035 \exp\left(-\frac{177000}{RT}\right) \tag{4.28}$$

The equation proposed by Zheng [ZHG'13] or that from Turnbull [SIN'07, ZUR'06] for pure iron lead to similar order of magnitude:

$$M_{Zheng} = \frac{0.429}{T}\exp\left(-\frac{120000}{RT}\right) \tag{4.29}$$

$$M_{Turnbull} = \frac{2.04}{T}\exp\left(-\frac{148000}{RT}\right) \tag{4.30}$$

The parameters in the Turnbull function were calculated using the activation energy for iron self-diffusion at grain boundaries given by Sinclair *et al*. [SIN'07]. However, the latter mobility values are probably relevant for pure iron but are too high relative to our studied driving forces and temperatures. In fact, if we consider a driving force of about 1 MPa (corresponding to a density of dislocations ρ = 1.4x10^{15} m^{-2}), Turnbull model gives for instance a total displacement of the boundary of 66 mm at 650°C during 150s, which seems unrealistic for the studied alloys. This discrepancy is probably explained by the presence in the studied steel of substitutional alloying elements but also numerous carbides in the ferritic matrix that will slow down the interface movement by pinning effect. This is probably the reason why Zhu *et al.* [ZHU'15b] proposed mobility values far lower (4.31) to deal with ferrite-pearlite steels:

$$M_{Zhu} = 1.2 \times 10^5 \exp\left(-\frac{325000}{RT}\right) \tag{4.31}$$

This equation presents however a too high temperature sensitivity (too high activation energy) even though it conducts to realistic interface motion in the studied conditions (64 µm at 650°C during 150s). This is the reason why we finally decided to adopt a modified Turnbull expression (4.32), as Zurob and Sinclair. The Turnbull mobility is in fact an upper bound and can be parametrized using a calibration factor β (typically higher than 0.1 for austenite):

$$M_{HAB} = \beta\frac{2.04}{T}\exp\left(-\frac{148000}{RT}\right) \tag{4.32}$$

To obtain reasonable values for our interfaces we applied this expression with a low beta value (β = 0.05). Our final mobility equation shows thus the same activation energy than the one retained for pure

iron but with a lower pre-exponential factor to account for alloying elements and possible pinning effect by the carbides which slow down the interface movements.

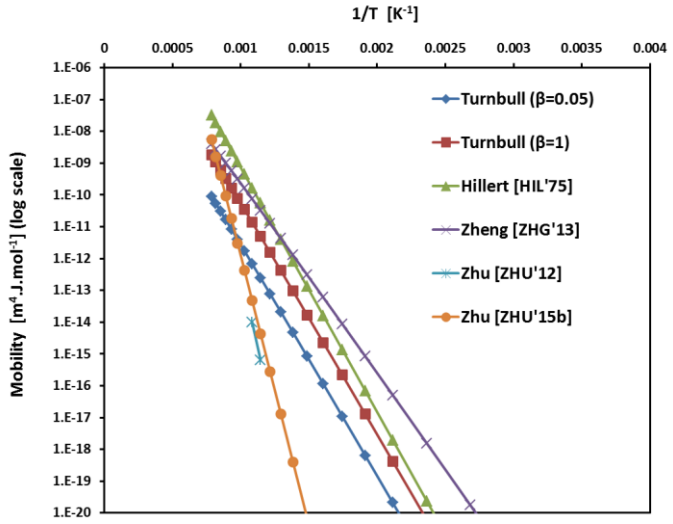

Figure 4.18: Interface mobility proposed by different authors for high angle boundary in ferrite.

Finally, the recrystallized fraction X is given according the extended volume theory (4.33) [SIN'07]:

$$X = 1 - exp(-X_{ext}) \tag{4.33}$$

4.3.2.b Calibration of the model and discussion

The parameters of the model were calibrated on the experiments presented above (isothermal holding at 650°C and continuous heating at 3 and 30°C.s^{-1}). The free parameters are the initial size of dislocation cells r_0, the surface energy of high angle boundaries γ as well as the K_1 and K_{ad} parameters controlling the low angle boundaries mobility.

The initial size of subgrain was set to r_0 = 0.3 µm, in accordance with our SEM observations. The surface energy γ was set to 400 mJ.m^{-2}, close to the value proposed by Sinclair *et al.* [SIN'07] for ferritic steels (600 mJ.m^{-2}) or by Zhu *et al.* [ZHU'12] (800 mJ.m^{-2}) . For the calculations in this section, we used the initial density of dislocations calculated with the micromechanical model of strain partition (ρ = 2.2x10^{15} m^{-2} instead of 1.4x10^{15} m^{-2}, as experimentally measured) to be able in the future to couple both models seamlessly. Accounting for the volume driving force available in the studied steel, it leads to a critical radius for nucleus of about 0.8 µm, which seems consistent with our experimental observations. K_1 and K_{ad} were set to 12.0 and 2.0, respectively, to obtain a reasonable agreement with the experimental data. These values are close to the one used by Rehman [REH'13]. The results of the model are compared with the recrystallization kinetics determined via our new method (diffraction spots) during the continuous heating experiments (cf. Fig.14(a)) and isothermal holding at 650°C (cf. Fig.14(b)). The previous equations were solved explicitly and sequentially (integration step time = 0.15s) with Excel. For the three studied cases, the agreement is noteworthy, in particular the description of the incubation period (T* in fact), well captured by the model. The simulation of the isothermal holding at 550°C (not represented here) shows the absence of recrystallization, as observed experimentally. It sustains our choice for the activation energy in the equation (4.17). The slopes of the kinetic curves as well as the extent of the temperature ranges in which recrystallization occurs are also rather well captured.

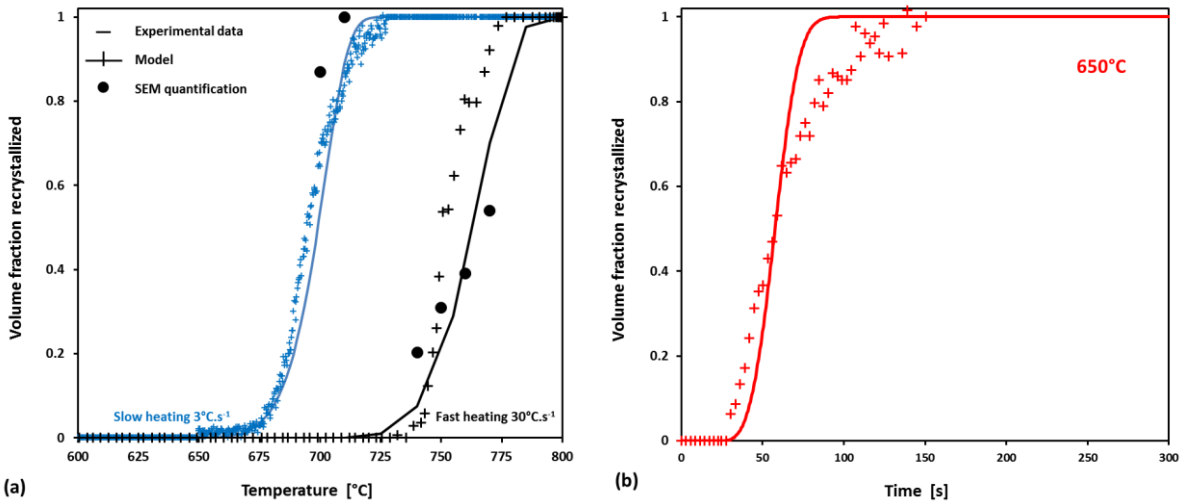

Figure 4.19: Experimental (HEXRD and SEM) and simulated recrystallized fraction for the studied annealing schedules. (a) As a function of temperatures during continuous annealing at slow and fast heating rates and (b) as function of time during an isothermal holding at 650°C.

Figures 4.20 represent the evolutions of the mean recrystallized grain size and the density of nuclei N as a function of the temperature for the continuous annealing schedules (slow and fast heating rates are represented in blue and black, respectively). The numbers of nuclei during the active stages of recrystallization , i.e. between 650°C and 710°C for the low heating rate and between 730°C and 780°C) are about 0.5×10^{16} and 3×10^{16} nuclei per m^3, respectively. These values correspond to mean distances separating the nuclei, being 5.8 and 4.6 µm, respectively. It is consistent with our experimental observations (cf. Chapter 2) and also with the values found in literature. Zhu *et al*. [ZHU'15b] calculated 400 nuclei per 40 μm^3, (0.6×10^{16} nuclei per m^3), hence a distance of 7.6 µm for similar steels. In contrast, Sinclair *et al*. used a significantly lower value (0.05×10^{16} nuclei.m^{-3}), but for a steel having far larger initial grain size [SIN'07]). The predicted mean radii of recrystallized grains are about 7 and 4 µm, respectively, at the end of the active recrystallization stage within an assumed unlimited volume. These values are consistent with the observed microstructures in 710H3 and 800H30 samples, but are overestimated by construction (extended volume theory). These grain sizes are much larger than the critical radius for nucleation, indicating that the growth process is not necessarily as negligible as supposed in previous section. The volume of the sole nuclei represents in fact a transformed fraction of about 5%. Nevertheless, it appears that the nucleation flux alone is almost sufficient to reproduce the observed global kinetics. Figure 4.21 shows for instance the predicted kinetics considering constant recrystallized grain sizes during continuous heating. Their values were set to 5 and 3 µm for slow and fast heating rates, respectively, to obtain a good agreement. It reinforces the fact that the recrystallization kinetics is essentially governed by the nucleation process, supporting here our assumption to treat our HEXRD experiments. However, this question remains to be discussed more in details and further explored.

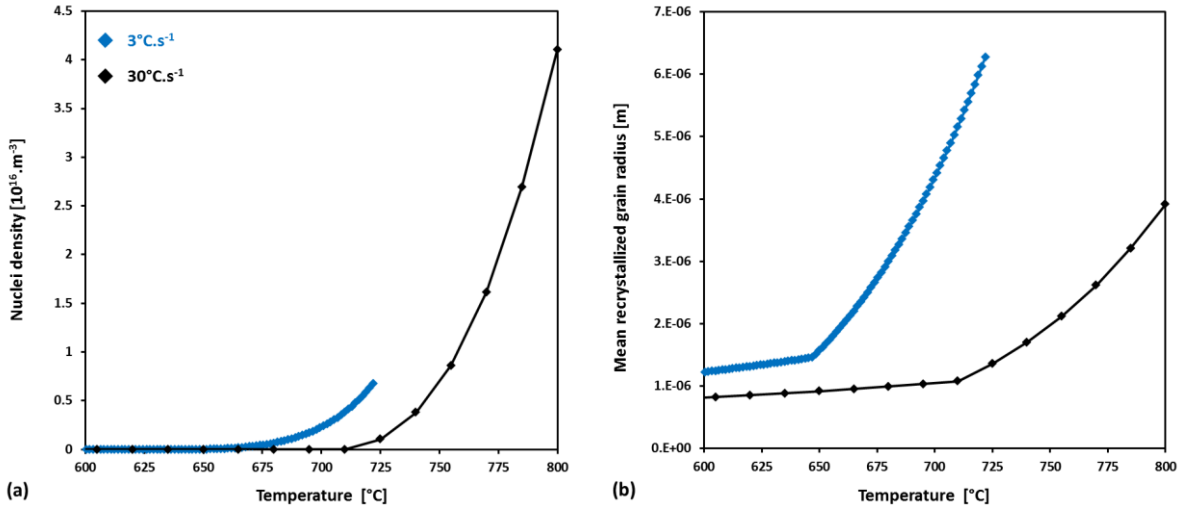

Figure 4.20: Evolutions of (a) the integrated density of nuclei N and (b) the mean recrystallized grain size $\overline{R}$ as a function of the temperature for the continuous annealing schedules. Slow and fast heating rates are represented by the blue and black curves, respectively).

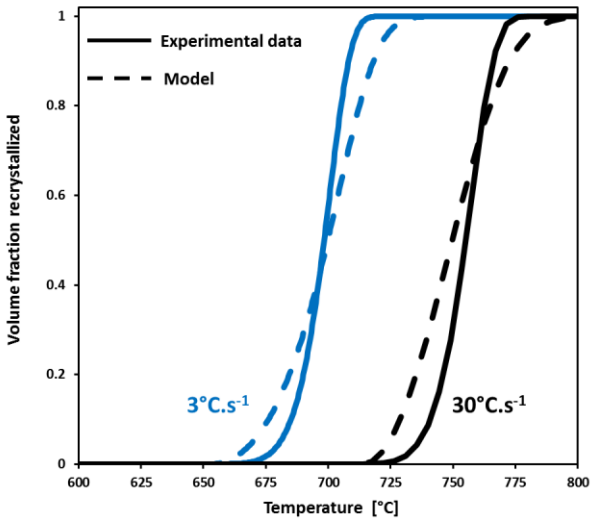

Figure 4.21: Comparison between the prediction of the model considering increasing mean radii (continuous lines) and constant mean radii (dashed lines). The mean grain sizes were set to 5 µm and 3 µm for slow and fast heating rates, respectively to obtain a good agreement.

4.3.2.c Effect of the cold-rolling ratio

Recrystallization kinetics is strongly sensitive to the deformation state [DOH'97]. In most cases, the higher the deformation, the higher the driving force is for the transformation [ZHA'14b, LIU'16]. In this thesis (cf. Chapter 2 for instance), we mainly focused our interest on a heavily deformed ferrite/pearlite structure (61% cold-rolling ratio). Nevertheless, we also performed several *in situ* experiments on a less deformed material (33% reduction, 3°C.s^{-1} heating rate). The micromechanical model of Bouaziz *et al.* [BOU'02] was again employed to calculate the strain partition between ferrite and pearlite for less severe conditions as well as the expected dislocation densities in ferrite prior annealing. Figure 4.22(a) shows the calculated behavior of phases during the cold-rolling operation while Figure 4.22(b) displays the dislocation density as function of the cold-rolling ratio. When stopping the rolling after only 33% reduction, the dislocation density in ferrite is significantly lower than after 61% (namely 0.70x10^{15} m^{-2}

instead of 2.40x10^{15} m^{-2}), in accordance with the local deformation in ferrite which is lower (0.47 instead of 1.17). These values were introduced in our recrystallization model to simulate the effects of the cold-rolling ratios.

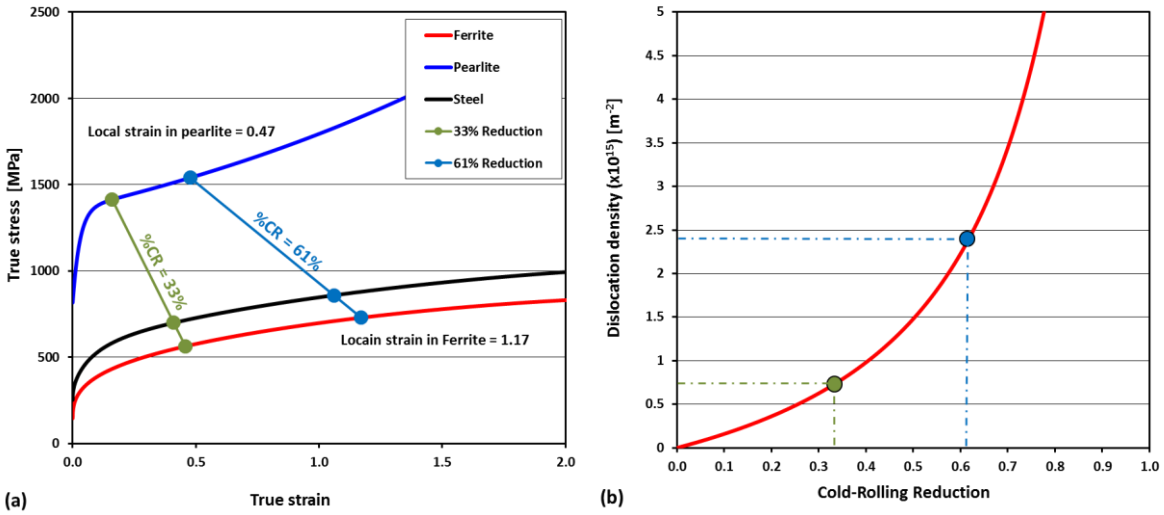

Figure 4.22: (a) Mechanical behaviors of constituting ferrite and pearlite phases during cold-rolling of the studied steel, calculated by the model of Bouaziz *et al*. [BOU'02]. The two highlighted particular states correspond to the 33% and 61% cold-rolling ratios. (b) Calculated dislocations densities in the ferritic phase of the studied steel as a function of the cold-rolling reduction. (c)

Figure 4.23 shows a comparison between experimental and simulated recrystallization kinetics, for 33 and 61% cold-rolled steels (green and blue curves, respectively). From the simulations, the kinetic delay induced by the CR difference (assuming a dislocation density of 0.70x10^{15} m^{-2}) is too important compared to that observed experimentally (+50°C instead of +30°C). Bearing in mind that the model is extremely sensitive the initial dislocation density, a much satisfying agreement was obtained using a dislocation density of 0.80x10^{15} m^{-2}. According to the micromechanical model, this value is achievable in ferrite for a minimum CR ratio equal to 35%, that remains a value extremely close to that applied experimentally (probably in the range of uncertainty).

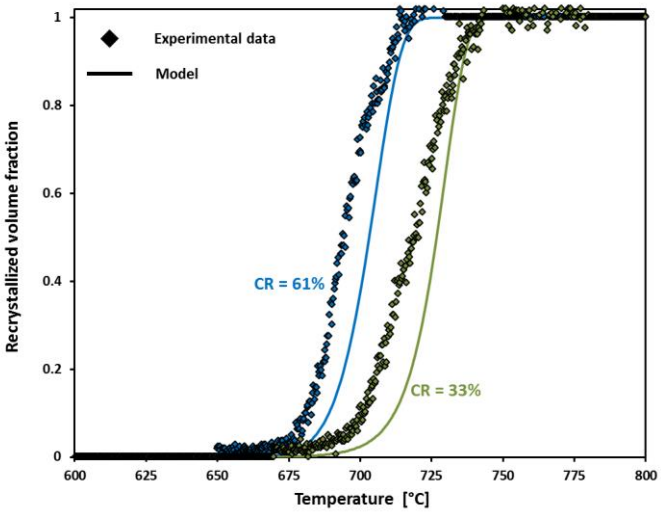

Figure 4.23: Comparison between experimental and simulated recrystallization kinetics of the ferritic matrix for two cold-rolling ratios (33 and 61%, respectively represented in green and blue).

The model finally permits to identify also the critical strain to enable recrystallization during studied annealing schedule. For instance, to be fully recrystallized after 600s at 800°C, the ferrite requires an initial density of dislocation of 8.00×10^{13} m^{-2} and thus a minimum cold-rolling ratio of 5%.

4.4 Summary and conclusions

HEXRD experiments were conducted to characterize *in situ* the recovery and recrystallization in the studied steels along anisothermal (heating at constant heating rate) and isothermal annealing sequences. The Williamson-Hall method coupled with Smallman's equation has been used to determine the evolution of the dislocation densities all along the studied thermal treatments. We have in parallel set up and developed an innovative approach based on isolated diffraction spots appearing on the Debye-Scherrer rings when recrystallization occurs to quantify also in real time the fraction of recrystallized ferrite. The apparition rate of these diffraction spots on the DS ring is assumed to be proportional to the recrystallization extent in bulk. Hence, the material is considered entirely recrystallized once the number of individual spots reaches a plateau. The values provided by our new method have been validated by SEM/EBSD observations and empirical modeling calibrated with more conventional methods.

The limits and the resolution of this new method still needs to be studied but it offers a fantastic opportunity to study in real-time coupled phenomena in steel and other alloys. We have in particular discussed the influence of the texture, the presence of non-recrystallized pearlite or the correlation between the nucleation and growth mechanisms and observed spots.

During isothermal treatments on the studied steel, only recovery process is active at 450°C and 500°C while recrystallization takes also place at 650°C. The analysis of the continuous annealing at fast heating rate reveals that only recovery takes place in the 380-730°C temperature range while recrystallization and reverse austenite transformation started concomitantly, once Ac_1 was exceeded. At low heating rate, recovery starts also at 380°C but recrystallization occurs between 650 and 710°C, i.e. just before the phase transformation. These findings corroborate our SEM observations in chapter 2 as well as the findings of Kulakov and Ollat [KUL'13, OLL'17b] on similar steels.

A physically based model describing both recovery and recrystallization and their couplings have been developed and adapted to the case of cold-rolled ferrite-pearlite steels. This development has been made keeping in mind the constraint of calculation time for product line management. This is a reason why mean-field approach has been preferred to a local field framework. The decrease in dislocation density has been modeled thanks to the Friedel's seminal work. The predicted evolutions do not perfectly reproduce the experimental measurements, but the trends are however well captured.

A new model was built to predict recrystallization kinetics, inspired by the nucleation model developed by Zurob *et al*. [ZUR'02, ZUR'06] and the growth model by Sinclair *et al.* [SIN'07]. The nucleation flux is calculated considering that a subgrain becomes a new recrystallized grain if it size reaches a critical value. The growth of new grains is governed by a mobility equation. Only the mean radius of recrystallized grain is calculated by considering the competition between nucleation and growth processes. Finally, the recrystallized fraction is calculated using the extended volume theory. The parameters and mobility functions were calibrated to best reproduce observed experimental trends.

The experimental kinetics determined during continuous heatings and isothermal holding at 650°C were very well replicated as well as the grain sizes measured on the SEM micrographs. The prediction of the model once adjusted has been challenged to assess the effect of the cold-rolling ratio on recrystallization kinetics with a very reasonable agreement.

REFERENCES

[ADH'18] Adhikary, M., Chakraborty, A., Das, A., T, V., B, R.K., 2018. Influence of annealing texture on dynamic tensile deformation characteristics of Dual phase steel. Materials Science and Engineering: A 736, 209–218. https://doi.org/10.1016/j.msea.2018.08.103

[AYA'11] Ayad, A., Allain-Bonasso, N., Rouag, N., Wagner, F., 2011. Grain Orientation Spread Values in if Steels after Plastic Deformation and Recrystallization. Materials Science Forum 702–703, 269–272. https://doi.org/10.4028/www.scientific.net/MSF.702-703.269

[BAI'62] Bailey et Hirsch, J., PB, 1962. The recrystallization process in some polycrystalline metals. Proceedings of the Royal Society of London. Series A. Mathematical and Physical Sciences 267, 11–30. https://doi.org/10.1098/rspa.1962.0080

[BOU'02] Galtier, A., Bouaziz, O., Lambert, A., 2002. Influence de la microstructure des aciers sur leur propriétés mécaniques. Mécanique & Industries 3, 457–462.

[CAH'50] Cahn, R.W., 1950. A New Theory of Recrystallization Nuclei. Proceedings of the Physical Society. Section A 63, 323–336. https://doi.org/10.1088/0370-1298/63/4/302

[CHB'14] Chbihi, A., Barbier, D., Germain, L., Hazotte, A., Gouné, M., 2014. Interactions between ferrite recrystallization and austenite formation in high-strength steels. Journal of Materials Science 49, 3608–3621. https://doi.org/10.1007/s10853-014-8029-2

[DOH'97] Doherty, R.D., Hughes, D.A., Humphreys, F.J., Jonas, J.J., Jensen, D.J., Kassner, M.E., King, W.E., McNelley, T.R., McQueen, H.J., Rollett, A.D., 1997. Current issues in recrystallization: a review. Materials Science and Engineering: A 238, 219–274. https://doi.org/10.1016/S0921-5093(97)00424-3

[FAI'79] Faivre, P., Doherty, R.D., 1979. Nucleation of recrystallization in compressed aluminium: studies by electron microscopy and Kikuchi diffraction. Journal of Materials Science 14, 897–919. https://doi.org/10.1007/BF00550722

[FRI'64] Friedel, J. (1964). Dislocations Pergamon. New York, 274., n.d.

[FUR'95] Furu, T., Ørsund, R., Nes, E., 1995. Subgrain growth in heavily deformed aluminium—experimental investigation and modelling treatment. Acta Metallurgica et Materialia 43, 2209–2232. https://doi.org/10.1016/0956-7151(94)00410-2

[GSH'02] Ghosh, G., Olson, G.B., 2002. The isotropic shear modulus of multicomponent Fe-base solid solutions. Acta Materialia 50, 2655–2675. https://doi.org/10.1016/S1359-6454(02)00096-4

[GUR'10] Gurruchaga, K., Martinez-de-Guerenu, A., Soto, M., Arizti, F., 2010. Magnetic Barkhausen Noise for Characterization of Recovery and Recrystallization. IEEE Transactions on Magnetics 46, 513–516. https://doi.org/10.1109/TMAG.2009.2029069

[HAL'14] Halder, C., Madej, L., Pietrzyk, M., 2014. Discrete micro-scale cellular automata model for modelling phase transformation during heating of dual phase steels. Archives of Civil and Mechanical Engineering 14, 96–103. https://doi.org/10.1016/j.acme.2013.07.001

[HIL'75] Hillert, M., 1975. Diffusion and interface control of reactions in alloys. Metallurgical Transactions A 6, 5–19. https://doi.org/10.1007/BF02673664
[HUA'04] Huang, J., Poole, W.J., Militzer, M., 2004. Austenite formation during intercritical annealing. Metallurgical and Materials Transactions A 35, 3363–3375. https://doi.org/10.1007/s11661-004-0173-x

[HUM'04] Humphreys, F.J., Hatherly, M., 2004. Recrystallization and Related Annealing Phenomena. Elsevier, Burlington.

[KAN'11] Kang, J.-Y., Lee, H.-C., Han, S.H., 2011. Effect of Al and Mo on the textures and microstructures of dual phase steels. Materials Science and Engineering: A 530, 183–190. https://doi.org/10.1016/j.msea.2011.09.071

[KHO'11] Khodabakhshi, F., Kazeminezhad, M., 2011. The effect of constrained groove pressing on grain size, dislocation density and electrical resistivity of low carbon steel. Materials & Design 32, 3280–3286. https://doi.org/10.1016/j.matdes.2011.02.032

[KHR'11] Khorsand Zak, A., Abd. Majid, W.H., Abrishami, M.E., Yousefi, R., 2011. X-ray analysis of ZnO nanoparticles by Williamson–Hall and size–strain plot methods. Solid State Sciences 13, 251–256. https://doi.org/10.1016/j.solidstatesciences.2010.11.024

[KUC'82] Kučera, J., Stránský, K., 1982. Diffusion in iron, iron solid solutions and steels. Materials Science and Engineering 52, 1–38. https://doi.org/10.1016/0025-5416(82)90067-2

[KUL'13] Kulakov, M., Poole, W.J., Militzer, M., 2014. A Microstructure Evolution Model for Intercritical Annealing of a Low-carbon Dual-phase Steel. ISIJ International 54, 2627–2636. https://doi.org/10.2355/isijinternational.54.2627

[LAU'03] Lauridsen, E.., Poulsen, H.., Nielsen, S.., Juul Jensen, D., 2003. Recrystallization kinetics of individual bulk grains in 90% cold-rolled aluminium. Acta Materialia 51, 4423–4435. https://doi.org/10.1016/S1359-6454(03)00278-7

[LAU'06] Lauridsen, E.M., Schmidt, S., Nielsen, S.F., Margulies, L., Poulsen, H.F., Jensen, D.J., 2006. Non-destructive characterization of recrystallization kinetics using three-dimensional X-ray diffraction microscopy. Scripta Materialia 55, 51–56. https://doi.org/10.1016/j.scriptamat.2006.02.028

[LI'62] Li, J.C.M., 1962. Possibility of Subgrain Rotation during Recrystallization. Journal of Applied Physics 33, 2958–2965. https://doi.org/10.1063/1.1728543

[LIU'16] Liu, Z., Olivares, R.O., Lei, Y., Garcia, C.I., Wang, G., 2016. Microstructural characterization and recrystallization kinetics modeling of annealing cold-rolled vanadium microalloyed HSLA steels. Journal of Alloys and Compounds 679, 293–301. https://doi.org/10.1016/j.jallcom.2016.04.057

[LU'11] Lü, Y., Molodov, D.A., Gottstein, G., 2011. Recrystallization kinetics and microstructure evolution during annealing of a cold-rolled Fe–Mn–C alloy. Acta Materialia 59, 3229–3243. https://doi.org/10.1016/j.actamat.2011.01.063

[MAD'13] Madej, L., Sieradzki, L., Sitko, M., Perzynski, K., Radwanski, K., Kuziak, R., 2013. Multi scale cellular automata and finite element based model for cold deformation and annealing of a ferritic–pearlitic microstructure. Computational Materials Science 77, 172–181. https://doi.org/10.1016/j.commatsci.2013.04.020

[MIO'02] Miodownik, M.A., 2002. A review of microstructural computer models used to simulate grain growth and recrystallisation in aluminium alloys. Journal of Light Metals 2, 125–135. https://doi.org/10.1016/S1471-5317(02)00039-1
[NES'95] Nes, E., 1995. Recovery revisited. Acta Metallurgica et Materialia 43, 2189–2207. https://doi.org/10.1016/0956-7151(94)00409-9

[OLL'17b] Ollat, M. 2017. Characterization and modeling of microstructural evolutions during the thermal treatment of cold-rolled Dual-Phase steels. PhD report. https://tel.archives-ouvertes.fr/tel-01920855

[PER'10] Peranio, N., Li, Y.J., Roters, F., Raabe, D., 2010. Microstructure and texture evolution in dual-phase steels: Competition between recovery, recrystallization, and phase transformation. Materials Science and Engineering: A 527, 4161–4168. https://doi.org/10.1016/j.msea.2010.03.028

[PES'03] Pešička, J., Kužel, R., Dronhofer, A., Eggeler, G., 2003. The evolution of dislocation density during heat treatment and creep of tempered martensite ferritic steels. Acta Materialia 51, 4847–4862. https://doi.org/10.1016/S1359-6454(03)00324-0

[POU'11] Poulsen, S.O., Lauridsen, E.M., Lyckegaard, A., Oddershede, J., Gundlach, C., Curfs, C., Juul Jensen, D., 2011. In situ measurements of growth rates and grain-averaged activation energies of individual grains during recrystallization of 50% cold-rolled aluminium. Scripta Materialia 64, 1003–1006. https://doi.org/10.1016/j.scriptamat.2011.01.046

[RAD'15] Radwański, K., 2015. Application of FEG-SEM and EBSD Methods for the Analysis of the Restoration Processes Occurring During Continuous Annealing of Dual-Phase Steel Strips. steel research international 86, 1379–1390. https://doi.org/10.1002/srin.201400361

[RAY'85] Ray, R.K., 1985. Deformation and recrystallization textures in a dual-phase steel. Journal of Materials Science Letters 4, 67–70. https://doi.org/10.1007/BF00719899

[REH'13] Rehman, M.K., Zurob, H.S., 2013. A Novel Approach to Model Static Recrystallization of Austenite During Hot Rolling of Nb Microalloyed Steel. Part I: Precipitate-Free Case. Metallurgical and Materials Transactions A 44, 1862–1871. https://doi.org/10.1007/s11661-012-1526-5

[RIB'04] Ribárik, G., Gubicza, J., Ungár, T., 2004. Correlation between strength and microstructure of ball-milled Al–Mg alloys determined by X-ray diffraction. Materials Science and Engineering: A 387–389, 343–347. https://doi.org/10.1016/j.msea.2004.01.089

[RIB'10] Ribárik, G., Ungár, T., 2010. Characterization of the microstructure in random and textured polycrystals and single crystals by diffraction line profile analysis. Materials Science and Engineering: A 528, 112–121. https://doi.org/10.1016/j.msea.2010.08.059

[SAA'60] Saada, G., 1960. Sur le durcissement dû à la recombinaison des dislocations. Acta Metallurgica 8, 841–847. https://doi.org/10.1016/0001-6160(60)90150-4

[SAL'14] Sallez, N., Boulnat, X., Borbély, A., Béchade, J.L., Fabrègue, D., Perez, M., de Carlan, Y., Hennet, L., Mocuta, C., Thiaudière, D., Bréchet, Y., 2015. In situ characterization of microstructural instabilities: Recovery, recrystallization and abnormal growth in nanoreinforced steel powder. Acta Materialia 87, 377–389. https://doi.org/10.1016/j.actamat.2014.11.051

[SAV'10] Savran, V.I., Offerman, S.E., Sietsma, J., 2010. Austenite Nucleation and Growth Observed on the Level of Individual Grains by Three-Dimensional X-Ray Diffraction Microscopy. Metallurgical and Materials Transactions A 41, 583–591. https://doi.org/10.1007/s11661-009-0142-5

[SEN'08] Senuma, T., Takemoto, Y., 2008. Model for Predicting the Microstructural Evolution of Extralow Carbon Steels. ISIJ International 48, 1635–1639. https://doi.org/10.2355/isijinternational.48.1635
[SIN'07] Sinclair, C.W., Hutchinson, C.R., Bréchet, Y., 2007. The Effect of Nb on the Recrystallization and Grain Growth of Ultra-High-Purity α-Fe: A Combinatorial Approach. Metallurgical and Materials Transactions A 38, 821–830. https://doi.org/10.1007/s11661-007-9106-9

[SLA'18] Ben Haj Slama, M. 2018. "Etude multi-échelle et in situ des évolutions microstructurales en conditions isothermes d'aciers bainitiques en lattes ». PhD report. http://docnum.univ-lorraine.fr/public/DDOC_T_2018_0042_BEN_HAJ_SLAMA.pdf

[SMA'57] Smallman, R.E., Westmacott, K.H., 1957. Stacking faults in face-centred cubic metals and alloys. Philosophical Magazine 2, 669–683. https://doi.org/10.1080/14786435708242709

[STE'14] Stechauner, G., Kozeschnik, E., 2014. Self-Diffusion in Grain Boundaries and Dislocation Pipes in Al, Fe, and Ni and Application to AlN Precipitation in Steel. Journal of Materials Engineering and Performance 23, 1576–1579. https://doi.org/10.1007/s11665-014-0921-z

[ZAK'10] The recrystallization process in some polycrystalline metals, 1962. . Proceedings of the Royal Society of London. Series A. Mathematical and Physical Sciences 267, 11–30. https://doi.org/10.1098/rspa.1962.0080

[UNG'14] Ungár, T., Ribárik, G., Zilahi, G., Mulay, R., Lienert, U., Balogh, L., Agnew, S., 2014. Slip systems and dislocation densities in individual grains of polycrystalline aggregates of plastically deformed CoTi and CoZr alloys. Acta Materialia 71, 264–282. https://doi.org/10.1016/j.actamat.2014.03.024

[LAN'12] Van Landeghem, H.P., Gouné, M., Redjaïmia, A., 2012. Nitride precipitation in compositionally heterogeneous alloys: Nucleation, growth and coarsening during nitriding. Journal of Crystal Growth 341, 53–60. https://doi.org/10.1016/j.jcrysgro.2011.12.056

[VER'98] Verdier, M., Brechet, Y., Guyot, P., 1998. Recovery of AlMg alloys: flow stress and strain-hardening properties. Acta Materialia 47, 127–134. https://doi.org/10.1016/S1359-6454(98)00350-4

[WAN'06] Y.Wang. 2006. "Etude et modélisation de l'effet du revenu sur les évolutions des microstructures, du comportement thermomécanique et des contraintes résiduelles de trempe". PhD report. https://hal.univ-lorraine.fr/tel-01752753

[WH'53] Williamson, G, Hall, W.., 1953. X-ray line broadening from filed aluminium and wolfram. Acta Metallurgica 1, 22–31. https://doi.org/10.1016/0001-6160(53)90006-6

[YE'02] Ye, W., Le Gall, R., Saindrenan, G., 2002. A study of the recrystallization of an IF steel by kinetics models. Materials Science and Engineering: A 332, 41–46. https://doi.org/10.1016/S0921-5093(01)01715-4

[ZHA'14a] Zhang, B., 2014. Calculation of self-diffusion coefficients in iron. AIP Advances 4, 017128. https://doi.org/10.1063/1.4863462

[ZHA'14b] Zhang, H., Pradeep, K.G., Mandal, S., Ponge, D., Raabe, D., 2014. New insights into the austenitization process of low-alloyed hypereutectoid steels: Nucleation analysis of strain-induced austenite formation. Acta Materialia 80, 296–308. https://doi.org/10.1016/j.actamat.2014.07.073

[ZHU'12] Zhu, B., Militzer, M., 2012. 3D phase field modelling of recrystallization in a low-carbon steel. Modelling and Simulation in Materials Science and Engineering 20, 085011. https://doi.org/10.1088/0965-0393/20/8/085011

[ZHU'15b] Zhu, B., Chen, H., Militzer, M., 2015. Phase-field modeling of cyclic phase transformations in low-carbon steels. Computational Materials Science 108, 333–341. https://doi.org/10.1016/j.commatsci.2015.01.023

[ZUR'02] Zurob, H.S., Hutchinson, C.R., Brechet, Y., Purdy, G., 2002. Modeling recrystallization of microalloyed austenite: effect of coupling recovery, precipitation and recrystallization. Acta Materialia 50, 3077–3094. https://doi.org/10.1016/S1359-6454(02)00097-6

[ZUR'06] Zurob, H., Brechet, Y., Dunlop, J., 2006. Quantitative criterion for recrystallization nucleation in single-phase alloys: Prediction of critical strains and incubation times. Acta Materialia 54, 3983–3990. https://doi.org/10.1016/j.actamat.2006.04.028

Chapter 5

Austenite transformation kinetics: *In situ* characterization and physical based modeling

This chapter deals with the austenite transformation kinetics during annealing of the CR DP microstructure. The literature review shows that the austenite transformation kinetics strongly depends on the heating rate. Faster heating leads to faster kinetics during subsequent isothermal hold and higher final amounts of austenite. Interactions with ferrite recrystallization process are invoked to explain this trend, as well as considerations on the nucleation-growth rate of austenite: the austenite transformation kinetics is strongly influenced by the chemical composition of the phases, especially the Mn concentration in the cementite particles. It is also linked with the morphogenesis of the austenite microstructure. Two main nucleation sites are identified for the austenite: fragmented/spheroidized pearlite island boundaries and isolated carbides located at ferrite grain boundaries.

We present here first an experimental study of the austenite transformation kinetics, which was measured *in situ* via HEXRD experiments for slow and fast heating rates up to 800°C (3 and 30°C.s^{-1}) followed by isothermal treatment at 800°C for 600s. The results are interpreted in the light of experimental data and analyses presented in previous chapters, regarding the microstructure evolutions (especially austenite nucleation sites), the evolutions of cementite compositions in Mn and the recrystallization kinetics. Conclusions regarding the phenomena influencing significantly the austenite transformation kinetics are presented.

On this experimental basis, a physically based smodel of phase transformations is introduced. It is based on DICTRA simulations; literature survey highlights that such simulations provide an intermediate modeling approach between phenomenological JMAK rules and full-field simulations such as phase field or cellular automata. Latter approaches do not currently consider the cementite phase in the microstructure or the diffusion of Mn at long distances. Compared to previous DICTRA simulations in the literature, anisothermal treatments are considered here. Moreover, emphasis is put at understanding independently the austenite transformation process respectively from pearlite islands and isolated carbides; the latter are generally neglected. Thanks to a geometrical representation of the overall CR DP steel initial microstructure, the overall austenitization kinetics is derived and compared to the experiments.

Finally, on this basis, simple modelling approaches are introduced for the purpose of computer-efficient simulations of the austenitization process.

Content

5.1 Literature review

This literature review is focused on the kinetics aspects of the austenitization process in CR DP steels, while Chapter 2 concentrated more on the microstructural aspects and the morphogenesis of the austenite microstructure. This section starts from experimental characterizations of kinetics, before showing the existing thermokinetic analyses. Finally, the existing kinetic simulation approaches are presented.

5.1.1 Austenite transformation global kinetics

The heating rate strongly influences the austenite transformation kinetics during the annealing of CR DP steels [HUA'04, AZI'11, CHB'14, KUL'13, LI'13, BAR'15, TOM'18]. For example, Huang *et al*. [HUA'04] established by dilatometry the austenite transformation kinetics during isothermal hold preceded by heating at two different rates, 1°C.s^{-1} or 100°C.s^{-1} (cf. Fig. 5.1). They compared two initial states, hot-rolled (HR) and cold-rolled (CR) for the same Fe-0.06C-1.9Mn (%$_{wt}$) steel. Higher heating rate involves faster austenite transformation kinetics and higher final amount of austenite than the slower heating. The final amount of austenite transformed may even exceed that expected from the thermodynamic equilibrium value in some cases. [KUL'13, LI'13, CHB'14, BAR'15, TOM'18]. These effects are more pronounced for the CR than for the HR state. Similar trends were established later on in the references cited above, and interpreted with microstructural observations. As for the kinetics during the heating stage itself, no clear influence of heating rate was established. Several origins of the faster austenite transformation associated with fast heating have been proposed.

First possible origin of the faster transformation kinetics after faster heating in CR steels is the interaction with the recrystallization. At fast heating (ca. 100°C.s^{-1}), recrystallization and phase transformation are concomitant (strong interaction [KUL'13]), whereas the interaction is weak at slow heating (ca. 1°C.s^{-1}): recrystallization is completed before the start of the transformation (cf. Chapter 2). In presence of non-recrystallized ferrite grains, nucleation and growth of austenite is accelerated. The defected ferrite provides a high density of nucleation sites and fast diffusion paths for substitutional and interstitial elements (e.g. [KUL'13]). Stored energy would also increase the transformation driving force. As for the recrystallization kinetics itself, it has been reported to be slowed down in the presence of the first grains of austenite [KUL'13, CHB'14, BAR'15].

Processing maps [KUL'13, OLL'17] show the range of annealing treatment parameters for which strong interactions will occur. For instance, the processing map of [KUL'13] (Figure 5.2) was established by using a recrystallization kinetics model. It shows the temperature of start and finish of recrystallization as a function of the heating rate. Calculated critical heating rates were in good agreement with industrial experiences. This study also highlighted the influence of the initial microstructure.

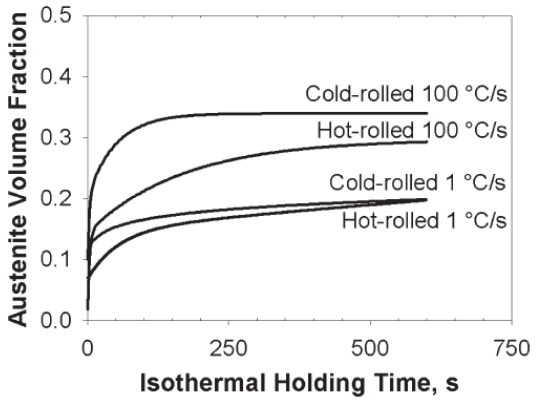

Figure 5.1: Effect of the heating rate (1 and 100°C.s^{-1}) on transformed austenite volume fraction during isothermal holding at 750°C for a hot-rolled and cold-rolled Fe-0.06C-1.85Mn-0.11Mo (%$_{wt}$) steel; OE austenite fraction is 26% [HUA'04].

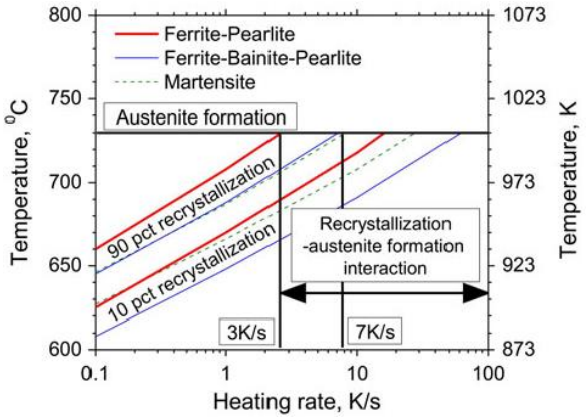

Figure 5.2: Processing map showing the interaction recrystallization / austenite transformation depending on the heating rate [KUL'13].

The austenite transformation kinetics is not only influenced by the interaction with the recrystallization. The nucleation-growth kinetics of the austenite has in itself a significant influence. According to [AZI'11], faster heating shifts the austenite transformation to higher temperature, resulting in faster kinetics, due to larger driving force and diffusivities. There would be more austenite growth fronts in the microstructure because of the higher number density of austenite grains. Such interpretation would explain for example the faster kinetics after faster heating in [HUA'04] in HR microstructure (Figure 5.1), hence without recrystallization. The interpretations given in [HUA'04] also take into consideration the consequences of the morphogenesis on the austenitization kinetics.

Hence, the factors controlling the rate for nucleation and growth of austenite are essential, as was elaborated in literature review of Chapter 2 on microstructural observations. The phase's compositions have also a significant influence on kinetics, as will be seen in next Section on thermokinetic analyses.

5.1.2 Thermo-kinetic analyses

Purpose of thermokinetic analyses is to predict kinetics stages in the austenite transformation and to predict at which temperature these processes will occur. We summarize here the conclusions reached on two model initial microstructures: ferrite-pearlite or spheroidized cementite (i.e. isolated carbides in ferritic matrix). This will serve to interpret the austenitization process in DP steels, whose main austenite nucleation sites are the pearlite colonies and isolated carbides, as seen in Chapter 2.

5.1.2.a Identification of kinetic stages

In the case of a ferrite-pearlite microstructure, the seminal study of Speich *et al.* [SPE'81] on Fe-C-Mn dual-phase steels established experimentally and by the simulation that the austenite transformation follows successive kinetic stages illustrated in Figure 5.3.

Stage 1: Pearlite dissolution: austenite nucleates on pearlite island boundaries and dissolves quickly the pearlite. After complete dissolution, the former pearlite island is replaced by a rich-carbon austenite grain whose carbon content is far higher than at equilibrium.

Stage 2: Austenite growth into ferrite controlled by C diffusion through austenite (2a) and then by Mn diffusion through ferrite (2b). Stage (2a) involves no Mn redistribution; in stage (2b), Mn starts to diffuse in turn from ferrite to austenite. Since Mn diffusion is slower than that of carbon, this transition marks a pronounced kinetic slowdown.

Stage 3: Slow Mn activity equilibration by Mn diffusion through austenite. Due to the sluggish diffusion of Mn in austenite (two orders of magnitude slower than in ferrite), this last stage requires longer time.

The same stages for the austenitization process were established in [KAM'15, LAI'16, OLL'17], still considering an initial ferrite-pearlite microstructure.

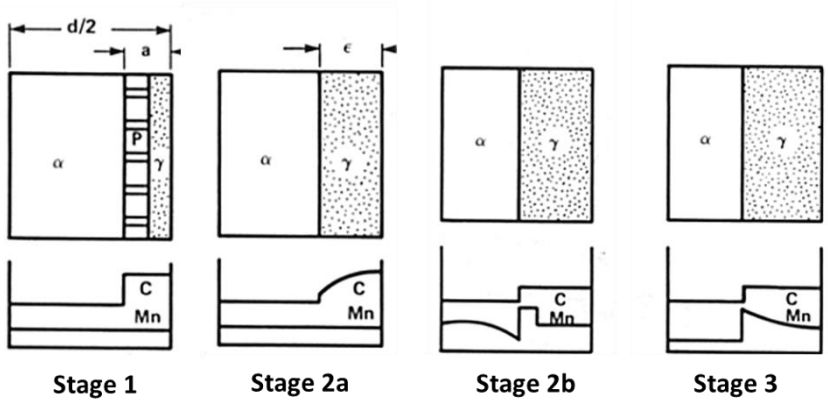

Figure 5.3: Kinetic stages involved during austenite transformation from a ferrite-pearlite initial microstructure up to the completion of ortho-equilibrium [SPE'81].

In the case of an initial microstructure composed of isolated carbides in a ferrite matrix (e.g. spheroidized cementite), no such clear succession of kinetic stages could be established experimentally. However, this was achieved by the simulation. For instance, in [LAI'16], DICTRA software was utilized with the geometrical representation in Figure 5.4(a): the cementite carbide is placed at the center of a spherical simulation cell and initially surrounded by the ferrite matrix. The austenite then forms a shell around the carbide. Three kinetic stages were predicted (cf. Fig 4.5(b)): (i) fast cementite dissolution and austenite growth into ferrite driven by C diffusion in austenite; (ii) Mn partitioning from ferrite; (iii) Mn diffusion in austenite.

These stages could not be identified experimentally for several reasons. First, in most investigated DP steels, the main sources of carbon are the pearlite colonies, whereas the isolated carbides are either absent or even disregarded when they exist [KUL'13, BAR'15]. Even in [LAI'16], where a more "model" initial microstructure composed of spheroidized cementite was considered, the kinetic stages were not clearly observable experimentally. This may be ascribed to the specific kinetics associated with each individual cementite precipitate, which depends on the specific carbide size and composition. As a result, the overall macroscopic kinetics would be overlapped.

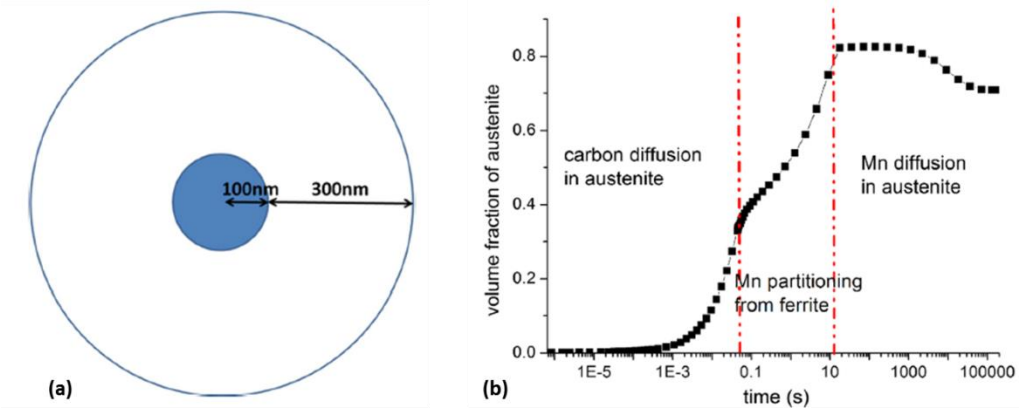

Figure 5.4: DICTRA simulation of austenite transformation starting from a cementite particle initially isolated in a ferrite matrix (Fe-0.3-3.5Mn steel). (a) Geometrical representation. (b) Evolution of the austenite volume fraction [LAI'16].

Hence, for both model microstructures ferrite-pearlite or isolated carbides, two successive steps are the dissolution of cementite, (during which all of the three phases ferrite austenite and cementite are present), followed by a ferrite/austenite transformation. Let us mention that in high-carbon steels (typically hyper-eutectoid, see e.g. [ENO'18]) the last stage is replaced by cementite/austenite transformation.

5.1.2.b Transition from slow to fast kinetic regimes – influence of cementite composition

As seen in previous Section, austenite can grow either with redistribution of substitutional elements between the phases (slow regime) or with the sole diffusion of carbon, while the alloy elements composition remains unchanged (fast regime). Slow and fast regimes occur respectively at low and high temperature ranges (both above Ae_1). There is a critical temperature which separates both temperatures ranges; it will be termed here as partition no partition transition temperature (PNTT) [ENO'18]. The PNTT is calculated from thermodynamic analyses.

Emphasis is put here on cementite dissolution, which received much attention in the context of dual phase steels annealing. In a seminal study, Hillert *et al.* [HIL'71] highlighted the strong influence of the cementite concentration in substitutional elements on its dissolution kinetics: the higher the concentration, the slower the kinetics. Their thermodynamic analyses were applied successfully later in several studies [LIU'91, MIY'10, GOU'12, XIA'13, ENO'18]. Two of these analyses are introduced here.

One assumes that the austenite forms a shell around the cementite and then grows simultaneously into the cementite and the ferrite (geometry A in Figure 5.5(a) [MIY'10]). If the austenite growth is controlled by carbon diffusion, the carbon concentration profile schematized in Figure 5.5(b) should be established. But for this to happen, the carbon activity in austenite has to be higher at the γ/θ interface than at the γ/α interface.

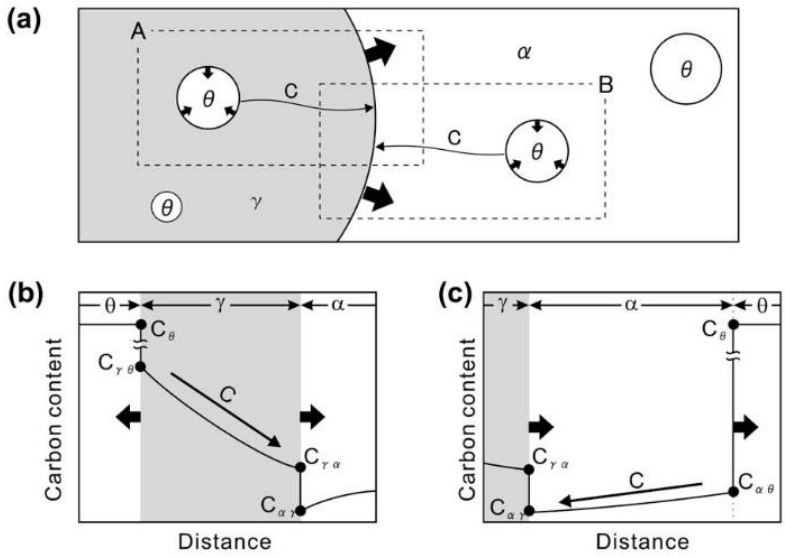

Figure 5.5: Schematic illustrations of austenite growth and dissolution of cementite accompanied by carbon diffusion; (b) carbon diffusion in austenite (geometry A) and (c) carbon diffusion in ferrite (geometry B) [MIY'10].

Such situation is represented in the Figure 5.6(a) [WEI'13]. The schematic Fe-C-Mn diagram represents the metastable γ/α and γ/θ equilibria. C_0 is the M concentration in cementite, while F_0 stands for that of ferrite. One assumes that the austenite inherits these concentrations by growing into the ferrite and the cementite. Hence, I_1 and I_2 dots represent the interfacial compositions of the austenite in contact with cementite and ferrite, respectively. The dotted lines represent the corresponding carbon iso-activities (a_{c1} and a_{c2}). For a high temperature (Figure 5.6(a)), the carbon activity a_{c1} is above a_{c2}, which induces a chemical driving force for carbon diffusion. Austenite growth without partition is possible. When the temperature is decreased, the α+γ/γ and γ/γ+θ phase field boundaries come closer. At the PNTT, the iso-activity lines coincide (Figure 5.6(b)). Below the PNTT, austenite growth requires the bulk diffusion of the substitutional elements (Figure 5.6(c)); carbon activity is homogeneous in austenite.

Geometry B (cf. Fig 5.5(a)) was also considered in [MIY'10]. It assumes that the cementite dissolves inside the ferrite, while the diffusing species diffuse out the cementite to the growing austenite through the ferrite. Details of the corresponding PNTT temperature calculations are in [MIY'10].

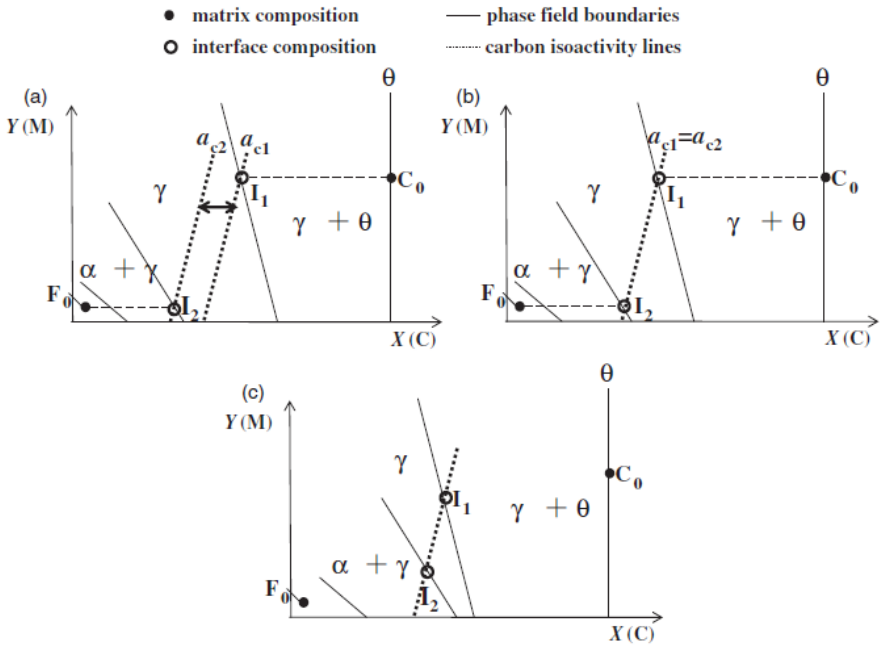

Figure 5.6: Schematic isothermal sections of the Fe-C-M system illustrating austenite growth under (a) NPLE conditions or (b) PLE conditions. (c) Illustration of the PNTT determination using the carbon activity balance.

Hence, it is possible to calculate the PNTT temperature if thermodynamic data are available. For instance, in [GOU'12], the PNTT was calculated as a function of the Mn concentration in cementite in a Fe-C-Mn steel, assuming geometry A (Figure 5.7(a)). The PNTT increases with increasing Mn concentration as expected. These calculations are in accordance with isothermal austenite transformation kinetics determined at 750°C (Figure 5.7(b)). Kinetics is fast or slow when the Mn concentration in cementite is respectively low or high (6.7 and 15.5 $\%_{wt}$, respectively).

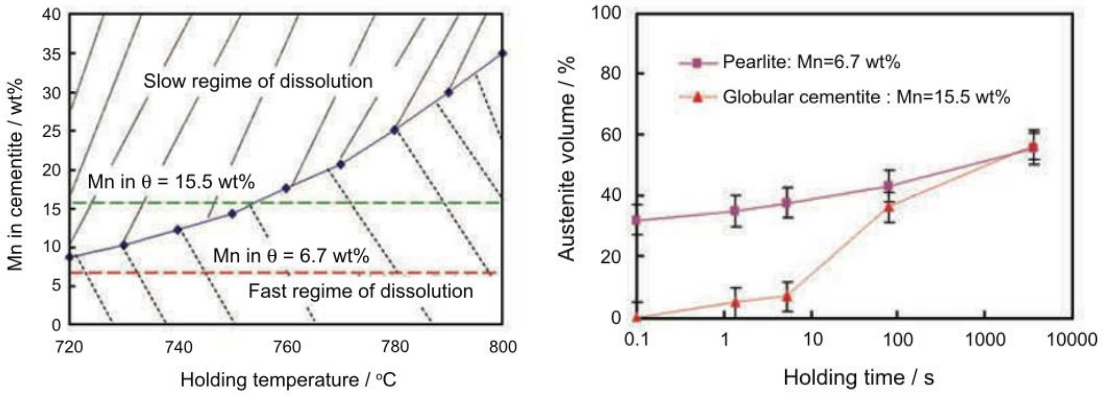

Figure 5.7: (a) PNTT vs. Mn concentration in cementite in some Fe-C-Mn steel. (b) Experimental austenite transformation kinetics at 750°C for two Mn concentrations in cementite [GOU'12].

In [MIY'10], the respective effect of substitutional elements Mn, Cr and Si on spheroidized cementite dissolution kinetics was compared at single temperature 1073K. Cr element has a strong slowing-down effect compared to Mn and Si (for the considered concentrations in cementite) according to the experiments. For Cr element, the calculated PNTT is higher than 1073K, confirming that the dissolution of Cr-enriched cementite occurs in slow partition mode, involving diffusion of Cr. In [LI'11], the same analysis as in [MIY'10] was carried out, but to interpret the dissolution of pearlite. Although geometries A and B concern individual carbides, the analysis was adapted to pearlite as detailed in [LI'11]. Conclusions similar to [MIY'10] were drawn regarding the respective effect of Mn, Cr and Si elements.

It is stressed that local equilibrium (LE) is assumed in previous analyses, which is the most frequent assumption. However, few studies also considered paraequilibrium (PE) [MIY'10, SPE'81], or even growth in mixed-mode (cf. Section 5.1.4). In [MIY'10], the LE assumption was in better agreement with the experiments than the PE assumption.

5.1.3 Kinetics simulations

One step further in the understanding of the austenitization process is to predict its kinetics. This section summarizes the existing simulation studies and modelling approaches.

The Johnson-Mehl-Avrami-Kolmogorov (JMAK) law [AVR'39] describes global phase transformation kinetics during isothermal treatments. It has been established for nucleation-growth processes (phase transformations, recrystallization), and it is generally used as a phenomenological relationship:

$$Y = 1 - \exp(-bt^n) \tag{5.1}$$

Y is the volume fraction of austenite, b and *n* the JMAK kinetics parameters.

To consider anisothermal conditions, one assumes an additivity hypothesis (e.g. [DEN'92]). In [KUL'13, OLL'17], annealing of CR DP steels was simulated by using JMAK rule to predict both austenite transformation and recrystallization kinetics. [OLL'17] established strategies to handle the interactions between austenite transformation and recrystallization. Drawbacks of JMAK global models are the empirical data established on specific steel composition and initial microstructure; the microstructure description is limited to the volume fraction of austenite and recrystallized fraction.

Physically based models predict the nucleation and growth rate of the austenite. Contrary to previous empirical approach, the parameters consist of thermodynamic, mobility data and microstructural features such as grain sizes. This makes these models more adaptable to various steel compositions or initial microstructures. Few models of austenite transformation in literature consider the nucleation stage. This comes probably from the lack of experimental data regarding the nucleation of austenite. In [ROO'83], the nucleation rate of austenite in an eutectoid steel was assumed to follow an Arrhenius relationship. Microstructural parameters such as the pearlite interlamellar spacing were accounted for. This approach was later utilized in [CAB'01]. In [ZHU'15], site saturation was assumed for nucleation at pearlite boundaries, while classical theory of heterogeneous nucleation [LAN'88] was used to calculate the nucleation rate of austenite at ferrite grain boundaries. Let us mention that in the case of the austenite to ferrite transformation, the nucleation stage was examined in more detail: see for instance [LAN'88].

Most simulations concern the austenite growth stage. Different modelling approaches were undertaken from analytical models to full-field simulations. Except in [MEC'15, OLL'18], common assumptions are the local equilibrium (LE) between adjacent phases and the limitation of the growth rate by the bulk diffusion of the species.

Analytical models are based on a mathematical solution of the diffusion equation [AAR'75] with accounting of the mass balance at the interface. Some function is established to give the interface position and velocity as a function of time. The calculations are very fast, but the drawback is in the strict limit conditions, which imposes oversimplified geometrical representation of the microstructure. Temperature has also to be constant so that the compositions at the interface, which are determined by the LE, stay constant. In [AKB'94, ATK'95] the austenite transformation kinetics from ferrite/cementite mixture was modeled assuming planar geometry. Semi-infinite phases cementite and ferrite were assumed, which

makes impossible to consider the full dissolution of cementite and the soft-impingement of the diffusion fields in the ferrite. Kinetics transitions as that presented in Section 5.1.3.b thus cannot be predicted. Nevertheless, outcomes of these studies are the good estimates of the interface velocity at the beginning of the austenite transformation. Inverse TTT transformation diagrams were established on this basis and the influence of steel composition was also examined.

Semi-analytical models assume simplified composition profiles in the phases. The mathematical treatment is less rigorous, but this allows representing more realistically the geometry of the microstructure. In [WYC'81] austenite transformation from cementite and ferrite mixture was modeled assuming either planar of spherical geometry. For the planar geometry, carbon-controlled parabolic austenite growth is described with Zener's approximation [ZEN'49]. Once carbon activity is equilibrated, Mn-diffusion control takes over; linear Mn composition profiles are assumed in the ferrite. Interface position and interfacial compositions (operative tie-line) have to be computed at each time step, but the computations remain extremely fast. The model of [WYC'81] allows to predict the transition from C-diffusion control to Mn control and the soft impingement of the Mn concentration profiles in ferrite. It also predicts the shape of the Mn concentration profiles that will subsist in the austenite because of the sluggish diffusion of Mn in this phase. Such semi-empirical approach has been followed more recently in [MEC'15] (see below) and in [ENO'18] to predict the kinetics of austenite formation during continuous heating of low-carbon martensite.

DICTRA commercial software allows full numerical treatment of the diffusion equation in one dimension (1D), assuming planar, cylindrical or spherical symmetry. Main assumptions and numerical features were presented in Chapter 1. DICTRA is coupled to Thermocalc in order to compute the chemical potential of the species. Apart from providing "ready-for-use" simulation tool, DICTRA software allows to treat multi-component diffusion with accounting of cross-term diffusion coefficients and the dependence of the mobilities on the local composition. Nevertheless, most DICTRA simulations in literature concern ternary systems (in [WEI'13], quaternary system was considered). Most frequently, LE is assumed between adjacent phases, but it is also possible to assume PE, or to impose a finite mobility.

In [LIU'91], cementite dissolution was simulated at 910°C in an Fe-C-Cr steel. Transition from fast C-control to slow Cr control (with Cr diffusion in cementite) was calculated, confirming the sequence predicted in [HIL'71]. Satisfactory agreement with the experiments was obtained. More recently, the austenite transformation starting from a ferrite/cementite mixture was considered [GOU'12, XIA'13, LAI'16, OLL'17]. In [WEI'13], ferrite austenite transformation starting from as-quenched martensite with some residual austenite was considered in a high-Si steel. In all these studies, the DICTRA simulations confirmed the characteristics of the austenite transformation which were established experimentally or predicted theoretically. First, the occurrence of successive kinetics stages; an example [LAI'16] was presented in Section 5.1.3.a. Second, the existence of transition temperatures between fast and slow regimes of cementite dissolution (cf. Section 5.1.3.b). Simulations in isothermal condition below or above the PNTT confirmed that the austenite transformation occurs respectively with or without partition of the alloying elements.

Other interesting outcome of the DICTRA simulations is the possibility to predict "overshoots" of austenite fraction (e.g. [HUA'04]): for certain annealing conditions, the austenite fraction can go above the orthoequilibrium (OE) value. For example, this is the case in the simulation shown in Figure 5.4 [LAI'16] on Fe-C-Mn system, in which the maximum fraction of austenite goes higher than the OE value. The last kinetics stage (starting at ca. 10 s) corresponds to a decrease of the austenite fraction down to the equilibrium value. According to [LAI'16] and similar studies [WEI'13, KAM'15, OLL'17], the austenite is formed under out of equilibrium conditions during previous fast kinetics stage. The reason is that heterogeneous Mn composition profiles persist in the austenite due to the sluggish diffusion in this phase. As a result, the ferrite ends up out of equilibrium with too high amount of Mn. On last stage, ferrite amount increases, making decrease its Mn concentration towards the equilibrium value.

Full-numerical treatment of the diffusion equation in 1D was also done in [MEC'15] and [OLL'18]. The numerical method was based on the Murray-Landis finite difference approach [MUR'59]. Main purpose was actually to consider deviations from local equilibrium at the interface. Austenite growth was assumed to grow under mixed-mode control, which means that the interface has a finite mobility. As introduced by Christian [CHR'81], the interface velocity reads:

$$v = M\,\Delta G \tag{5.2}$$

where M is the interface mobility and ΔG the driving force exerted on the interface.

In most simulations, M is assumed infinite: ΔG is equal to zero, i.e. LE holds at the interface (PE assumption is also possible [MEC'15]). Conversely, when the diffusion is much faster than the interface motion, the velocity is controlled by the mobility. The finite mobility is due to the transfer of the atoms from the ferrite or the cementite to reconstruct the new austenite lattice. This process is thermally activated (M follows an Arrhenius law).

Models of [MEC'15, OLL'18] are adapted from mixed-mode models initially introduced for the reverse austenite to ferrite transformation [BOS'07, BOS'09]. Deviations to local equilibrium for this transformation have been investigated for many years (see e.g. [PUR'11, GOU'15]).

In [MEC'15], paraequilibrium is assumed, meaning that only carbon diffusion is considered. Mixed-mode assumption predicts slower kinetics than full diffusion or full interface control (it is not intermediate). The simulations are not compared to experiments. Ollat *et al*. [OLL'18] simulated continuous heating followed by isothermal annealing. Full interface control is predicted below 800°C and mixed-mode above. Mobility is claimed as an efficient way (provided it is adjusted for the considered steel) to describe complex phenomena such as multicomponent solute drag or kinetics transitions from carbon toward Mn controlled transformation.

Full-field two-dimensional (2D) simulations (cellular automata, phase field) were already introduced in Chapter 2, showing the possibilities of these techniques for predicting the austenite morphogenesis and the interaction between austenite transformation and ferrite recrystallization. Other advantage as pointed out in [JAC'99] is the possibility to set as initial state a microstructure taken from experimental micrographs, with potentially complex morphologies. These new approaches have nevertheless some limitations currently. There is no treatment of carbide dissolution: pearlite is treated as one single "phase", and isolated carbides have not been considered so far. This may be due to the different scale between carbide size and austenite grain size. Moreover, the chemical composition of the cementite is not accounted for. Other limitation is that only the carbon diffusion has been considered so far. The volume finite simulations of [JAC'99] are carried out on a binary Fe-C steel. In Fe-C-Mn steel, [RUD'11] assumed NPLE or PE growth. Similarly, in [ZHU'15], only carbon diffusion was considered, but solute drag was introduced in this phase field model, to take account of the effects of the alloying elements at the diffuse interface.

5.2 Austenite transformation kinetics: *in situ* HEXRD characterization

Present section focuses on the austenite formation kinetics, whereas Chapter 2 presented in detail the microstructure evolution in terms of the localization of the nucleation sites, the morphogenesis of the austenite microstructure (banded vs. necklace), highlighting the role of isolated carbides and the interactions with the recrystallization.

5.2.1 Experiments

5.2.1.a Annealing schedules

The annealing schedules applied during HEXRD experiments are identical to those realized for the microstructural characterizations in Chapter 2. The heat treatment comprises two steps (Figure 5.8): the cold-rolled samples are heated from room temperature to the annealing temperature of 800°C, followed by 10 min holding before helium quenching. Heating rates 3 and 30°C.s^{-1} are considered like in previous chapters, with an additional heating rate of 100°C.s^{-1}. Hence, the annealing schedules are still designated by 800H3, 800H30 and 800H100.

One points out that the continuous heating step was recorded in fast acquisition mode (10 Hz). More precisely, the fast acquisition mode was triggered 60 s before the start of the heating. Slow mode was re-activated after 60 s holding at 800°C until the end of the treatment. In slow mode, patterns are acquired every 3 s (~0.33 Hz). As explained in Chapter 1, the resolution in temperature is lower under fast acquisition mode.

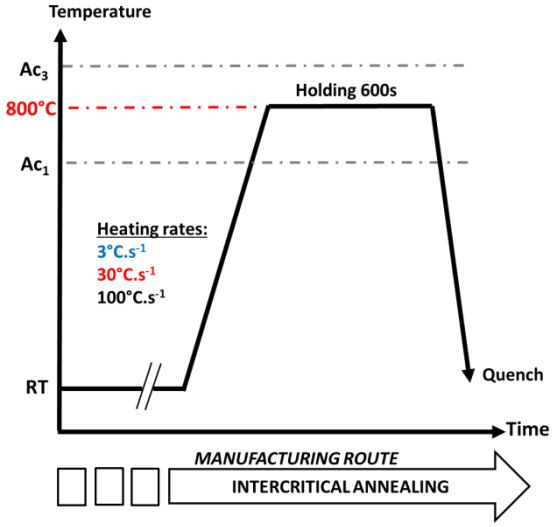

Figure 5.8: Thermal cycles applied for the time-resolved HEXRD *in situ* experiments.

5.2.1.b Exploitation of the 2D-patterns

The post-treatment procedure (Rietveld refinement) of the XRD patterns is detailed in Chapter 1. It has been possible to consider austenite and ferrite phases, whereas, cementite phase was disregarded because of the low carbon concentration (0.1 %$_{wt}$) of the steel. Figure 5.9 shows the DS rings recorded at 650°C and 800°C during the heating at 3°C.s^{-1}, along with the integrated intensity 2θ (I-2θ) profiles. Additional I-2θ profile at 760°C is added to highlight the start of austenite transformation.

Continuous DS rings are obtained thanks to the large number of diffracting grains (ca. 2 x 10^5), leading to powder diffraction conditions. At 650°C, only visible DS rings are those of ferrite. At 800°C, these become weaker because of the lower ferrite mass fraction, while austenite rings are clearly visible. Cementite peaks are observable neither on the DS rings nor on the integrated I-2θ profiles, owing to the low fraction of cementite, ca. 1.5 $\%_{wt}$, consistently with the alloy composition. Figure 5.10 is a magnification of the of I-2θ profiles in 2θ range where cementite peaks are present. A log-scale is necessary to put into evidence the cementite peaks. The cementite could be detected only at temperatures above 600°C. This may be ascribed to the recovery which suppresses defects in the material. From 650 to 755°C, the intensity of the cementite peaks decreases due to the cementite dissolution. Hence, the presence or not of the cementite could be detected by HEXRD. Nevertheless, the cementite mass fraction could not be determined by Rietveld refinement because of the too low intensity of the peaks. For this reason, cementite was neglected during the phase quantification. This induces a small error in the quantification of α and γ phases amount, which will be included in the error bars.

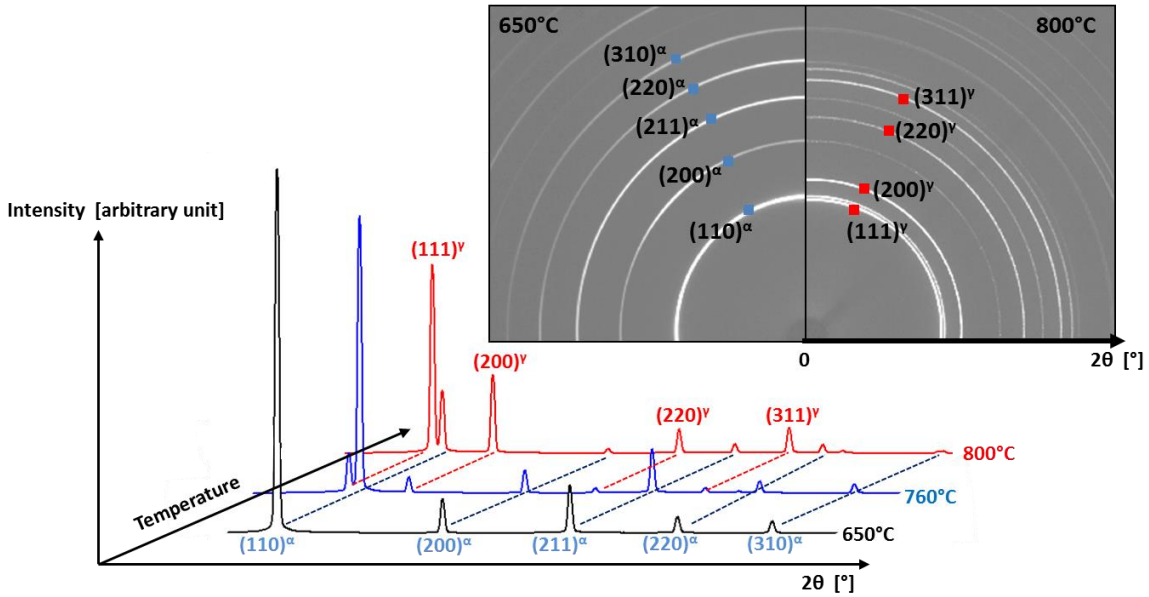

Figure 5.9: 2D Debye-Scherrer (DS) rings recorded at 650 and 800°C during heating at 3°C.s^{-1}. Intensity-2θ profiles from circular integration of the DS rings at 650, 760 and 800°C.

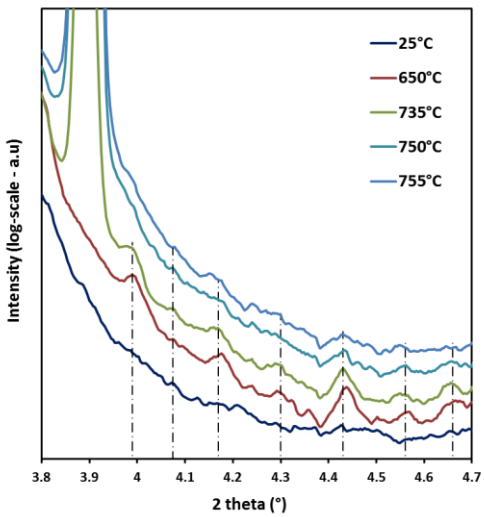

Figure 5.10: Magnification of the intensity 2θ profiles highlighting the cementite peaks whose position is shown by the dashed lines.

5.2.2 Austenite transformation kinetics: slow heating (800H3 sample)

The evolution of the austenite mass fraction measured by HEXRD on the 800H3 sample is shown in Figure 5.11. Heating to 800°C and holding are represented separately. On the heating curve, results from image analysis of SEM micrographs are also plotted (equal volume and mass fractions are assumed), (cf. Chapter 2). Main stages of the austenitization process identified by SEM are also represented: nucleation of austenite, transformation of pearlite and formation of the necklace austenite morphology.

The transformation start temperature is detected by XRD at 710°C. This is in good agreement with the SEM micrographs, in which first austenite grains are observable between 700 and 710°C. These first grains are located exclusively at isolated carbides on recrystallized ferrite grain boundaries and triple-junctions. Nucleation at pearlite island boundaries starts later, between 720 and 730°C. The austenite transformation kinetics shows two stages on heating, slow then fast. From 710 to 730°C, the austenite mass fraction remains inferior to 1.5% (XRD) or 3.5% (SEM). At 730°C, the transformation kinetics accelerates. Two processes occur simultaneously: growth of austenite into pearlite and growth of austenite from isolated carbides located at prior ferrite grain boundaries. After the acceleration at 730°C, there are no more stages visible in the kinetics curve up to 800°C. Nevertheless, significant evolutions occur in the microstructure: last detection of cementite by XRD at 766°C, pearlite full transformation between 760 and 780°C. The necklace austenite morphology develops by the decoration of the ferrite grain boundaries. This process is achieved between 750 and 780°C. At 800°C, austenite mass fraction reaches 50%, in accordance with microstructural observations (Fig. 2.16 (m-n)).

During the subsequent isothermal holding, the austenite fraction increases toward the Ortho-Equilibrium value, which is reached after ca. 300 s. Two kinetics stages may be distinguished, fast then slow with a smooth transition after ca. 30 s. Accordingly, the SEM micrographs confirm a strong increase of the austenite volume fraction from 0 s to 60 s and few evolution from 60 s to 600 s.

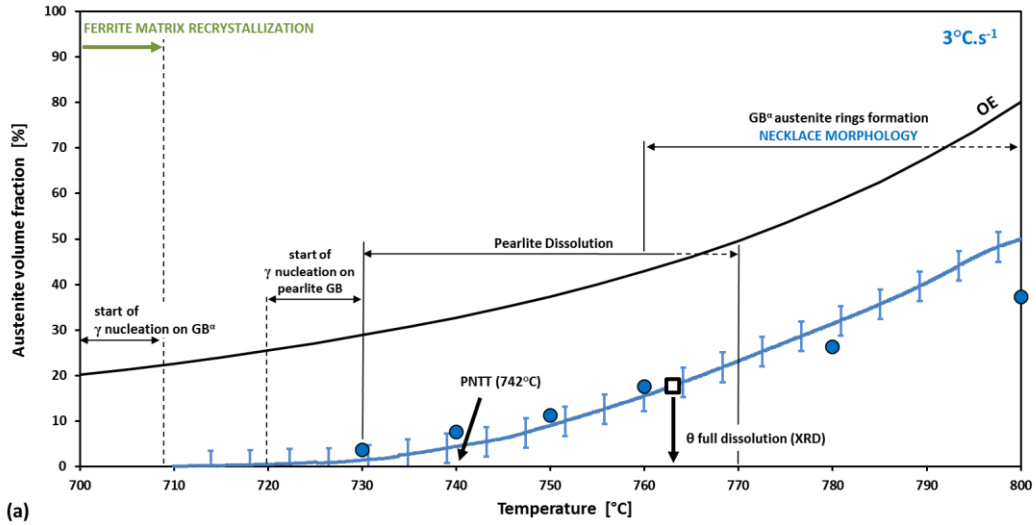

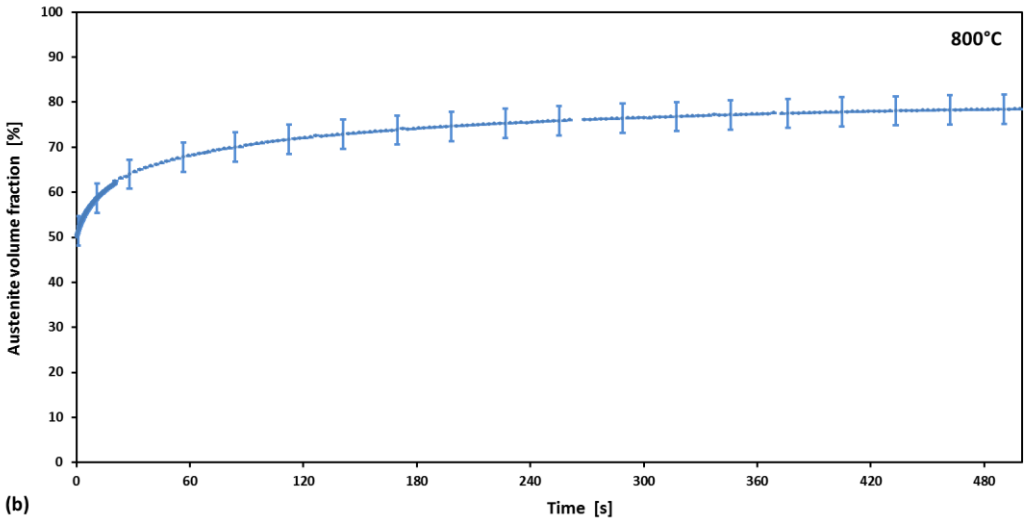

Figure 5.11: measured volume fraction of austenite during (a) slow heating 3°C.s^{-1} up to 800°C and (b) subsequent isothermal holding at 800°C for 600s.

5.2.3 Austenite transformation kinetics: fast heating (800H30 and 800H100 samples)

Figure 5.12 shows the evolution of the austenite mass fraction during heating at 30°C.s^{-1}. Main microstructure evolutions observed by SEM are also represented, as for 800H3 sample. In addition, the recrystallization kinetics determined during the same experiment (cf. Chapter 4, Fig. 4.12) is plotted. Ferrite recrystallization start is detected by SEM at 710-720°C, sooner than by XRD. Austenite starts to be detected by XRD at 738°C. The austenite transformation start is detected earlier by SEM, successively at linear cementite carbide arrays located at boundaries of non-recrystallized ferrite grains (710-720°C), at carbides located at recrystallized ferrite grains boundaries and pearlite island boundaries (720-730°C).

Three kinetics stages can be distinguished. Up to 752°C, the austenite mass fraction remains inferior to 2%. After this first sluggish stage, the austenite transformation kinetics accelerates drastically at 745°C, up to 765°C. This acceleration is concomitant with the onset of ferrite recrystallization. Pearlite transformation, which starts at 740°C, is preponderant according to SEM micrographs, but austenite forms also from isolated carbides. At 765°C, the transformation kinetics decreases. The slow-down is ascribed to slower growth of austenite inherited from dissolved pearlite islands, dissolution of remaining isolated carbides and pearlite. Last detection of cementite by XRD (756°C) occurs before the end of pearlite transformation according to SEM micrographs (up to 770°C). At 790°C occurs a final acceleration, which has no interpretation so far. During subsequent isothermal holding at 800°C, the austenite fraction increases towards a final value which is higher than OE by ca. 5%. Two kinetics stages, fast then slow follow each other with a smooth transition after ca. 30 s. These two stages are again confirmed by SEM observations, like in 800H3 sample.

Figure 5.12(b) shows the evolution of the austenite mass fraction determined by XRD during heating at 100°C.s^{-1}, and subsequent holding at 800°C. During heating the austenitization kinetics exhibits the same three stages as at 30°C.s^{-1}. The fast second stage (745-765°C) is faster in the 800H100 sample. The amount of austenite at any given temperature is higher than at 30°C.s^{-1}, but this can be explained in part by the uncertainty in temperature due to fast mode acquisition (ΔT=10°C at 100°C.s^{-1}). During subsequent isothermal holding at 800°C, the austenite fraction increases towards a final value which is higher than OE by ca. 10%. Two kinetics stages, fast then slow follow each other with a smooth transition after ca. 30 s.

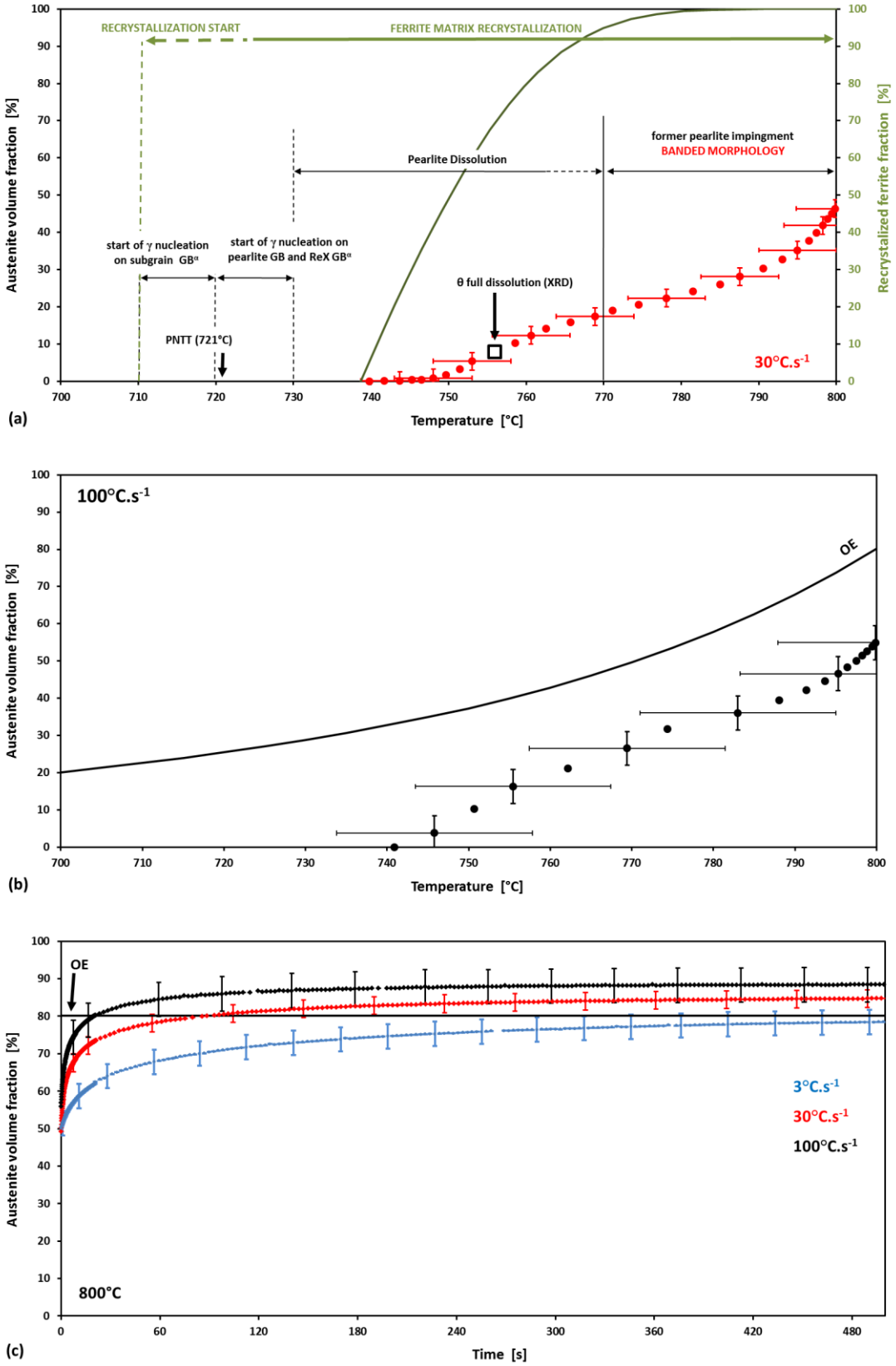

Figure 5.12: measured volume fraction of austenite during heating (a) 30°C.s^{-1} and (b) 100°C.s^{-1} up to 800°C. (c) Subsequent isothermal holding for 600s.

5.2.4 Discussion

Our experiments are in agreement with several trends reported in literature.

First, the global transformation kinetics enhancement associated with fast heating rates is clearly observed. During heating, the higher the heating rate, the higher the austenite transformation kinetics (except during sluggish first stages). During isothermal hold at 800°C the higher the previous heating rate, the higher the fraction of austenite at any time.

Second, fastest heating treatments (800H30, 800H100) lead to a fraction of austenite which exceeds that expected according to the thermodynamic equilibrium, whereas slow heating (800H3) leads to the expected equilibrium fraction. Moreover, the fraction shift is increased with increasing heating rate.

Third, different kinetics stages can be identified: at least two on heating, sluggish then fast for slow heating (800H3) and maybe three stages on heating for hast heatings (800H30 and 800H100). During isothermal hold at 800°C, smooth transition from fast to slow regime occurs.

These observations may highlight the influence of three processes which are known to interact with the austenite transformation according to the literature: the recrystallization of the ferrite, the enrichment of the cementite carbides in Mn, the fragmentation/spheroidization of the cementite inside the pearlite colonies.

5.2.4.a Interaction with recrystallization

Slow heating (3°C.s^{-1}) enables the complete recrystallization of the ferrite before the start of the austenite transformation (weak interaction), whereas fast heating (30 or 100°C.s^{-1}) leads to strong interaction transformation/recrystallization. Put together, these experiments do not show any clear influence of the ferrite recrystallization on the austenite transformation kinetics.

At 30°C.s^{-1}, the start of the austenite transformation in fast regime is concomitant with the start of the ferrite recrystallization, at ca 750°C. This is put into evidence by the respective kinetics plotted in Figure 5.12(a). The SEM observations (Chapter 2) confirm that the austenite grains nucleated on isolated carbides are frequently located at the boundaries of recrystallized ferrite grains. But this does not necessarily mean that austenite nucleation and growth was faster at recrystallized ferrite grain boundaries. The presence of austenite grains on these sites can also be interpreted by the pinning of the recrystallizing ferrite grains by the first grains of austenite. In fact, the acceleration of the overall kinetics at 740-750°C comes in large part from the pearlite islands transformation, as mentioned in Chapter 2.

At 3°C.s^{-1} heating rate, recrystallization is completed before the start of the austenite transformation. The fast regime of austenite transformation starts at 730°C. This could suggest that austenite transformation from isolated carbides is faster when the ferrite is fully recrystallized. Indeed, at 730°C, the pearlite islands have not yet started to transform (pearlite islands transformation starts at ca. 740°C). However, this early acceleration of the austenite transformation kinetics at 3°C.s^{-1} can be due to the slow heating rate, which lets more time for the thermally activated nucleation and growth of austenite to occur.

5.2.4.b Enrichment of the cementite in Mn

As recalled in the literature survey (Section 5.1.3.a), dissolution of cementite is more sluggish when its concentration in Mn is increased. This section deals with the possible consequences on the overall austenitization kinetics. Slow heating (3°C.s^{-1}) enables a significant enrichment in Mn of the cementite before the start of the austenite transformation. The Mn u-fraction reaches 11% after slow heating at 3°C.s^{-1} to 700°C (cf. Chapter 3), both in isolated carbides and in pearlite. Conversely, fast heating (30 and 100°C.s^{-1}) does not leave sufficient time to enrich the cementite, whose composition remains the

same as in the HR state, ca. 6.5% u-fraction. One can calculate the critical temperature (PNTT), above which fast cementite dissolution (controlled by carbon diffusion) becomes possible.
The PNTT was calculated as a function of the Mn u-fraction in cementite (Figure 5.13); it is equal to 721°C for 800H30 and 800H100 samples and 736°C for 800H3 sample. "Geometry A" (Figure 5.5) was considered, i.e. a cementite particle embedded in an austenite shell, which is itself embedded in a ferrite matrix. This geometry is obviously representative of the isolated carbides. One reminds that according to [LI'11], "geometry A" is also suitable to interpret the dissolution of lamellar pearlite, despite the different geometry. However, "geometry A" can clearly not represent the fragmented pearlite, as it consists of cementite carbides embedded in a ferrite matrix. "Geometry B" would be more relevant; associated PNTT was also calculated, but the calculated temperatures, significantly higher than for Geometry A, are not shown. In fact, it will be seen in the DICTRA simulation study that the fragmented pearlite can dissolve quickly even with the redistribution of the alloying elements (i.e. it can be fast even below the PNTT of geometry B).

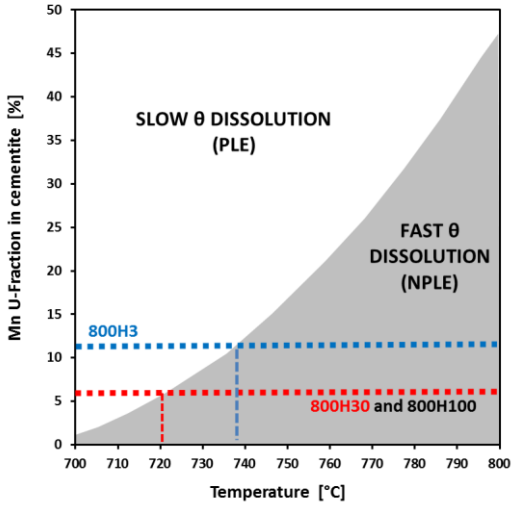

Figure 5.13: Calculated PNTT for the change from slow to fast regime of cementite dissolution as a function of Mn composition in cementite and holding temperature (cf. Chapter 3, Section 3.1.5). The cementite compositions measured in Chapter 2 for the two heating rates, 3 and 30°C.s^{-1} are referred to by the blue and red dotted lines, respectively.

During slow heating (3°C.s^{-1}), the sluggish kinetics between 710 and 730°C is due to slow regime of the isolated carbides dissolution involving partition of alloying elements, as the temperature is below the calculated PNTT, 736°C. The acceleration of the kinetics at 730-740°C may be ascribed to the transition to the fast regime, controlled by the diffusion of carbon, but it is rather thought to come in large part from the start of the pearlite dissolution, according to the SEM observations.
At 30°C.s^{-1}, the austenite transformation kinetics remains slow up to a temperature of 740°C, at which the pearlite starts to dissolve. As the PNTT is equal to 721°C for this sample, the isolated carbides could have dissolved in fast, carbon-controlled mode. It can be seen that if this occurred, it did not accelerate significantly the overall kinetics. Accordingly, in the SEM micrographs, growth of the austenite grains nucleated on isolated carbides does not seem particularly fast.
Hence, from these observations one concludes that the cementite composition in Mn did not influence significantly the overall austenite transformation kinetics. But this does not mean that the specific dissolution kinetics of each isolated carbide is not affected, as will be seen in the DICTRA simulations.

5.2.4.c Fragmentation / spheroidization of the cementite inside pearlite colonies

Our experiments may put into evidence the effect of the fragmentation and the spheroidization of the cementite in pearlite islands, although further experiments would be necessary to confirm this. At 100°C.s^{-1}, the austenite transformation kinetics follows the same stages as at 30°C.s^{-1}, but the fraction of austenite formed is larger at any given temperature (even with accounting of the uncertainty in temperature). This is not due to the cementite composition, which is the same in 800H30 and 800H100 samples. As for recrystallization, it occurs at same temperature ranges for both samples.
Possible origin of the different kinetics is that the less fragmented pearlite in 800H100 sample would be easier to dissolve. Indeed, it is the fast stage of austenite transformation between 740 and ca. 760°C, dominated by pearlite dissolution, which is faster at 100°C.s^{-1}, whereas later stages present similar kinetics at 30 and 100°C.s^{-1}. Previous studies [DAS'93, GAN'09] demonstrated that lamellar pearlite dissolves faster than when it is spheroidized.

To conclude, the overall austenitization kinetics is not clearly influenced by the strong or weak interaction with recrystallization (but the morphogenesis is strongly affected); the cementite enrichment in Mn does not influence significantly the overall kinetics, except possibly during first sluggish stage of slow heating. Possible influence of the degree of fragmentation of the pearlite is suggested, but it has to be confirmed by further investigations. At this point, the trends regarding the kinetics can be interpreted as follows.

- The transition from slow to fast regime on heating is due in large part to the start of the pearlite transformation, whatever the heating rate. The SEM micrographs show that the pearlite starts to dissolve at similar temperature range 740-750°C for both 3 and 30°C.s^{-1} heating rates. One points out again that fast, carbon-controlled transformation of fragmented pearlite is not possible thermodynamically. DICTRA simulations of Section 5.4.2 will justify that fast transformation of pearlite is nevertheless possible.

- The dissolution of the isolated carbides does not modify the shape of the austenitization kinetics curves, contrary to the case of the pearlite. First reason is that these carbides contain only ca. one third of the carbon in the microstructure. Moreover, each isolated carbide will dissolve with a specific kinetics determined by its size and composition in Mn. The respective kinetics associated with each carbide are spread over a large temperature range.

Several trends have still to be explained: the increased kinetics at faster heating rate during the heating stage, the faster kinetics during isothermal hold after faster heating and the austenite fraction "overshoots". This is the purpose of the DICTRA simulations.

5.3 DICTRA modeling strategy

This section deals with the setup of the DICTRA simulations. Influence of meshing, step time, cell sizes are not addressed here. The reader is referred to the work of Arlazarov or Ollat [ARl'14, OLL'17] for a detailed review. 800H3 and 800H30 annealing schedules will be simulated for comparison with the experimental data.

5.3.1 Thermodynamic hypotheses, diffusivity data

The alloy bulk composition is simplified to the ternary Fe-0.1C-1.9Mn (%wt) system. Si and Cr are neglected consistently with their low concentration in the alloy, ca. 0.2%wt. This simplification has few consequences on the thermodynamics of the system. For instance, the equilibrium austenite volume fraction at 800°C is increased from 81% with full alloy composition to 86% with the simplified composition. Besides, the TCFE9 database is assessed at highest order on the quaternary C-Fe-Mn-Si system. Hence, thermodynamic computations considering the full Fe-C-Mn-Cr-Si system would involve extrapolations from lower-order systems according to the CALPHAD method [DIC'17]. Considering the Fe-C-Mn-Cr-Si system would thus increase significantly the DICTRA simulation time without real gain in precision. Other benefit of the ternary system is the easier interpretation of the simulation results.

It was decided to neglect the local Mn-composition fluctuations associated with the presence of the Mn-rich bands. The difference between minimum and maximum compositions (1.83 and 2.02%$_{wt,}$ respectively, see Chapter 2) supports this choice.

The interface conditions are parametrized to be controlled by local equilibrium (LE), permitting the simulation of either NPLE or PLE regimes, depending on the calculation (there is no a priori assumption). Curvature effects (Gibbs Thompson), morphological evolutions or interaction between particles (coarsening) were disregarded in our simulations.

As mentioned in Chapter 1, the mobility data are taken from the MOBFE2 database (coupled with TCFE9 to get the diffusivities). There is no accounting of any acceleration of the diffusion by the presence of defects (dislocations, grain boundaries). In contrast to Chapter 3, the Mn diffusion coefficient inside cementite is not increased.

5.3.2 Geometrical representation of the microstructure

5.3.2.a Selection of DICTRA simulation cell geometries

On the basis of the literature survey and our microstructural observations (cf. Chapter 2), the austenite is assumed to nucleate and grow from two different sites: the pearlite islands and the isolated carbides located at the ferrite grain boundaries. As represented in Figure 5.14(a), the austenite will nucleate around the isolated cementite particles and then grow towards the surrounding ferrite, while the carbide is dissolving to supply carbon. For pearlite, two distinct stages are considered. Firstly, the pearlite islands transform to austenite, as schematized in Figure 5.14(b). After completion of this transformation, there remains an austenite grain supersaturated in carbon. Secondly, the latter newly formed austenite grain grows further within the surrounding ferrite matrix (Figure 5.14(c)).

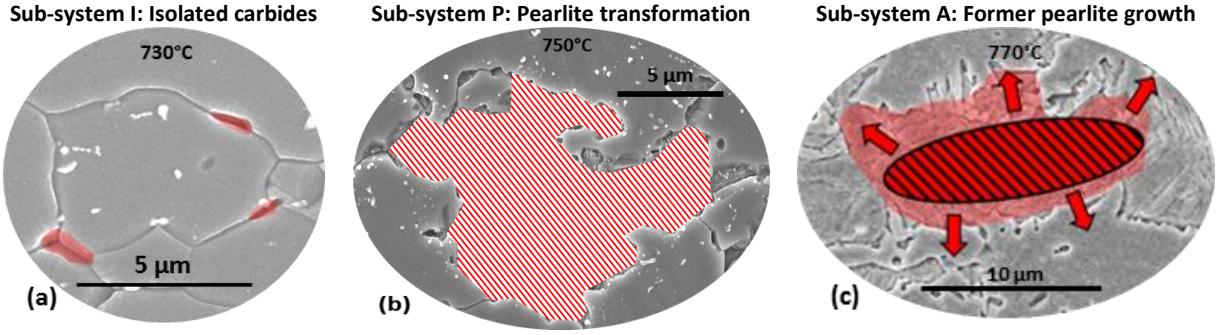

Figure 5.14: Microstructure observations of the three sub-systems to be simulated with DICTRA: (a) dissolution of the isolated cementite particles localized on the grain/subgrain boundaries. (b) Transformation of pearlite islands leading to carbon-rich austenite (CRA) grain. (c) CRA grain growth into the surrounding ferritic matrix. (780H3 Sample).

Consistently, three sub-systems will be modeled with DICTRA (Figure 5.15):

Sub-system I: Isolated carbide dissolution

Sub-system P: Pearlite transformation leading to the formation of the CRA grain

Sub-system A: CRA grain growth into the surrounding ferrite matrix.

Selection of a spherical geometry is straightforward for systems I and A. As for the pearlite, there is no detailed geometrical representation possible with DICTRA. Purpose of the simulation cell in Figure 5.15 is to represent the austenite growth front moving into a fragmented pearlite colony. In cell P, only one fragment of cementite is represented, but two important aspects of the process are accounted for: the fast diffusion of carbon and manganese in ferrite from the cementite to the austenite, and the short diffusion distances. Nevertheless, the cell P does not represent the fact that some fragments of cementite may get surrounded by the growing austenite. The final stage of cementite dissolution in an austenite matrix is thus not represented.

The sub-systems are considered as closed systems, independent from each other (no impingement). This simplifying assumption will be discussed in the next section.

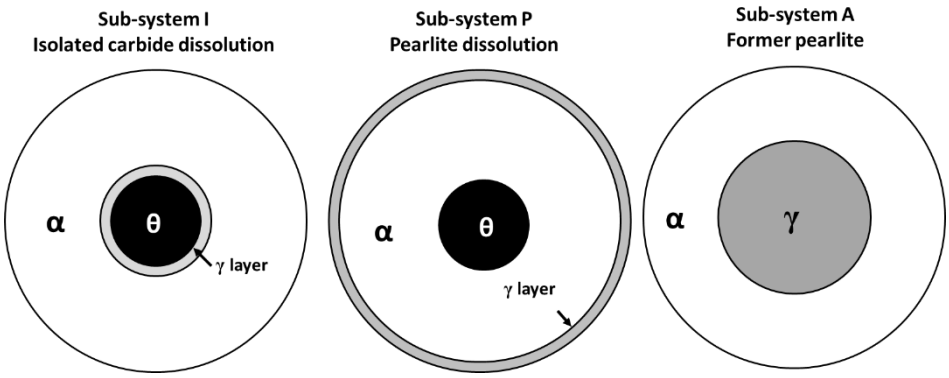

Figure 5.15: Schematic of DICTRA simulation cells for sub-systems I, P and A.

5.3.2.b Representation of the global ferrite-pearlite microstructure

Figure 5.16 shows the representation of the microstructure from the point of view of our modeling approach with DICTRA. The starting microstructure consists of pearlite islands and isolated carbides distributed in the ferrite matrix (Figure 5.16(a)). It is assumed that the isolated carbides have one single size and that these carbides are homogeneously distributed in the ferrite matrix. Hence, one unique cell size is considered for sub-system I (no size distribution considered for the carbides).

- Upon annealing, the austenite will consume the pearlite colonies, until formation of carbon supersaturated austenite grains which inherits the former pearlite grain size (Figure 5.16(b)). This part of the simulation concerns the sub-system P.
- Then the resulting carbon-rich austenite (CRA) grains grow into the surrounding ferrite matrix (sub-system A), as schematized in Figure 5.16(c).
- Meanwhile, austenite transformation from isolated carbides will be described by sub-system I.

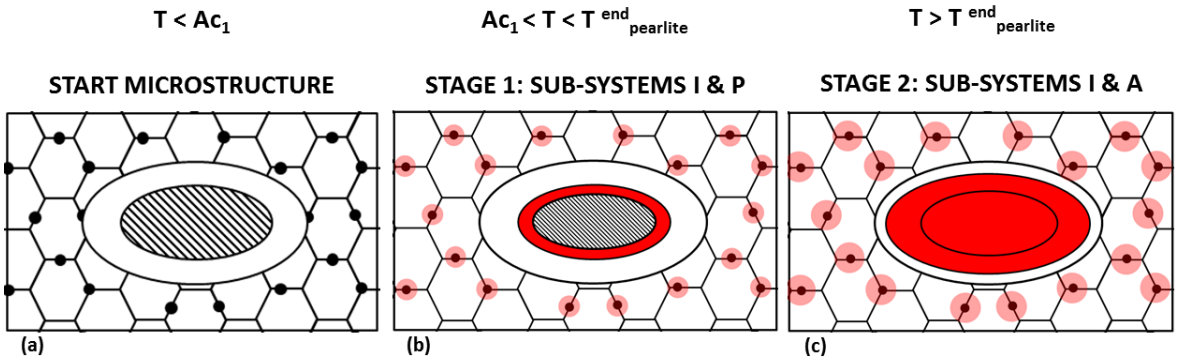

Figure 5.16: Scheme of the geometrical representation of the microstructure: sequence of the austenite transformation.

It is assumed that the cells P, A and I are closed systems. There is no transfer of C and Mn elements “at long distance” between the former pearlite regions and the isolated carbides. Other strong assumption concerns the localization of the isolated carbides with respect to the A sub-system. In the “real microstructure”, the large austenite grains which result from pearlite transformation will expand into the surrounding matrix and possibly overlap the closest isolated carbides, which will then dissolve in the austenite (Figure 5.17). This is impossible to describe with DICTRA. Hence a strong simplification is to

assume that the isolated carbides are localized outside the cell A, so at some distance from the pearlite islands.

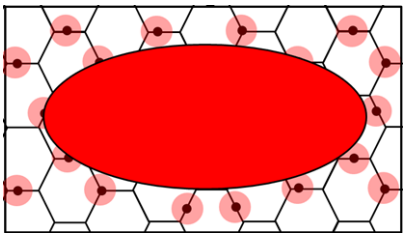

Figure 5.17: Scheme highlighting the overlap of the growing austenite grains from former pearlite with the closest intergranular cementite particles.

The size of the simulation cells and the compositions are based firstly on the experimental characterizations on the 700H3 and 700H30 specimens, which reflect the state of the microstructure just before the start of the austenite transformation. The size of the simulation cell P is directly determined by the size of the spheroidized carbides in the pearlite (R=75 nm) and the knowledge of the average carbon concentration in the pearlite (1.78 $\%_{at}$). By a mass balance on the carbon element, the thickness of the ferrite "shell" in cell P can then be calculated.

Definition of I and A cell sizes is much less straightforward. Only known microstructural parameters are respectively the isolated carbide size and the initial size of the CRA grains which is taken as the pearlite islands size. However, microstructural observations are lacking to give directly the size of the ferrite shell in respective cells I and A. Indeed, the number density of isolated carbides could not be measured. As for the cell A, the lacking microstructural information is the maximum size reached by the austenite grains which grew from former pearlite. Due to the complexity of the microstructure (cf. Fig. 2.16(m)), this size could not be measured.

Hence the definition of cells I and A cannot be based on microstructural data. It was found more appropriate to define the cell sizes on the basis of their overall composition in carbon. Most straightforward choice would be to impose inside each cell I and A the nominal carbon content of the steel (0.46 $\%_{at}$). It will be seen in next section that this "intuitive" choice is far from being appropriate.

5.3.2.c Distribution of the carbon in the microstructure

The carbon distribution is highly heterogeneous in the initial microstructure. Upon annealing, this heterogeneity will be partially reduced, but it will remain significant. This section presents how this is dealt with in our geometrical representation of the microstructure. The carbon distribution in the initial microstructure is represented by the following molar balance:

$$f^P X_c^P + f^M X_c^M = X_c^0 \tag{5.3}$$

where f^P and f^M denote the fraction of pearlite and the matrix (meaning here a ferrite / isolated carbides mixture). X_c^P and X_c^M are the carbon molar fraction in the pearlite (X_c^P=1.78 $\%_{at}$) and the matrix (X_c^M=0.20 $\%_{at}$). X_c^0 is the alloy nominal carbon content (0.46 $\%_{at}$). It is assumed that all the phases have the same molar volume.

The carbon is highly concentrated in the pearlite, which contains 63% of the nominal carbon for a volume fraction of 16%, while the matrix contains 37% of the carbon for a volume fraction of 84%. The proportion of carbon inside the pearlite (63%) is denoted r.

Once the pearlite is dissolved and transformed into an austenite grain, a new molar balance can be written:

$$f^{A} X_c^{A} + f^{I} X_c^{I} = X_C^0 \tag{5.4}$$

where f^{A} and f^{I} are the volume fractions represented by the sub-system A and I, respectively. X_c^{A} and X_c^{I} are the related carbon nominal compositions considered in the sub-systems.

The A sub-system should inherit the carbon of the pearlite. Hence, 63% of the carbon should be in sub-system A. This means that the following relationship has to be verified:

$$f^{A} X_c^{A} = \mathrm{r}\, X_C^0 \tag{5.5}$$

and reciprocally for the sub-system I:

$$f^{I} X_c^{I} = (1 - \mathrm{r})\, X_C^0 \tag{5.6}$$

These equations highlight that once the pearlite is dissolved, carbon concentration heterogeneities may subsist in the microstructure. For instance, if sub-system A represents a low volume fraction, its related carbon concentration will be high, meaning that the whole microstructure will remain significantly heterogeneous in carbon. Figure 5.18 shows the carbon concentration in each sub-system A and I as a function of their respective volume fraction. Calculations are based on previous equations. As expected, increasing the fraction of respective sub-system I or A tends to decrease its carbon concentration.

Two limit cases are represented. First one denoted “start condition” assumes that the carbon supersaturated austenite grains (sub-system A) do not grow into the surrounding ferrite. The carbon concentration would remain $X_c^{A} = 1.78$ $\%_{at}$. This is obviously unrealistic as the further growth of the former pearlite bands was clearly observed on the SEM micrographs (cf. Chapter 2). Other limit case assumes that both A and I sub-systems would have the bulk carbon content of the steel (i.e. the microstructure becomes fully homogenized in carbon). Some intermediate values of f^{I} and f^{A} volume fractions have to be selected, despite the absence of precise microstructural basis to conduct this choice. Two criteria are considered here.

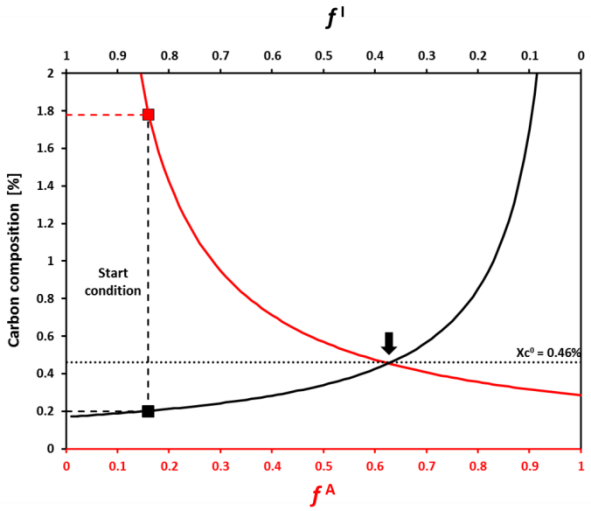

Figure 5.18: Evolution of the respective mean carbon compositions X_c^{I} (black curve) and X_c^{A}(red curve) as function of the sub-system volume fractions.

First criterion is an approximate microstructural parameter: the number of isolated carbides per pearlite colonies. Order of magnitude of this number can be estimated on the micrographs (Chapter 2). According to our geometrical representation, this number is equal to ratio of the volume of cell A over the volume of cell I V_A/V_I. Figure 5.19 shows the evolution of this ratio as a function of X_c^I. Two curves are plotted for heating rates 3 and 30°C.s^{-1}. V_A/V_I ratio is higher for fast heating, since the isolated carbide size (hence the I cell size) is smaller (R=75 nm instead of 110 nm at 3°C.s^{-1}). Increasing X_c^I makes increase the ratio V_A/V_I, as the volume V_I is decreased and the volume V_A is increased correspondingly. It can be seen that the ratio V_A/V_I approaches rapidly unrealistically high values if X_c^I is increased too much. For example, if one assumes that both cells A and I have the nominal carbon content of the steel (X_c =0.46 $\%_{at}$) a ratio of ca. 1000 per pearlite grain is found for the heating rate 30°C.s^{-1}. This ratio is clearly too high if one considers the micrographs of the initial microstructures (cf. Fig 2.14), even with accounting of the 2D observation. Hence, one concludes from this criterion that one has to select a value of X_c^I as low as possible.

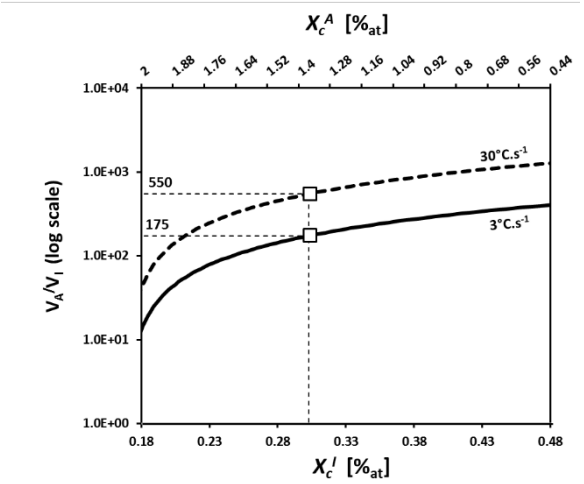

Figure 5.19: Evolution of the V_A/V_I ratio, representative of the number of isolated carbides present in the ferrite matrix for each pearlite grain.

Second criterion concerns the amount of austenite which can be formed in each sub-system, which depends on its respective carbon content. At the end of isothermal holding at 800°C, the overall amount of austenite F_γ transformed in the whole microstructure should be close to the equilibrium value (86% for the simplified alloy nominal composition), in accordance with the experiment (cf. Fig. 5.11 and 5.12). The overall amount of austenite F_γ reads:

$$F_\gamma = f^A f_\gamma^A + f^I f_\gamma^I \tag{5.7}$$

where f_γ^A and f_γ^I are the equilibrium austenite volume fractions inside the respective sub-systems.

Assuming that the equilibrium fraction of austenite is reached at 800°C in both sub-systems, Figure 5.20 shows the overall fraction of austenite at orthoequilibrium (F^{OE}) as a function of X_c^I. F^{OE} increases from ca. 67% at X_c^I=0.20$\%_{at}$ to reach a plateau at ca. X_c^I=0.32 $\%_{at}$. The reason is that with low X_c^I values, the volume fraction of system I is large, whereas the OE fraction of austenite is low in this system. According to the XRD experiments (cf. section 5.2), the fraction of austenite at the end of annealing should be close or even above the OE value. Hence, conclusion of the second criterion is to select a value of X_c^I such as F^{OE} has the maximum value (in the plateau of the curve).

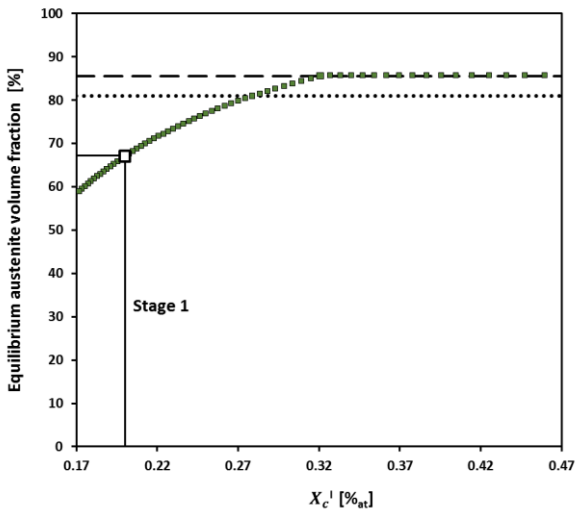

Figure 5.20: Evolution of the global OE austenite phase fraction obtained after summation F_γ^{OE} as function of the mean carbon composition considered within: (a) sub-system I and (b) reciprocally within sub-system A.

Combining with previous microstructural criterion, which led to smallest possible values of X_c^I, the best choice for X_c^I, is the smallest one "on the plateau". A "round value" X_c^I=0.3%$_{at}$ is taken. For the following, the considered equivalent nominal compositions X_c^I and X_c^A are consequently 0.30%$_{at}$ and 0.66 %$_{at}$, respectively. The related equivalent volume fractions of systems I and A are f^I = 0.56 and f^A = 0.44 %$_{vol}$.

5.3.3 Austenite nucleation

Consistently with the experiments, heatings at 3 and 30°C.s^{-1} (denoted HR3 and HR30) are modeled. This means that one has to know at which temperature the austenite will start to be present. Simplest option is to take the experiments as a basis. Otherwise, some calculations can be done. Nevertheless, as shown in the literature survey, the austenite nucleation has been scarcely studied and few models have been established. DICTRA software proposes two options:

- "Active phase", meaning that the austenite is present as soon as the simulation is launched.
- "Inactive phase": austenite is absent at the simulation start. Its presence is triggered once the driving force exceeds some user-defined value. By default, the driving force for nucleation is set to 10^{-5} x RT J.mol^{-1}, R being the gas constant and T the temperature. This value is commonly used in literature [LAI'16, HUY'18].

Both options were experimented. With the "inactive phase" option, the austenitization starts too early. "Nucleation" is triggered as soon as the Ae_1 temperature is reached, whatever the heating rate. The transformation kinetics are largely over-estimated relative to the experiment. Hence, the nucleation driving force should be adapted, but this almost amounts to imposing directly the temperature of austenite nucleation. Therefore, the "active phase" option was employed. The temperature at which the simulation is started was calculated by using the empirical formula of Kasatkin [KAS'84] which gives the Ac_1 temperature as a function of the alloy composition:

Ac_1(°C)= 723 - 7.08Mn + 37.7Si + 18.1Cr + 44.2Mo + 8.85Ni + 50.1V + 21.7Al + 3.18W + 297S - 830N - 11.5C Si - 3.10Si Cr - 57.9C Mo – 15.5Mn Mo -5.28C Ni – 0.80Cr Ni – 27.4C V + 30.8Mo V – 0.84Cr^2 - 3.46Mo^2 - 0.46Ni^2 - 28V^2

where the compositions are in weight percent. One stresses that the heating rate is not accounted for.

For both systems I and P, the same Ac_1 temperature was calculated to 720°C. This temperature is consistent with the SEM observations: first austenite grains were detected in temperature range 710-720°C in both 800H3 and 800H30 samples. The initial austenite layer thickness was set to 0.1 nm.
It is stressed that in the following simulations, there is no calculation of any nucleation rate (i.e. fast saturation of the nucleation sites is assumed). The consequences of this strong assumption will be elaborated in the Discussion part.

5.3.4 Cell sizes and compositions

The cell sizes and compositions were calculated in accordance with the TEM composition measurements and SEM morphological analyses carried out on the 700H3 and 700H30 specimens. This section presents how the cell parameters are defined. The parameters are then detailed case by case for P, I and A cells.

5.3.4.a Cell dimensions

The cell dimensions for each system I, P and A are derived from molar balances regarding the carbon. (Chapter 1 reminded how molar volumes are dealt with in DICTRA).

- In system P, the radius of the cementite is taken to 75 nm, the average measured value. The thickness of the ferrite shell surrounding the cementite is defined such that the overall carbon content in the cell is equal to the value estimated previously inside the pearlite, 1.78 at.% (Chapter 3).
- In system I, the radius of the cementite is taken to 100 and 75 nm at 3 and 30°C.s^{-1} respectively, according to the measurements (Chapter 2). The cell I contains a carbon concentration X_c^I=0.30 $\%_{at}$, as justified in previous Section.
- In system A, the radius of the austenite is deduced from the size of the pearlite islands (radius 2.5 µm). The cell A contains a carbon concentration X_c^A=0.66 $\%_{at}$, as justified in previous Section.

5.3.4.b Initial compositions in Mn

In systems I and P, the initial Mn concentration in cementite depends on the heating rate. The values are taken from Chapter 3 (see the following tables). In system A, Mn (and C) compositions were considered fully homogenized within the whole austenite grain volume, even though the initial Mn partition inside the cementite platelets (at least 6.5% in substitutional site fraction) could involve local subsisting heterogeneities periodically spaced, (so-called “ghost pearlite”). It can be assumed that these heterogeneities are too far from the austenite/ferrite interface to influence its velocity. In ferrite, the Mn content is calculated such that the overall Mn content has the bulk steel composition (1.94 $\%_{at}$) in all sub-systems I, P and A.

5.3.4.c Initial composition of austenite

In systems I and P, one has to define somewhat arbitrarily some initial carbon composition profile inside the austenite phase in order to start the simulation. The constraint is to avoid deviating too much from some local equilibrium tie-line at both interfaces γ/α and γ/θ. Otherwise, the numerical simulation

will fail to start. The NPLE tie-lines (γ inherits u-Mn content of α or θ) were found to represent a good choice to help the calculations to start. One stresses that once the simulation has achieved to start, the operative tie-lines at the γ boundaries can deviate in a short time from this initial guess.

5.3.4.d Space discretization

In DICTRA software, each phase is represented by a region. Each region is discretized using unidimensional grids. Meshing nodes were distributed according to a geometrical progression in ferrite and cementite in order to get a finer mesh close to the moving phase boundaries. A linear grid spacing is used for the austenite in I and P cells, a geometrical grid in A cell. Both time and spatial discretization were optimized in order to reduce the computation time, without losing accuracy.

P, I and A cell parameters are summarized in the following figures and tables.

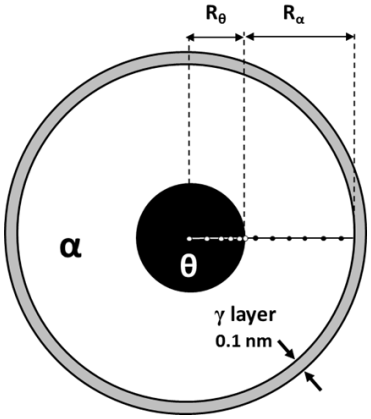

	Meshing		
	Radius [nm]	*n*	*f*
Cementite θ	75	50	0.995
Ferrite α	128	50	1.02
Austenite γ	0.1	10	1

	Phase compositions			
	3°C.s^{-1}		30°C.s^{-1}	
	X_{Mn} [%at]	Xc [%at]	X_{Mn} [%at]	Xc [%at]
Cementite θ	10.5	25	4.75	25
Ferrite α	1.32	6.17 x 10^{-2}	1.70	5.00 x 10^{-3}
Austenite γ	1.36	3.07	1.75	2.89

Figure 5.21: DICTRA cell P definition for heating rates 3 and 30°C.s^{-1}. *n*: number of nodes in each region; f: geometrical progression factor.

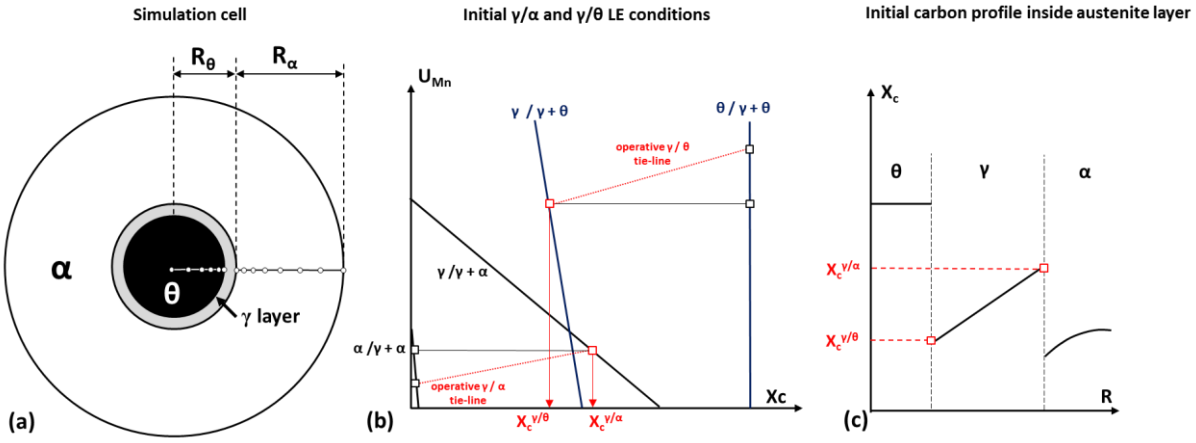

	Phase compositions			
	3°C.s^{-1}		30°C.s^{-1}	
	X_{Mn} [%at]	Xc [%at]	X_{Mn} [%at]	Xc [%at]
Cementite θ	10.5	25	4.75	25
Ferrite α	1.85	5.67 x 10^{-2}	1.90	3.00 x 10^{-2}
Austenite γ/θ	14.4	2.81	6.16	1.65
Austenite γ/α	1.9	3.13	2	2.94

	Meshing					
	3°C.s^{-1}			30°C.s^{-1}		
	Radius [nm]	Nodes	*f*	Radius [nm]	Nodes	*f*
Cementite θ	110	100	0.995	75	50	0.995
Ferrite α	455	100	1.01	298	50	1.01
Austenite γ	0.1	10	1	0.1	10	1

Figure 5.22: (a) DICTRA cell I definition; (b) schematic of initial NPLE tie-lines at austenite interfaces; (c) schematic of the initial carbon profile in the austenite.

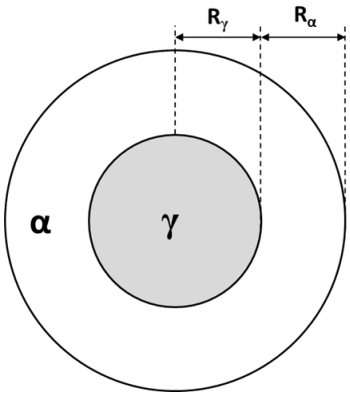

	Phase compositions	
	X_{Mn} [%$_{at}$]	Xc [%$_{at}$]
Ferrite α	1.94	7.86e-03
Austenite γ	1.94	1.78

	Meshing		
	Radius [nm]	Nodes	*f*
Ferrite α	1030	100	1.01
Austenite γ	2500	100	0.95

Figure 5.23: DICTRA cell A definition for heating rates 3 and 30°C.s^{-1}. *n*: number of nodes in each region; f: geometrical progression factor

5.4 Simulation of austenite transformation during slow and fast heating

5.4.1 Isolated Carbide dissolution: sub-system I

Figure 5.24 shows the calculated evolution of the austenite volume fraction on heating and subsequent holding at 800°C for both heating rates 3 and 30°C.s^{-1}. Three kinetics stages follow each other on heating: slow, very fast and intermediate rate up to 800°C. During isothermal hold, austenite fraction reaches or overcomes the OE value in less than 10 s after respectively slow and fast heating. The cementite dissolves during first and second stages (its fraction is not plotted for clarity).

First stage corresponds to sluggish austenite growth into cementite and ferrite involving the partition of the alloying elements at both γ/θ and γ/α interfaces. For both heating rates, the partition of Mn is shown by the Mn composition profiles at 720°C. The α/γ tie-lines at 720°C confirms the Mn partition from ferrite to austenite. Consistently with the thermodynamic analysis, the temperature is close to or below the PNTT during this sluggish stage: fast carbon-controlled kinetics is impossible.

Second stage corresponds to fast dissolution of cementite, controlled by the diffusion of carbon and without partition of the Mn. Operative tie-lines at α/γ interface (748°C at 3°C.s^{-1} and 725°C at 30°C.s^{-1}) illustrate the NPLE growth regime (i.e. austenite inherits the bulk Mn concentration of the ferrite). In the corresponding Mn composition profiles, one observes a "spike" of Mn inside the cementite and a "negative spike" inside the ferrite. There is a small gradient of carbon concentration inside the austenite. In accordance with thermodynamic calculations, the NPLE mode occurs above calculated PNTTs for both heating rates.

Third stage corresponds to a pronounced slow-down of the kinetics related to the completion of the cementite dissolution process. The HR30 heating is easier to interpret first. It can be seen that the austenite fraction is almost equal to the NPLE fraction. The tie line and the Mn profile at 780°C and 800°C

confirm the limited partition of Mn. Hence heating at 30°C.s^{-1} is too fast to allow significant redistribution of Mn, whereas C has time to equalize its activity throughout the austenite. The situation is different for the slow heating at 3°C.s^{-1}, which lets enough time for Mn to partition from the ferrite to the austenite, while the carbon has sufficient time to equalize its activity throughout the simulation cell. This is illustrated by the Mn composition profile at 753°C, 780°C and 800°C. As a result, the austenite fraction goes above the NPLE fraction.

Last stage during isothermal hold corresponds to fast (less than 10 s) equilibration of the system after the heating at 3°C.s^{-1}, as illustrated by the final tie-lines. It is kinetically controlled by the fast diffusion of Mn in ferrite as shown by the Mn concentration profiles at 800°C. After the heating at 30°C.s^{-1}, the austenite fraction also reaches a plateau in less than 10 s, but the final fraction exceeds the OE value by ca. 10%. The kinetics is also controlled by the Mn diffusion in ferrite, as shown by the Mn profiles. After both heatings, significant heterogeneities in Mn concentration subsist in the austenite. This is due to the low diffusivity of Mn in this phase. Three areas are distinguished.

- The Mn concentration is locally high at the previous position of the cementite carbides. The local carbon concentration is slightly higher because of the effect of Mn on carbon activity. After 10 s at 800°C the Mn has only started to diffuse out to Mn-poor regions. These local over-concentrations do not affect significantly the Mn mass balance in the cell, as the volume fraction of cementite is very small.
- The volume of austenite adjacent to the cementite shows a nearly flat Mn profile for both heating rates. These regions correspond to the growth of austenite into ferrite in NPLE mode, where the austenite inherited the initial concentration of ferrite.
- Outermost region corresponds to the austenite growth in LEP mode. The profile of Mn concentration was "drawn" by the evolution of the α/γ tie-line. On heating at 3°C.s^{-1}, the Mn partitioned to austenite over a long distance, as LEP mode prevailed during the third stage. Conversely at 30°C.s^{-1}, Mn partition started only during holding at 800°C.

The "overshoot" of austenite OE fraction after fast heating is interpreted by the absence of Mn partition up to 800°C. As a result, the ferrite ends up highly supersaturated in Mn. Redistribution of Mn from ferrite to austenite would make increase the ferrite amount and make move backward the interface. This would require a long time, as Mn diffusion in austenite would be necessary. Such observation was done for instance in the simulations of [LAI'16].

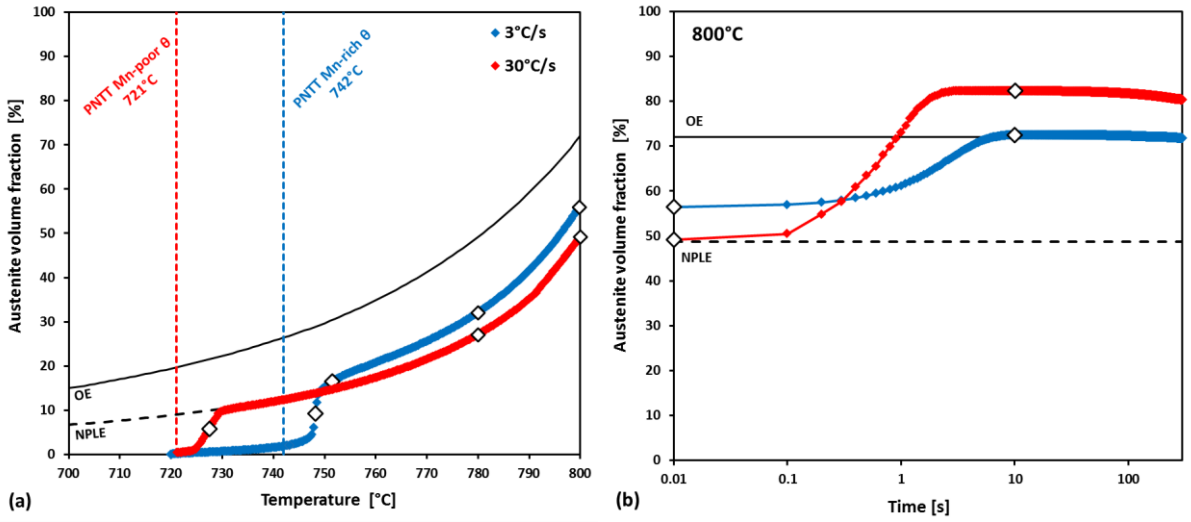

Figure 5.24: Austenite volume fraction transformed during the dissolution of the isolated cementite particles within matrix for slow and fast annealing schedules (blue and red curves, respectively) (a): during heating step and (b) during the subsequent isothermal holding at 800°C. Empty dots highlight particular stages of the transformation detailed in the discussion.

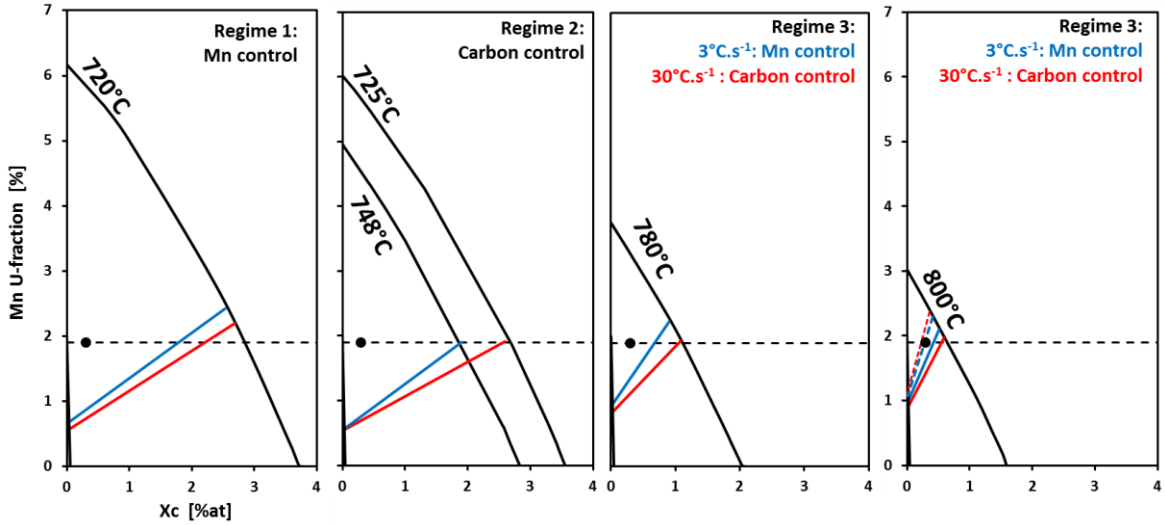

Figure 5.25: Isothermal Fe-C-Mn diagrams where the operative α/γ tie-lines identify the austenite growth regimes. The dashed line represents the Mn composition of ferrite.

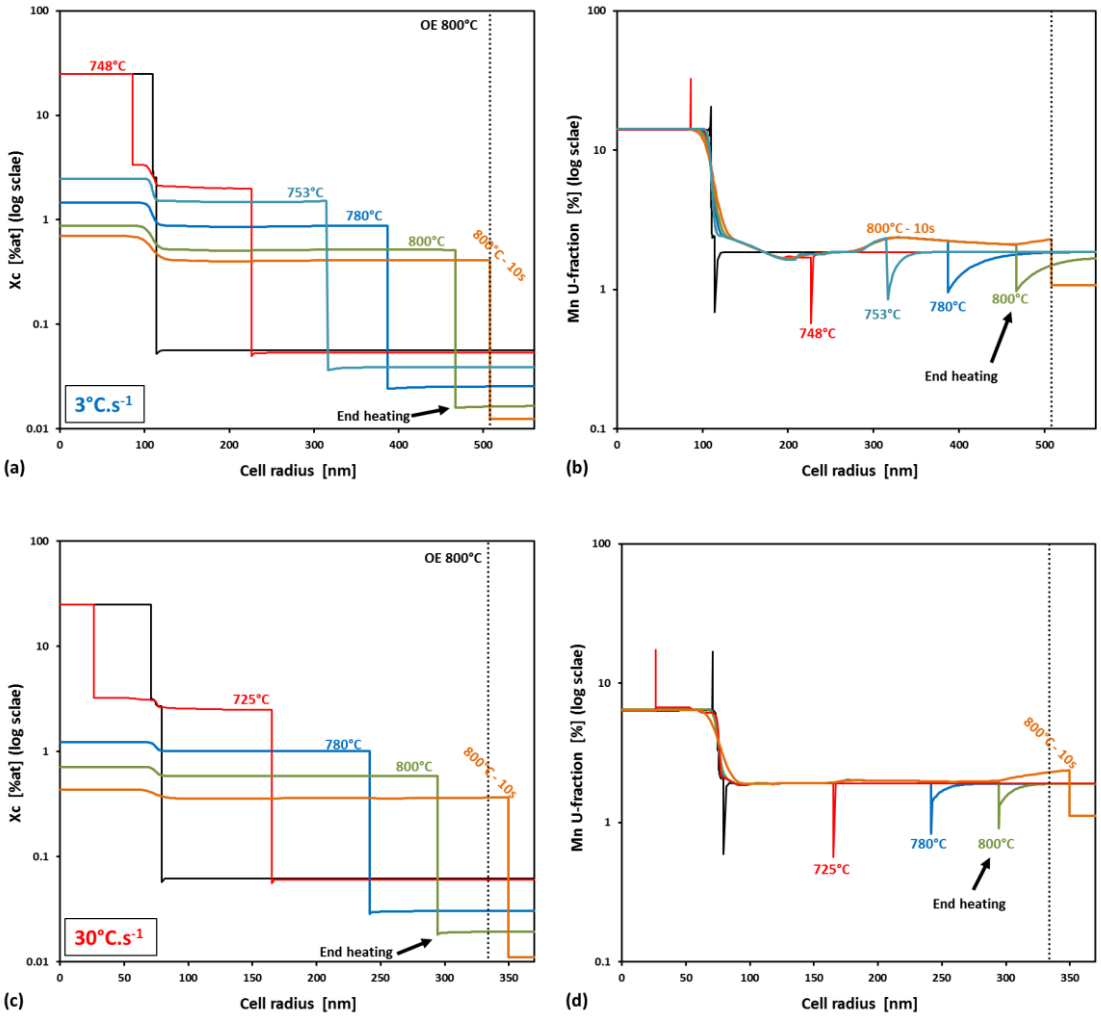

Figure 5.26: Carbon and Mn composition profiles at different temperatures and times. (a-b) and (c-d) correspond to slow and fast heating, respectively.

5.4.2 Pearlite transformation: sub-system P

Figure 5.27 shows the austenite formation kinetics in cell P and the evolution of the operative LE tie-line of the α/γ interface. One reminds first that the cell P differs from the cell I because the austenite is in contact only with ferrite. As a result, both carbon and Mn can diffuse quickly through the ferrite, from cementite to austenite, leading to significant partition of Mn. One has to point out some numerical difficulties with simulation at heating rate 30°C.s^{-1}. The carbon mass balance was well respected up to the end of the simulation, but not that of Mn. Namely, the mass balance given by DICTRA at end of simulations indicated a Mn nominal composition equivalent to 2.40%$_{at}$, instead of the initial value 1.94%at.

The kinetics is similar for both heating rates, but aforementioned numerical difficulties make difficult detailed comparison. The tie-lines indicate that the austenite growth occurs with partition of Mn, as expected from the fast Mn diffusion in ferrite. There are no clearly identifiable kinetic regimes. The higher the temperature, the faster the kinetics, which is simply ascribed to the higher diffusivities. The austenite transformation ends up once the Ae_3 temperature is reached, namely at 757°C. Hence, the sub-system A simulation detailed in the next section will be initiated from this temperature, by considering that the pearlite grain volume is now integrally made of austenite. Simulation results for sub-system P are not detailed more, due to the lack of geometrical representativeness with respect to the true fragmented pearlite morphology.

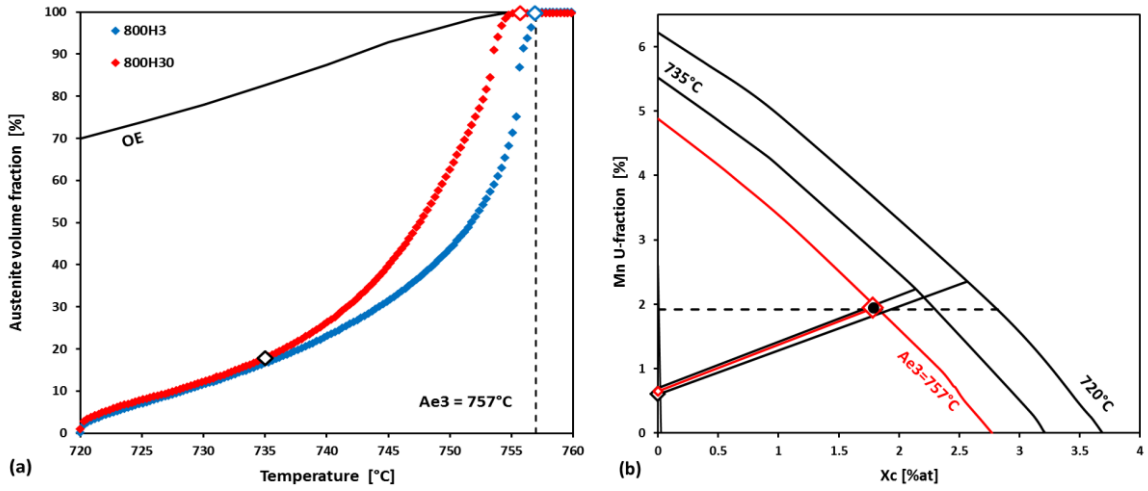

Figure 5.27: (a) simulated kinetics of pearlite transformation during slow and fast heating (blue and red curves, respectively). (b) Operative LE tie-lines at the α/γ moving interface represented for the temperatures highlighted with the empty dots in (a). The black dot reflects the sub-system nominal composition and the black continuous line refers to the OE austenite fraction calculated according the sub-system A nominal composition.

5.4.3 Austenite growth from former pearlite: sub-system A

Figure 5.28 shows the calculated evolution of the austenite fraction during heating at 3 or 30°C.s^{-1} and the isothermal holding at 800°C. According its high carbon nominal composition (X_c^A = 0.66%$_{at}$) and the related thermodynamic equilibrium, the sub-system A must be fully austenitized at 800°C. The evolutions differ significantly between both heating rates. During the slow heating, the amount of austenite follows the NPLE fraction and reaches 100% at 795°C. During fast heating, the austenite fraction has not enough time to "follow" the NPLE fraction. At 800°C, 80% of austenite is formed. Full austenitization is achieved in less than 1 s at 800°C. The operative α/γ tie-lines (Figure 5.29) are identical for both heating rates whatever the temperature. They confirm the austenite growth under NPLE mode. As a result, the cell A ends up fully austenitized and completely homogeneous in Mn.

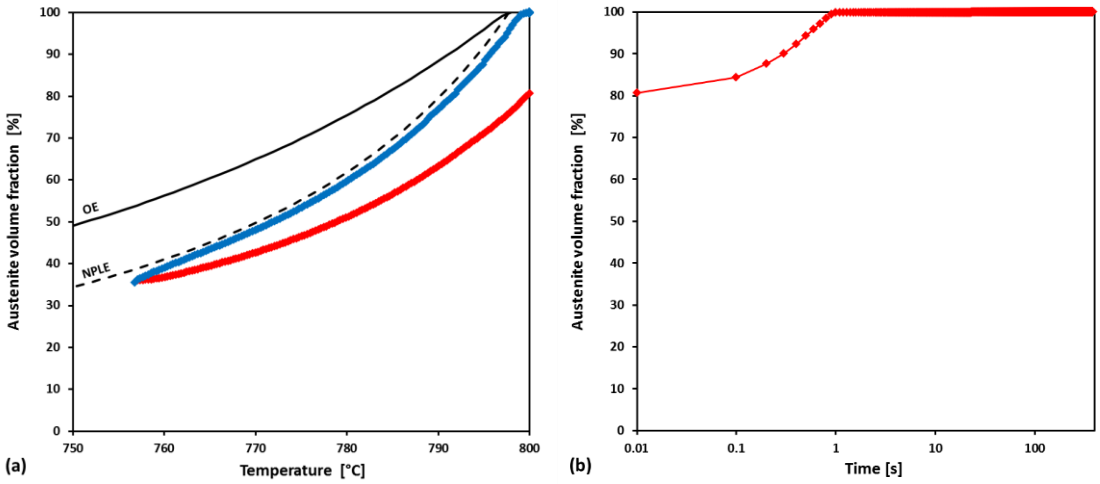

Figure 5.28: Austenite volume fraction transformed after full pearlite transformation (former sub-system P) from 757 to 800°C (a) and during the subsequent isothermal holding at 800°C. Blue and red curves represent the slow and fast annealing schedules, respectively.

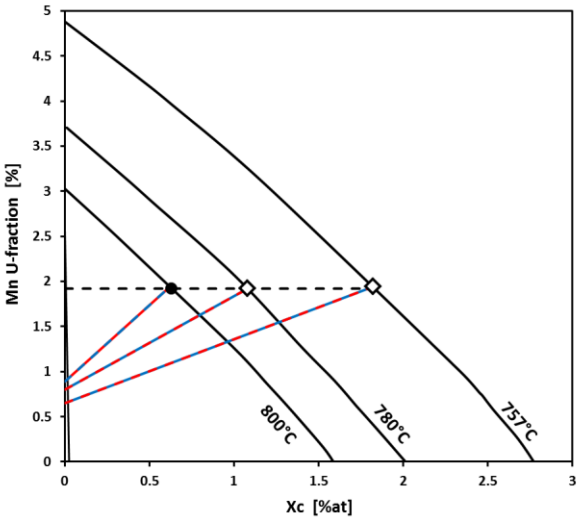

Figure 5.29: Ternary Fe-C-Mn isothermal diagrams in which the operative LE of the α/γ tie-lines highlighting the kinetics regime of pearlite transformation for both heating rates at 757, 780 and 800°C.

5.4.4 Discussion on DICTRA simulations

The simulations on the I sub-system highlight several features of the austenite transformation process from an isolated carbide: (i) the occurrence of successive kinetics stages, (ii) the strong influence of the carbide concentration in Mn on the kinetics and (iii) the formation of Mn heterogeneities in the austenite. Previous studies already established similar trends, but were restricted to isothermal transformations [MIY'10, GOU'12, LAI'16]. Here, the specificities of anisothermal treatments are highlighted.

The austenite transformation on heating starts with a first sluggish stage and accelerates when fast, carbon-controlled cementite dissolution becomes possible. The transition to fast kinetics clearly occurs when the PNTT is reached. This means that the composition of Mn in cementite determines the

temperature at which the austenite transformation will start at a significant rate. This can be seen in Figure 5.13, where the calculated PNTTs have been plotted (721°C and 742°C at 30°C.s^{-1} and 3°C.s^{-1} respectively). Nevertheless, there is some temperature gap between the PNTT and the actual acceleration of the austenite transformation. This gap is due to the anisothermal treatment. At 30°C.s^{-1}, it is ascribed to the high heating rate. The gap of ca. 5°C represents a few tenths of second. At 3°C.s^{-1}, some partition of Mn has started before the PNTT is reached. This reduces the accuracy of the PNTT calculation, which is based on the initial composition of the phases.

Once the carbide has dissolved, the ferrite to austenite transformation goes on. At high heating rate (30°C.s^{-1}), the austenite fraction follows the NPLE value, because the Mn has not enough time to partition from ferrite to austenite. In such case, it is possible to predict the austenite transformation kinetics without detailed kinetics simulation. One just needs to know the PNTT temperature and the austenite NPLE fraction vs. temperature. Conversely on slower heating (3°C.s^{-1}), Mn has time to partition and this cannot be neglected. Computer-efficient models like e.g. [WYC'81] can handle this. Such models can also predict the critical heating rate above which the Mn will not have time to partition.

After fast heating, the austenite fraction exceeds the OE value at the end of the isothermal hold at 800°C. In accordance with literature (e.g. [LAI'16]), this occurs because the austenite was formed with Mn composition out of equilibrium in previous stages. As Mn has no time to partition, the austenite ends-up with too low amount of Mn in comparison with equilibrium.
A simple method to estimate the austenite fraction in excess is proposed here. One assumes that on heating, the austenite forms under NPLE mode. At the end of heating, a fraction f_γ^{NPLE} is formed with the bulk Mn composition of the steel, as suggested by the simulations (Figure 5.30). During the isothermal hold at 800°C, one assumes that the austenite then forms a supplementary fraction (f^+) with the OE Mn content. This assumption is justified by the composition profiles and the tie-lines in Figure 5.25: Mn has sufficient time to partition by fast diffusion in ferrite. Hence, the molar balance on Mn in Eq. (5.8) should be verified. Calculation gives f_γ^+ = 33%, hence a total austenite fraction 82%, which is in good agreement with the maximum fraction according to the simulation after fast heating (82%).

	800°C	
	NPLE	OE
f_γ	49 %	72 %
U_{Mn}^{α}	1.94	1.15
U_{Mn}^{γ}	1.94	2.44

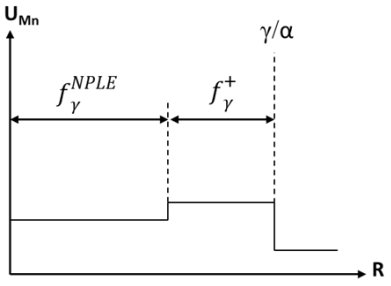

Figure 5.30: Simplified Mn molar balance to predict the excess of austenite fraction after fast heating.

$$f_\gamma^{NPLE} \times 1.94 + 2.44 \times f_\gamma^+ + (1 - f_\gamma^+ - f_\gamma^{NPLE}) \times 1.15 = 1.94 \quad (5.8)$$

Final interesting outcome of the DICTRA simulations in I cell is the prediction of residual heterogeneities of Mn in the austenite. As mentioned in Section 5.4.1, this concerns first the previous position of the carbides (termed as ghost cementite in [LI'10, SCO'18]). The Mn mass balance in the microstructure is not much affected, because of the small fraction of cementite. Significant Mn composition heterogeneities are also predicted outside the previous cementite position. Experimental assessment of such heterogeneities would be interesting.

Simulations on sub-system P are not elaborated here due to the limited representativeness of cell P with respect to the true morphology of the fragmented cementite. Nevertheless, the simulations in sub-system P confirm the fast transformation of pearlite to austenite, related to the fast diffusion of the species in the ferrite and to the short diffusion distances. The predicted partition of Mn is in accordance with the calculated PNTT temperature related to "Geometry B" (cf. Fig. 5.21), which is far higher than the temperatures considered during the simulation. Despite the partition of the alloying elements, the austenite transformation in system P is extremely fast. It is completed when the local Ae_3 temperature (757°C, for X_c = 1.78 $\%_{at}$) is reached whatever the considered heating rate or Mn enrichment in the cementite.

Austenite transformation process in sub-system A is quite simple: for both heating rates the austenite fraction follows the NPLE value until full austenitization (local Ae_3 in cell A is equal to 757°C). Hence, sub-system A ends up with uniform Mn composition. The kinetics is carbon-controlled and extremely fast. Kinetics modelling is actually not necessary, as it is reasonable to assume that the austenite fraction follows the NPLE value on heating. At faster heating, the austenite transformation is too slow to follow the NPLE fraction, but the discrepancy is very small. For example, after heating at 30°C.s^{-1}, the time necessary to complete the transformation is less than 1 s, once the annealing temperature 800°C has been reached.

More complex situation would have occurred if larger size of A cell had been considered. As the carbon content of A cell would be lower, austenite fraction at equilibrium would be less than 100%. After growth in NPLE mode, different kinetics stages involving the partition of Mn between ferrite and austenite would have occurred, like investigated for example in [WEI'13]. We carried out complementary DICTRA simulations (not shown here) to confirm this behavior.

5.5 Comparison between simulations and experiments

Before presenting the comparisons between the simulations and the experiment, it is reminded that the DICTRA simulations were carried out assuming a simplified composition of the steel (ternary system Fe-C-Mn). The consequence is to overestimate the austenite fraction. For example, at 800°C the austenite fraction at OE for the full steel composition is 81% instead of 86% for the simplified steel composition. The three sub-systems are combined to obtain the global austenite transformation kinetics simulated with DICTRA, following the summation procedure below.

5.5.1 Calculation of global kinetics from specific kinetics in I, P, A cells

According to our geometrical representation of the microstructure and the austenitization process (Figure 5.16), two stages are distinguished:

- Stage 1, pearlite transformation into austenite and austenite formation from isolated carbides.

Simulations on cells P and I contribute to the overall kinetics. The overall austenite fraction reads:

$$f^{\gamma} = f^{P} f_{\gamma}^{P} + f^{I} f_{\gamma}^{I} \tag{5.9}$$

where f^{P} and f^{I} stand for the volume fraction of sub-systems P and I, respectively. f_{γ}^{P} and f_{γ}^{I} are the volume fraction of austenite transformed in the latter sub-systems. As seen in Chapter 2 and 3, the initial volume fraction of pearlite is 16%. As justified in Section 5.3.2.c, volume fraction of system I is equal to 56%. (Hence a remaining fraction 28% does not transform during Stage 1).

Stage 2: growth of austenite grains which result from pearlite transformation into ferrite and continuation of the austenite transformation from isolated carbides (cells A and I). The overall volume fraction of austenite reads:

$$f^{\gamma} = f^{A} f_{\gamma}^{A} + f^{I} f_{\gamma}^{I} \tag{5.10}$$

where f^{A} stands for the volume fraction of sub-system A and f_{γ}^{A} the volume fraction of austenite inside sub-system A. The volume fractions of sub-system A and I are equal to 44% and 56% respectively, as justified in Section 5.3.2.c.

5.5.2 Slow heating

Figures 5.31 (a) and (b) compare the global kinetics simulated with DICTRA with the HEXRD experiments presented in Section 5.2.2. First sluggish kinetics on stage 1 agrees well with the experimental data up to 740°C. However, two successive accelerations of the calculated kinetics occur at ca. 745 and 757°C, leading to a significant overestimation (ca. 15%) with respect to the experimental curve. These temperatures correspond respectively to the dissolution of the isolated carbides and the pearlite. Conversely, the experimental curve does not show any sharp acceleration of the kinetics, except the transition from sluggish to fast regime starting at 730°C, but which is rather progressive. In the experimental curve, isolated carbide and pearlite transformation events are actually not clearly distinguishable.

Stage 2 (ferrite to austenite transformation) marks a kinetics slowdown in the simulation. The discrepancy with the experiment remains nearly constant up to ca. 785°C; it increases further up to 800°C. After completion of the heating stage, the simulated austenite fraction reaches 73%, i.e. about 30% more than that experimentally measured.

When the isothermal holding at 800°C starts, the sub-system A is integrally austenitized, while the sub-system I has almost reached the austenite fraction expected from thermodynamic equilibrium. There remains thus only a very low fraction of austenite to transform. The ortho-equilibrium austenite volume is reached in less than 10s holding. Thus, the simulated kinetics curve exhibits a sharp end, contrary to the experimental curve which shows a progressive slow-down; thermodynamic equilibrium is reached after 300 s holding at 800°C according to the experiment.

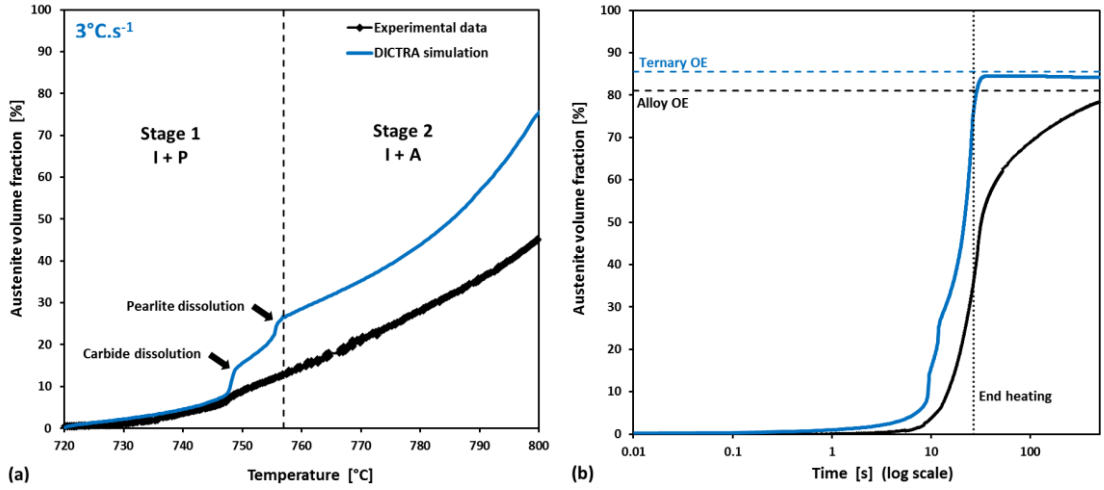

Figure 5.31: Comparison between calculated (DICTRA) and experimental (HEXRD) austenite volume fractions during (a) fast heating at 3°C.s^{-1} and (b) for the whole thermal treatment (heating stage + holding).

5.5.3 Fast heating

During fast heating, the simulated and experimental kinetics curves show a time discrepancy inferior to ca. 1 s (Figure 5.32(b)). Plotted as a function of temperature (Figure 5.32(a)), the calculated austenite fraction curve shows a discrepancy with the experiment (overestimation ca. 15%) which is established at the start of the transformation and then remains nearly constant up to 800°C. The austenite transformation starts in temperature range 720-730°C according to the simulation, instead of 740-750°C according to the experiment. Like for slow heating, two marked accelerations are visible in the simulation curve at ca. 730°C and 755°C, corresponding respectively to isolated carbide and pearlite transformation. The kinetics are well captured by the simulation during stage 2. At 800°C, the calculated fraction of austenite reaches 63%, vs. 45% experimentally. During isothermal hold at 800°C, the austenite fraction reaches quickly a maximum value (90%) in short time (less than 3 s). Like for the slow heating, the transformation ends abruptly, whereas the experimental kinetics shows a much more progressive slow-down. The final austenite fraction exceeds the OE value by ca. 5%, in accordance with the experiment.

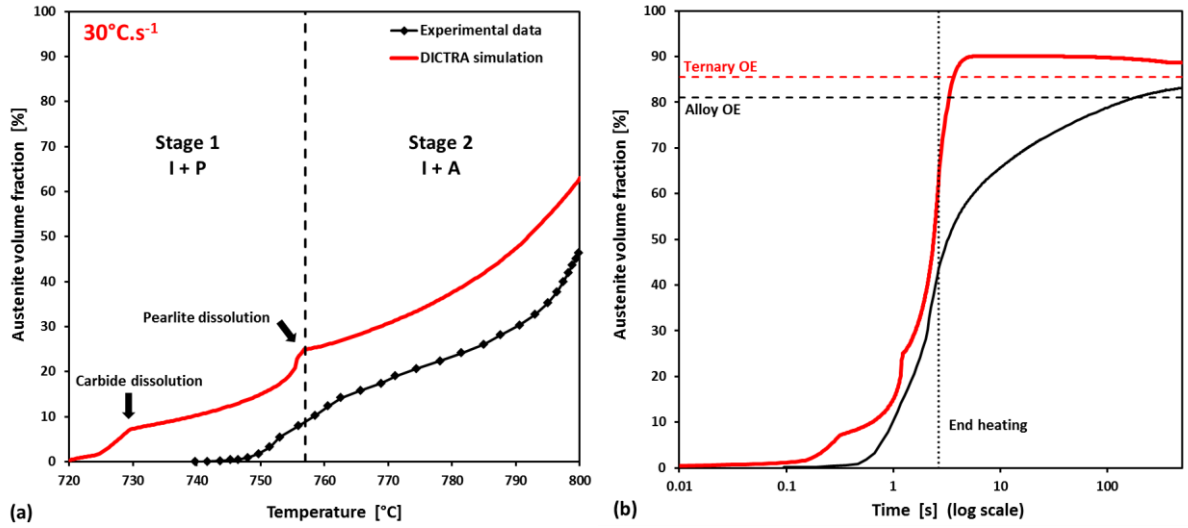

Figure 5.32: Comparison between calculated (DICTRA) and experimental (HEXRD) austenite volume fractions during (a) fast heating at 30°C.s^{-1} and (b) for the whole thermal treatment.

5.5.4 Discussion

Despite the strong simplifications in the representation of the microstructure, the thermokinetic simulation with DICTRA permitted to understand further and to predict several features of the austenitization process.

- The overall austenite transformation kinetics is predicted with reasonable accuracy during the heating stage. The time discrepancy between simulation and experiment remains of the order of 1 s during heating at 30°C.s^{-1} and a few seconds during heating at 3°C.s^{-1}. The overestimation of the kinetics with respect to the experiment comes in part from the simplification of the steel composition, which conducts to overestimate the austenite fraction by ca. 5%.
- In the case of the slow heating at 3°C.s^{-1}, the first sluggish stage of the isolated carbides dissolution is well predicted thanks to the thermokinetic simulation which takes account of the partition of the Mn below the PNTT.
- In line with the analysis of experiments (Section 5.3.2.b), it has not been necessary to consider any influence of the ferrite recrystallization on the austenite transformation (such as accelerated

diffusion). This does not mean that the recrystallization has no effect at all on the austenitization process. It determines strongly the austenite microstructure morphogenesis as shown in Chapter 2. However, the effect on the austenite transformation kinetics is not obvious, as elaborated in Section 5.2.4.a.

- The fragmented pearlite transformation to austenite occurs in the same narrow temperature range 735-755°C whatever the heating rate and the pearlitic cementite composition, in accordance with microstructural observations. Fast transformation is possible with redistribution of Mn, because of the short diffusion distance and fast diffusion in ferrite, as demonstrated by the simulations.
- The simulations describe properly the out of equilibrium austenite transformation leading to final austenite fraction exceeding the OE, and final Mn heterogeneities in austenite. These successful predictions are due to the description of the austenite transformation process from the isolated carbides (in I sub-system).

Nevertheless, several important experimental trends are not reproduced:

- The faster transformation kinetics during faster heating: experimentally, the austenite fraction vs. temperature curves at $3°C.s^{-1}$ and $30°C.s^{-1}$ are not significantly different (cf. Fig. 5.11 and 5.12). This means that the amount of austenite transformed per unit time is much higher at $30°C.s^{-1}$ than at $3°C.s^{-1}$. In opposition with these experimental trends, the calculated fraction of austenite is lower at $30°C.s^{-1}$ than at $3°C.s^{-1}$ when the temperature 800°C is reached.
- The smooth, progressive experimental kinetics during the heating, whereas sharp accelerations are predicted by the simulations, when the isolated carbides and the pearlite dissolve.
- The pronounced slow-down of the kinetics during isothermal hold at 800°C for both heating rates, whereas fast and abrupt termination of the transformation is predicted by the simulation.

These discrepancies come in large part from the simplified representation of the microstructure. Strongest assumptions are:

- The separation of P/A and I sub-systems into isolated systems, whereas in the true microstructure, these sub-systems interact with each other. In the real microstructure:
- The isolated carbides can be surrounded by the growing CRA grains and then dissolve inside the austenite; these can also dissolve at some distance of a nearby CRA grain, by diffusion from the carbide to the CRA grain through the ferrite.
- The CRA grains are confined inside a too small A sub-system, leading to 100% austenite in present simulations at ca. 800°C. This in contradiction with the SEM micrographs (Figures 2.19 and 2.21): CRA grain growth is far from being complete at the start of the isothermal hold.
- The immediate saturation of the nucleation sites related to the isolated carbides, as our simulations do not include any nucleation rate. This is in contradiction with the microstructural observations of Chapter 2, where progressive austenite nucleation on isolated carbides was put into evidence. (Besides, immediate nucleation at pearlite boundaries is justified).
- The unique size and composition assumed for the carbides (either isolated or inside pearlite), whereas the experiments (Chapter 2 and Chapter 3) showed that there is a distribution of carbide sizes and compositions.
- The unique size of the fragmented pearlite islands.
- There is no accounting of the percolation of the microstructure. As shown in Chapter 2, the microstructure at some point is better described by ferrite grains surrounded by growing austenite (instead of austenite grains expanding into a ferrite matrix according to our representation in A and I cells).

The discrepancies mentioned above are interpreted as follows:

- The too sharp acceleration of the calculated kinetics associated with the isolated carbides dissolution comes from the assumed immediate nucleation and the assumption of one single size and composition of these carbides. In the real microstructure, the dissolution of these carbides is spread over a larger temperature range.
- The sharp acceleration upon pearlite transformation is due to the absence of pearlite island size distribution.
- The absence of progressive slowdown during isothermal hold at 800°C has two origins:
  - The too small size of cell A: fast transformation in NPLE mode is completed or almost completed at 800°C at both heating rates. Inside a larger cell A, transition to more sluggish growth involving Mn partition would eventually have occurred.
  - The non-accounting of the percolation.
- The too slow kinetics predicted on fast heating at 30°C.s^{-1} has no straightforward interpretation. One can cite [AZI'11] where it is shown that faster heating leads to larger number density of austenite nuclei (see Section 2.1.3.a). Hence, introducing a nucleation rate could improve this part of the simulations. As for the interaction with recrystallization, it is again not thought to have a clear effect on the kinetics as mentioned previously.

Despite these limitations, this simulation study provides the basis for a simplified and computer-efficient modeling of the austenite transformation kinetics, at least inside respective cells I and A.
In cell I, one can consider the following stages:

- Immediate dissolution of cementite once the PNTT is reached.
- Growth of austenite under NPLE mode (austenite fraction follows the NPLE value)
- Growth of austenite with partition of Mn and diffusion of Mn in ferrite.

Both first stages only require thermodynamic calculation (PNTT, NPLE austenite fraction vs. temperature). Only the last stage needs a kinetics simulation. The computer-efficient model of [WYC'81] for instance can be employed for this part of the simulation.

This sequence is the same in cell A, except that the first stage consists of the transformation of the fragmented pearlite. It does not need to be described with a detailed kinetics model, as it occurs quickly in narrow temperature range which depends weakly on the heating rate or the pearlitic cementite Mn composition.

Some effort has still to be done to represent properly the overall microstructure. This concerns the respective fractions of cells A and I, the introduction of a distribution of isolated carbides sizes and compositions and the introduction of the percolation. Development of a nucleation-growth model may also be envisaged as computer-efficient tool suitable for industrial application.

5.6 Conclusion

The austenite transformation kinetics have been measured *in situ* via HEXRD experiments during which intercritical annealing to 800°C were reproduced using slow and fast heating rates (3 and 30°C.s^{-1}). It was shown that the transformation occurs faster on heating when a fast heating rate is applied. Fast heating also leads to faster austenite transformation kinetics during subsequent isothermal hold at 800°C; the final austenite fraction exceeds the thermodynamic equilibrium value after faster heating.

During heating, two stages of the kinetics occur at both heating rates: slow then fast. The acceleration is concomitant with the transformation of the pearlite islands. The Mn concentration in cementite has no strong effect on the overall kinetics. There is no clear influence of the ferrite recrystallization on the austenite transformation kinetics. Its impact is rather limited to the morphogenesis of the austenite microstructure.

A new simulation framework has been introduced to investigate separately with DICTRA software the austenite transformation from the isolated inter-granular cementite particles and from the pearlite bands. Simulation parameters (carbide size, compositions, …) are derived from experimental characterizations, but simplified ternary Fe-C-Mn system is considered. Only adjustable parameter is the respective volume fraction of both sub-systems in the overall microstructure.

In both cases, the austenite growth into cementite and ferrite have been modeled with particular attention on interface conditions and by identifying the rate-limitant process (either carbon diffusion in austenite, or Mn diffusion in ferrite, then austenite). Previous similar studies of literature focused on isothermal conditions; we focused here on anisothermal treatments. Moreover, we consider both sites for austenite formation: pearlite islands and isolated carbides; the latter are generally neglected in literature.

The transformation of fragmented pearlite depends weakly on the heating rate or the pearlitic cementite composition in Mn. It occurs very fast with partition of Mn, made possible by the fast diffusion in ferrite. The resulting carbon-rich austenite (CRA) grain then grows into the surrounding ferrite with NPLE mode until reaching the maximum fraction at 800°C predicted by NPLE in a short time. Hence this part of the process also depends weakly on the heating rate.

Conversely the isolated carbides dissolution is strongly dependent on heating rate and Mn composition. Sluggish dissolution involving Mn partition occurs below the PNTT, followed by fast carbon-controlled dissolution above the PNTT. The PNTT is increased for higher Mn concentration in cementite. These effects are not clearly visible on the experimental global austenitization kinetics, as the carbides have various sizes and compositions. The austenite formed from these carbides grows then into ferrite first in NPLE mode, then with partition of Mn involving Mn diffusion in ferrite.

Out of equilibrium austenite formation can lead to austenite fraction “overshoots” with respect to equilibrium, in accordance with the experiment, which can be predicted as a function of heating rate. This is an essential outcome of the simulations: the austenite fraction depends more on the heating rate than on the cementite composition in Mn. Other interesting outcome is the prediction of C and Mn heterogeneities in austenite, the latter being remnants of enriched carbides or signature of the α/γ tie-line evolution during the austenite growth. Such heterogeneities are well known in DP steels and our approach with sub-systems may allow to predict these.

Further work has to be done to improve the representation of the overall microstructure, but the bases are set for the fast, computer-efficient modeling of austenite transformation from pearlite and isolated carbides as separate nucleation sites.

REFERENCES

[AAR’75] Aaronson, H. I. (Ed.). (1975). Lectures on the theory of phase transformations. Metallurgical Society of AIME., n.d.

[AKB’94] Akbay, T., Reed, R.C., Atkinson, C., 1994. Modelling reaustenitisation from ferrite/cementite mixtures in Fe-C steels. Acta Metallurgica et Materialia 42, 1469–1480. https://doi.org/10.1016/0956-7151(94)90165-1

[ATK’95] Akbay, T., Atkinson, C., 1996. The influence of diffusion of carbon in ferrite as well as in austenite on a model of reaustenitization from ferrite/cementite mixtures in Fe-C steels. Journal of Materials Science 31, 2221–2226. https://doi.org/10.1007/BF01152931

[ARL’14] A. Arlazarov. (2014). "Evolution des microstructures et lien avec les propriétés mécaniques dans les aciers 'Medium Mn'. PhD report

[AVR'39] Avrami, M., 1939. Kinetics of Phase Change. I General Theory. The Journal of Chemical Physics 7, 1103–1112. https://doi.org/10.1063/1.1750380

[AZI'11] Azizi-Alizamini, H., Militzer, M., Poole, W.J., 2011. Austenite Formation in Plain Low-Carbon Steels. Metallurgical and Materials Transactions A 42, 1544–1557. https://doi.org/10.1007/s11661-010-0551-5

[BAR'15] Barbier, D., Germain, L., Hazotte, A., Gouné, M., Chbihi, A., 2015. Microstructures resulting from the interaction between ferrite recrystallization and austenite formation in dual-phase steels. Journal of Materials Science 50, 374–381. https://doi.org/10.1007/s10853-014-8596-2

[BOS'09] Bos, C., Sietsma, J., 2009. Application of the maximum driving force concept for solid-state partitioning phase transformations in multi-component systems. Acta Materialia 57, 136–144. https://doi.org/10.1016/j.actamat.2008.08.060

[BOS'07] Bos, C., Sietsma, J., 2007. A mixed-mode model for partitioning phase transformations. Scripta Materialia 57, 1085–1088. https://doi.org/10.1016/j.scriptamat.2007.08.030

[CAB'01] Caballero, F.G., Capdevila, C., Andrés, C.G.D., 2001. Mathematical Modeling of Iron and Steel Making Processes. Modelling of Kinetics of Austenite Formation in Steels with Different Initial Microstructures. ISIJ International 41, 1093–1102. https://doi.org/10.2355/isijinternational.41.1093

[CHB'14] Chbihi, A., Barbier, D., Germain, L., Hazotte, A., Gouné, M., 2014. Interactions between ferrite recrystallization and austenite formation in high-strength steels. Journal of Materials Science 49, 3608–3621. https://doi.org/10.1007/s10853-014-8029-2

[CHR'81] Christian, J.W., 1982. Deformation by moving interfaces. Metallurgical Transactions A 13, 509–538. https://doi.org/10.1007/BF02644415

[DAS'93] Das, S.K., Biswas, A., Ghosh, R.N., 1993. Volume fraction dependent particle coarsening in plain carbon steel. Acta Metallurgica et Materialia 41, 777–781. https://doi.org/10.1016/0956-7151(93)90010-P

[DEN'92] Denis, S., Farias, D., Simon, A., 1992. Mathematical Model Coupling Phase Transformations and Temperature Evolutions in Steels. ISIJ International 32, 316–325. https://doi.org/10.2355/isijinternational.32.316

[ENO'18] Enomoto, M., Li, S., Yang, Z.N., Zhang, C., Yang, Z.G., 2018. Partition and non-partition transition of austenite growth from a ferrite and cementite mixture in hypo- and hypereutectoid Fe-C-Mn alloys. Calphad 61, 116–125. https://doi.org/10.1016/j.calphad.2018.03.002

[GAN'09] Gang, U.G., Lee, S.H., Nam, W.J., 2009. The Evolution of Microstructure and Mechanical Properties of a 5052 Aluminium Alloy by the Application of Cryogenic Rolling and Warm Rolling. MATERIALS TRANSACTIONS 50, 82–86. https://doi.org/10.2320/matertrans.MD200801

[GAR'81] Garcia, C.I., Deardo, A.J., 1981. Formation of austenite in 1.5 pct Mn steels. Metallurgical Transactions A 12, 521–530. https://doi.org/10.1007/BF02648551

[GOT'11] Lischewski, I., Gottstein, G., 2011. Nucleation and variant selection during the α–γ–α phase transformation in microalloyed steel. Acta Materialia 59, 1530–1541. https://doi.org/10.1016/j.actamat.2010.11.017

[GOU'15] Gouné, M., Danoix, F., Ågren, J., Bréchet, Y., Hutchinson, C.R., Militzer, M., Purdy, G., van der Zwaag, S., Zurob, H., 2015. Overview of the current issues in austenite to ferrite transformation and the role of migrating interfaces therein for low alloyed steels. Materials Science and Engineering: R: Reports 92, 1–38. https://doi.org/10.1016/j.mser.2015.03.001

[GOU'12] Gouné, M., Maugis, P., Drillet, J., 2012. A Criterion for the Change from Fast to Slow Regime of Cementite Dissolution in Fe–C–Mn Steels. Journal of Materials Science & Technology 28, 728–736. https://doi.org/10.1016/S1005-0302(12)60122-4

[HIL'71] Hillert, M., 1971. Diffusion controlled growth of lamellar eutectics and eutectoids in binary and ternary systems. Acta Metallurgica 19, 769–778. https://doi.org/10.1016/0001-6160(71)90133-7

[HUA'04] Huang, J., Poole, W.J., Militzer, M., 2004. Austenite formation during intercritical annealing. Metallurgical and Materials Transactions A 35, 3363–3375. https://doi.org/10.1007/s11661-004-0173-x

[HUY'18] Huyan, F., Yan, J.-Y., Höglund, L., Ågren, J., Borgenstam, A., 2018. Simulation of the Growth of Austenite from As-Quenched Martensite in Medium Mn Steels. Metallurgical and Materials Transactions A 49, 1053–1060. https://doi.org/10.1007/s11661-018-4497-3

[JAC'99] Jacot, A., Rappaz, M., 1999. A combined model for the description of austenitization, homogenization and grain growth in hypoeutectoid Fe–C steels during heating. Acta Materialia 47, 1645–1651. https://doi.org/10.1016/S1359-6454(99)00005-1

[KAM'15] Kamoutsi, H., Gioti, E., Haidemenopoulos, G.N., Cai, Z., Ding, H., 2015. Kinetics of Solute Partitioning During Intercritical Annealing of a Medium-Mn Steel. Metallurgical and Materials Transactions A 46, 4841–4846. https://doi.org/10.1007/s11661-015-3118-7

[KAS'84] Kasatkin, O.G., Vinokur, B.B., Pilyushenko, V.L., 1984. Calculation models for determining the critical points of steel. Metal Science and Heat Treatment 26, 27–31. https://doi.org/10.1007/BF00712859

[KIR'87] Kirkaldy, J.S., Young, D.J., 1987. Diffusion in the condensed state. Institute of Metals ; Institute of Metals North American Publications Center [distributor for] North America, London : Brookfield, VT, USA.

[KUL'13] Kulakov, M., Poole, W.J., Militzer, M., 2013. The Effect of the Initial Microstructure on Recrystallization and Austenite Formation in a DP600 Steel. Metallurgical and Materials Transactions A 44, 3564–3576. https://doi.org/10.1007/s11661-013-1721-z

[LAI'16] Lai, Q., Gouné, M., Perlade, A., Pardoen, T., Jacques, P., Bouaziz, O., Bréchet, Y., 2016. Mechanism of Austenite Formation from Spheroidized Microstructure in an Intermediate Fe-0.1C-3.5Mn Steel. Metallurgical and Materials Transactions A 47, 3375–3386. https://doi.org/10.1007/s11661-016-3547-y

[LAN'88] Lange, W.F., Enomoto, M., Aaronson, H.I., 1988. The kinetics of ferrite nucleation at austenite grain boundaries in Fe-C alloys. Metallurgical Transactions A 19, 427–440. https://doi.org/10.1007/BF02649256

[LI'11] Li, Z.-D., Miyamoto, G., Yang, Z.-G., Furuhara, T., 2011. Kinetics of Reverse Transformation from Pearlite to Austenite in an Fe-0.6 Mass pct C Alloy and the Effects of Alloying Elements. Metallurgical and Materials Transactions A 42, 1586–1596. https://doi.org/10.1007/s11661-010-0560-4

[LI'13] Li, P., Li, J., Meng, Q., Hu, W., Xu, D., 2013. Effect of heating rate on ferrite recrystallization and austenite formation of cold-roll dual phase steel. Journal of Alloys and Compounds 578, 320–327. https://doi.org/10.1016/j.jallcom.2013.05.226

[LIU'91] Liu, Z.-K., Höglund, L., Jönsson, B., ågren, J., 1991. An experimental and theoretical study of cementite dissolution in an Fe-Cr-C alloy. Metallurgical Transactions A 22, 1745–1752. https://doi.org/10.1007/BF02646498

[MEC'15] Mecozzi, M.G., Bos, C., Sietsma, J., 2015. A mixed-mode model for the ferrite-to-austenite transformation in a ferrite/pearlite microstructure. Acta Materialia 88, 302–313. https://doi.org/10.1016/j.actamat.2015.01.058

[MOH'11] Mohanty, R.R., Girina, O.A., Fonstein, N.M., 2011. Effect of Heating Rate on the Austenite Formation in Low-Carbon High-Strength Steels Annealed in the Intercritical Region. Metallurgical and Materials Transactions A 42, 3680–3690. https://doi.org/10.1007/s11661-011-0753-5

[MIY'10] Miyamoto, G., Usuki, H., Li, Z.-D., Furuhara, T., 2010. Effects of Mn, Si and Cr addition on reverse transformation at 1073K from spheroidized cementite structure in Fe–0.6 mass% C alloy. Acta Materialia 58, 4492–4502. https://doi.org/10.1016/j.actamat.2010.04.045

[MUR'79] WD. Murray, F. Landis. "Numerical and Machine Solutions of Transient Heat-Conduction Problems Involving Melting or Freezing: Part I—Method of Analysis and Sample Solutions". *J. Heat Transfer* 81(2), 106-112 (May 01, 1959) (7 pages) doi:10.1115/1.4008149

[OFF'02] Offerman, S.E., van Dijk, N.H., Sietsma, J., Grigull, S., Lauridsen, E.M., Margulies, L., Poulsen, H.F., Rekveldt, M.T., van der Zwaag, S., 2002. Grain Nucleation and Growth During Phase Transformations. Science 298, 1003–1005. https://doi.org/10.1126/science.1076681

[OLL'17] Ollat, M. 2017. "Characterization and modeling of microstructural evolutions during the thermal treatment of cold-rolled steels", PhD report.

[OLL'18] Ollat, M., Militzer, M., Massardier, V., Fabregue, D., Buscarlet, E., Keovilay, F., Perez, M., 2018. Mixed-mode model for ferrite-to-austenite phase transformation in dual-phase steel. Computational Materials Science 149, 282–290. https://doi.org/10.1016/j.commatsci.2018.02.052

[PUR'11] Purdy, G., Ågren, J., Borgenstam, A., Bréchet, Y., Enomoto, M., Furuhara, T., Gamsjager, E., Gouné, M., Hillert, M., Hutchinson, C., Militzer, M., Zurob, H., 2011. ALEMI: A Ten-Year History of Discussions of Alloying-Element Interactions with Migrating Interfaces. Metallurgical and Materials Transactions A 42, 3703–3718. https://doi.org/10.1007/s11661-011-0766-0

[ROO'83] Roósz, A., Gácsi, Z., Fuchs, E.G., 1983. Isothermal formation of austenite in eutectoid plain carbon steel. Acta Metallurgica 31, 509–517. https://doi.org/10.1016/0001-6160(83)90039-1

[RUD'11] Rudnizki, J., Böttger, B., Prahl, U., Bleck, W., 2011. Phase-Field Modeling of Austenite Formation from a Ferrite plus Pearlite Microstructure during Annealing of Cold-Rolled Dual-Phase Steel. Metallurgical and Materials Transactions A 42, 2516–2525. https://doi.org/10.1007/s11661-011-0626-y

[SAN'08] San Martín, D., Rivera-Díaz-del-Castillo, P.E.J., García-de-Andrés, C., 2008. *In situ* study of austenite formation by dilatometry in a low carbon microalloyed steel. Scripta Materialia 58, 926–929. https://doi.org/10.1016/j.scriptamat.2008.01.019

[SAV'07] Savran, V.I., Van Leeuwen, Y., Hanlon, D.N., Kwakernaak, C., Sloof, W.G., Sietsma, J., 2007. Microstructural Features of Austenite Formation in C35 and C45 alloys. Metallurgical and Materials Transactions A 38, 946–955. https://doi.org/10.1007/s11661-007-9128-3

[SPE'81] Speich, G.R., Demarest, V.A., Miller, R.L., 1981. Formation of Austenite During Intercritical Annealing of Dual-Phase Steels. Metallurgical and Materials Transactions A 12, 1419–1428. https://doi.org/10.1007/BF02643686

[TOM'18] Thomas, L.S., Matlock, D.K., 2018. Formation of Banded Microstructures with Rapid Intercritical Annealing of Cold-Rolled Sheet Steel. Metallurgical and Materials Transactions A 49, 4456–4473. https://doi.org/10.1007/s11661-018-4742-9

[WYC'81] Wycliffe, P.A., Purdy, G.R., Embury, J.D., 1981. Growth of Austenite in the Intercritical Annealing of Fe-C-Mn Dual Phase Steels. Canadian Metallurgical Quarterly 20, 339–350. https://doi.org/10.1179/cmq.1981.20.3.339

[XIA'13] Xia, Y., Enomoto, M., Yang, Z., Li, Z., Zhang, C., 2013. Effects of alloying elements on the kinetics of austenitization from pearlite in Fe–C–M alloys. Philosophical Magazine 93, 1095–1109. https://doi.org/10.1080/14786435.2012.744484

[YAN'85] Yang, D.Z., Brown, E.L., Matlock, D.K., Krauss, G., 1985. Ferrite recrystallization and austenite formation in cold-rolled intercritically annealed steel. Metallurgical Transactions A 16, 1385–1392. https://doi.org/10.1007/BF02658671

[YAN'91] Yang, J.R., Bhadeshia, H.K.D.H., 1991. Acicular ferrite transformation in alloy-steel weld metals. Journal of Materials Science 26, 839–845. https://doi.org/10.1007/BF00588325

[YAN'16] Yang, Z.N., Xia, Y., Enomoto, M., Zhang, C., Yang, Z.G., 2016. Effect of Alloying Element Partition in Pearlite on the Growth of Austenite in High-Carbon Low Alloy Steel. Metallurgical and Materials Transactions A 47, 1019–1027. https://doi.org/10.1007/s11661-015-3272-y

[ZEN'49] Zener, C., 1949. Theory of Growth of Spherical Precipitates from Solid Solution. Journal of Applied Physics 20, 950–953. https://doi.org/10.1063/1.1698258

[ZHG'13] Zhang, G.-H., Chae, J.-Y., Kim, K.-H., Suh, D.W., 2013. Effects of Mn, Si and Cr addition on the dissolution and coarsening of pearlitic cementite during intercritical austenitization in Fe-1mass%C alloy. Materials Characterization 81, 56–67. https://doi.org/10.1016/j.matchar.2013.04.007

[ZHU'15] Zhu, B., Chen, H., Militzer, M., 2015. Phase-field modeling of cyclic phase transformations in low-carbon steels. Computational Materials Science 108, 333–341. https://doi.org/10.1016/j.commatsci.2015.01.023

Conclusion and Outlooks

Conclusions

Ferrite/Martensite Dual-Phase steels are largely used in the form of thin sheets in the automotive industry for their excellent balance between resistance and strength and thus for their lightening potential. They are elaborated by continuous casting, hot- and cold- rolling, followed by a continuous annealing. During the heating and the soaking stages of this latter process, the deformed ferrite/pearlite microstructure obtained after rolling evolves is transformed into a recrystallized ferrite-austenite microstructure. This PhD thesis aimed at understanding the different metallurgical mechanisms occurring during these manufacturing stages as carbides ripening, recovery, recrystallization and austenite transformation and all their possible interactions. Through this work, the mechanisms were characterized at different scales and by in situ technics on an industrial steel and modeled by physical based approaches.

The morphogenesis of the ferrite-austenite microstructure during annealing from the deformed ferrite-pearlite microstructure has been first studied at low magnification (SEM), in order to understand qualitatively the possible interactions between the latter mechanisms.
A low heating rate ($3°C.s^{-1}$) permits a full recrystallization of ferrite before austenite transformation occurs (710°C). The austenite appearing during intercritical annealing comes mainly from the transformation of pearlite bands. The formation of austenite around ferrite grains is also possible thanks to intergranular cementite particles inherited from the hot-rolling process. They dissolve to the benefit of austenite whose growth is promoted along the recrystallized ferrite grain boundaries, forming austenite rings around the ferrite grains creating the so-called “necklace” topology.
Fast heating ($30°C.s^{-1}$) does not enable the recrystallization to occur before phase transformation (720°C). Thus, during reverse transformation, pearlite bands are transformed but austenite also nucleates on the inter-granular cementite particles which kept their initial aligned distribution along deformed ferrite grain boundaries. One obtains then the “banded” morphology made alternatively of the transformation of pearlite bands and linear arrays of carbides parallel to the former pearlite bands.

As already shown in the literature, our experiments demonstrate that recrystallization and austenite transformation kinetics as well as the resulting spatial and morphological distribution of the phases are highly sensitive to the heating rates. The work carried out tends to confirm Li *et al.*’s representation of these related interactions.

The Mn composition of cementite throughout the manufacturing route was measured by TEM from the pearlite transformation at 570°C (occurring just before coiling process) to the cementite dissolution during subsequent annealing at about 700°C. Pearlite transformation occurs with a signification Mn partition between ferrite and pearlite (6.5%). The measured enrichment has been predicted with a remarkable agreement by a thermodynamic analysis inspired by Hutchinson et al..
Slow heating ($3°C.s^{-1}$) permits a further increase in Mn enrichment of cementite. The equilibrium composition, i.e. a high concentration of Mn in cementite (11%) is attained before carbide dissolution. On the contrary, fast heating ($30°C.s^{-1}$) does not let time to Mn for further partition. The cementite keeps its initial Mn concentration before dissolution. All these experimental results are sustained by DICTRA simulations after the reassessment of the Mn diffusion coefficient. A simplified 1-D Finite Difference tool that reproduces the results obtained by DICTRA with a far better CPU-efficiency has been developed and is now also available for product line management.

A unique methodology has been developed to track *in-situ* and concurrently the recovery, the recrystallization and the austenitization during continuous heating and/or isothermal holding of the

studied steel. This method is based on HEXRD experiments on a synchrotron beamline and the obtained measurements were validated by more conventional microscopy techniques.

For both slow and fast heatings, recovery is initiated near about 380°C. During slow heating, the recrystallization starts at 675°C and ends at 710°C, hence before the reverse transformation starts. For fast heating, recrystallization starts at the same temperature as the reverse transformation at 720°C. In isothermal condition, recrystallization occurred only for temperature as high as 650°C.

Physically based models describing both recovery and recrystallization and their couplings have been developed and adapted to the case of cold-rolled ferrite-pearlite steels. The nucleation flux is governed by the SIBM theory and the growth of new grains is calculated by a mobility equation. The recrystallized fraction is calculated using the extended volume theory. The parameters and mobility functions were calibrated to best reproduce observed experimental trends. The experimental kinetics determined during continuous heating and model isothermal holding were very well replicated as well as the grain sizes measured on the SEM micrographs. The prediction of the model once adjusted has been challenged to assess the effect of the cold-rolling ratio on recrystallization kinetics with a very reasonable agreement.

Austenite transformation kinetics were measured *in situ* via HEXRD experiments for slow and fast heating rates up to 800°C (3 and 30°C.s^{-1}). Austenite volume fraction transformed during the heating stage are similar regardless the heating rate, highlighting the fact that the transformation is faster when fast heating. The transformations are slow below 740°C but speeds up when pearlite dissolution starts. The microstructures are half austenitized at end of the heating step, but the thermodynamic equilibrium is far from being achieved. For both heatings, the transformation saturates after 300s during a further isothermal at 800°C. Transformation after fast heating produces a higher austenite amount than expected from the thermodynamic equilibrium.

DICTRA simulations were carried out to study separately and independently the growth of austenite nucleated on pearlite islands (with a banded morphology inherited from the cold-rolling stage) and on intergranular isolated cementite particles. In both cases, it occurs into two stages; the dissolution of cementite and the growth in ferrite.

The dissolution of the pearlite bands occurs at 740°C, independently from the heating rate and from their Mn enrichments. This finding obtained by simulation is consistent with our microstructural characterization. The dissolution stage of pearlite is followed by a rapid growth of the newly formed austenite bands into the surrounding ferritic matrix.

The dissolution of intergranular cementite particles depends on their Mn composition. A transition temperature between a slow and fast dissolution regime has been identified, suggesting that the carbide dissolution is delayed to high temperatures if cementite is enriched in Mn. After dissolution, the growth of resulting austenite is controlled by the local equilibrium prevailing at the austenite/ferrite interface. It occurs with partition of manganese at low heating rates and without at high rates. As a consequence, transformations kinetics is faster at high heating rate and hardly depends on previous carbide enrichment.

During the heating stage of the studied annealing cycle, global transformation kinetics is rather well captured by DICTRA simulations considering the two sub-systems but is overestimated during the soaking stage. When slow heating, austenite nucleation onsets close to the predicted Ac_1 temperatures. In contrast, with slow heating, one pointed out the fact that recrystallization was necessary to permit austenite nucleation on the isolated intergranular carbides.

Our three most important results are thus summarized as follows:

The recrystallization process during annealing affects significantly the distribution of phases during annealing of a deformed ferrito-perlitic structure. The underlying mechanism of interactions

suggests a key role played by intergranular carbides in ferrite, which will serve as preferred nucleation sites.

Cementite is formed with Mn partition during hot-rolling and this enrichment is reinforced during subsequent heat treatments (coiling and annealing). However, the levels of encountered enrichments in the studied steels are not sufficient to have a strong impact on transformation kinetics.

The austenite transformation kinetics of the studied steels during continuous heating can only be understood and modeled if the dissolution of cementite and the growth of austenite are considered separately at the level of pearlitic islands and isolated carbides. The high sensitivity of austenite transformation kinetics observed at low temperature in the studied steel is explained by different growth modes of austenite, with or without partitioning of manganese. Under these simplifying assumptions, the kinetics predicted overestimate nonetheless the slow kinetics observed during holdings at high temperatures.

Outlooks

This work provides numerous new opportunities for future researches in different fields. Most of them have already been discussed in the text and are just reminded below:

- All the data gathered during the HEXRD have not been exploited yet! For instance, annealing treatments at very high heating rates (100°C.s^{-1}) have been also conducted. These results could serve to assess the limit of our models but also to explore the interest of new manufacturing ways for DP steels (inductive heating for instance). Model microstructures (fully ferritic or fully pearlitic) with the local compositions/deformations of the ferrite-pearlite microstructures have also been studied (continuous heating and model isothermal holding). These data could be also useful to calibrate the kinetic models of chapter 5.

- It seems now very important to understand better the formation of intergranular carbides during hot-rolling and how they evolve during the recrystallization. In fact, our work has revealed a surprising increase in the number of intragranular carbides during the heating stage and a possible dissolution/precipitation mechanism to investigate. This process could explain why austenite precipitation starts at lower temperature than expected on the intergranular carbides after recrystallization.

- The new HEXRD methodology to follow in situ recrystallization process of ferrite need surely to be validated on more known systems. The use of advanced set-up could also permit to avoid observed texture effect (rotating sample).

- It would probably be very useful to continue DICTRA modelling work on sub-systems by introducing a unified and average system to describe the growth of austenite after percolation (typically for fractions higher than 30%). At this point, other geometrical configurations could also be tested (inverted spherical growth). The objective is, of course, to better understand why kinetics is poorly described during holding (overestimated).

- Last but not least, a simplified mean-field approach for predicting austenite growth remains to be developed to permit fast calculations in industrial conditions. To do, the model of Wycliffe *et al.* has already been identified as a serious and convincing candidate.

Appendix: re-assessment of the diffusion coefficient for Mn in cementite

In chapter 2, the value of the diffusion coefficient for Mn inside cementite was increased by a factor 2000 to ensure good agreement between our experimental results and thermokinetic simulations. In the same manner, several authors claimed the need in reassessing this value, since many studies showed strong discrepancies between experiments and theory [LIU'09, SON'14, WU'18]. Recently, Wu and Hutchinson [WU'18] have proposed a new diffusion coefficient, being significantly higher in comparison to that employed so far. For that purpose, they performed a large number of measurements during isothermal holdings in the 400-600°C temperature range. In current section, one aims at clarifying the origin of the mobility values stored in the MOBFE2 database. The coefficient used in this work is compared with the original one from the MOBFE2 database as well as the one recently established by Wu and Hutchinson.

Diffusion coefficient for Mn inside cementite according the MOBFE2 database

The values of the diffusion coefficients are determined from numerous possible experiments, whose an exhaustive list is given in [MEH'07]. Because of experimental difficulties, these measurements are performed on convenient C-M binary systems, where M stands any substitutional component. Table A summarizes for instance the multicomponent systems which have been studied to build the MOBFE2 thermodynamic database [MOB2]

Binary:

Ferrite α	C-Fe	C-Cr	Cr-Fe	Cr-N	Cr-Ni	Fe-N	Fe-Ni	Al-Fe		
Austenite γ	Al-Cr	Al-Ni	C-Fe	C-Ni	Co-Fe	Cr-Fe	Cr-Ni	Cu-Fe	Fe-Mn	Fe-N

Ternary:

Ferrite α	C-Cr-Fe			
Austenite γ	Al-Cr-Ni	C-Cr-Fe	C-Fe-Ni	Co-Fe-Ni

Higher order systems:

Ferrite α	C-Cr-Fe-N-Ni
Austenite γ	C-Cr-Fe-N

Table A: list of the multi-components systems experimentally investigated to build the MOBFE2 database. [MOB2]

Thus, the data were produced only from ferrite and austenite, but not from iron carbides as cementite. More important, exact data accounting for ternary systems are missing, whereas it is the most encountered cases. In practice, the diffusion coefficients for higher order systems are determined by extrapolating the values of the concerned binary systems. For example, in the Fe-C-Mn system, the relevant coefficients are calculated upon extrapolating the experimental values from Fe-C and Fe-Mn systems. For a detailed description of the extrapolation procedure, the reader is referred to [DIC'16]. Lastly, the various authors who have investigated Mn diffusion in steels (referred in [MEH'07]) did not investigate temperatures lower than 700°C, raising the question about the validity of this coefficient for lower temperatures and sustaining the initiative of Wu and Hutchinson.

DICTRA does not provide any information about the manner with which the diffusion coefficient for Mn inside cementite is computed. From Agren *et al.* [AGR'86], the Arrhenius law describing the diffusion coefficient for Mn diffusion in cementite was arbitrary considered to be the same than that for Mn diffusion in austenite, following a suggestion from Hillert *et al.* [HIL'69].

Comparison of the diffusion coefficients

Figure 1 and Table B compare the standard diffusion coefficient for Min in cementite stored in the DICTRA MOBFE2 database (black line), the one reassessed in Chapter 3 (red line) and the new one recently established by Wu and Hutchinson. One reminds that in Chapter 3, the standard diffusion coefficient of DICTRA was multiplied by a factor 2000 to obtain a good agreement between experiments and simulations.

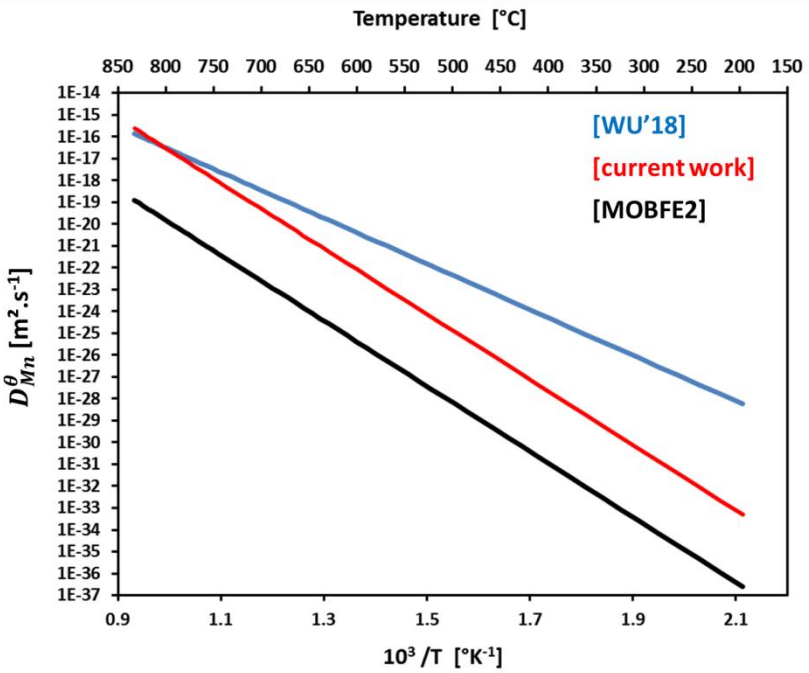

Figure 1: Comparison between the diffusion coefficient values for the standard one stored in the MOBFE2 database (black), the one employed in the current investigation and the new one published by [WU'18]. The related Arrhenius law parameters are reported in Table B.

	MOBFE 2	Current work	Wu and Hutchinson
Pre-exponential factor	1.05×10^{-5}	2.1×10^{-3}	7.86×10^{-7}
Activation enthalpy ($kJ.mol^{-1}$)	286000	286000	200550

Table B: Arrhenius law parameters for the Mn diffusion coefficient in cementite.

References

[AGR'86] Agren, J., Abe, H., Suzuki, T., Sakuma, Y., 1986. The dissolution of cementite in a low carbon steel during isothermal annealing at 700°C. MTA 17, 617–620. https://doi.org/10.1007/BF02643980

[DIC'16] https://www.thermocalc.com/media/46093/Diffusion-Module-DICTRA-User-Guide-2016a.pdf

[LIU'09] Liu, Y., Zhang, L., Du, Y., Yu, D., Liang, D., 2009. Atomic mobilities, uphill diffusion and proeutectic ferrite growth in Fe–Mn–C alloys. Calphad 33, 614–623. https://doi.org/10.1016/j.calphad.2009.07.002

[MEH'07] H. Mehrer, Diffusion in Solids: Fundamentals, Methods, Materials, Diffusion-Controlled Processes, Springer, Berlin; New York, 2007.

[MOB2] https://www.thermocalc.com/media/6014/dbd_mobfe3.pdf

[SON'14] Song, W., Choi, P.-P., Inden, G., Prahl, U., Raabe, D., Bleck, W., 2014. On the Spheroidized Carbide Dissolution and Elemental Partitioning in High Carbon Bearing Steel 100Cr6. Metallurgical and Materials Transactions A 45, 595–606. https://doi.org/10.1007/s11661-013-2048-5

[WU'18] Wu, Y.X., Sun, W.W., Styles, M.J., Arlazarov, A., Hutchinson, C.R., 2018. Cementite coarsening during the tempering of Fe-C-Mn martensite. Acta Materialia 159, 209–224. https://doi.org/10.1016/j.actamat.2018.08.023

Mécanismes métallurgiques et leurs interactions au recuit d'aciers ferrito-perlitiques laminés: caractérisation et modélisation

Les aciers Dual Phase (DP) ferrito-martensitiques sont largement utilisés sous la forme de tôles minces dans la construction automobile en raison de leur excellent compromis résistance/ductilité et donc pour leur potentiel d'allègement. Ils sont élaborés par coulée continue, laminage à chaud et à froid suivis d'un recuit continu. Durant l'étape de chauffage et de maintien de ce recuit, la microstructure ferrito-perlitique déformée issue des étapes de laminage se transforme en microstructure ferrito-austénitique recristallisée. L'expérience montre que les cinétiques de recristallisation et de transformation ainsi que la distribution spatiale et morphologique des microstructures résultantes sont très sensibles aux vitesses de chauffage. Ce travail de thèse s'intéresse aux différents mécanismes expliquant cette sensibilité comme la maturation des carbures, la restauration, la recristallisation de la ferrite et la transformation austénitique et toutes leurs interactions. Ces mécanismes métallurgiques ont été caractérisés à différentes échelles et par des approches in situ sur un acier industriel puis modéliser par des approches à base physique pour guider une possible production.

Après un premier chapitre dédié aux techniques expérimentales et de modélisations utilisées, le second chapitre de ce travail s'intéresse principalement à la caractérisation de la morphogénèse des microstructures ferrito-austénitique en microscopie électronique à balayage (MEB). Le troisième chapitre est une étude détaillée en Microscopie Electronique à Transmission (MET) et par modélisation thermocinétique (ThermoCalc, DICTRA) de la composition des carbures tout au long du processus, du laminage à chaud au recuit. Restauration et recristallisation sont étudiées au chapitre 4 principalement par des expériences in situ en Diffraction des Rayons X à Haute Energie (DRXHE) sur ligne de lumière synchrotron et modélisées par une approche originale à champs moyen. Enfin, le chapitre 5 propose une étude sous DICTRA pour comprendre les cinétiques de transformation austénitique en fonction des vitesses de chauffe. Cette approche est novatrice car elle prend en compte les carbures intergranulaires de la ferrite, a été conduite en conditions anisothermes et propose une analyse fine des modes de croissance de l'austénite associées au manganèse, élément clef de la composition de ces alliages.

MOTS CLES : ferrite, perlite, recristallisation, modélisation, diffraction, austénitisation

Metallurgical mechanisms and their interactions during the annealing of cold-rolled ferrite-pearlite steels: characterization and modeling

Ferrite/Martensite Dual-Phase steels are largely used in the form of thin sheets in the automotive industry for their excellent balance between resistance and strength and thus for their lightening potential. They are elaborated by continuous casting, hot- and cold- rolling, followed by a continuous annealing. During the heating and the soaking stages of this latter process, the deformed ferrite/pearlite microstructure obtained after rolling evolves is transformed into a recrystallized ferrite-austenite microstructure. The experiments show that recrystallization and austenite transformation kinetics as well as the resulting spatial and morphological distribution of the phases are highly sensitive to the heating rate. This PhD thesis aims at understanding the different metallurgical mechanisms explaining this particular sensitivity as carbides ripening, recovery, recrystallization and austenite transformation and all their possible interactions. The mechanisms were characterized at different scales and by in situ technics on an industrial steel and model by physical based approaches in order to drive future production lines.

After a first chapter dedicated to the experimental and modeling methods, the second chapter deals with the characterization of the morphogenesis of ferrite-austenite microstructures by Scanning Electron Microscopy (SEM). Chapter 3 is a study by Transmission Electron Microscopy (TEM) and by thermokinetic modeling (ThermoCalc, DICTRA) of the chemical composition of carbides along with manufacturing, from hot-rolling to annealing. Recovery and recrystallization are studied in chapter 4 by the means of in situ High Energy X-Ray Diffraction (HEXRD) experiments conducted on a synchrotron beamline and modeled by an original mean-field approach. Finally, chapter 5 proposes an analysis with DICTRA to understand austenite transformation kinetics as function of heating rates. The proposed approach is innovative as it accounts for intergranular carbides in the ferrite matrix, is conducted in non-isothermal conditions and propose a fine analysis of growth modes of austenite associated to manganese, a key alloying element of the studied steels.

KEY WORDS: ferrite, pearlite, recrystallization, modeling, diffraction, austeniti